Anne Marthine Rustad

Modeling and Control of Top Tensioned Risers

Thesis for the degree of doctor philosophiae

Trondheim, November 2007

Norwegian University of
Science and Technology
Faculty of Engineering Science and Technology
Department of Marine Technology

NTNU
Innovation and Creativity

NTNU
Norwegian University of Science and Technology

Thesis for the degree of doctor philosophiae

Faculty of Engineering Science and Technology
Department of Marine Technology

ISBN 978-82-471-4011-6 (printed ver.)
ISBN 978-82-471-4025-3 (electronic ver.)
ISSN 1503-8181

Theses at NTNU, 2007:183

Printed by Tapir Uttrykk

Abstract

This doctoral thesis presents new research results on the control of top tensioned risers in deep waters. The main motivation for this work is the development of a riser control system which control the top tension of the individual risers in an array, such that collisions between adjacent risers are prevented. The risk of collision increases with increasing water depth, and as the oil and gas industry is moving to ever deeper waters, riser interaction has become an issue of considerable concern. The two main design parameters to avoid collision are riser spacing and top tension, which both are expensive alternatives. Hence, new solutions are needed and dynamic control of the top tension is the solution proposed here.

A mathematical model of the riser system is developed. It includes two risers in a tandem arrangement which are connected to a tension leg platform (TLP) through their top nodes, forcing the risers to follow the prescribed motions of the TLP in the horizontal direction. In the vertical direction the riser motion is decided by the actuator which is a tensioner system. The risers are also exposed to current forces which are found by considering hydrodynamic interaction. The risers are modeled using the finite element method (FEM). This model is verified by the commercial software RIFLEX.

For the purpose of control applications, the model needs to be computationally fast, but still be able to describe the main physics of the real system. The number of elements needed to keep a desired level of accuracy is therefore investigated. Different means to measure the performance of the model are considered, and among these, payout measurements reflected the displacement of the riser in the best manner. In addition measurements at the wellhead, like payout and tension, are both accurate and available at most installations today. Hence, the proposed control objectives are mainly based on keeping the top tension, payout or total riser length equal for the risers of concern.

A simulation study showed that the dynamic variation of the riser elongation needed to be taken into account in the control algorithm for deep water risers. The reason was that the large difference between tension in the two risers resulted in a significant length difference that had to be compensated for by different payout. In shallow waters the difference between the riser elongations

is smaller, and equal payout is shown to be appropriate. Equal tension, which is used by the industry today, could be applied for small current velocities. A second control objective principle was to measure the relative horizontal distance between the risers keeping it at a desired distance. This method showed promising results, but is dependent on measurements that are not easily available today. The best control objective used in the controller design was found to be equal effective length, meaning that the sum of the payout and the actual riser length should be equal for all risers. Introducing this method may reduce the needed spacing between the risers and thereby reduce the wellbay area on the TLP. A simulation study with model based supervisory switched control showed how the different controller structures and parameters could be included in the feedback loop depending on the operational conditions and riser behavior.

The main contributions in this work are the mathematical modeling of the riser/TLP system, the model analysis, and the proposed controller architecture, including the control objectives and the supervisory switched control concept.

Acknowledgements

This thesis represents the main results of my doctoral studies from August 2004 through August 2007. The work has primarily been carried out at the Norwegian University of Science and Technology (NTNU) and partly at Massachusetts Institute of Technology (MIT). My funding has been provided by the Research Council of Norway through the Center for Ships and Ocean Structures (CeSOS) at NTNU and the Leiv Eiriksson mobility programme.

The work of this thesis has been a true joint project, supervised by Professor Asgeir J. Sørensen and Professor Carl Martin Larsen. I would like to thank Asgeir for his guidance and enthusiastic encouragement, for always backing me up and providing advices both within research and life in general when needed. I deeply appreciate the guidance of and collaboration with Carl Martin. His expertise on modeling and understanding of the physical system has been of invaluable help and inspiration. I would like to thank him for always having his door open for discussions throughout this project.

I am grateful to Professor Michael S. Triantafyllou and Dr. Franz S. Hover for their hospitality and advices during my research stay at MIT from October 2005 through April 2006. Dr. Elizabeth Passano should be thanked for her patience in questions concerning RIFLEX. Another thanks to the MSc students who have suffered under my supervision; André H. Jacobsen for working on TLP modeling, and Simen F. Stølen for cooperation on the riser verification in shallow waters which is included in this thesis. I appreciate the company of my officemates Anders S. Wroldsen at NTNU and Kristoffer H. Aronsen at MIT. I would also like to thank my colleges at CeSOS and the Department of Marine Technology in particular the administration by Sigrid B. Wold and Marianne Kjølås for organization, Dr. Susan Swithenbank and Dr. Jamison Szwalek for proofreading, and Kari Unneland, Jon Refsnes and Per Ivar Barth Berntsen for fruitful discussions.

Finally, I would like to express my gratitude to my friends and family for their support and continuous motivation. A special thanks to my parents and my sister Lene Annette for their love and support during these years with research.

Trondheim, August 2007 Anne Marthine Rustad

Notation

Abbreviations

ACPM	Accurate control plant model
CeSOS	Center for Ships and Ocean Structures.
CFD	Computational fluid dynamics
CPM	Control plant model
DNV	Det Norske Veritas
DOF	Degree of freedom
DP	Dynamic positioning
ESM	Error state maneuvering
FCPM	Fast control plant model
FEM	Finite element method
FPSO	Floating production storage offloading
GoM	Gulf of Mexico
LF	Low frequency
PDE	Partial differential equation
PPM	Process plant model
R1, R2	Riser 1, riser 2
RC	Riser characteristics
ROC	Riser operational conditions
SCR	Steel catenary riser
TLP	Tension leg platform
VIV	Vortex induced vibrations
WF	Wave frequency
WIO	Wake induced oscillations

Characters

The Roman and Greek letters most frequently used throughout the thesis are given here. Bold types are used exclusively to denote vectors and matrices. Bold uppercase denotes matrices and bold lowercase denotes matrices for one riser

element or vectors. All symbols used in the specific contexts are explained when first introduced.

Roman

A, A_e, A_i	Cross-sectional, external and internal riser area
A_{TLP}	Amplitude of the harmonic TLP motion
$\mathbf{C}, \mathbf{c}_i$	System and element damping matrices
C_D	Drag coefficient
C_M, C_m	Inertia and added mass coefficients
D, D_e, D_i	Diameter, external diameter, internal diameter
E	Young's modulus of elasticity
$\mathbf{f}_{ext}, \mathbf{f}_{int}$	External and internal force vectors
$\mathbf{K}, \mathbf{k}_i$	System and element stiffness matrices
K_D, K_I, K_P	Controller gains
l, l_r	Riser length
l_i	Riser element length
l_t	Tendon length
$\mathbf{M}, \mathbf{m}_i$	System and element mass matrices
n, N	Number of elements
P_i, P_{top}	Effective axial tension in element i and the applied top tension
$\mathbf{r}$	Riser position vector
$\mathbf{R}_g^f, \mathbf{R}_{y,x}$	Rotation matrices
$\mathbf{T}_i^f$	Transformation matrix from i- to f-frame
T_j	Top tension of riser j
T_{TLP}	Period of the harmonic TLP motion
v_i	Current velocity in node i
x_i	Horizontal riser position of node i
x_{TLP}	TLP surge position
z_i	Vertical riser position of node i
$\mathbf{w}_{eff}$	Effective weight

Greek

Δ	Difference
γ	Norm function
μ	Monitoring error
ρ	Process switching signal
ρ_f, ρ_s, ρ_w	Density of the internal fluid, steel and water
σ	Controller switching signal
τ	Controller contribution
θ_i	Inclination of element i
ξ	Payout

Contents

Chapter 1

Introduction

Oil and gas are by far Norway's largest export industries, being more than 50% of the export value in 2006 (Ministry of Petroleum and Energy and the Norwegian Petroleum Directorate, 2007). The first oil in Norwegian territory was found in 1969 at the Ekofisk field, located at 70-75m water depth. The first production started there in 1972. Since then, knowledge and experience have developed, and the petroleum industry in Norway presently has expertise on offshore installations in harsh environment and deep water, which is based on disciplines like hydrodynamics, structural mechanics, oceanography, automatic control, material science, etc. However, as new oilfields are explored and developed, new challenges arise and new knowledge and research are needed. New contributions are searched for within each discipline. It is believed that by integrating the different disciplines, further progress can be made. At the Center for Ships and Ocean Structures (CeSOS) at the Norwegian University of Science and Technology (NTNU), the disciplines of hydrodynamics, structural mechanics and automatic control are integrated as a strategy to contribute to the innovation of ships and ocean structures. New approaches will hopefully result in new solutions to currently unsolved problems. This thesis is situated at the intersection between structural mechanics and automatic control, but also some hydrodynamics are included. This is illustrated in Fig. 1.1 with a cross marking where this thesis can be found discipline-wise. Working in a multi-discipline field creates new problems, but also opens for new possibilities.

1.1 Motivation

Offshore petroleum production began in the most shallow waters. As these reservoirs are exploited together with an increasing demand for oil and gas, the petroleum industry has been moving to ever deeper waters. Riser technology is an

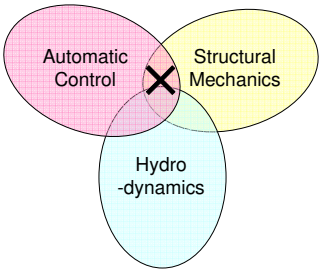

Figure 1.1: Intersection of the different disciplines found in this work.

important issue both when considering field development costs and technological feasibility. In deeper waters interference between adjacent top tensioned risers in an array is an issue of considerable concern (DNV, 2005). Collision may lead to dents in the riser pipe and also damage in the coating, with fatigue and corrosion as possible consequences. Even a single collision event may be damaging if the collision takes place with sufficiently high impact.

If the riser spacing and properties are kept constant, the risk of collision will increase with increasing water depth, since the static deflection due to the uniform current drag is proportional to the square of the length (Huse, 1993). In deep waters this means that even a relatively small difference in static forces may lead to mechanical contact. In addition flow separation and shielding effects between risers in an array can change the local flow velocity. This difference in current forces may cause large relative motions and lead to contact between neighboring risers. There are mainly two design parameters that will prevent collision between risers:

1. Increasing the riser spacing.

2. Increasing the top tension.

Both may result in significant cost penalties. Increasing the riser spacing means increasing the size of the wellbay (Fig. 1.2). This has influence on the global platform parameters like deck space and load carrying capacity. The other option is increasing the top tension to a high and constant level, which will increase the wear and tear on the cylinders in a heave compensation system. The main objective of this work is to prevent, or at least reduce, the number of collisions by applying control of the riser top tension.

For deep water production systems, riser solutions are traditionally divided into two main groups; (1) subsea wellheads (wet trees) with flexible risers up to a floater like a semi-submersible or a production ship (floating production

Figure 1.2: The wellbay on the TLP Snorre (www.statoil.com).

storage offloading - FPSO), and (2) tensioned risers with wellhead on a compliant platform, like tension leg platform (TLP), spar[1] or deep draft floater (DDF). These are the dry tree solutions for floating production systems. Dry tree systems are often the preferred solution for production as they provide easy access to the well for maintenance, intervention and workover. Alternative platform solutions, while still using dry tree systems, are proposed by Often (2000) for a semi-submersible with heave compensation system, and by Mortazavi *et al.* (2001) for deep draft caisson vessel with buoyancy cans. Pollack *et al.* (2000) suggest a weight based tension leg deck (TLD) to which the risers are locked for a dry tree solution on FPSOs. This solution allows long stroke for spread moored ship-shaped vessels. Wanvik and Koos (2000) present a two tier well riser tension system, which is a mechanical alternative to hydraulic cylinders working in series. This system separates the low frequency stroke motion from the wave induced stroke motion.

Top tensioned risers operated from spars and TLPs are arranged in clusters of (near) vertical riser arrays. The number of individual risers in an array may be 20 or more, which may consist of different risers applied for production, drilling, workover, export, etc. The problem of riser collision can be restricted to tensioned risers operated from a TLP or a spar located in deep waters. This is due to the small space available for the high number of risers, in addition to the increased

[1] A spar is a vertical, cylindrical buoyant platform, usually manned.

deflection for long risers.

A TLP is chosen as the platform concept for this work. The main reason is that tensioned risers can be applied at a TLP with a relatively small requirement for stroke capacity even at large TLP offsets. This is a consequence of the geometric restrictions for heave motions caused by the axially rigid tendons. For other floaters like spars, FPSOs and semi-submersibles, the demand for stroke capacity will be much higher, which means that other riser solutions like steel catenary risers (SCR) or flexible risers are preferred. Hence, the control system presented in this thesis is most likely to be applied on a TLP.

Deep water TLPs are mainly found in the Gulf of Mexico (GoM), but there are also some west of Africa and off the coast of Brazil. A TLP solution was considered at the Ormen Lange field 100km west of mid-Norway at 850m water depth, but a system with subsea wells and pipelines to the onshore plant was chosen. This solution is possible for a reservoir mainly consisting of gas. For a reservoir with heavier hydrocarbons this solution may not be possible. Ellida is a large oilfield 60km north of Ormen Lange and located at 1200m water depth. The field was discovered in 1997, but it is unknown if the field is commercial viable. However, if it is decided to develop the field, a TLP could be a possible solution here.

1.2 Previous Work

Most research within the field of collision between risers focuses on the hydrodynamic interaction between them. In addition some work has been done on the actual collision forces and the damage it may cause. Little or nothing has been done to actively control the riser motions. Dynamic behavior and collision of risers have been studied by several scientists the last decade. DNV (2005) gives a thorough introduction to riser interference, and the definitions given in the recommended practice will be followed here.

Each top tensioned riser in an array is exposed to environmental loads from waves, currents, and forced floater motions, both at wave frequency (WF) and low frequency (LF). Whether or not collision between two neighboring risers occurs depends on factors like top tension, riser spacing, floater offset, environmental loads, hydrodynamic interaction, and riser properties to mention some. Direct wave loads on the upper part of the riser and first order floater motions are assumed insignificant for such heave compensation systems, because the collision is most likely to occur in the midsection of the riser, where the deflection is largest due to current loads. The assessment of riser interference is therefore mainly based upon the assumption of a steady state current profile.

Little information regarding interaction effects due to wave loading is found

(Duggal and Niedzwecki, 1993), while significant effort has been applied to investigate hydrodynamic interaction in steady current, see Huse (1987, 1993, 1996), Huse and Kleiven (2000) and Kavanagh *et al.* (2000). A reference should also be made to Blevins (1994) and Zdravkovich (2003) for numerous experiments on hydrodynamic interaction between cylinders. Note that within the field of hydrodynamics, cylinders is the general term used to denote marine risers, tendons, cables, etc. For more industrial studies, the term riser is often used. We will strive to use the terms in the same way as in each referred paper. Zdravkovich (1977) gives a careful review on flow between two circular cylinders in various arrangements in steady flow. Zdravkovich (2003) presents arrangements with three or more cylinders, and an extensive list of references may be found here.

Experiments by Tsahalis (1984), Bokaian and Geoola (1985), and recent studies by DNV (2003) and Kalleklev *et al.* (2003) have shown that interaction between neighboring risers will not have any hydrodynamic influence on the upstream riser beyond a certain distance. Furthermore, the literature distinguishes between three different kinds of forces acting on the downstream riser in the wake of an upstream riser. These effects are (DNV, 2005):

- Mean force and shielding effects bringing the risers closer together.
- Wake induced oscillation (WIO) on the downstream riser.
- Vortex induced vibrations (VIV) resulting in amplified drag coefficients on both risers.

The mean forces are modeled by two different methods; the parametric wake field model and the parametric mean force model. Both can be applied in finite element method (FEM) models. The parametric wake field model is a semi-empirical static wake formulation which accounts for the interaction between stationary individual cylinders in steady current. This was studied by Huse (1987, 1993, 1996), and is based on the analytic expression of a turbulent wake by Schlichting (1968). The inflow of a cylinder situated in the wake of an upstream cylinder can be computed at any location. The drag force is computed by taking the actual velocity into account, but keeping the drag coefficient constant. A mean transverse force is formulated for cylinders more arbitrarily placed in the wake. In Huse (1993), a scheme for calculating the inflow of an array of cylinders is proposed.

The parametric mean force model was derived by Blevins (1994). In this method the hydrodynamic forces are accounted for by introducing mean drag and lift forces on the downstream cylinder as a function of the distance from the upstream cylinder. The mean lift force is directed towards the wake centerline, where the current velocity is smallest. The drag and lift coefficients in

the parametric mean force model need to be established by model tests or by two dimensional numerical methods like computational fluid dynamics (CFD). Gopalkrishnan *et al.* (1994) and Wu *et al.* (1999) have investigated the drag and lift forces in steady current. The purpose of both studies was to gain necessary information in order to assess the onset of potentially interference problems and collision. Blevins (2005) developed a model for steady lift and drag forces on a cylinder in the wake of an upstream one by using theoretically based equations fitted to data from experiments. Wu *et al.* (2001*a*,*b*) investigated the onset criteria for wake induced instability, assuming two identical cylinders in steady uniform flow. The interest for tendon and riser interference in the work of Tsahalis (1984) and Gopalkrishnan *et al.* (1994) is related to Shell's activity on deep water TLPs like Auger and Mars. An ongoing research program has been in progress since 1989 (Allen *et al.*, 2005). Most of these results are published in confidential reports, and have not been accessible to the public.

The parametric mean force model is also able to capture WIO. The study of WIO dates back to the early 1970's and the study of power transmission lines. References could be made to for instance Simpson (1971), Price (1975) and Tsui (1977). For marine applications, these motions were first observed and described by Huse (1996) and later by Wu *et al.* (2002). The risers are exposed to current over a very long length relative to the diameter, and the flow around the risers will cause large hydrodynamic interaction forces. These may cause slowly varying, large amplitude motions of very irregular behavior, occurring about the first natural mode of motion. Such motions may also occur at significantly lower frequencies, which means that they are quasi-static and caused by unstable hydrodynamic forces. WIO are in any case found at frequencies substantially lower than the vortex shedding frequency. Lately, Fontaine *et al.* (2007) reproduced WIO in model scale and identified the different regimes (stable, unstable and critical). The onset criteria for WIO and clashing between SCRs were proposed.

A slightly different approach on the parametric wake force model was proposed by Sagatun *et al.* (2002). The basis in this model was a parametric force representation for both upstream and downstream riser based on coefficients found from CFD. In addition to mean forces, dynamic forces are described in the time domain using position dependent force parameters. The objective was to assess whether or not adjacent risers move in the wake of an upstream riser. Sagatun *et al.* (2002) postulated that the slowly varying WIO controlled the relative position of the risers, while VIV with higher frequencies and velocities accounted for most of the energy in a riser collision. However, note that the large riser displacement governed by mean force and WIO are found to be unaffected by VIV, except from the magnified drag force (Tsahalis, 1984, DNV, 2003). Tsahalis (1984) also found that the VIV responses are different for the upstream and downstream

risers. The VIV response for the downstream riser is given by the mean water velocity of the riser, which is different from the velocity on the upstream riser due to the wake effect.

Kavanagh *et al.* (2000) did VIV model tests and outlined how riser interference for deep water risers was assessed using a combination of wake flow modeling, global interference analysis and VIV prediction. Allen *et al.* (2005) investigated the riser interference on flexible risers, with focus on VIV and Reynolds number. VIV is in itself subject to research as it is important for fatigue as well as to calculate drag forces on the riser, see for instance Kaasen *et al.* (2000) and Halse (2000). For the amplified drag coefficient, see Sarpkaya and Shoaff (1978) and Vandiver (1983).

The design practice of today does not allow collision neither under normal nor extreme conditions (DNV, 2005). As keeping the risers clustered in an array with small riser spacing is an advantage with respect to both economy and operation, the industry is considering accepting that riser collision occurs. Nygård *et al.* (2001) investigated the stress levels generated by the impact between two neighboring risers. The result indicated acceptable stress levels and served as a first step to allow some impacts to occur. Herfjord *et al.* (2002) presented a numerical model for the simulation of the interaction and clashing of flexible risers. The work includes methodology for contact dynamics of interacting risers and recorded riser impacts, collision statistics and stress analysis. The impact of collision and participating mass for colliding risers is also treated in Sagatun *et al.* (1999) and Neto *et al.* (2002). Leira *et al.* (2002) have used the method from Sagatun *et al.* (2002) in a case study to estimate extreme response and fatigue damage for colliding risers. Kalleklev *et al.* (2003) proposed a design practice that properly accounts for collision between risers in operating conditions typical for major deep water locations. Lately, Baarholm *et al.* (2005) did model tests to better understand the mechanics that drive the risers to collision, including relative velocity at the time of collision which is a measure on its intensity. Both bare risers and risers with VIV suppression (strakes) or bumpers along the collision zone were tested. These measured results provided benchmarks for code validation of riser collisions. Little has been done on experiments for more than two risers. However, Huang *et al.* (2004) examined the wake shielding for three risers in a towing tank. Significant drag reduction on the downstream cylinders was found.

During the last decade, some doctoral theses on modeling and control of cables have been written at NTNU. Fard (2000) investigated vibration control of flexible mechanical systems (i.e. VIV on marine risers) with focus on passivity of nonlinear beams. Aamo (2002) applied FEM to model and analyze passivity properties of mooring lines, and found that passive controllers could be applied for dynamic line tensioning in a mooring system. Türkyilmaz (2004) modeled a towed

seismic cable and investigated its passivity properties. Ersdal (2004) developed a FEM model for towed flexible cylinders and investigated the hydrodynamic forces on cylinders in axial flow through experiments. Fredheim (2005) worked on current forces on net structures, including experiments on drag and lift forces on an array of risers. Johansen *et al.* (2006) presented a new model for dynamics of inextensible cables, by separating axial and transverse motion. Lately, Wroldsen (2007) has been working on cable models based on differential algebraic equations for efficient computation and realtime purposes.

Control of risers is in its infancy and little is published. An exception is the work of Sabri *et al.* (2003) who use active control to make it possible to connect a riser to a wellhead in harsh weather. A reduced model for the behavior of the bottom riser end and a control law were developed. Only position measurements at the bottom riser end and the control action at the top are needed to follow the reference trajectory. This method is patented, see Sabri *et al.* (2006).

For drilling operations, the top and bottom riser angles are of concern, and should not exceed an upper limit of 2-4 degrees during drilling. To achieve this, the position of the drilling vessel is optimized by including the inclination measurements in the feedback loop for the dynamic positioning (DP) system. The use of riser angle positioning system (RAPS) was first investigated by Dean (1980). The system was successfully tested aboard the drillship Discoverer Seven Seas in 1979. Suzuki *et al.* (1995) used modal expressions for a riser at 4000m water depth with current loads in the upper 1000m. To control the riser angles, actuators like thrusters or remote operated vehicles (ROV) were suggested to be used along the riser. The DP system for drilling vessels with automatic control of the riser end angle (REA) was proposed by Imakita *et al.* (2000). The objectives were (1) to minimize the REA by vessel positioning and (2) to perform ship position based on REA measurements with riser angle sensor and neural network. Ship positioning sensors were not used as the proposed system should act as a backup for commercial available positioning systems, either satellite based or hydroacoustics with fixed reference systems on the seabed. Sørensen *et al.* (2001) proposed an optimal setpoint chasing algorithm for drilling vessels in deep waters. The main objectives were to minimize the bending stiffness along the riser and the riser angles at the top and bottom joints. Sørensen *et al.* (2002) were also motivated to use riser angle as a reference system for drilling risers, in addition to the existing systems. Improving the quality of position measurements will increase the availability of the drilling vessel in bad weather, and give a fast payback of the investment. The design principle of a riser angle positioning reference system (RAPR) with an observer model is proposed. The riser model is a quasi-static FEM model and accounts for varying current loads and top tension. The requirement for redundant positioning references motivated also Høklie *et al.* (2002). They estimated vessel positioning by measuring the riser angles and

using Kalman filtering technics. A dynamic mathematical model is tuned by combining the vessel position measurement and riser inclinations and use this to estimate the current profile. After the initial tuning, the model is able to estimate the vessel position based on the riser inclination measurements and the estimated current profile. The system was initially tested with success aboard the drill ship Saipem 1000 west of Africa at 1100m and 2300m water depth in June 2002.

Active heave compensation is used today under drilling and in crane operations for offshore equipment. The first is commercially available, for instance by Aker Kværner (2007) and National Oilwell Varco (2007*a*). Korde (1998) investigated an actively controlled heave compensation aboard deep water drillships subjected to irregular waves. Active control of a heave compensated crane during the water entry phase for the equipment is addressed by Sagatun (2002). Johansen *et al.* (2003) made model experiments where the strategy was to synchronize the load with the waves in the moon pool. Recently Perez and Steinmann (2007) performed an analysis of operability and constraints in terms of vessel motions and heave compensator stroke capacity.

However, heave compensation of top tensioned production risers has not earlier been investigated. The top tension is today kept constant by passive systems. In order to avoid collisions Huse and Kleiven (2000) proposed a strategy based on equal payout for risers in an array. All risers were connected to a common frame in the top end, and no collision could be observed in steady current. The work in this thesis is motivated by the work of Huse and Kleiven (2000). But instead of keeping the risers fixed to a plate, the top tension of each riser is controlled individually using the payout of the heave compensator as the measured input.

1.3 Main Contributions

The main contributions found in this thesis are summarized here. Parts of this thesis have earlier been published. References to these publications are given below.

- Firstly, the work in this thesis has shown that it is possible to prevent collision between neighboring risers by use of top tension control and measurements at the riser end and wellhead onboard the TLP. This was first shown in Rustad *et al.* (2006), and later in Rustad *et al.* (2007*b*,*c*). Control of risers by changing the top tension has not previously been published.

- A two-dimensional model for the TLP and riser system exposed to current is developed. How the specified motion from the TLP acts on the risers is not earlier published. This modeling is found in Chapter 3 and is published in Rustad *et al.* (2007*c*).

- The mathematical system model is verified by the commercial software RIFLEX (Fylling *et al.*, 2005) in Chapter 4. Parts of this are found in Rustad *et al.* (2007*c*). An extensive analysis on how many elements are needed for the various applications and purposes is found in Chapter 7. This has not been published earlier.

- Four different riser control objectives are formulated. These include two existing objectives; one used in the industry today and one earlier proposed by Huse and Kleiven (2000). In addition, two new control objectives are proposed here. These are presented and investigated in Chapters 6.1 and 8, respectively, and could to a large extent also be found in Rustad *et al.* (2007*b*,*c*). The control objectives are presented for two risers in a tandem arrangement, but can be expanded to three dimensions and a matrix of risers.

- A model based, supervisory switched control system is proposed and simulated in Sections 6.4 and 8.5, respectively. This case study is also presented in Rustad *et al.* (2007*a*).

1.4 Organization of the Thesis

The outline of the thesis is as follows:

Chapter 2 introduces the TLP concept and the background for the TLP solution. The most famous existing platforms are presented.

Chapter 3 presents the mathematical modeling of the system. This consists of two risers in a tandem arrangement, exposed to TLP motions in the top end and current forces. The riser tensioner system, being the actuator in the system is also modeled.

Chapter 4 verifies the riser model from Section 3.5. The validation of the model for different water depths and bottom end connections is investigated.

Chapter 5 gives an overview of the physical implementation of the system being the actuator, measurement and controller system design.

Chapter 6 presents the controller architecture. This includes the control objectives, riser operational conditions and the different controllers.

Chapter 7 analyses the control plant model thoroughly. Both the quasi-static and dynamic models are simulated with varying TLP position and top tension.

Chapter 8 shows the simulation results. These includes investigation of the different control objectives and a case study with supervisory switched control.

Chapter 9 summarizes the main conclusions of this thesis and proposes further work.

Appendix A includes additional details of the mathematical modeling, not included in Chapter 3.

Appendix B gives the environmental data, riser data and controller gains used in the simulations in Chapter 8.

Chapter 2

Tension Leg Platform

The main purpose of the TLP model in this thesis is to represent the platform motions at the wellhead area where the risers are linked to the platform. The surge motions will act as a prescribed dynamic boundary condition in the riser analysis, while heave relative to vertical motions of the upper riser end is subjected to active control. Heave motions of a TLP have two components. One is cause by dynamic elastic strain and deflections of the tendons, which will influence the true distance between its ends. The other component is referred to as *surge induced heave*, and is easily understood by realizing that the inclined tendon will have another vertical distance from the seafloor than its true length. The motions caused by local tendon dynamics are significantly smaller than the surge induced component - in particular in extreme wave conditions - and is neglected in this work. This was done for the case of simplicity, but could have been included without any conceptual changes in the approach. Conclusions from this study are hence valid even if this simplification was made. This chapter is mainly based on Demirbilek (1989*b*), Faltinsen (1990) and Larsen (1995).

2.1 Background for the TLP Solution

Offshore platform concepts are usually classified into two major categories; *fixed* and *compliant*. Fixed platforms stand at the seabed and remain in place by a combination of their weight and/or piles driven into the soil. Little or no motions are observed for such structures. The fixed platforms resist the environmental forces like wind, wave and current by generating large internal reaction forces. The first offshore oil and gas fields were found in shallow waters, and mainly fixed structures were build in the first decades of offshore oil production. Fixed platforms will normally have natural periods shorter than 5s and their responses which are caused by extreme waves will therefore be quasi-static since such waves

typically will have periods above 10s.

As offshore development moved towards deeper waters, the application of conventional fixed jackets approached its limits principally imposed by the dynamic behavior of the structures (Litton, 1989). With increasing water depths, fixed platforms become more flexible, and their natural periods started to enter the high energy levels of the ocean waves. To keep the eigenperiods away from this damaging range, fixed structures had to be designed to be stiffer, requiring more steel and exponentially increasing costs.

The obvious alternative to fixed platforms in deep water is to use compliant platforms. The basic idea is to allow for rigid body motions with eigenperiods longer than wave periods ($T > 30$s). Compliant platforms may be divided into three types; floaters, towers and TLPs.

A floating platform will have all its structural eigenperiods well below 5s, which means that ordinary wave loads will not give any structural dynamic response. However, dynamics of rigid body motions for floaters are of concern. Eigenperiods are controlled by the geometry of the water-plane (heave, pitch and roll) and design of the anchor system (surge, sway and yaw). These eigenperiods are normally above wave periods, but resonance may still occur due to wind and higher order wave forces. Hydrodynamic damping is the key to reduce these types of response. Any anchored vessel, semi-submersible, spar and FPSO belong to this category.

Towers are fixed to the seafloor by an arrangement that eliminates, or at least reduces, the bending moment at the bottom end. Horizontal motions of the deck are compliant, but vertical motion components are equivalent to a fixed platform.

A TLP acts like a floater with regard to in-plane motion components (surge, sway and yaw), but like a fixed platform for the out-of-plane components (heave, roll and pitch). The governing parameters for the in-plane stiffness are the tension and length of the tendons, while the cross section area, modulus of elasticity and length of the tendons decides out-of-plane stiffness. The design premises for the tendon system are hence to determine these parameters so that desired values of the eigenfrequencies can be obtained.

In addition to considering the sensitivity of the platform to external environmental forces, the choice of platform system depends upon other considerations. Amongst these are the technical and economic factors, including water depth, production rate, reservoir size, service life and removal requirements. However, in deep waters the major factor in selecting the platform for a field development plan is the cost which is correlated to its weight. The cost of the floating system, especially that of the TLP, are relatively insensitive to changes in the water depths compared to the cost of the compliant towers and fixed structures (Litton, 1989). Hence, economic factors make the compliant platforms and the TLPs in particular one of the leading candidates for major deep water developments,

especially when a dry tree solution is preferred.

2.2 The TLP Concept

The basic idea behind the TLP concept was to make a platform that is partly compliant and partly rigid. In order to maintain a steel riser connection between the seafloor and the production equipment on the platform, heave, roll and pitch motions had to be minimized and are rigid degrees of freedom. The horizontal forces due to waves on the vertical cylinders will always be larger in the horizontal plane than in the vertical direction. Hence, by making in-plane motions compliant, the largest environmental forces can be balanced by inertia forces instead of by forces in rigid structural members. This idea can be realized by a pendulum using buoyancy to reverse gravity forces (Larsen, 1995).

The TLP is defined as a compliant structure, but might also be classified as a moored structure. In general, the TLP is similar to other column stabilized moored platforms with one exception; the buoyancy of a TLP exceeds its weight, and thus the vertical equilibrium of the platforms requires taut moorings connecting the upper structure to a foundation at the seabed. These taut mooring are called tension legs, tethers or tendons. Drilling and production risers connecting the platform to the wellhead template on the seafloor are in general not a part of the TLP mooring system (Demirbilek, 1989*a*). The different parts of the TLP are illustrated in Fig. 2.1, and defined by the American Petroleum Institute (1987) as follows:

- **The hull** consists of the buoyant columns, pontoons and the intermediate structure bracings.
- **The deck structure** supports operational loads. It is a multilevel facility consisting of trusses, deep girders and deck beams.
- **The platform** consists of the hull and deck structure.
- **The foundation** is found at the seabed and consists of templates and piles, or even a gravity system.
- **The tendons** connects the platform to the foundation at the seabed.
- **The mooring system** consists of the tendons and the foundation.
- **The risers** include drilling, production and export risers.
- **The well system** includes flowlines, risers, riser tensioners, wellhead and the subsea well templates.

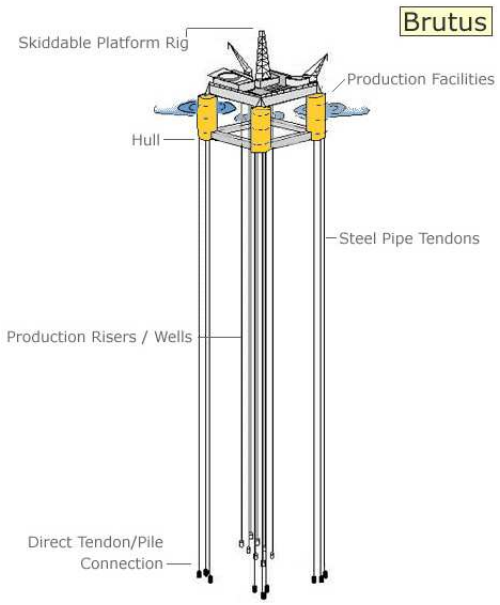

Figure 2.1: The layout of the Brutus TLP in the GoM (www.offshore-technology.com).

- **The tension leg platform** includes all the above, in addition to all deck equipment and the hull system.

2.3 Existing Platforms

Interest in TLPs dates back to 1960 and many studies have examined the applicability of this concept for deep water developments (Demirbilek, 1989*a*). During the next two decades, and especially after the installation of the Hutton TLP in 1984, the TLP concept began attracting more attention from the offshore industry as an appropriate structure for deep water applications.

There are at the moment installed approximately fifteen TLPs, of which three are found in the North Sea. The others are found in the Gulf of Mexico, on the west coast of Africa and off the coast of Brazil. The increase in water depth for TLPs is illustrated in Fig. 2.2. The deepest installed TLP today is the Magnolia platform. Below follows a list with short descriptions of the some of the most famous platforms.

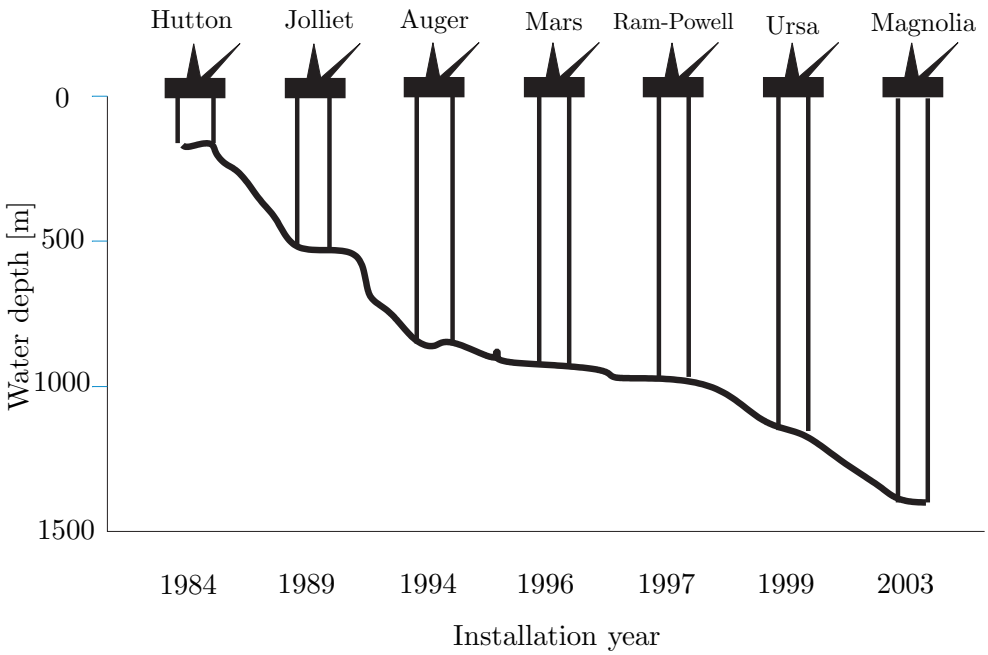

Figure 2.2: The development of TLPs and riser depths.

Hutton (UK) The Hutton TLP was the first of its kind and was installed by Conoco in the British sector of the North Sea in 1984. The installation serves as a combined drilling/wellhead, production, and quarter platform on a medium sized oil and gas field at 150m water depth. A conventional steel jacket would be a less costly alternative, but the TLP solution was chosen to gain experience with this concept for future applications on larger water depths. The tendons are made of thick-walled tubes with conical threaded couplings. These tendons have large submerged weight which will contribute to unwanted deflections when the tendons are inclined (Larsen, 1995).

Snorre (Norway) The Snorre field lies in the central North Sea approximately 200km west of Florø in Norway at 310m water depth. It was installed in 1988 by Saga Petroleum, and the production started in 1992 (Ministry of Petroleum and Energy and the Norwegian Petroleum Directorate, 2007). Snorre was developed in two phases and the production facilities comprise a steel TLP on the southern part of the field and a subsea production system tied back to the TLP (Offshore Tecnology, 2007). 36 wells are drilled from the TLP. The Snorre TLP is moored to the seabed by sixteen steel tendons 0.8m in diameter. The platform is an in-

Figure 2.3: The Snorre TLP (www.statoil.com).

tegrated drilling, production and living quarter installation. The main difference between Snorre and Hutton is that Snorre is much larger, it has four columns instead of six, and the tendons have larger diameter and smaller wall thickness (Larsen, 1995). Fig. 2.3 shows a picture of the Snorre TLP.

Jolliet (USA) The Jolliet platform was the first real deep water TLP and was installed by Conoco on the Green Canyon field in the GoM at 536m water depth in 1989. This platform is significantly smaller than both Hutton and Snorre, and is often referred to as a tension leg wellhead platform (TLWP) (Larsen, 1995).

Auger (USA) By the Auger platform, the TLP concept was brought to a new frontier. The platform is of the same size as Hutton, but the water depth is even larger than for Jolliet with 872m. Many of the design principles from Jolliet are found at Auger. Note that the tensioned risers on Auger are inclined in order to decrease the spacing distance between the wellheads on the deck compared to the needed spacing at the seafloor. Auger has catenary anchor lines in addition to the tendons. These serve two main purposes; (1) to increase lateral stiffness and thereby reduce static offset due to wind and current, and (2) to enable the platform to have a wanted offset position during well drilling and maintenance (Larsen, 1995).

Figure 2.4: The Mars TLP after the hurricane Katrina (www.worldoil.com).

Heidrun (Norway) The Heidrun platform was installed in 1995 at 345m water depth. It is the first and only concrete TLP, and has significantly larger displacement than the earlier TLPs. The hull and tendons system have been tuned to minimize first order wave motions, but the result was that *ringing* (see Sec. 3.4) became a bigger problem for this TLP than for the others (Larsen, 1995).

Mars (USA) Mars was installed in 1996 by Shell at 950m water depth and had the water depth record when installed. It is also the largest producing TLP in the GoM. The Mars platform's drilling rig was heavily damaged during Hurricane Katrina in August 2005 (see Fig. 2.4). It was shut down, as it was exposed to over four hours of sustained winds of 270km/h, with gusts over 320km/h (Paganie, 2006). The production at Mars resumed on May 22 2006, after undergoing a series of repairs to its damaged platform rig and export pipelines.

Ursa (USA) Shell began the field production at Ursa in 1999, at approximately 1200m water depth. This TLP is designed to simultaneously withstand hurricane force waves and winds. The deck is composed of six modules: wellbay, quarters, power, drilling and two process modules. The deck modules are an open truss frame design (90x90x15m) with a total steel weight of 12,500 tons. There are twelve well slots, and the well layout on the seafloor is arranged in a rectangular pattern (30x18m). The TLP supports a single modified API platform-type

(a) Before the hurricane Rita. (b) Upside down following the hurricane Rita.

Figure 2.5: The Typhoon TLP of SeaStar design (www.upstreamonline.com).

drilling rig (leased) equipped with a surface blow out preventer (BOP) and high pressure drilling riser.

Morpeth (USA) The three-legged Morpeth SeaStar is a mini-TLP and the first TLP without surface completions. It was successfully installed in 1998 in 518m water depth at a cost of less than $100 million (Rigzone, 2007).

Brutus (USA) Brutus is a Shell installation at 910m water depth with production start in 2001. The batch setting of the eight wells was completed on January 3 2000. Four of the planned development wells for the eight-slot TLP were subsequently predrilled, with the well layout on the seafloor arranged in a rectangular pattern. Brutus is Shell's fifth TLP in the GoM and the seventeenth deep water project in the GoM in which Shell was involved (Rigzone, 2007).

Typhoon (USA) Chevron's mini-TLP Typhoon of SeaStar design was installed in July 2001 at 700m water depth. It severed from its mooring and capsized following the hurricane Rita fall 2005. It was floating upside down when found after the hurricane. Fig. 2.5 shows the platform before and after the hurricane Rita struck.

Matterhorn (USA) This mini-TLP is an Atlantia SeaStar design of the type previously installed on such deep water projects as Chevron's Typhoon and British-Borneo's Morpeth and Allegheny fields. At 1350m, however, the Matterhorn SeaStar was the largest when built in November 2003, and doubled the

size of the previous units. It was the first unit of this design to incorporate dry trees.

Marco Polo (USA) The Marco Polo field is located at 1300m water depth in the GoM. The field was discovered in April 2000. In 2003, the last two development wells were drilled. The field was developed with a dry tree TLP installed in January 2004. It came online in July 2004 and is expected to reach peak production of 50,000 barrels of oil equivalent per day (Rigzone, 2007).

Magnolia (USA) The Magnolia field by Conoco Phillips was installed at 1433m water depth, a new record depth for this type of floating structure in the GoM. The production started in December 2004. The field is located approximately 50 km from the existing infrastructure, which will enable Magnolia to be a regional off-take point for future developments or third party tie-ins located in Southeastern Garden Banks area (Offshore Tecnology, 2007).

Kizomba (Angola) The Kizomba deep water project is located off the west coast of Angola. The field was installed in August 2005 at 1260m water depth. Kizomba A consists of three main components. The drilling center is a TLP that includes a rig and 36 slots for drilling the project's oil and gas wells. The TLP contract was awarded to ABB in partnership with Heerema of Holland. Moored nearby is a FPSO, designed to take all of the oil produced from the platform, process it and store it until the oil can be offloaded onto waiting tankers (Rigzone, 2007).

Chapter 3

Mathematical Modeling

Mathematical models may be formulated in various levels of complexity. We usually distinguish between *process plant models* and *control plant models* (Sørensen, 2005). The process plant model (PPM) is a comprehensive model of the actual physical process. The main purpose of this model is to simulate the real plant dynamics, including environmental disturbances, control inputs and sensor outputs. A successful numerical simulation for design and verification of our control system require a sufficiently detailed mathematical model of the actual process. The control plant model (CPM) is simplified from the process plant model containing only the main physical properties. It may be a part of the model-based controller. The CPM is often formulated such that the analytical stability analysis becomes feasible.

This chapter will focus on the process plant model. The system modeled here consists of two risers connected to a TLP through the top nodes, forcing the top nodes to follow the prescribed motion from the TLP in the horizontal direction. The top nodes are free in the vertical direction, only affected by the top tension acting as a vertical force. In addition the risers are exposed to current forces that are found by considering hydrodynamic interactions between the risers.

Interaction between two cylinders is often classified into two categories according to the space between them; the *proximity interference* when the two cylinders are close to each other, and *wake interference* when one cylinder is in the wake of an upstream cylinder (Zdravkovich, 1985). Top tensioned marine riser systems normally fall into the latter category, although proximity interference also can take place. It is also found that the in-line motions are much larger than the transverse motions. We will focus on two risers in a tandem arrangement, were the centers of the two risers are aligned parallel to the free stream (Fig. 3.1). It is assumed that a two-dimensional model will capture the most important dynamics of the riser array system. Analysis of the three-dimensional effects are subject

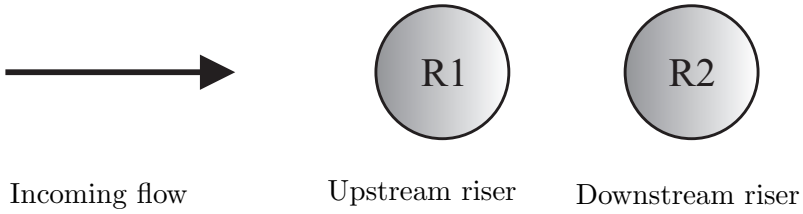

Figure 3.1: The risers in a tandem arrangement.

for further research.

3.1 Current Models

Current models could be divided in two: (1) Surface current, needed for ships and floaters, and (2) full current profile, for use in load models for risers, tendons, anchor lines, etc. Two different geographical areas are chosen to investigate the risers behavior under various current velocity conditions. These are:

- The Ormen Lange field in the North Sea.
- The Gulf of Mexico (GoM).

Common to these selected areas are that they are:

- Located in deep waters.
- Tend to have strong current velocities, with different profiles.
- TLPs are already situated here or considered situated here.

The current profiles from these areas will be explained in more detail. In addition, some linear, theoretical profiles will be investigated. There are three main components in the resulting current profile:

- Wind generated currents.
- Tide generated currents.
- Major ocean currents.

The formulas for these current components can be found in Faltinsen (1990). Here, we have used in-plane profiles which may vary in velocity through the water column. The profiles from the North Sea and GoM are design profiles,

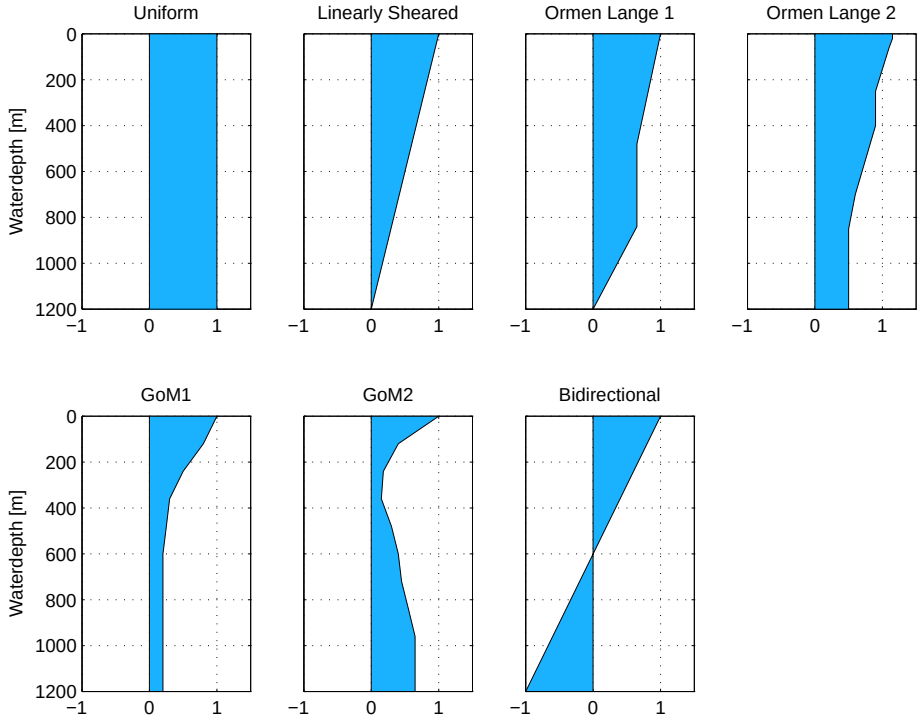

Figure 3.2: The simulated current velocity profiles in m/s.

based on measurements and dimensioned for 1200m water depth. All current velocity profiles are illustrated in Fig. 3.2. The current velocity data are given in Appendix B.1.1, and can be summarized as:

- **Uniform current (theoretical)** meaning constant current velocity for the entire water column.
- **Linearly sheared current (theoretical)** which denotes a linearly decreasing current velocity throughout the water column, with a given velocity at the sea surface and 0m/s at the seafloor.
- **Ormen Lange 1** which is a one year return period current profile for the Ormen Lange field based on Herfjord *et al.* (2002) and extended to 1200m water depth by linearly decreasing the velocity from 0.65m/s at 850m down to 0m/s at the seabed.
- **Ormen Lange 2** which is a one year return period current profile found in Aker Maritime (2002), originally given in Norsk Hydro (2001). It is

extended from 850m to 1200m water depth. The current between these depths are considered constant at 0.5m/s.

- **Gulf of Mexico 1 (GoM1)** which is a wind driven current velocity profile in the GoM, based on a non-dimensional profile in Nowlin *et al.* (2001). It is dimensioned for 1200m water depth and 1m/s current velocity at the sea surface.

- **Gulf of Mexico 2 (GoM2)** which is a current profile with a loop eddy in the top layer, also based on Nowlin *et al.* (2001) and scaled the same way as GoM1.

- **Bidirectional current (theoretical)** which represents a linear shear current with opposite current directions at the sea surface and the seabed.

For the current profiles related to a geographical area, a further explanation is given. The Ormen Lange field is close to the shelf edge. This gives often strong and variable current, and might potentially cause operational challenges (van Smirren *et al.*, 1999). In Fig. 3.2 the current velocities are seen to be large at the sea surface due to wind generated current, but also large all the way down to the seabed since the field is close to the shelf edge. For the rest of the analysis and simulations in this thesis, the Ormen Lange 2 is used. It will be referred to as the Ormen Lange design current profile or just the Ormen Lange profile.

For GoM2 a loop eddy is seen to reduce the current at 200-400m water depth, whereas the velocity increases again for even larger water depths. The loop currents found in the GoM are due to a large flow of warm water that dominates the circulation within the eastern part of the GoM. It is due to the Gulf Stream which flows northwards between Cuba and the Yucátan peninsula, Mexico. Some of the current moves straight north into the GoM, and then loops east and south before it exits to the east through the Florida Straits. Some loop currents tear off the main stream and flow clockwise westward into the GoM (Wikipedia, 2007*a*, NOAA Coastal Services Center, 2007). This is illustrated in Fig. 3.3.

Last, a bidirectional shear current is presented. A bidirectional current profile can be found west of Shetland, and is due to a residual warm flow northeastward usually in the upper layer, and a southwestern cold flow in the lower layer. In addition to the residual flow there are tidal currents. Here a simple linear, bidirectional shear current is introduced to investigate the riser behavior and verify the model for a wider range of environmental conditions.

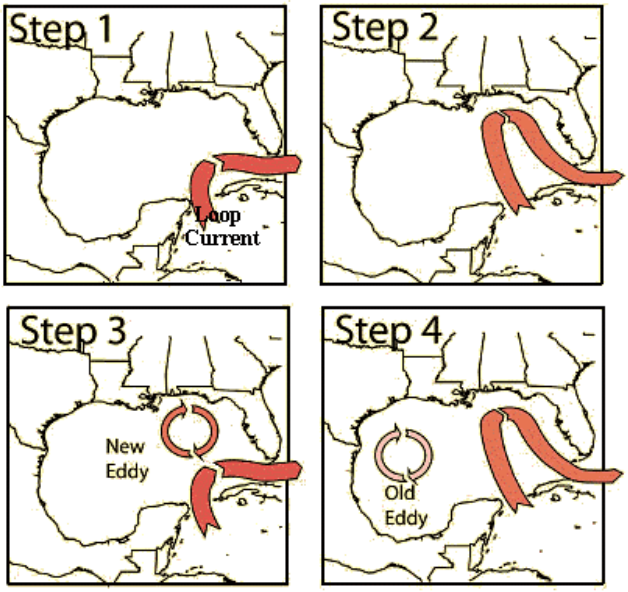

Figure 3.3: Loop current in the Golf of Mexico (www.oceanexplorer.noaa.gov).

3.2 Hydrodynamic Interaction

Recall form Section 1.2 that interaction between two neighboring risers will not have any hydrodynamic influence on the upstream riser (R1) beyond a certain distance, and that R1 can be treated as an isolated riser (Kalleklev *et al.*, 2003, DNV, 2003). The attention will therefore be given to the hydrodynamic influence on the downstream riser (R2). Also remember the three most important effects for assessment of riser interaction (DNV, 2005):

1. Mean force and shielding effects, tending to bring the risers closer.
2. WIO on the downstream riser.
3. VIV leading to amplified drag coefficients for both risers.

In this thesis we will focus on shielding effects, which is of main importance when calculating the mean current force, and hence the position of the second riser in the wake. The two latter effects will not be included in the simulations, but are briefly described here for completeness. Inclusion of these effects may have an influence on the relative riser displacements, but to a lesser extent on the control strategy.

Since the riser model is two-dimensional in a tandem arrangement, the lift force is not included, and Huse's model for wake shielding effects is an appropriate model choice.

3.2.1 Shielding Effects

R2 experiences reduced mean drag force due to shielding effects, depending on the location in the wake. A semi-empirical static wake formulation to account for the hydrodynamic interaction between individual risers in steady current was proposed by Huse (1993). The reduced velocity field in the wake of the upstream cylinder, see Fig. 3.4, is given by

$$V_r\left(x,y\right) = k_2 V_c \sqrt{\frac{C_D D_e}{x_s}} e^{-0.693\left(\frac{y}{b}\right)^2}, \tag{3.1}$$

where V_c is the incoming current velocity on R1, C_D is the drag coefficient, D_e is the diameter of the upstream riser, and y is the distance away from the centerline of the incoming velocity profile. x_s and b are defined as

$$x_s = x + \frac{4D_e}{C_D}, \quad b = k_1\sqrt{C_D D_e x_s}, \tag{3.2}$$

where $k_1 = 0.25$ and $k_2 = 1.0$ for a smooth circular cylinder. x is the distance behind the upstream riser R1, and x_s is the distance between the downstream riser R2 and a virtual wake source upstream of R1. The wake may be influenced by VIV of the upstream riser, but this effect is considered insignificant for the present use of the wake model. The mean inflow on the downstream riser is hence given by

$$V_{mean} = V_c - V_r. \tag{3.3}$$

It is assumed that mechanical contact occurs when the distance between the riser centers is equal to one riser diameter (1D). The parametric wake model is only applicable for the far wake region larger than two diameters (2D) behind R1. The behavior of the flow in the near region is not adequately described as this is a highly nonlinear phenomenon, where R2 might experience negative drag forces (Kavanagh *et al.*, 2000). The center-to-center distance should therefore preferably be kept larger than 2D. A more extended presentation of how (3.1) is derived, is found in Appendix A.1.

3.2.2 Wake Induced Oscillation

The WIO is described as a broad band buffeting force due to oncoming turbulent flow and vortices shed from the upstream riser. This may result in a LF, large-amplitude motion of the downstream riser which wander around in the wake

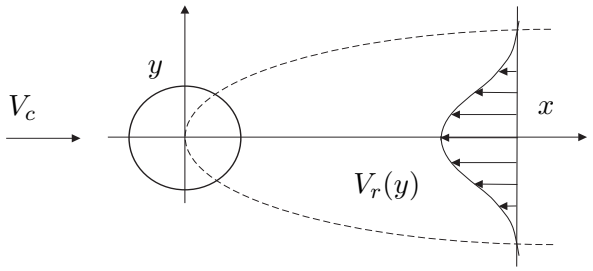

Figure 3.4: The decrease in the in-line water particle velocity in the wake region, from Huse (1993).

and is likely to cause collision (Huse, 1996, Wu *et al.*, 2002). In one experiment Huse (1996) investigated the interaction between cylinders. It was observed that in addition to the high frequency VIV response of amplitudes up to one half of the diameter, the downstream cylinder also had LF in-line oscillations of an apparently very irregular nature with the peak-to-peak stroke of these oscillations up to 30 to 40 diameters or more. These motions occur at the first mode of the riser. Later Wu *et al.* (2002) found the peak-to peak range to be 20D. A more detailed review on existing models are found in DNV (2005). However, this kind of oscillations and the physics behind it is so far not well understood. It will therefore not be implemented in this work, and is subject for further research.

3.2.3 Vortex Induced Vibrations

Recall that the large displacements due to shielding effects and WIO are found to be independent of VIV, except from the magnified drag coefficient (Tsahalis, 1984, DNV, 2003, 2005). Therefore, an amplified drag coefficient due to VIV needs to be included. The amplified drag is modified with VIV amplitude A and diameter D. One of the used relations presented by Vandiver (1983) is

$$C_D' = C_D \left(1 + 1.043 \left(2\frac{\sqrt{2}A}{D} \right) \right)^{0.65} . \tag{3.4}$$

A conservative estimate is to select a high value for the upstream riser and a low value for the downstream riser. This will bring the risers closer together in their static positions. Anyhow, very little information is available for VIV behavior for a downstream riser. In this study we have used equal and constant drag coefficients for both risers. The drag coefficients are not used explicitly in the controller algorithm, and will therefore not have impact on the conclusions as such.

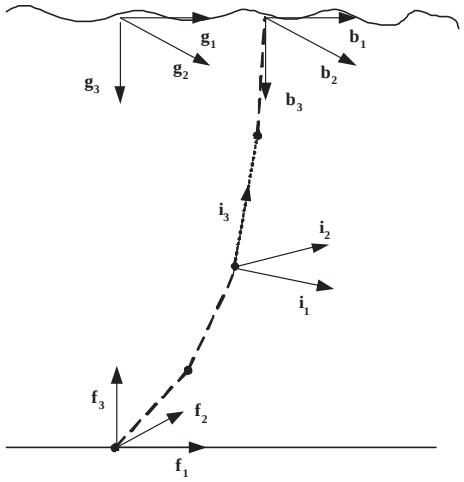

Figure 3.5: The coordinate systems: f - fixed frame for first riser, g - global frame at the surface, b - body frame of TLP, i - element frames.

3.3 Kinematics and Coordinate Systems

Four orthogonal coordinate systems are used to describe the riser and TLP motions, see Fig. 3.5. A bold letter with subscript $i = \{1, 2, 3\}$ denotes the unit vector along the x, y and z axes in the frame respectively, i.e. $\mathbf{f}_1$ denotes the unit vector along the x-axis for the seafloor fixed frame. The coordinate systems are all right-hand systems.

seabed fixed frame (f-frame): The f-frame (o_f $\mathbf{f}_1$ $\mathbf{f}_2$ $\mathbf{f}_3$) is considered inertial and is fixed to the seafloor. The positions of all the riser nodes in the global system are described relative to this frame. $\mathbf{f}_1$ points to the right, $\mathbf{f}_2$ points into the plane and $\mathbf{f}_3$ points upwards normal to the earth surface.

Body-fixed frame (b-frame): The b-frame (o_b $\mathbf{b}_1$ $\mathbf{b}_2$ $\mathbf{b}_3$) is fixed to the body of the TLP with axes chosen to coincide with the principal axes of inertia for the body with origin in the center of gravity. $\mathbf{b}_1$ is the longitudinal axis pointing forward, $\mathbf{b}_2$ is the transversal axis pointing starboard, and $\mathbf{b}_3$ is the normal axis pointing downwards.

Global frame (g-frame): The g-frame (o_g $\mathbf{g}_1$ $\mathbf{g}_2$ $\mathbf{g}_3$) is fixed to the sea surface right above the f-frame with a distance in heave direction equal to the water depth and is also considered inertial. $\mathbf{g}_1$ points to the front side of the TLP, $\mathbf{g}_2$ points to starboard, and $\mathbf{g}_3$ points downwards normal to the

Earth surface. The position vector $\mathbf{r}_{TLP,bg}^{\ g} = [x_{bg}^g, y_{bg}^g, z_{bg}^g]^T$ describes the position of the b-frame relative to the g-frame expressed in the g-frame. The origin, o_g, is located on the mean water free-free surface so that z_g passes through the center of the TLP when it is in its static undisturbed equilibrium.

Local riser frames (i-frame): The i-frames (o_i $\mathbf{i}_1$ $\mathbf{i}_2$ $\mathbf{i}_3$) used in the finite element modeling (FEM) are located in the i-th node of the riser and is a local frame for each element i. $\mathbf{i}_1$ is to the right of the element, $\mathbf{i}_2$ is pointing into the plane, and $\mathbf{i}_3$ is along the axial direction of the element pointing upwards. The forces acting on the element, such as tension, effective weight and current due to drag are computed in this frame for each element and thereafter transformed to the f-frame. There are as many i-frames as there are number of elements in the FEM model.

3.4 Tension Leg Platform

Recall that the TLP is a partly rigid and partly compliant structure. The eigenfrequencies for in-plane motions must be below frequencies for wave energy and the frequencies for the out-of-plane motions must be above. With respect to the horizontal degrees of freedom, the TLP is compliant and behaves similar to other floating structures. The horizontal degrees of freedom surge, sway and yaw are inertia dominated with eigenperiods around 1-2 minutes, well above the range of first order waves with periods of 5-20s. With respect to the vertical degrees of freedom, it is stiff and resembles a fixed structure. The vertical degrees of freedom heave, roll and pitch are stiffness dominated with eigenperiods in the order 2-4s, and well below the period of the exciting first order waves (Larsen, 1995).

The eigenfrequencies in all six degrees of freedom (DOFs) are tuned relative to the first order wave loads. Thus, loads at the wave frequencies do not excite the TLP at its natural frequencies. On the other hand, second or higher order loads at the sum and difference frequencies can produce significant resonant excitations at the TLP natural frequencies because of the small amount of damping available at these frequencies (Faltinsen, 1990, Mekha *et al.*, 1996).

- Higher order components and sum frequencies ($2\omega_i$, $2\omega_j$, $\omega_i + \omega_j$) in waves may give significant resonance oscillations for the TLP in heave, roll and pitch known as *ringing* and *springing*. The restoring forces are due to the tendons and the mass forces due to the TLP, and they are excited by the nonlinear wave effects. Ringing is associated with transients effects, while springing is steady-state oscillations (Faltinsen, 1990).

- Loads on difference frequencies ($\omega_i - \omega_j$) will give slowly varying wave loads that may give rise to resonant in-plane motions. Excitation from wind gusts may appear in the same frequency range and contribute significantly to such motions (Faltinsen, 1990, Mekha *et al.*, 1996).

Both these nonlinear phenomena should be considered when designing a TLP. The ringing and springing phenomena have impact on the upper and lower limits of the tendon force. The mean wave drift and current loads on the hull will induce a *mean offset force*. Assuming linear analysis as the water depth increases, the eigenperiod of the riser system increases as well. The first eigenperiod for a riser at 1200m water depth is approximately 30-40s depending of the top tension and cross section properties. As the riser eigenperiod is approaching the eigenperiods in surge and sway for the TLP, induced motions from these components may have more influence on the riser dynamics than in more shallow waters.

3.4.1 TLP Surge Modeling

Floater models and analysis are usually divided into two groups; *separated or de-coupled analysis* and *coupled analysis*. For separated analysis the vessel motions are found first. The effects from moorings and risers are included as nonlinear position dependent forces or stiffness. The damping or velocity dependent forces, which are important for estimation of the LF motion may be neglected. In the second step, the dynamic response on the risers and moorings are analyzed, using the vessel response from step one as a forced displacement on the top node. The main problem with this method is that inertia and drag forces on the risers and tendons are not accounted for. These effects could be large in deep waters (Ormberg *et al.*, 1998, Chen *et al.*, 2002). The term coupled analysis means simultaneous analysis of vessel motions, mooring systems and riser dynamics where the full interaction is taken into account. The main drawback with this method is that it is very time consuming since a nonlinear time domain simulation is required. Much effort has been put into the investigation of coupled and separated analysis and solutions in between, see Mekha *et al.* (1996), Ormberg and Larsen (1997), Ormberg *et al.* (1997, 1998), Ma *et al.* (2000), Chaudhury and Ho (2000), Chen *et al.* (2002). For an extensive description of TLP, tendons and mooring, see Demirbilek (1989*b*).

In this study we assume that the TLP motions influence the riser behavior. However, the risers do not affect the TLP motion. The TLP represents the specified motion in surge for the top node of each riser. Hence, a de-coupled analysis model is applied. Since the system model is two-dimensional, only the

surge motion for the TLP is needed. It is modeled as a LF harmonic motion

$$x_{TLP} = A_{TLP} \sin\left(\frac{2\pi}{T_{TLP}} t\right) + x_{off}, \tag{3.5}$$

where x_{off} is the static TLP offset, A_{TLP} is the amplitude, and T_{TLP} is the period of the TLP motion.

3.4.2 Kinematics

The motions of the TLP are given as the motion of the b-frame relative to the g-frame in the g-frame with the position vector position vector $\mathbf{r}_{TLP,bg}^{\ g} = [x_{bg}^g, y_{bg}^g, z_{bg}^g]^T$. As the riser motions are expressed in the f-frame, the rotation matrix between the f- and g-frames is needed. The transformation from g- to f-frame is given by the diagonal matrix

$$\mathbf{R}_g^f = diag\,(1,\ -1,\ -1)\,. \tag{3.6}$$

Since both frames are considered inertial and fixed with a translation in heave direction only, all axes are parallel, and the x-axes are always pointing in the same direction. In a two dimensional system, only the surge motion of the TLP is needed to define the prescribed motion of the riser. Hence, the motion in x-direction for the TLP described in the g-frame is equal to the x-position given in the f-frame. Thus the frames are omitted for the surge position of the TLP, x_{TLP}.

3.4.3 Riser Stroke Calculations

Marine risers made of steel have very low structural strength against lateral loading unless they are tensioned. It is therefore important to maintain the upper end tension at a certain level under all realistic conditions, irrespective of platform motions, dynamic riser response and internal flow parameters. The tensioner system will therefore act as a heave compensating system with an adequate stroke capacity and ability to maintain a near constant tension (Larsen, 1993).

If the relative platform/riser motion exceeds the stroke capacity, unwanted loss of tension or tension increase will occur. Such situations may result in excessive bending stresses in the riser, excessive rotations of the ball joint or excessive riser tension. Such loads may cause damage to the well template or the riser tensioning system. Other unwanted effects might be mechanical interaction between neighboring risers or between the riser and the platform. When designing the riser tensioner system, consequences of such events must be taken into considerations (Larsen, 1993).

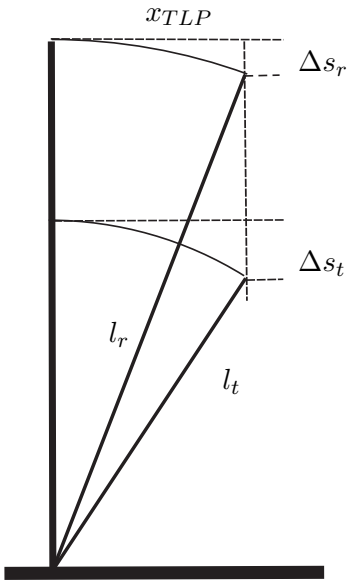

Figure 3.6: Setdown due to tendon/riser geometry.

The platform vertical motion is the most important parameter that defines stroke. For a TLP with vertical and parallel tendons in the initial zero offset position, motions in surge direction will not induce any pitch motion, but will be coupled to the vertical motion referred to as *surge induced heave* or *setdown*. Using the Pythagorean theorem and assuming both risers and tendons to be straightlined, the relative setdown between the riser and the platform can be found. The position of the platform is controlled by the tendons. The offset in surge, x_{TLP}, is equal for the risers and the tendons, but as the risers are longer and hence have larger radius, their setdown is smallest. The relative setdown, Δs, is found as

$$\Delta s = \Delta s_t - \Delta s_r = \left(l_t - \sqrt{l_t^2 - x_{TLP}^2} \right) - \left(l_r - \sqrt{l_r^2 - x_{TLP}^2} \right), \tag{3.7}$$

where Δs_t and Δs_r are the tendon and riser setdown respectively, and l_t and l_r are the tendon and riser lengths. This is illustrated in Fig. 3.6. For given l_t and l_r, we can calculate the setdowns for the upper end of the risers and tendons. The relative setdown is for normal TLP designs small, even for large water depths and offsets, due to the tendon and riser geometry. Hence, the requirement for heave compensation due to surge induced offset is small.

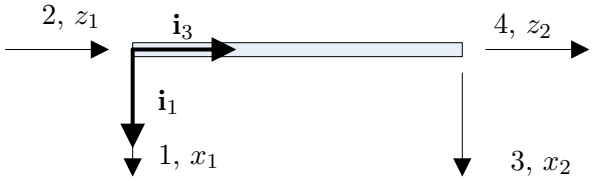

Figure 3.7: The bar element with four DOFs. Node 1 to the left with the two first DOFs. Node 2 to the right with the third and fourth DOFs.

3.5 Riser FEM Modeling

The partial differential equation (PDE) governing the static and dynamic behavior of a riser can not be solved exactly for arbitrary riser problems and load patterns. Hence, a numerical method is required, such as the finite element method (FEM). The stiffness matrix in the FEM model will have an elastic and a geometric component. The elastic stiffness matrix accounts for the axial and bending stiffness as present in any beam, while the geometric stiffness matrix will take into account the changes of the global geometry and the stiffening effect from the tension. As the depth is increasing, the riser will behave more and more like a cable, and the geometric stiffness will become more important than the elastic stiffness. Hence, the geometric stiffness gives the main contribution to lateral resistance against the static and dynamic forces acting perpendicular to the longitudinal riser axis.

At larger water depths a simplification of the riser model can be made by neglecting the bending stiffness and assuming free rotations at the ends. In cases where the global geometry is of major importance this will only introduce a small error. Hence, a model consisting of bar elements is sufficient. Each bar element in a two dimensional model can be described with four DOFs, that is two translational DOFs in both ends of the element. x is transverse of the element, positive to the right along $\mathbf{i}_1$, and z is along the element, positive upwards along $\mathbf{i}_3$, see Fig. 3.7.

The riser is fixed to the seabed, and the top node displacement is prescribed in the horizontal direction, whereas it is free to move vertically. Note, however, that the top tension, P_{top}, is introduced at the upper end, which prevents the riser from collapsing. The tension vector, $\mathbf{f}_{top}$, is an external force and will be found on the right hand side of the equation of motion according to

$$\mathbf{f}_{top} = \begin{bmatrix} \mathbf{0}_{1\times(2n+1)} & P_{top} \end{bmatrix}^T. \tag{3.8}$$

In later chapters top tension is referred to as T, while P_{top} is used in the modeling

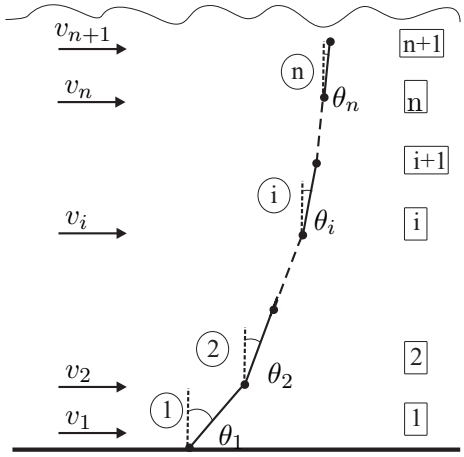

Figure 3.8: Numbering of the elements (encircled), nodes (boxes), current v_i in each node i and the inclination θ_i of each local element i, relative to the global frame.

as tension applied at the top node.

3.5.1 Transformations for the Riser Elements

The risers are modeled with n elements and $n+1$ nodes, with node number 1 at the seabed and node $n+1$ at the wellhead area on the platform. θ_i is the inclination of element i relative to the global coordinate system f-frame, which is situated at the seabed in the first node of the upstream riser. The numbering of elements, nodes and the inclination of each local element are illustrated in Fig. 3.8. v_i^f is the current in node i expressed in the inertial f-frame. Note that i is used as the numbering of the elements, nodes and the corresponding inclination. The positions x_i and z_i of the nodes along the riser are found through equilibrium iterations, and are used to calculate the sine and cosine of the inclination θ_i of each element, needed for use in the transformations between the global and local coordinate systems. The length of each element i is found by use of the Pythagorean theorem

$$\Delta x_i = x_{i+1} - x_i, \quad \Delta z_i = z_{i+1} - z_i, \quad l_i = \sqrt{\Delta x_i^2 + \Delta z_i^2}, \tag{3.9}$$

$$\cos\theta_i = \frac{\Delta z_i}{l_i}, \quad \sin\theta_i = \frac{\Delta x_i}{l_i}. \tag{3.10}$$

The transformation between the local i-frame and the global, fixed f-frame is described by a rotation about the y-axis (Fossen, 2002)

$$\mathbf{R}_{y,\theta} = \begin{bmatrix} \cos\theta & 0 & \sin\theta \\ 0 & 1 & 0 \\ -\sin\theta & 0 & \cos\theta \end{bmatrix}. \tag{3.11}$$

Since we are only considering a two-dimensional system with two DOFs in each node, the transformation matrix from i to f is written as

$$\mathbf{T}_{0,i}^{f}(\mathbf{r}) = \begin{bmatrix} \cos\theta_i & \sin\theta_i \\ -\sin\theta_i & \cos\theta_i \end{bmatrix}, \tag{3.12}$$

where $\mathbf{r}$ is the displacement vector, as the inclination in each element is given as a function of the positions, given in the seafloor fixed f-frame. For notational simplicity the superscript f is omitted as $\mathbf{r}$ is always given in the f-frame. The full displacement vector is given as

$$\mathbf{r} = \begin{bmatrix} x_1 & z_1 & x_2 & z_2 & \cdots & x_i & z_i & \cdots & x_n & z_n & x_{TLP} & z_{n+1} \end{bmatrix}^T. \tag{3.13}$$

For all four DOFs related to an element we have

$$\mathbf{T}_{i}^{f}(\mathbf{r}) = \begin{bmatrix} \mathbf{T}_{0,i}^{f}(\mathbf{r}) & \mathbf{0}_{2\times 2} \\ \mathbf{0}_{2\times 2} & \mathbf{T}_{0,i}^{f}(\mathbf{r}) \end{bmatrix}, \tag{3.14}$$

as the inclination of each element is a function of the positions of its nodes.

3.5.2 System Mass Matrix

For each element a mass matrix is defined based on the local coordinate system. The local mass matrix consists of three terms; the structural mass of the riser $\mathbf{m}_s$, the internal fluid $\mathbf{m}_f$, and the hydrodynamic added mass $\mathbf{m}_a$. The structural mass is given by

$$\mathbf{m}_{si} = \frac{\rho_s A l_i}{6} \begin{bmatrix} 2 & 0 & 1 & 0 \\ 0 & 2 & 0 & 1 \\ 1 & 0 & 2 & 0 \\ 0 & 1 & 0 & 2 \end{bmatrix}, \tag{3.15}$$

where ρ_s is the density of the riser material steel, A is the cross sectional area of the riser, and l_i is the length of element i found from (3.9). The internal fluid is included as well

$$\mathbf{m}_{fi} = \frac{\rho_f A_{int} l_i}{6} \begin{bmatrix} 2 & 0 & 1 & 0 \\ 0 & 2 & 0 & 1 \\ 1 & 0 & 2 & 0 \\ 0 & 1 & 0 & 2 \end{bmatrix}, \tag{3.16}$$

where A_{int} is the internal area of the riser, and ρ_f is the density of the internal fluid. The derivation of the consistent mass matrix structure is found in Appendix A.2.1. The local added mass in the axial z-direction is assumed to be zero, while the added mass for a circular cylinder in the lateral x-direction is equal to the displaced water volume (Sumer and Fredsøe, 1997). The matrix for the added mass is then given as

$$\mathbf{m}_{ai} = \frac{\rho_w C_m A_e l_i}{6} \begin{bmatrix} 2 & 0 & 1 & 0 \\ 0 & 0 & 0 & 0 \\ 1 & 0 & 2 & 0 \\ 0 & 0 & 0 & 0 \end{bmatrix}, \tag{3.17}$$

where A_e is the area found from the exterior diameter D_e, and ρ_w is the density of water. The coefficient C_m is called the hydrodynamic added mass coefficient. The total local mass matrix $\mathbf{m}_i$ for each element i in its own frame is then the sum of the three terms written as

$$\mathbf{m}_i = \mathbf{m}_{si} + \mathbf{m}_{fi} + \mathbf{m}_{ai}. \tag{3.18}$$

Each local matrix $\mathbf{m}_i$ is transformed to the global f-frame fixed to the seabed, and all the local mass matrices are assembled to form the global mass matrix $\mathbf{M}$ for the riser. Each local mass matrix is transformed to f-frame by

$$\bar{\mathbf{m}}_i = \mathbf{T}_i^f \mathbf{m}_i \mathbf{T}_i^{fT} = \begin{bmatrix} \bar{\mathbf{m}}_{11}^i & \bar{\mathbf{m}}_{12}^i \\ \bar{\mathbf{m}}_{21}^i & \bar{\mathbf{m}}_{22}^i \end{bmatrix}, \tag{3.19}$$

where $\bar{\mathbf{m}}_i$ is the mass matrix for element i in the global f-frame. For $\bar{\mathbf{m}}_{11}^i$ the superscript is used to recognize the element number, and the subscript is used to identify the different parts of the mass matrix, needed for the concatenation to the global matrix. $\mathbf{T}_f^i$ is the transformation matrix from the f-frame to the i-frame. The full, global mass matrix in the f-frame for n elements is then

$$\mathbf{M} = \begin{bmatrix} \bar{\mathbf{m}}_{11}^1 & \bar{\mathbf{m}}_{12}^1 & & & & \\ \bar{\mathbf{m}}_{21}^1 & \bar{\mathbf{m}}_{22}^1 + \bar{\mathbf{m}}_{11}^2 & \bar{\mathbf{m}}_{12}^2 & & & \\ & \bar{\mathbf{m}}_{21}^2 & \bar{\mathbf{m}}_{22}^2 + \bar{\mathbf{m}}_{11}^3 & & & \\ & & & \ddots & & \\ & & & & \bar{\mathbf{m}}_{22}^{n-1} + \bar{\mathbf{m}}_{11}^n & \bar{\mathbf{m}}_{12}^n \\ & & & & \bar{\mathbf{m}}_{21}^n & \bar{\mathbf{m}}_{22}^n \end{bmatrix}. \tag{3.20}$$

The global mass matrix $\mathbf{M}$ is always given in the f-frame, and the superscript f is hence omitted. The size of the global matrix is $2(n+1) \times 2(n+1)$.

3.5.3 System Stiffness Matrix

The local stiffness matrix consists of two terms; the elastic stiffness, $\mathbf{k}_E$, and the geometric stiffness, $\mathbf{k}_G$. The geometric stiffness matrix includes the effective axial tension P_i acting on the particular element i. The elastic stiffness matrix works in the axial direction, whereas the geometric stiffness in the lateral direction. The resulting stiffness matrix $\mathbf{k}_i$ for the element i in its own frame becomes

$$\mathbf{k}_i = \mathbf{k}_{E_i} + \mathbf{k}_{G_i} = \frac{1}{l_i}\left(EA \begin{bmatrix} 0 & 0 & 0 & 0 \\ 0 & 1 & 0 & -1 \\ 0 & 0 & 0 & 0 \\ 0 & -1 & 0 & 1 \end{bmatrix} + P_i \begin{bmatrix} 1 & 0 & -1 & 0 \\ 0 & 0 & 0 & 0 \\ -1 & 0 & 1 & 0 \\ 0 & 0 & 0 & 0 \end{bmatrix} \right), \tag{3.21}$$

where E is Young's modulus of elasticity. The derivation of the consistent stiffness matrix is found in Appendix A.2.2. The effective axial tension P_i in each element is according to Appendix A.4 related to the elongation of the element by

$$P_i = \frac{EA}{l_0}\Delta l_i, \quad \Delta l_i = l_i - l_0, \tag{3.22}$$

where l_0 is the initial length of an element in a stressfree riser. To calculate the global stiffness matrix for the riser, we transform each local stiffness matrix from its local i-frame to the global f-frame, similar to what was done with the mass matrix. These are concatenated to the global stiffness matrix $\mathbf{K}$ in the same way as the mass matrix. The full, global stiffness matrix in the f-frame for n elements is then

$$\mathbf{K} = \begin{bmatrix} \bar{\mathbf{k}}_{11}^1 & \bar{\mathbf{k}}_{12}^1 & & & & & \\ \bar{\mathbf{k}}_{21}^1 & \bar{\mathbf{k}}_{22}^1 + \bar{\mathbf{k}}_{11}^2 & \bar{\mathbf{k}}_{12}^2 & & & & \\ & \bar{\mathbf{k}}_{21}^2 & \bar{\mathbf{k}}_{22}^2 + \bar{\mathbf{k}}_{11}^3 & & & & \\ & & & \ddots & & & \\ & & & & \bar{\mathbf{k}}_{22}^{n-1} + \bar{\mathbf{k}}_{11}^n & \bar{\mathbf{k}}_{12}^n \\ & & & & \bar{\mathbf{k}}_{21}^n & \bar{\mathbf{k}}_{22}^n \end{bmatrix}. \tag{3.23}$$

3.5.4 Structural Damping

The damping experienced by a riser is a combination of the structural damping and hydrodynamic damping, resulting from both radiation and viscous dissipation of energy, see Faltinsen (1990) and Mekha *et al.* (1996). The structural damping is due to the strain and elasticity properties of steel. The damping matrix for a tensioned steel riser is based on proportional Rayleigh damping and assumed proportional to the global stiffness matrix (Berge *et al.*, 1992)

$$\mathbf{C} = \alpha_2 \mathbf{K}. \tag{3.24}$$

The coefficient α_2 can be found from simple equations if the total damping level is known at a specified frequency. The term proportional to mass is neglected in order to avoid damping from rigid body motions. In this work we have assumed that the structural damping is 1.5% of the critical damping at the eigenperiod of $T = 10$s. Frequencies lower than this will have smaller damping, and the damping is assumed linearly increasing with logarithmic increasing ω, such that $\lambda = 0.15\%$ for $T = 100$s. Thus, the material damping is small relative to the hydrodynamic damping. A further discussion on use of the Rayleigh damping can be found in Appendix A.2.3.

3.5.5 Hydrodynamic Forces

The hydrodynamic forces on the risers are computed using Morison's equation modified for a moving circular cylinder. The horizontal hydrodynamic force on a strip of the cylinder can be written

$$df_{hyd} = \rho_w C_M \frac{\pi D_e^2}{4} a dz - \rho_w C_m \frac{\pi D_e^2}{4} \ddot{r} dz + \frac{1}{2} \rho_w C_D D_e \left(v - \dot{r}\right) \left|v - \dot{r}\right| dz, \quad (3.25)$$

where v and a are the undisturbed water velocity and acceleration, $\dot{r}$ is the response velocity, and $\ddot{r}$ is the structure's acceleration. $C_M = C_m + 1$ is the inertia force coefficient. The acceleration of the water has a material derivative, $a = \frac{Dv}{Dt}$, as the water velocity field is varying in space due to shielding effects, but this is assumed to be small. This and the fact that the wave induced water motion is assumed negligible for a riser in deep waters, means that the first term of (3.25) can be neglected. The added mass term is already included in the mass term on the left hand side of the equation of motion. Hence, the only hydrodynamic force included on the right hand side is the drag force df_{drag}, which is the last term of (3.25). This drag force is calculated for each element and summarized as concentrated forces in each node. The force vector $\mathbf{f}_{drag}$ is found at the right hand side in the equation of motion given in (3.27) later in the text.

The added mass C_m for a circular cylinder is known to be 1.0. However, this value may for the downstream cylinder be influenced by the wake. VIV for both risers may also cause some variations of C_m. For this application such effects are considered to be insignificant, and a constant value is therefore applied in this study. The drag coefficient is influenced by similar effects as added mass, and C_D is known to depend on the flow velocity for a specific cross section. However, it is not easy to describe such variations, and it is therefore common practice for engineering purposes to assume a constant value. This approach is taken in the present study, and a value of $C_D = 1.0$ for both risers is applied. It is also important to note that variations of C_D will not alter any conclusions regarding

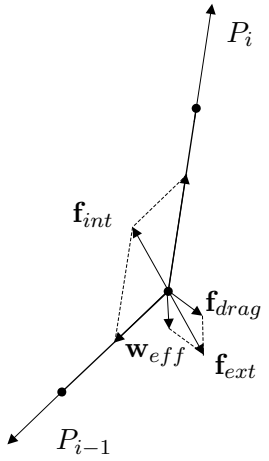

Figure 3.9: Balanced internal and external force.

the control system design for this study since the estimates of drag forces are not needed for control purposes.

3.5.6 Load and Equilibrium Iteration

The modeled system contains nonlinearities in the mass, stiffness and damping matrices in addition to the nonlinearities due to response dependent drag forces. The top tension defines geometric stiffness according to (3.21) and will vary in time as it is the control input. The forces acting on each element, such as tension, effective weight and drag are computed in the i-frame for each element and thereafter transformed to the f-frame. A detailed description is given in Appendix A.3.

As in traditional FEM, the nonlinearities are solved numerically by incremental formulation with the Newmark-β time integration method and Newton-Raphson equilibrium iteration. For each time step the force equilibrium between the internal force $\mathbf{f}_{int}$, due to tension, and the external force $\mathbf{f}_{ext}$, due to drag forces $\mathbf{f}_{drag}$ and effective weight $\mathbf{w}_{eff}$, is found, as illustrated in Fig. 3.9. A combined load and equilibrium iteration is needed since drag forces depend on the relative velocity $v - \dot{r}$, and the lateral stiffness of the riser will vary due to dynamic tension variation. Iteration continues until an equilibrium solution is found with desired accuracy.

3.5.7 TLP Prescribed Forces

The complete stiffness, damping and mass matrices found for the riser can be divided into submatrices that contain the free and prescribed (fixed or with specified motion) DOFs respectively. The columns and rows corresponding to the prescribed DOFs are removed from the original system matrices, meaning that only the free DOFs are present in the dynamic equation of motion. The fixed DOFs are the positions at the bottom (both $x_{i=1}$ and $z_{i=1}$), whereas $x_{n+1} = x_{TLP}$ at the top node is the only node with specified motion. The specified motion will give contribution to the vector with dynamic loads found on the right hand side of the equation of motion, see (3.27). These contributions are found from elements in the original riser system matrices that links the free DOFs to the DOFs with specified motions (spe). For the present case this contribution will be given by

$$\mathbf{f}_{TLP} = \mathbf{m}_{spe}\ddot{x}_{TLP} + \mathbf{c}_{spe}\dot{x}_{TLP} + \mathbf{k}_{spe}x_{TLP}, \tag{3.26}$$

where $\mathbf{f}_{TLP}$ is the force vector that originates from the TLP motions. $\mathbf{m}_{spe}$, $\mathbf{c}_{spe}$ and $\mathbf{k}_{spe}$ are columns in the original riser system matrices that correspond to x_{TLP}, and hence are removed from the riser system matrices used in the dynamic equation of motion.

3.5.8 Dynamic Equation of Motion

In the dynamic equation of motion, the mass-damper-spring system for the free DOFs in the riser system are found on the left hand side. On the right hand side the external forces from top tension, current and drag forces, and the specified motion from the TLP is included

$$\mathbf{M}(\mathbf{r})\,\ddot{\mathbf{r}} + \mathbf{C}(\mathbf{r})\,\dot{\mathbf{r}} + \mathbf{K}(\mathbf{r})\,\mathbf{r} = \mathbf{f}_{top} + \mathbf{f}_{drag} - \mathbf{f}_{TLP}, \tag{3.27}$$

where $\mathbf{r}$ is the riser position vector, $\mathbf{f}_{top}$ is the top tension, and $\mathbf{f}_{drag}$ is the drag forces from current and riser motions. The superscript f is omitted as the equation of motion is always given in the f-frame. In this equation the fixed and prescribed DOFs are removed from the equation, and the influence from specified DOFs is included on the right hand side as a force acting on the system. The riser position vector is then

$$\mathbf{r} = \begin{bmatrix} x_2 & z_2 & \cdots & x_i & z_i & \cdots & x_n & z_n & z_{n+1} \end{bmatrix}^T. \tag{3.28}$$

Note that this vector corresponds to the entire position vector found in (3.13), but the prescribed DOFs are left out. The dynamic simulation algorithm could be found in Fylling *et al.* (2005).

3.5.9 Quasi-Static Equation of Motion

The quasi-static equation of motion includes the position dependent terms of (3.27). This means that only the nonlinear stiffness for the riser system is found on the left hand side. On the right hand side the static external forces are given. These include the top tension, the nonlinear viscous drag forces due to the current, while the relative velocity is left out, and the specified, position dependent force from the TLP. This gives

$$\mathbf{K}(\mathbf{r})\,\mathbf{r} = \mathbf{f}_{top} + \mathbf{f}_{cur} - \mathbf{f}_{TLP,qs}, \tag{3.29}$$

where

$$df_{cur} = \frac{1}{2}\rho_w C_D D_e v|v|dz, \tag{3.30}$$

$$\mathbf{f}_{TLP,qs} = \mathbf{k}_{spe} x_{TLP}. \tag{3.31}$$

The algorithm for simulation of the quasi-static model is found in Appendix A.4.

3.6 Actuator and Constraints

The riser tensioner system or heave compensator can be implemented as a hydraulic cylinder with a piston. Today, this setup strives to keep the tension close to constant. This is obtained by using a compressed air volume as a soft spring in the hydraulic system. Hence, no active control is needed. Designing the heave compensator such that the payout is controlled, will still give the same physical constraints. These could be divided into two groups; (1) constraints due to stroke and (2) constraints due to tension. The stroke parameters are based on the definitions by Larsen (1993), slightly modified, and illustrated in Fig. 3.10. The *initial position* refers to a riser and platform condition without offset or environmental forces, and a desired level of top tension. The *static position* is a particular case with defined environmental and operational conditions. *Payout* is the distance between the bottom of the cylinder and the top of the riser, positive downwards. The *stroke variation* is the maximum length variation the tensioner system can provide. The *dynamic stroke* is the length variation needed to tension the riser. The dynamic stroke must compensate for the relative motion between the platform and the riser subjected to all environmental conditions.

In addition to the boundaries given by the limitations for payout and stroke, the top tension forces on the riser is physically constrained with upper and lower boundaries. If this tension is too low, i.e. less than the effective weight of the riser, the riser will experience buckling. Hence, the lower limit for tension should be the effective weight plus a safety margin. The upper tension limit is restricted

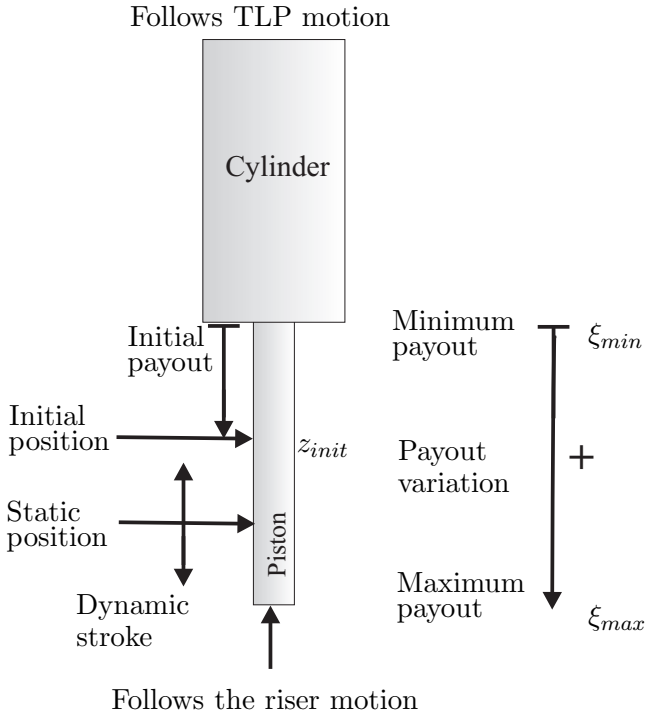

Figure 3.10: Stroke parameters of one individual cylinder.

by the yield stress for the riser material and chosen such that the maximum axial stress is less than 40% of the yield stress for steel. A given tensioning system will also have limitations regarding maximum tension due to limitations of pressure in the hydraulic system, and a tension rate limit on how fast tension may be varied.

The non-compensated initial position, z_0, is defined with the design tension and no environmental forces or offsets, and it will be equal for all risers in the present study. When the TLP is in an offset position, the setdown of the initial position can be found from the tendon geometry, such that the initial position compensated for setdown, Δs_T is found from

$$z_{init}(t) = z_0 - \Delta s_T(t). \tag{3.32}$$

The measured parameter used in the control loop is the payout for each piston, denoted ξ_j. Payout is defined positive when it adds elongation to the riser and negative in the opposite direction. *Minimum payout*, $\xi_{\min}$, means that the piston is as far into the cylinder as possible, for simplicity assumed zero here. *Maximum*

payout, $\xi_{\max}$, refers to the position with maximum free piston length. The *initial payout*, ξ_0, is the distance between the lower end of the cylinder and the initial position. The total *dynamic payout* is given as

$$\xi_j(t) = \xi_0 + z_{init}(t) - z_{j,n+1}(t),\ j = 1, 2, \tag{3.33}$$

where $z_{j,n+1}$ is the vertical top position of riser j.

Chapter 4

Model Verification

RIFLEX is a commercial FEM program for static and dynamic analysis of slender marine structures (Fylling *et al.*, 2005). For the purpose of control system design, a more convenient numerical procedure and software code has been implemented in Matlab/Simulink. The motivation behind this chapter is to validate the riser model from Chapter 3 and verify that it is appropriate as a model of the real world used in the simulations and for the purpose of control system design, despite the simplifications made in the modeling. The model should give a good picture of the global geometry of the riser, with focus on the maximum horizontal displacement and the vertical riser top position, exposed to varying TLP positions and tensions. Features often included in riser analysis, which are of less importance in this case are:

- Bending stiffness EI in the riser model.
- End conditions, i.e. bending stiffeners in the top and bottom end points.
- Stress.

Hence, in the presented Simulink model, the simplifications can be summarized as:

- No bending stiffness included.
- Free rotations in the ends.
- Few elements compared to typical structural analysis, 2-20 versus 400.

The first two of these items are assumed to be insignificant at large water depths (large length to diameter ratio), as long as the global geometry is of importance. In Section 4.7, a bending stiffener is implemented at the bottom end node for

the RIFLEX model, and compared to the Simulink model with free rotation to investigate the effect of such a simplification. Note that bending stiffness has been included in the RIFLEX model in all analyses presented herein. In the verification of the code, a relatively large number of elements ($N = 20$) are chosen to increase the resolution and accuracy. Four tests are run:

1. Quasi-static verification with increasing TLP offset.
2. Quasi-static verification with increasing top tension.
3. Dynamic verification with harmonic TLP motions.
4. Dynamic verification with harmonic top tension variations.

The quasi-static analyses are run with the static model given in (3.29). Only the terms proportional to the position $\mathbf{r}$ are included, while the dynamic terms proportional to velocity $\dot{\mathbf{r}}$ and acceleration $\ddot{\mathbf{r}}$ are ignored. The static riser configuration is calculated for each increment in TLP position or top tension. The dynamic analysis are run with the full dynamic model from (3.27). The TLP position and the top tension are harmonically varied.

4.1 Set-Up

The equilibrium solution in each time step is found numerically by incremental equilibrium correction. The Newton-Raphson method is used for equilibrium iterations within each time step. The integration method for the dynamic riser model is the Newmark-β method with fixed step size and constant acceleration in each time step. The implemented algorithm is found in Fylling *et al.* (2005). For the quasi-static algorithm, see Appendix A.4.

Most of the tests are run at 1200m water depth. For simplicity, the riser top is assumed to be at the level of the free surface, i.e. 1200m above the seafloor. The model run in RIFLEX consists of 400 elements, each of length 3m. The model implemented in Simulink is run with 20 elements which gives an element length of 60m. In order to limit the computation time for realtime control applications, it is of interest to minimize the number of elements applied in the riser model, while still maintaining a sufficient level of accuracy, such that the implemented model can represent the geometry of the real world. In Chapter 7, this model with the number of elements varying between 2 and 20 are analyzed and compared to investigate the size of the error introduced.

To verify the riser model, the analyses were run with seven different current velocity profiles, representing different geographical areas. A wide range of cases were analyzed to better investigate the robustness of the model. The current

velocity profiles are illustrated in Fig. 3.2 and described in Section 3.1. These current profiles were run with various current velocity amplitude, with surface velocity ranging from 0.3m/s to 2.5m/s, with most cases about 1m/s. The current velocity at the seabed varied from -1.0m/s for the bidirectional current profile to 1.2m/s for the amplified GoM2. Most cases were run with between 0m/s and 0.5m/s at the seabed. Current profile data are found in Appendix B.1.1. Physical riser data are found in Appendix B.2.

The Newmark-β method is unconditionally stable for linear systems. However, for nonlinear systems the step length the simulations must be small enough to capture system dynamics also for the stiff vertical DOFs. A step length of 0.1s is seen to be stable in all DOFs for all simulations.

4.2 Quasi-Static Verification with Increasing TLP Offset

The quasi-static riser model was verified first. The TLP offset was increased in steps of 5m from 0m to 70m, corresponding to 0 to 5.8% of the water depth. The static equilibrium solution is found for each TLP position for both the RIFLEX and the Simulink models. The models were run for all the different current profiles and with various current velocity amplitudes. Deflections of the riser with the design current from the Ormen Lange field with surface velocity 1.15m/s are seen in Fig. 4.1a). x and o mark the position along the riser with the maximum horizontal displacement for RIFLEX and Simulink, respectively. The riser models match close to perfect. The deviation in the vertical position of the node with max displacement is due to the relatively low number of elements in the Simulink model. The deviation for the riser configuration is seen to be small. 20 elements as seen in the Fig. 4.1, gave as expected a better correspondence between the RIFLEX and Simulink calculations than fewer elements, like 5 or 10, see Section 7.2.

The setdown is given in Fig. 4.1b). It is seen to correspond nicely for the two models. The setdown curve reflects the setdown due to surge, which also is used to describe the TLPs motion on a sphere surface. We achieved similar correspondence in snapshots and setdown for the other current profiles.

4.3 Quasi-Static Verification with Increasing Top Tension

In the second verification of the quasi-static riser model, the tension was increased from 1200kN to 2700kN in steps of 50kN. All current profiles were tested with

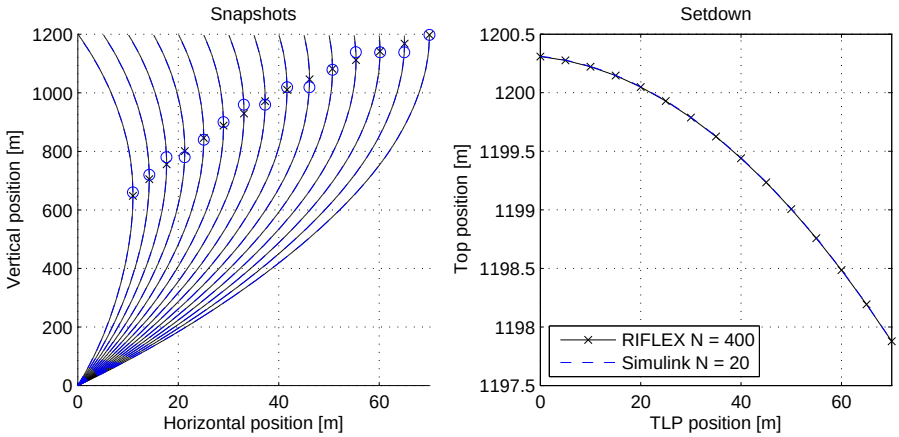

Figure 4.1: Deflections (a) and setdown (b) for the quasi-static riser model with TLP offsets from 0m to 70m and Ormen Lange design current. RIFLEX(– x) and Simulink (- -o).

TLP positioned in zero and 30m offset, $x_{off} = \{0, 30\}$m. The lower tension limit was the effective weight plus a safety margin for the structure connection at the seabed. The upper tension limit was given by a percentage of the yield stress for steel.

Fig. 4.2 shows the deflections of a riser exposed to the Ormen Lange current and increasing tension. As before, x and o mark the position along the riser with the maximum horizontal displacement for the RIFLEX and Simulink model, respectively. The curve to the right with horizontal displacement of approximately 20m corresponds to the lowest tension of 1200kN. For each curve the tension increases with 50kN and the deflection decreases correspondingly. Note that the vertical position of the max horizontal displacement increases when the tension increases. The reason is that the relative difference between top and bottom tension will decrease with increasing tension. This will lead to a more symmetric deflection shape for increasing tension in uniform current. The tension along the riser is decreased from top to bottom due to the effective weight of the riser.

Fig. 4.3 shows the deflections of the quasi-static riser model exposed to the bidirectional current velocity profile. Effects of the reduced tension along the riser are clearly seen at low tensions; the deflection is much larger in the lower half than the upper half, even with a symmetric current profile. This is particularly clear at low tensions. Also the deviation between the models in RIFLEX and Simulink is larger than for the other current profiles, and is clearly seen from the figure. The curvature is large, especially about 200m above the seabed. 20 elements seems to

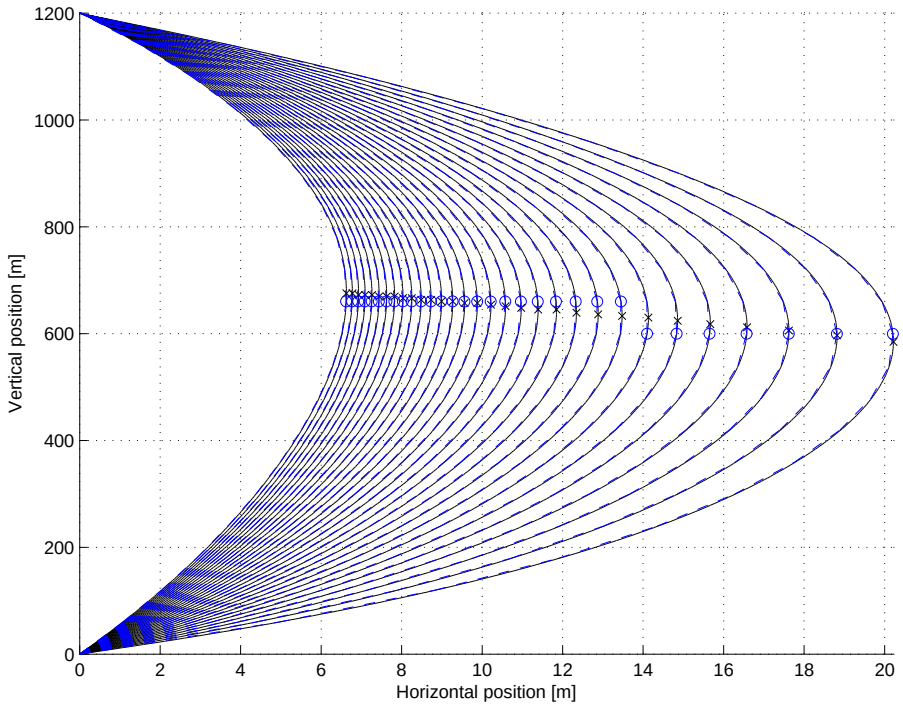

Figure 4.2: Deflections of the quasi-static riser model with increasing top tensions from 1200kN to 2700kN in steps of 50kN, and current profile from the Ormen Lange field. RIFLEX(– x) and Simulink (- -o).

be too few to describe the riser configuration accurately, i.e. more elements are needed to describe the configuration satisfactory, if the curvature is large. The model is seen to be closer to the RIFLEX model for large tensions giving less deflections. However, the important characteristics are kept and the model can picture the main riser configuration.

The relations between top tension, vertical top position and maximum horizontal displacement are investigated. The relations for the Ormen Lange design current is illustrated in Fig. 4.4. The verification showed good agreement between the models within the tension limits. For lower tensions, nonlinear effects like buckling may appear. These effects are not implemented in the Simulink model. Top tension less than the lower saturation limit is therefore not simulated.

The physical correspondence between the vertical top position, maximum horizontal displacement, top tension and geometric stiffness should be explained more thoroughly. This is best done by considering the numerical derivatives

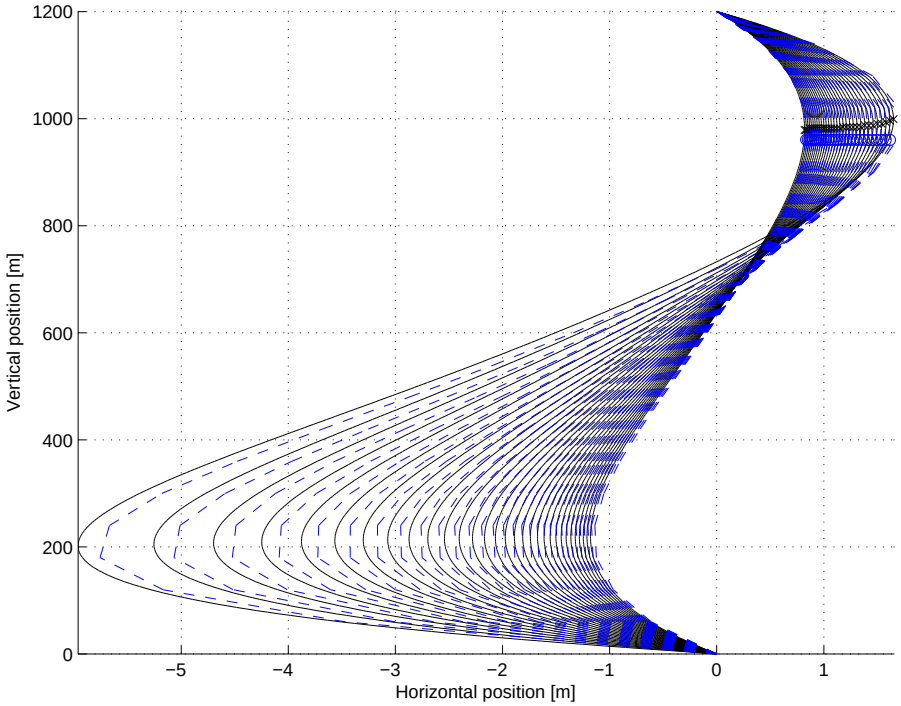

Figure 4.3: Deflections of the quasi-static model with increasing tension exposed to the bidirectional shear current. RIFLEX(– x) and Simulink (- -o).

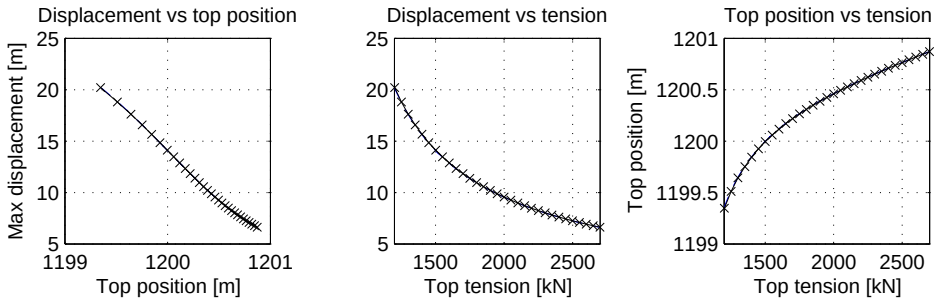

Figure 4.4: From left: a) Maximum horizontal displacement vs vertical top position, $x_{max}(z_{max})$, b) Maximum horizontal displacement vs top tension, $x_{max}(T)$, c) Vertical top position vs top tension, $z_{max}(T)$. All plots are for the quasi-static riser model exposed to the Ormen Lange profile. RIFLEX(– x) and Simulink (- -).

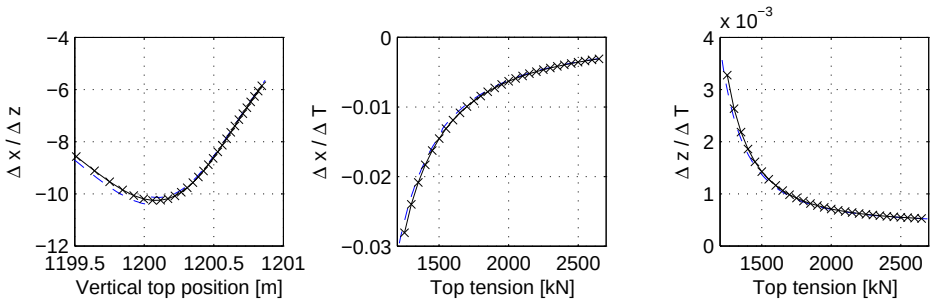

Figure 4.5: From left: a) The derivative of x w.r.t. z, $\frac{\Delta x}{\Delta z}(z)$ b) The derivative of x w.r.t. tension, $\frac{\Delta x}{\Delta T}(T)$, c) The derivative of z w.r.t. tension, $\frac{\Delta z}{\Delta T}(T)$. All for the design current at the Ormen Lange field, RIFLEX(– x) and Simulink (- -).

$\frac{\Delta x}{\Delta z}(z)$, $\frac{\Delta x}{\Delta T}(T)$ and $\frac{\Delta z}{\Delta T}(T)$ in Fig. 4.5. The effect of the increase in tension could be divided into three different stages depending on the tension level:

1. Low tension, large deflection.
2. Medium tension, medium deflection.
3. Large tension, small deflection.

The first of these may or may not be clearly seen in the analysis, depending on the current profile and the top tension. In the exploration of all stages, the top tension is increased with a fixed magnitude ΔT. For stage 1-3 above this results in:

Stage 1: Small tension, large deflection

- Large decrease in deflection.
- Large increase in top position, due to geometric flexibility.
- A fixed increase of z by Δz will give a medium decrease in displacement, Δx.

Stage 2: Medium tension, medium deflection

- Medium decrease in deflection.
- Medium increase in top position, reduced geometric flexibility; some contributions from elastic flexibility.

- A fixed increase in z gives a large decrease in displacement.

Stage 3: Large tension, small deflection

- Small decrease in the deflection.
- Small increase in top position, controlled by elastic flexibility, negligible geometric flexibility.
- A fixed increase in z gives a small decrease in displacement.

The geometric stiffness is proportional to the increase in tension, $\Delta \mathbf{K_G} \propto \Delta T$, meaning that a fixed increase in tension gives a proportional change in the geometric stiffness. For low tensions, a fixed increase has large effects on the geometry and the displacements. For large tensions, and already large geometric stiffness, an additional increase in tension, does not have the same effect.

There were also run tests with decreasing top position in RIFLEX. The top tension started at 2900kN and decreased corresponding to steps in the vertical top position of 5cm. These result are similar to what is presented here, and can be found in Rustad *et al.* (2007*c*).

4.4 Verification with Dynamically Moving TLP

The dynamics of the riser model and the influence from the drag forces were tested by harmonic motions in surge for the TLP, with amplitude $A_{TLP} = 20$m, and periods in the range $T_{TLP} = 60 - 300$s. The static offset was $x_{off} = 30$m, and the riser tension was kept constant at 1800kN. Fig. 4.6 shows snapshots of the dynamic riser motion at the Ormen Lange field simulated in Simulink with $T_{TLP} = 60$s. The dynamic envelope curves are found from RIFLEX. The snapshots fit nicely between the envelope curves given by RIFLEX. The top position versus time is plotted in Fig. 4.7a), while Fig. 4.7b) shows the correspondence between the top position and the TLP surge position. The change in top position is bigger for larger curvature of the riser. This was best seen when the TLP was moving from its maximum to its minimum offset, with the smallest surge period, $T_{TLP} = 60$s, seen in Fig. 4.6a).

Let us for simplicity assume modal representation of the riser. Then the riser top position could be said to be a function of time and space, i.e. TLP motion and deflection

$$z(t, x) = \Sigma_i \phi_i(x) \cdot q_i(t), \tag{4.1}$$

where $q_i(t)$ is dependent of time, being the TLP motion and the first mode shape. $\phi_i(x)$ is higher modes due to the deflection and resonance for the riser at its

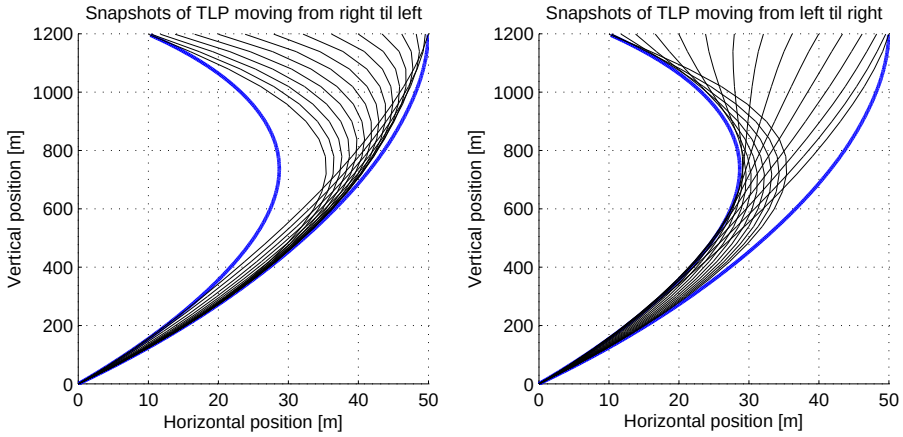

Figure 4.6: Snapshots of the TLP moving from right to left (a), and from left to right (b) for the Ormen Lange design current. The snapshots are from Simulink and the thick, blue lines are envelope displacement curves from RIFLEX.

eigenperiods. Depending on the period of the TLP, more resonance frequencies can be excited at higher modes. When the TLP is moved from left to right, Fig. 4.6b), the second mode is seen. This second mode can also be found in the top position versus time, in Fig. 4.7a), and is even more clearly seen in the simulations with small current velocities in the top layer, like the GoM2 velocity profile. The top node position in time for GoM2 is seen in Fig. 4.8a) and the top node position versus TLP surge in Fig. 4.8b). The first order mode shape is less dominating due to the smaller current velocities and smaller deflection. This will give smaller setdown of the top node, such that the second order mode shape is more visible. The second order mode shape is due to the TLP motion, causing resonance in the higher order modes. For longer surge periods, like $T_{TLP} = 300$s, the motions were close to quasi-static giving a smaller curvature and only the first mode shape was observed, not shown here. Also the setdown due to deflection was smaller, giving less need for stroke capacity than with faster TLP motions. To summarize, the TLP velocity has a large influence on the riser deflection, including the second mode shape. The riser setdown can be said to be dependent on the TLP motions, and hence the need for payout and stroke.

4.5 Verification with Dynamically Varying Tension

The fourth and last of the riser model verification tests included harmonic tension variations. The initial tension was 1950kN, with an amplitude of 750kN

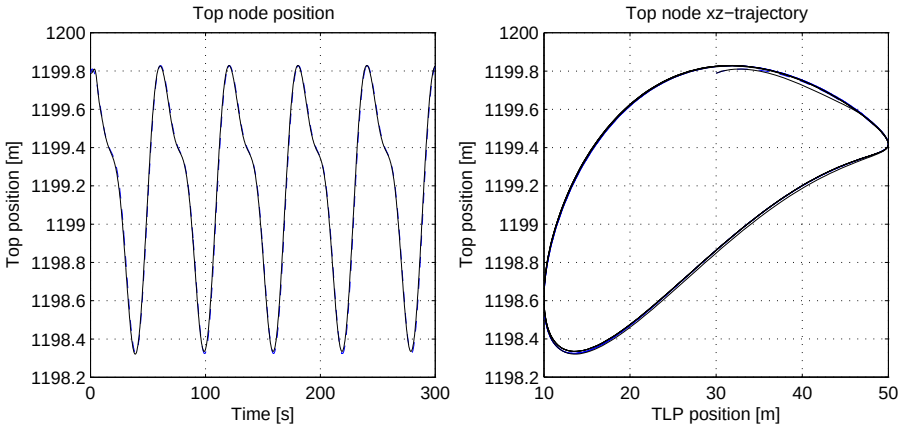

Figure 4.7: Top position as a function of time (a) and TLP motion (b) with period of 60s. RIFLEX(–) and Simulink (- -) for the Ormen Lange design current.

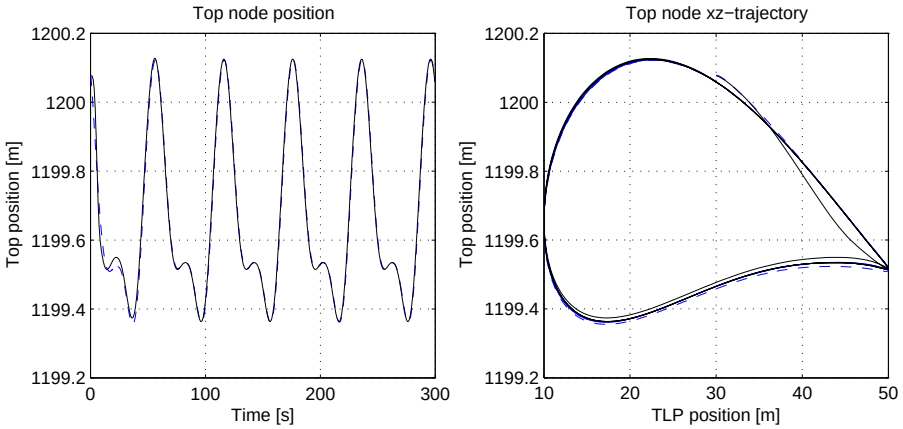

Figure 4.8: Top position as a function of time (a) and TLP motion (b) with period of 60s. RIFLEX(–) and Simulink (- -) for GoM2 current and TLP dynamic period of 60s.

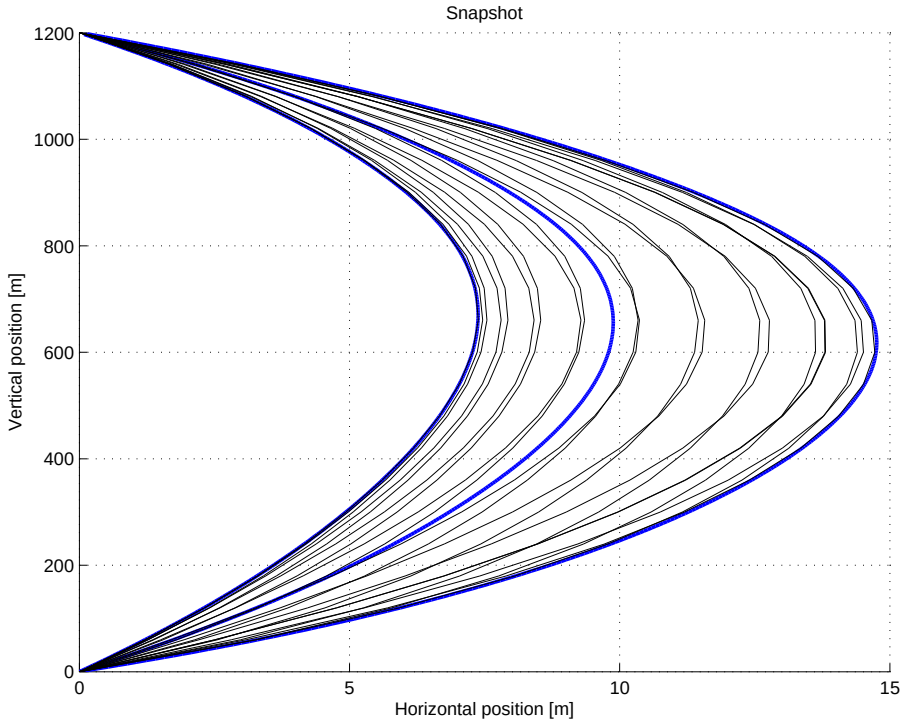

Figure 4.9: Snapshots with harmonically changing top tension for the Ormen Lange design current (black). The blue lines are the static configuration and envelope displacement curves from RIFLEX.

and periods of 60s and 120s. This gives maximum tension rates of 75kN/s and 37.5kN/s, respectively. This is far more than the limit of a conventional tension system. Hence, if the riser model is valid for these large and fast changes in tension, it will also be valid for slower limit rates. Simulations were run with currents corresponding to the Ormen Lange field, GoM2 and the bidirectional current profile. Fig. 4.9 shows the snapshots with dynamical tension variation of period 120s from Simulink. The thick lines are the static configuration for the initial tension and the envelope displacement curves from RIFLEX. The snapshots from Simulink are seen to be within these envelope curves. Fig. 4.10 shows the dynamic variation of the top tension (a) and the top position (b). The motion trajectory for vertical position versus tension is seen in Fig. 4.10 c). A transient period from the static initial condition is seen. The results from simulations with 60s are similar.

There were also run tests where the motion of the top node in RIFLEX was

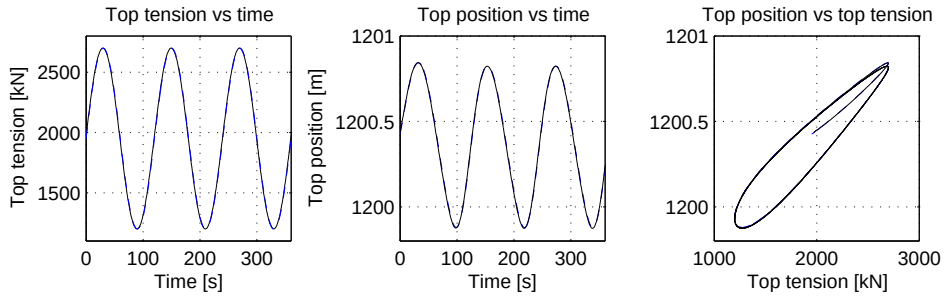

Figure 4.10: Top tension (a) and position (b) as functions of time, and top position vs top tension (c). RIFLEX(–) and Simulink (- -) for Ormen Lange design current.

a prescribed vertical sinusoidal. In the corresponding simulations in Simulink, sinusoidal tension was used. The correlation between tension and vertical top position is nonlinear and asymmetric, meaning that more tension is needed to lift the riser 0.5m than the reduction in tension when lowering the top with 0.5m. This is caused by hydrodynamic drag forces that will increase needed tension for an upwards motion, but decrease the tension reduction for a downwards motion. However, the results presented in this section are better suited for the purpose of verification. The results with prescribed motions are not presented here, but can be found in Rustad *et al.* (2007*c*).

4.6 Quasi-Static Verification at Shallow Waters

In deep waters, the lateral stiffness is assumed to be dominated by the geometric stiffness, and the riser behaves more like a cable. In shallow waters, the bending stiffness is assumed to be of considerable importance. To investigate the area of application for the riser model with free end rotations, it is tested in shallow water, being 300m and 600m. In even shallower waters, TLP and tensioned risers are not likely to be applied. Hence, it is not necessary to investigate the validation at even smaller water depths. This section is written in co-operation with Stølen (2007), and the test set-up is similar to the corresponding verifications for 1200m water depth. A linearly sheared current is used in all tests.

4.6.1 Increasing TLP Offset

At 300m water depth, the TLP offset is varied from 0m to 30m in steps of 2.5m. At 600m water depth the offset is varied from 0m to 40m in steps of 5m. The

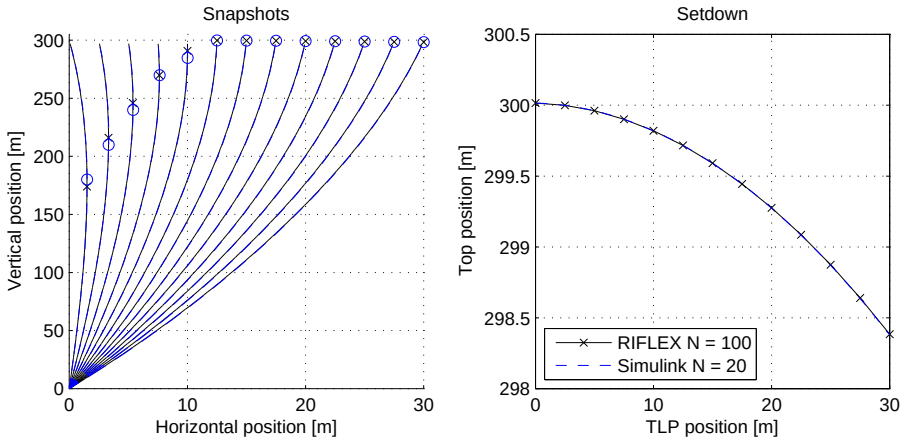

Figure 4.11: Deflections (a) and setdown (b) for the quasi-static riser model with TLP offsets from 0m to 30m, 300m water depth and linearly sheared current. RIFLEX(– x) and Simulink (- -o).

top tensions are 450kN and 900kN at 300m and 600m, respectively. This is the same top tension factor compared to the effective weight as for 1200m, with $T_f = 1.94$. The results for 300m and 600m are found in Fig. 4.11. Similar results are found for 600m. The deviation is small, both for the lateral deflections and the setdowns, similar to what is found at 1200m water depth.

4.6.2 Increasing Tension

The quasi-static analysis is now run with increasing tension at 300m and 600m water depth. For the 300m case the tension is increased from 250kN in steps of 25kN up to 700kN. The lower tension limit should be set to give a minimum tension at the bottom connection of the riser. The effective weight is 230kN which results in a minimum residual tension of 20kN at the bottom. This is less than the safety margin, and the boundaries for the validation of the Simulink model. The effect of bending stiffness is not included in the Simulink model such that the total stiffness is too small in particular at low tensions, and hence too large deflections must be expected. The deviations in Fig. 4.12a) for the rightmost curves are seen to be large (0.12m and 3.2%) for the lowest tension. For higher tensions, the bending stiffness is of less relative importance, and the agreement is better. Except for the two lowest tensions, which are out of range of the validity of the Simulink model, the relative error was less than 1%, and decreased for increased tensions.

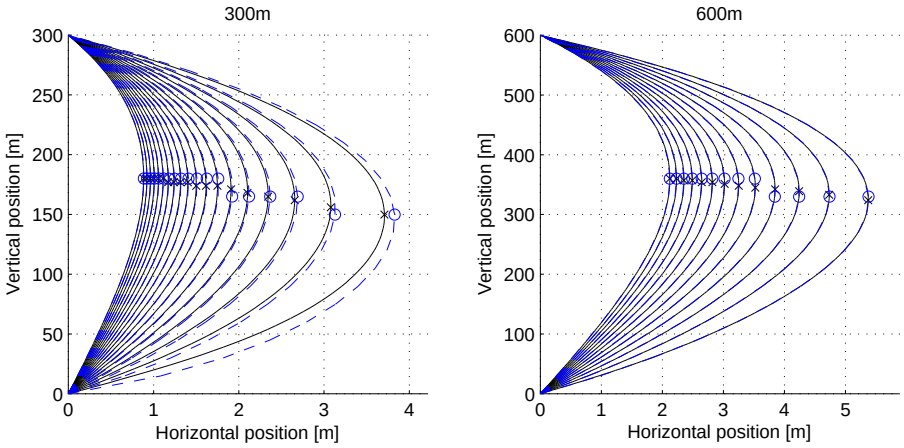

Figure 4.12: Deflections for the quasi-static riser model with increasing tension in (a) 300m and (b) 600m water depth and shear current. RIFLEX(– x) and Simulink (- -o).

At 600m water depth the tension is varied from 600kN to 1200kN in steps of 50kN. The effective weight is 450kN, giving a safety margin of 150kN. The snapshots in Fig. 4.12b) show satisfactory performance. The relative error was less than 0.1%.

4.7 Quasi-Static Verification with Stress Joint

The Simulink riser model has free rotation at the ends, and the end conditions are assumed to be insignificant for the global geometry in deep waters. The solution, with respect to stresses, is to tie down a marine riser to the seafloor through a ball joint. This has zero rotation stiffness and will eliminate bending stresses at the riser end. However, in most cases this is not a feasible solution. The main purpose of the stress joint is to provide a gradual transition between the relatively flexible riser and the rigid wellhead. The joint must have sufficiently flexibility to keep the bending stresses in the lower part of the riser at an acceptable level, but also sufficiently strong to resist the forces and moments introduced by the riser at the top of the wellhead. In this section the effect of a bending stiffener at the bottom connection will be analyzed. This section is written in co-operation with Stølen (2007).

A stress joint, with the same material specifications as the riser, is implement in RIFLEX. The risers will be located at 300m, 600m and 1200m water depths

and tested with increasing tensions like in Sections 4.3 and 4.6.2. No stress joint is implemented in the Simulink model. The objective is to test what effect the stress joint will have on the global geometry, and if the assumption of insignificance of the end connections is valid for the various water depths. These tests are needed since it has been assumed that the maximum horizontal displacement and the vertical riser top position are unaffected by the presence of a bending stiffener in deep waters, and that a ball joint can be used at the bottom connection. Fig. 4.13 shows the stress joint model, and Table 4.1 summarizes the geometric parameters. The internal diameter is the same for all segments and equal to the riser. The external diameter is increased from the riser thickness at the top to $4t$ at the bottom. Only one element is applied for each segment.

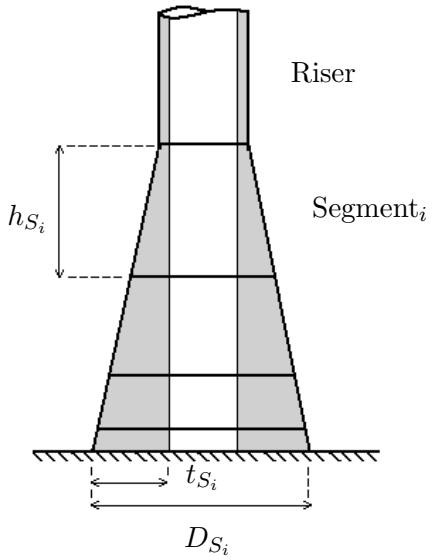

Figure 4.13: Stress joint configuration.

4.7.1 Shallow Water

The stress joint configuration was first tested at 300m water depth. The stress joint model is seen to give the riser a vertical orientation close to the bottom, see Fig. 4.14. The stress joint is seen to have a large impact on the curvature of the riser and also the maximum horizontal displacements. Recall from Section 4.6.2 that the lowest tensions (and rightmost curves) are not valid for the Simulink model in 300m, which does not include the effects from bending stiffness. The two lowest tension cases give a relative error of 17.3% and 10.1%. For higher

	h_{si}[m]	t_{si}[m]	D_{si}[m]
Riser	-	t	D
Segment 1	2.7	1.5 t	D + t
Segment 2	1.8	2.0 t	D + 2 t
Segment 3	1.0	3.0 t	D + 4 t
Segment 4	0.5	4.0 t	D + 6 t
Total stress joint	6	-	-

Table 4.1: Stress joint data.

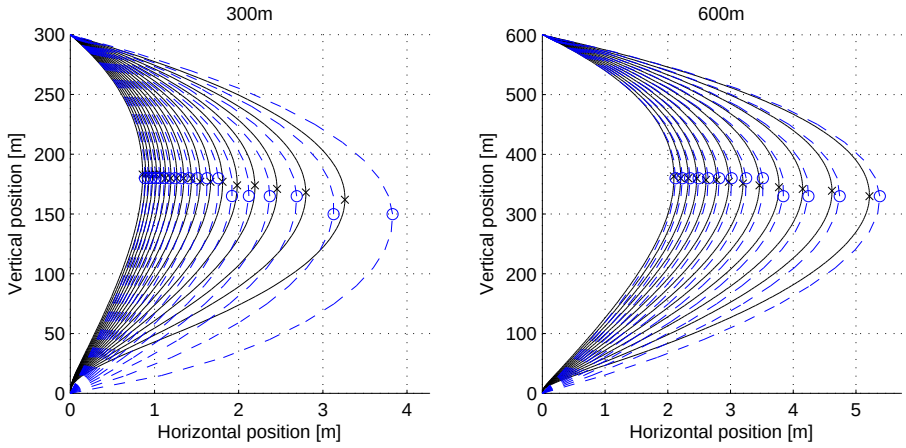

Figure 4.14: Snapshots for quasi-static riser model with stress joint of 6m, increasing top tension and linearly sheared current at (a) 300m and (b) 600m water depth. RIFLEX(– x) and Simulink (- -o).

tensions the deviations are much smaller decreasing from 6.2% down to less than 1% for the highest tensions.

The snapshots for 600m are shown in Fig. 4.14b). As expected the results are now in better agreement than for the 300 meter case. The stress joint imposed at the lower end has less influence on the curvature due to the increased riser length. The horizontal displacements are also less affected by the stress joint. For the lowest tension, the relative error in maximum horizontal displacement is 3.2% and less than 1% for tension higher than 850kN.

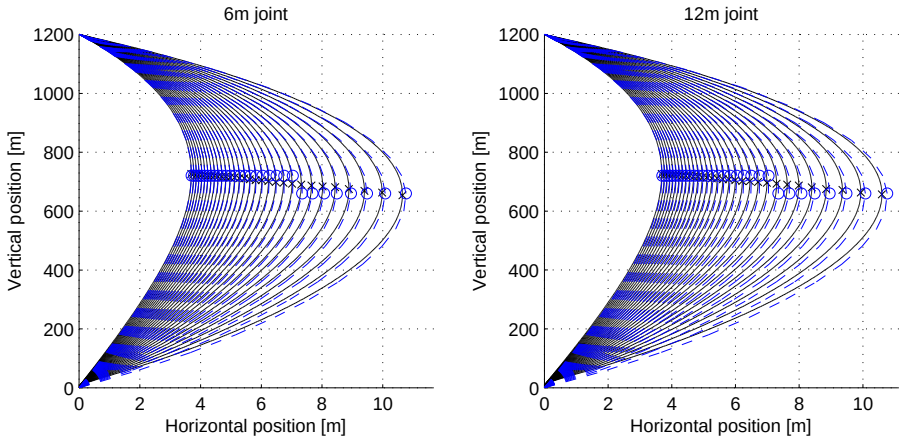

Figure 4.15: Snapshots for quasi-static riser model with increasing top tension at 1200m water depth including stress joint of (a) 6m and (b) 12m exposed to a linearly sheared current. RIFLEX(– x) and Simulink (- -o).

4.7.2 Deep Waters

The riser at 1200m water depth is tested in linearly sheared current with stress joints of 6m and 12m, see Fig. 4.15. For the 12m stress joint, all dimensions from Table 4.1 are doubled. The importance of the stress joint is seen to be less significant at this water depth, even for the longest stress joint. The correspondence between the RIFLEX and the Simulink model was better with the ball joint configuration. However, the deviations with the stress joint are still seen to be small, even for the lowest tensions. The RIFLEX model with 6m stress joint was also exposed to the Ormen Lange current. This gives larger deflection and larger horizontal deviations in meters (see Fig. 4.16), but the relative deviations are smaller. In Fig. 4.17 the relative errors in horizontal maximum deflection for each of the three cases are shown. The importance of a stress joint and inclusion of bending stiffness is seen to give largest error for tensions less than 1600kN. For tension higher than 1600kN, the error is less than 0.5%, even for the 12m stress joint.

4.8 Discussion

In this chapter the mathematical model developed in Chapter 3 has been verified. The verification was performed for both quasi-static and dynamic models. Both models were exposed to TLP motions and tension variations, and several different

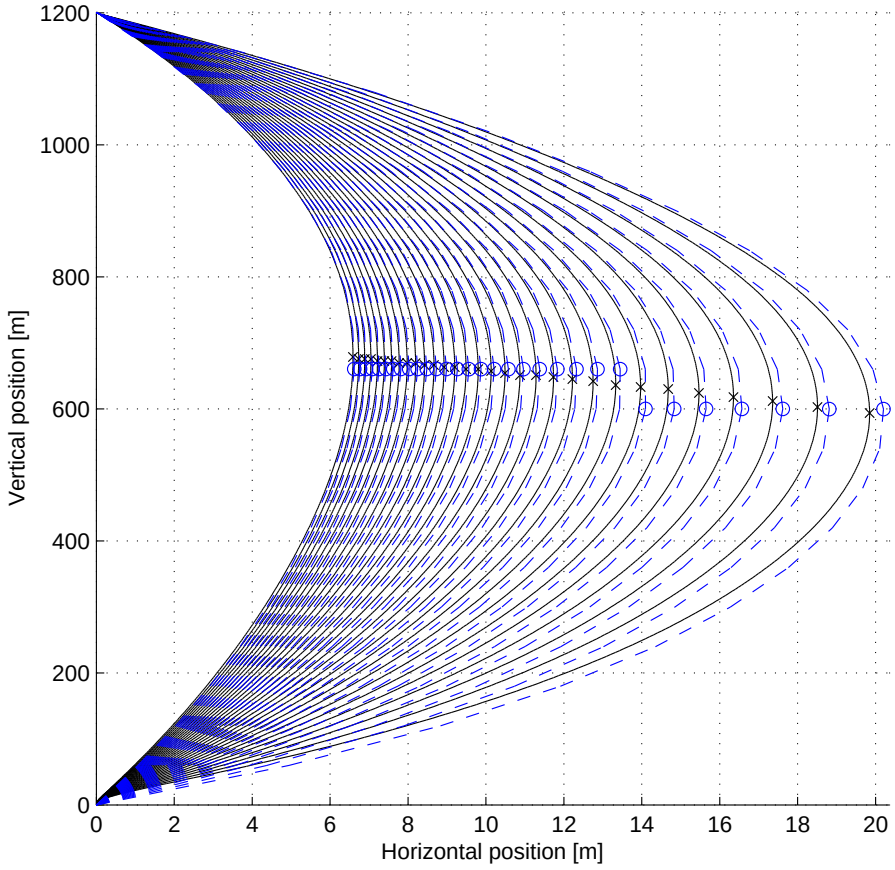

Figure 4.16: Snapshots for quasi-static riser model with a 6m stress joint and increasing top tension in 1200m waters exposed to the Ormen Lange design current. RIFLEX (–x) and Simulink (- -o).

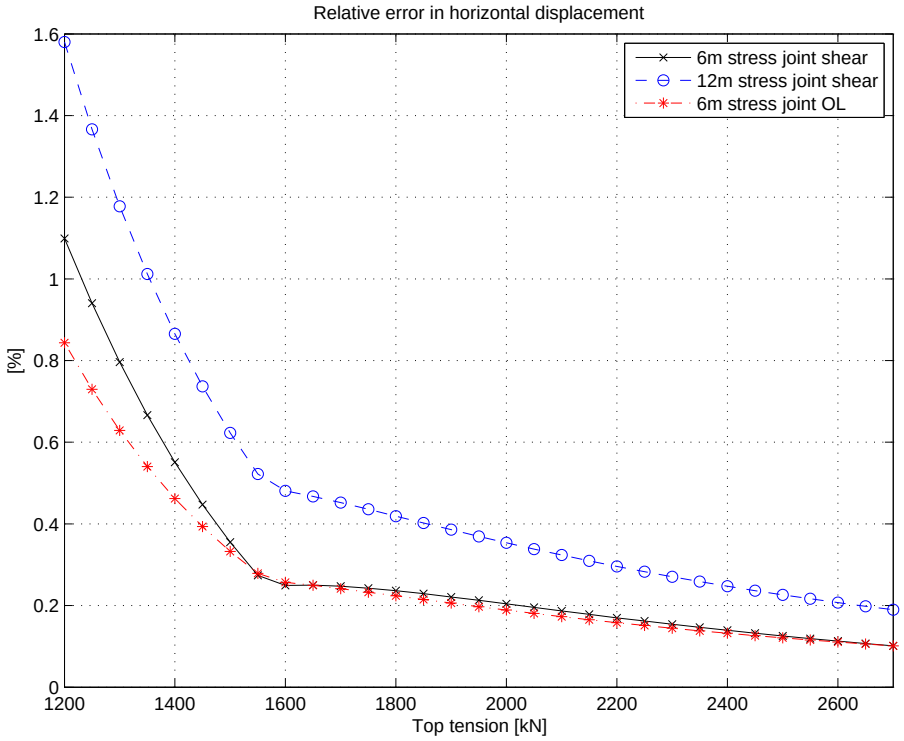

Figure 4.17: Relative error in horizontal maximum displacement for stress joints of 6m (–x) and 12m (- -o) in linearly sheared current and 6m (-.*) stress joint in Ormen Lange current.

current profiles with a wide range of current velocities have been analyzed.

The simulations have shown that there is a good agreement between the model from Chapter 3 and the RIFLEX model. The quasi-static model was tested in shallow waters, where the model with free rotations could be used for drilling purposes. It showed good performance at sufficiently high tension levels. For tension levels lower than the limit for the Simulink model, the effect of the neglected bending stiffness was seen. Hence, when applying this model, one should be aware of this effect, and avoid use of the model for low tension values. A stress joint was implemented in the RIFLEX model. The effect was large in shallow waters, especially at the lowest tensions, acting together with the bending stiffness. In deep waters, the effect of the stress joint on the global geometry is small and the assumption of free rotations at the ends is acceptable. The main focus has been deep waters and second order LF induced motions, as this is the

main motivation for the thesis. Note that WF motions have not been included in this verification.

20 elements have shown to be sufficient to describe the geometry of the riser in most cases. However, in cases with large curvature, like the bidirectional current profile, with zero offset and low tension, 20 elements did not describe the riser accurately, but could still draw the main configuration. Anyhow, in fully developed, undisturbed bidirectional current and the lowest top tension, the largest deflection is less than 2m in the upper half and less than 6m in the lower half, see Fig. 4.3. This is far less than the maximum deflection of approximately 20m with the lowest tension for the Ormen Lange current (Fig. 4.2). The small deflections are due to the second order mode shape. As the deflections are small, the risk of collision is limited and hence, no need for control. The Ormen Lange profile, on the other hand, gives a large deflection, which will increase the risk of collision. There is a good agreement with the RIFLEX model in all the relevant verification tests for this profile. It will therefore be used as the current profile in the simulations with control. However, in the riser analysis in Chapter 7, some additional current profiles will also be used.

Chapter 5

The Riser Control System Overview

This chapter aims to develop the control architecture and system design for the riser tensioning system. The main goal of this system is to prevent the risers from colliding subjected to the given constraints. This includes identification of the various stages of riser behavior depending on the environmental conditions, the control architecture, i.e. how the various parts are working together and the controller system design, including actuators and measurements.

5.1 Implementation Overview

The implementation of the system is shown in Fig. 5.1. The different parts of the system, is briefly described below, starting with the physical components.

The environment consists of wind, waves and current. The entire current profile has influence on the riser configuration. The current profiles are described in Section 3.1.

The TLP is described in Chapter 2 and modeled in Section 3.4. The TLP motions depend on the environmental conditions current, waves and wind.

The risers are modeled in Section 3.5. The behavior of the two risers depends on the TLP motions as well as the current velocity profile. On the other hand, the TLP motions are assumed independent of the risers.

The actuator is the riser tensioner system and a part of the implementation. By increasing or decreasing the tension and payout, the risers are tightened or loosened, and the lateral deflections are thereby affected.

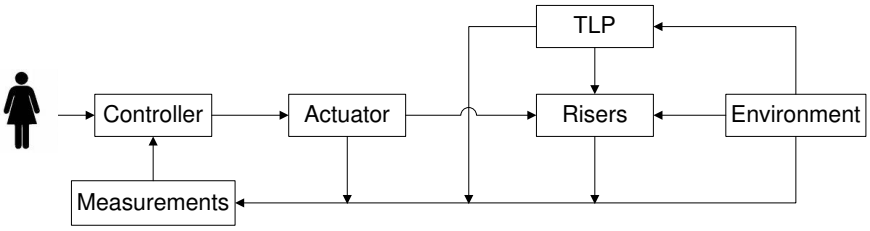

Figure 5.1: Outline of the implementation of the system.

The measurements used by the controller could be the current profile measurements, TLP motions, riser inclinations, relative horizontal distance, tensions and payouts for the risers.

The controller takes input from an operator or computes new optimal setpoints based on the measured inputs. The output is the control input for the actuator.

The environment, TLP and risers are described in Chapter 3. This chapter focuses on the actuator, measurements and controller system.

5.2 Actuator

The actuator in this system is the riser tensioner system, which is designed to carry the load of the risers and transfer it to the platform structure. In offshore operations the tension must be maintained independent of the movements of the platform. The TLP motions will induce motions on the risers and impact the tension. Current, wind gusts and second order LF wave forces cause the horizontal motions of the platform, introducing setdown in an offset positions. The WF oscillations of the riser are caused by first order wave loads. The compensation for the relative vertical motion between the TLP and the risers is called *heave compensation*. Heave compensators are usually divided into three groups; *passive*, *active* and a combination of these. The aim of the heave compensation system is to keep the riser tension unaffected by the vertical TLP motions. For riser systems today, this means to keep the tension close to constant.

Passive heave compensation systems can be described as spring-damper systems, and do not require any input of energy under operation. Most passive heave compensation systems are pneumatic-hydraulic systems with glycol and air in compression, and the load is balanced by the pressure of fluid volume act-

(a) Wire-line.

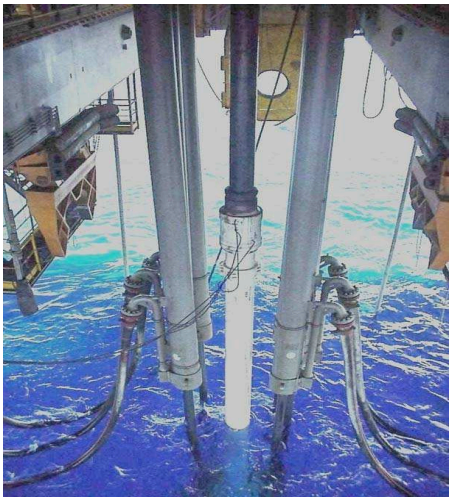

(b) N-line.

Figure 5.2: The different riser tensioner systems (National Oilwell Varco, 2007*b*).

ing on a piston. The spring is nonlinear due to the compressed gas volume. See Nielsen (2004) for more details.

There are two types of heave active compensators: (1) Wire-line and (2) N-line riser tensioner systems, see Fig. 5.2. Both riser tensioner systems give a nearly constant tension to the marine risers and compensate for rig motions. The N-line system has six cylinders in a ring. The system is symmetrical, so if one cylinder fails, the opposite cylinder is set free, and the remaining four keep on working. In drilling operations, the stroke length could be as much as 15m. In our application 2-3m could be sufficient. A tensioner system for production risers at Jolliet is shown in Fig. 5.3. The cylinders are installed in frames on the cellar deck and connected to a tensioner ring on the riser.

5.3 Measurements

To be able to run a supervisory, iterative FEM model we need to know the incoming current, the TLP motions and the top tension for each riser. To ensure that this monitoring model is giving a correct result, we could measure the payout and the top and bottom riser angles. The measured payout and the relative horizontal positions are used by the controller to calculate feedback.

Figure 5.3: Production riser tensioner system at the TLP Jolliet (National Oilwell Varco, 2007*b*).

5.3.1 Current

The incoming undisturbed current profile can be measured using an acoustic Doppler current profiler (ADCP). The current profile can be measured for water depths down to 2000m, depending on the configuration including the placement of the sensors, working frequency for the unit and cell size. ADCP measurement units are currently deployed on environmental monitoring buoys, offshore oil rigs and polar research moorings (RD Instruments, 2006). With increased operating depths, a single downward looking ADCP may not provide enough coverage. Fig. 5.4 shows how current profiles can be obtained in water depth larger than 1000m. Three different placements of the ADCPs may be used to cover the surface current, the mid-column current and the bottom current. Near the surface, the platform itself introduces changes in the current and wave field, due to its size and the use of thrusters for station keeping for floaters like the semi-submersible. Hence, the near surface current can not be reliably accomplished by using a current meter that measures the current in the direct vicinity of the rig. By using a horizontally directed ADCP the undisturbed, near surface current can be

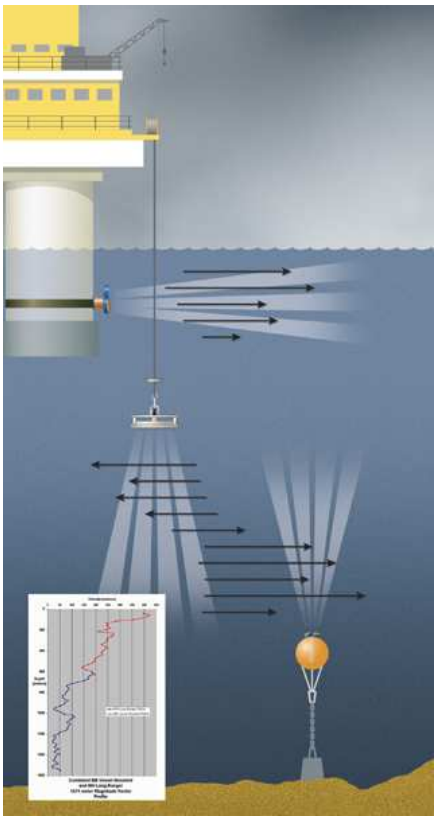

Figure 5.4: Using ADCP to cover the full current profile, including near surface, mid-column and bottom current (www.rdinstruments.com).

measured. While the near surface current is of main importance for the offset of the rig or platform, the mid-column velocity is affecting the riser deflections. The ADCP measuring the mid-column velocity is mounted on the rig or near the surface and directed downwards.

To measure the bottom current, an upward-looking ADCP is attached to the bottom structure or moored to the seabed. This bottom-mounted ADCP system collects current data and transmits it to the surface in realtime via an acoustic modem. In this way, the data of the upward-looking ADCP is combined with the down-looking and near surface data, to form the a continuous, full-water-column current profile.

5.3.2 TLP Motions

Several position measurement systems are commercially available, such as the local hydroacoustic position reference (HPR) system and the global navigation satellite system (GNSS). The two commercial satellite systems available today are the US system NAVSTAR GPS (NAVigation Satellite Timing And Ranging Global Positioning System) and the Russian GLONASS (GLObal NAvigation Satellite System), see Fossen (2002) and references therein. In addition a European satellite navigation system, *Galileo*, is under construction, estimated to begin operational services in 2010 (European Commission, 2007). The GPS system provides position measurements with an accuracy less than 1m in the horizontal direction, which is the typical accuracy for ship positioning systems today.

To find the acceleration and velocity of the TLP we can use available commercial inertial measurement technology. An inertial navigation system (INS) consists of a measurement part and a software part. The measurement part is called an inertial measurement unit (IMU), measuring the linear and angular accelerations. The software part is a state-observer, which computes the position, velocity and attitude from the measurements. To prevent the system from drifting, a GNSS is used as a reference for the position, and the resulting system is known as a *strapdown inertial navigation system* (Fossen, 2002).

It should also be noted that the company SeaFlex in cooperation with Kongsberg Maritime has developed a riser position reference system (RPR) which is an independent riser position reference system for a dynamic positioned drilling vessel. The position estimation is based on measured top tension and the top and bottom riser inclinations. The RPR is calibrated with other available position reference measurements (Høklie *et al.*, 2002).

5.3.3 Tension and Payout

The top tension can be found by measuring the pressure inside the pneumatic-hydraulic pistons. When we know the area of the piston stamp, the tension force can be calculated. The payout is found by counting magnetic coils along the piston. This is an accurate method down to the mm-level.

5.3.4 Top and Bottom Angles

The top and bottom angles for each riser could be measured by inclinometers, either electronic riser angle (ERA) or acoustic riser angle (ARA) measurements. The riser end connections are in this study modeled with free rotations. Recall that it in the industry is common to use bending stiffeners to prevent large rotations in the connections. We may therefore calculate larger end inclinations in this study than what is actually experienced in the industry. This simplification is

made as the main objective is to calculate the global geometry, and in deep waters this simplification will only introduce small errors in the end point position, see Section 4.7.

5.3.5 Relative Horizontal Distance

To determine the relative horizontal distance between two risers, one could use *acoustic location*. In water this technique is known as *sonar* (SOund Navigation And Ranging). There are two types; *passive sonars*, which listens without transmitting, and *active sonars* which creates pulses (*pings*) in order to produce echo. The time from transmission of a pulse to the reception is measured and converted to distance when we know the speed of sound in water (approximately 1500m/s). For a travel distance of 15m, the time will be 10ms, which is satisfactory for the sampling time here. The active sonar consists of a transmitter and receiver. These could be placed at the same location (monostatic operation) or at separate locations (bistatic). When more transmitters are used, spatially separated, it is called a multistatic operation (Wikipedia, 2007*b*).

5.4 Controller

To prevent collision between risers, control of the top tension is introduced. This dynamically control output could either be directly based on one or two of the measurements presented above, or there could be a model of the system (CPM) running in parallel, which use measurements as inputs to decide which action to take and calculate the feedback. Here, the first approach is used in investigation of the various control strategies, while the second approach is used in a more realistic case scenario.

Marine systems of today are required to operate in a wide range of environmental conditions while still giving acceptable safety and performance. For permanent installations, like the TLP, the all-year weather changes must be taken into consideration, also when designing the control system. In the North Sea the weather conditions can be harsh, and the TLP will experience large LF and WF motions, which again affect the risers. When installed in deep waters, the risers are more flexible than in shallow waters and behave more like cables. In addition, different static and/or dynamic properties of the risers in the array should be taken into consideration in the controller design. Hence, there could be large variations in the requirements for the controllers depending on both the operational conditions, riser properties and the water depth. We will later on denote this as *regimes*.

There may be two implementations of controller designs; one nonlinear controller covering all possible regimes or a combination of various controllers into

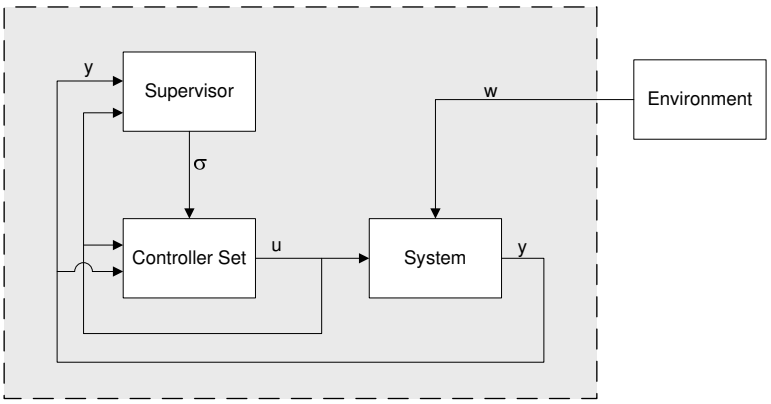

Figure 5.5: The hybrid control system.

one. The first solution may give a complicated controller, which could be almost impossible to design if the dynamics changes considerably. The second solutions is a concept of supervisory control switching between a set of controllers. Each controller is made for a pre-specified operational regime. Designing a controller for each regime is easier than one for all regimes. On the other hand, the drawback could be chattering between controllers, and complex logics and synchronizing functions handling the switching.

This switching between controllers may lead to instability. More general solutions are therefore developed to secure stability. A systematic approach can be found in Hespanha (2001), Hespanha and Morse (2002), Hespanha *et al.* (2003) and references therein. This strategy is called *supervisory control*, and makes it possible to switch between the different controllers corresponding to the current operational condition. A *hybrid system* often consists of continuous controllers and discrete switching between them. Nguyen (2006) and Nguyen *et al.* (2007) have proposed a hybrid control structure for dynamic positioning systems of marine vessels. The work on supervisory control in this thesis is motivated by the work of Nguyen (2006).

The two main blocks in the supervisory switched control system are the supervisor and the controller set (Fig. 5.5). The block representing the environment, w, affects the physical marine system, consisting of the TLP, the riser array, the actuator and the measurements. The measured values, y, are used as inputs in the supervisor and the controller. The supervisor monitors the configuration of the different risers and decides which controller set to use. The *controller switching signal*, σ, is sent to the controller. The correct controller is activated, and the output, u, is then sent to the actuator, forcing the risers to behave as desired.

The supervisor and the controllers are described in detail in Chapter 6.

Chapter 6

The Controller Architecture

This chapter aims to give a more thorough presentation of the controller architecture. This includes specifications of the different control objectives and a description of the riser operational conditions. The concepts and properties for a switched system in general are presented. A more in depth definition of terms and description of the supervisor, the controller and their components are given. All in all this describes the controller architecture and its components used in the simulations.

6.1 Control Objectives

The control objectives may be formulated based on two different principles subjected to available measurements. This can be measurements at the TLP wellhead, such as payout and top tension, or available measurements along the riser. The first control objective principle is based on wellhead measurements, whereas the second principle uses measurements of the relative horizontal distance between the risers, at one or more predefined depths, keeping it at a desired distance. For simplicity the objectives are presented for two risers, but they could easily be extended to an array of risers.

6.1.1 Control Objectives Based on Measurements at the Top

Today the top tension is kept close to constant by a passive heave compensation system for each riser

$$T_1 = T_2, \tag{6.1}$$

where T_j is the tension of riser $j = 1, 2$. Keeping the tensions constant and equal in both risers may lead to the following scenario: For the two risers in a tandem arrangement, R2 is in the wake of R1. Due to the shielding effects on R2, R1 will

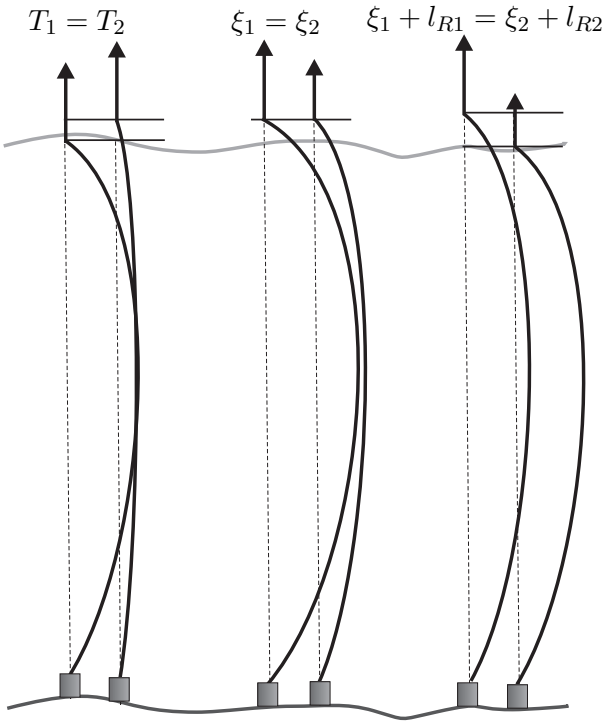

Figure 6.1: Effect of equal tension (a), equal payout (b), and equal effective length (c).

experience larger drag force than its downstream neighbor. If both risers have the same top tension, the deflection of R1 will exceed the deflection of R2, and the two risers may collide, shown in Fig. 6.1 a).

Another strategy is equal payout by connecting all risers to a common frame, proposed by Huse and Kleiven (2000), see Fig. 6.1b). This will give varying top tension on the risers depending on the drag forces and the position in the riser array. Equal payout by adjusting the top tension through automatic control is studied in this work, with the control objective

$$\xi_1 = \xi_2, \tag{6.2}$$

where ξ_j is the payout of riser j. Further work proposed in Rustad *et al.* (2007*b*,*c*) has shown that due to this tension variation, two equal risers will experience different length due to axial strain according to

$$\Delta l_R = \frac{\Delta T}{EA} l_{R0}, \quad \Delta T = T_1 - T_2, \tag{6.3}$$

where Δl_R is the length variation due to the difference in top tension ΔT of the two risers. l_{R0} is the untensioned initial riser length. Applying equal payout collision can still occur, but less frequent and in a smaller riser segment than for the equal tension strategy under the same environmental conditions. The risk of collision increases with increasing depth. In addition to the effect of axial strain increases for longer riser lengths and with larger tension variations.

We therefore propose a new control strategy letting the risers have equal effective length. By using automatic control of the heave compensators and top tension, the sum of payout and riser length should be equal such that the controller objective can be formulated as

$$\xi_1 + l_{R1} = \xi_2 + l_{R2}, \tag{6.4}$$

where l_{Rj} is the length of riser j. This means that in contrast to the strategy of equal payout we also compensate for the axial elasticity due to the tension variation, see Fig. 6.1c). By introducing this way of controlling the top tension, the risers may be placed with closer spacing without increasing the risk of collision.

Equation (6.3) is a simplification valid for equal risers. For two or more risers with different characteristics with respect to diameter, riser material or filling, a more general expression is needed. The riser length can be formulated as

$$l_{Rj} = l_{Rj}\left(T_{0j}\right) + \Delta l_{Rj}, \quad \Delta l_{Rj} = \frac{T_j - T_{0j}}{EA} l_{R0}, \tag{6.5}$$

where $l_{Rj}\left(T_{0j}\right)$ is the initial length of riser j with the initial tension T_{0j}. Δl_{Rj} is the elongation of riser j relative to its initial tension. The riser material is assumed linear as long as the tension is much smaller than the yield stress. Hence, an increase ΔT in top tension will give the same increase for all elements along the riser, and (6.5) is a good estimate on the riser elongation due to tension. Equation (6.4) could be then be rewritten as

$$\xi_1 + l_{R1}\left(T_{0j}\right) + \Delta l_{R1} = \xi_2 + l_{R2}\left(T_{0j}\right) + \Delta l_{R2}. \tag{6.6}$$

The initial length and static payout can be found individually. However, note that the payouts need to have the same initial positions for the equation to be valid, otherwise this difference needs to be included in the equation.

To summarize, we propose three different control objectives based on top measurements:

1. Equal tension: $T_1 = T_2$.
2. Equal payout: $\xi_1 = \xi_2$.
3. Equal effective length: $\xi_1 + l_{R1} = \xi_2 + l_{R2}$.

6.1.2 Control Objectives Based in Measurements Along the Riser

The second control objective principle is based on available measurements of the relative horizontal distance between the risers. In order to achieve near parallel risers, the horizontal distance between them should be constant and equal along the entire length of the risers. With only one measurement along the riser length, the distance between the risers $\Delta x_{R12,m}(z)$ should be equal to the distance at the top and bottom being the desired distance Δx_d. Hence,

$$\Delta x_{R12,m}(z) = \Delta x_d. \tag{6.7}$$

The measurement should be placed where the risers are likely to be closest, which is determined by the current profile. Note that we in this control objective do not need to consider the elasticity of the riser material directly.

6.1.3 Discussion

For the first principle of control objectives, reliable and accurate measurements of payout and tension are available today. Furthermore, the measurements and the actuator (top tension force) are found at the same location, thus preserving passivity properties of the closed loop system more easily due to collocated control. To calculate the total riser length as a function of time and tension, the initial riser length corresponding to the initial tension needs to be known.

If supervisory switched control is used, a system model is required and additional measurements of TLP motions, undisturbed current velocity profile and a good model for the hydrodynamic interaction are needed. These are used to calculate the smallest relative distance between the risers.

For the second principle of control objectives, the relative distance between the risers is measured directly. Hence, we do not need the additional measurements or a good process model for the linear controllers. The drawback of this method is that we are limited to a finite number of measurements, with predefined location along the riser. Also, we do not know if these are placed at the water depth where the risers are closest. As the measurements will be along the riser and the actuator is located at the top end, this set-up is not collocated. However, the system is much slower in the horizontal than the vertical direction, such that this may not be a problem after all. This may introduce some scattering in the vertical direction if the reference is not slow enough, but the horizontal direction will still be stable. We will in this work focus on the first principle of control objectives, as described in Section 6.1.1.

6.2 Riser Operational Conditions

The changes in the environmental conditions, in addition to the various riser types during operation and production, may require different control algorithms during the lifetime of a TLP/riser system. The purpose of the control system is to prevent collision for all environmental conditions, riser types and water depth, denoted as *regimes* or *riser operational condition* (ROC). A classification of the various regimes could help the design of appropriate controllers and smooth switching between them. The risers in an array may often have different physical properties. The external diameter, wall thickness, material and density of the internal fluid could vary, depending on whether the riser is used for drilling, production, export or workover to mention some. Together these factors decide the dynamics of the riser. The applications and properties of the riser, the *riser characteristics* (RC), also affect the controller gains. A specification of the different ROCs and the controllers based on these leads to a supervisory system where the time parameters and the necessary controller components are included according to the prevaling ROC. This concept of ROC is motivated by the work on *vessel operational conditions* (VOC) by Perez *et al.* (2006).

The aim of this section is to highlight the essential characteristics of the conditions that affect the dynamics of the riser system and use this information to decide which control action to perform.

6.2.1 Riser Characteristics

During drilling and production on offshore fields different riser types are used for different operations and purposes. Flexible risers or SCRs are not considered here. All risers referred to in this work are vertical steel risers, connected to a TLP. Some typical riser applications are:

- Drilling.
- Production.
- Workover/Maintenance.
- Export.
- Import.
- Injection.

The risers are specially made for each purpose, giving different properties which decides the risers physical behavior, both statically and dynamically. The most important parameters affecting the dynamics of a steel riser are:

- External diameter.
- Cross sectional area and wall thickness.
- Density of the riser contents.
- Riser length.
- Top tension.
- Elasticity.

Some of these parameters are closely related. The top tension level is dependent on the weight of the riser, i.e. the cross sectional area, the length of the riser and the density of the internal fluid.

The riser elongation is proportional to the modulus of elasticity times the cross sectional area. Hence, different cross sectional area will give different elongation according to the stiffness EA. The cross sectional parameters also contribute to a weight difference, increased or decreased by the difference in the density of the internal fluid between the risers. The effective weight decides the tension level along the riser, which together with the riser length is of major importance for the eigenperiods of the risers. For two otherwise equal risers, a difference in the variation of the contents affectes the total effective weight and the effective weight gradient. This could be seen statically as at which water depth the deflection is largest. A larger effective weight will have its maximum deflection at larger water depths than for otherwise equal risers.

The upper tension limit is decided by the yield stress for steel, whereas the lower limit is given by the effective weight plus a safety margin. Hence, for the otherwise equal risers with different contents, the upper tension limit is the same, but the lower limit is smaller for the riser with lighter contents.

Recall that the drag forces on the riser are proportional to the external diameter. For two risers with different external diameter, but equal weight per unit length, the riser with the largest diameter needs a larger top tension to compensate for the horizontal displacement due to the drag forces.

In extreme cases the longest riser eigenperiod can be close to the typical LF motions. For another riser case, the first eigenperiod could be close to the slowest WF motions. Hence, depending on the different dynamic properties and corresponding eigenperiods, resonance may occur at different frequencies. In addition it should be noted that the current field behind a riser and the shielding effect, is depending on the diameter of the upstream riser. The effects of the riser properties are not further investigated here, but should be taken into consideration when deciding the control strategy and the controller gains.

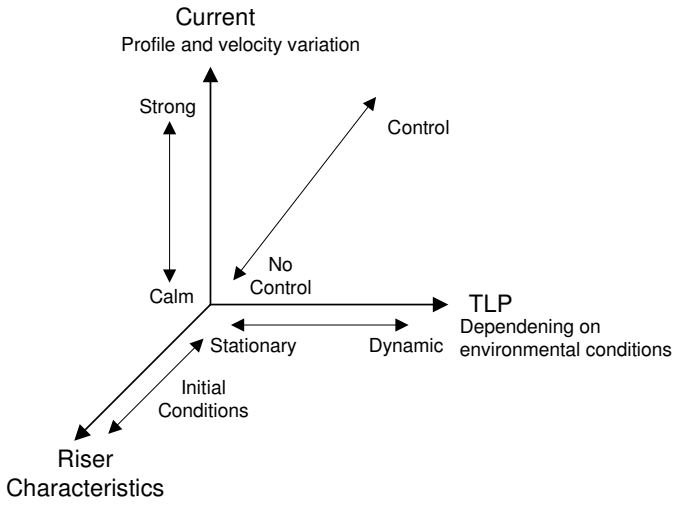

Figure 6.2: Riser operational conditions and influence on the controller choice.

6.2.2 Riser Operational Conditions

The ROC may be described by a triplet of attributes for a given riser

$$ROC := \langle Current,\ TLP,\ Riser\ Characteristics \rangle \tag{6.8}$$

where

Current refers to the current profile and velocity, acting on the riser array.

TLP refers to the motion of the floater which is affected by the environment; wind, waves and current.

Riser Characteristics (RC) refers to the static properties like riser length, diameters and cross-sectional area as well as the density of the internal fluid which may vary during the risers lifetime depending on the operation purpose.

The different RC along the out-of-plane axis decides which control objective to apply and an appropriate set of control gains. Figure 6.2 shows how these attributes are linked to the demand for control. The motion of the TLP due to the environmental conditions is the main parameter to compensate for. In harsh weather conditions the TLP will experience larger forces and motions and will induce more motions on the risers than in calm weather. Going to the right along the TLP axis will result in more motions and demand for a controller.

Large ocean currents give larger riser displacements. In addition, the characteristics of the current profile decide the riser configuration and where the deflection is largest. Going upward with increasing current velocity and possibly large changes in the velocity field may also require a controller. Hence, the further we move up and to the right, the larger is the demand for a controller. The decision is made in the switching logic block, see Section 6.4.3.

6.3 Switched Systems - Concept and Properties

This section is based on Hespanha (2001), Hespanha and Morse (2002) and Hespanha *et al.* (2003). The main idea with the supervisory switched controller is to automatically switch between different controllers depending on the situation. Note that the supervisor and the controller are decoupled. Hence, between switching times, the process is connected to one of the candidate controllers only, and the dynamics of the supervisor is not visible in the closed-loop system. This simplifies the stability analysis of the system. Detailed behavior of the supervisor or the controller set can be abstracted and we can concentrate on a small set of properties for the system.

Estimator-based supervisors continuously compare the behavior of the process with the behavior of the estimators or admissible process models to determine which model is best describing the actual process. The set of admissible process models considered in estimator-based supervision is

$$\mathcal{M} := \bigcup_{p \in \mathcal{P}} \mathcal{M}_p. \tag{6.9}$$

Each process model maps to a controller, which provides satisfactory performance for each model. The controller set is denoted

$$\mathcal{C} := \bigcup_{q \in \mathcal{Q}} \mathcal{C}_q. \tag{6.10}$$

p and q are the parameters taking values on the set $\mathcal{P}$ and $\mathcal{Q}$, respectively. A *controller selection function* $\chi : \mathcal{P} \to \mathcal{Q}$ maps each parameter value of $p \in \mathcal{P}$ with the corresponding index $q = \chi(p) \in \mathcal{Q}$ of controller $\mathcal{C}_q$ which provides satisfactory performance when connected to model $\mathcal{M}_p$. The estimator and controller may be described by linear or nonlinear systems according to

$$\begin{aligned} \mathcal{M} := \{\dot{\mathbf{x}}_E &= \mathbf{A}_E(\mathbf{x}_E, \mathbf{u}, \mathbf{y}),\ \mathbf{y}_p = \mathbf{C}_E(p, \mathbf{x}_E, \mathbf{u}, \mathbf{y}), \\ \mathbf{e}_p &= \mathbf{y}_p - \mathbf{y} : p \in \mathcal{P}\}, \end{aligned} \tag{6.11}$$

$$\mathcal{C} := \{\dot{\mathbf{x}}_q = \mathbf{F}_q(\mathbf{z}_q, \mathbf{y}),\ \mathbf{u} = \mathbf{G}_q(\mathbf{z}_q, \mathbf{y}) : q \in \mathcal{Q}\}, \tag{6.12}$$

where $\mathbf{x}_E$ is the estimation of the state vector, $\mathbf{u}$ is the control input vector, $\mathbf{y}$ is the process output vector, $\mathbf{y}_p$ is the output estimate vector, $\mathbf{e}_p$ is the estimation error vector, and $\mathbf{z}_q$ is the state vector of the controller. The decision logic compares all the estimation errors and $\mathbf{e}_p$ can be regarded as a measure of the likelihood that the actual process is inside the ball $\mathcal{M}_p$.

6.3.1 System Properties

For the formal stability proofs of supervisory switched system, the following definition of a switched system (Hespanha, 2001) is used

$$\dot{\mathbf{x}} = \mathbf{A}_\sigma(\mathbf{x}, \mathbf{w}), \tag{6.13}$$

$$\mathbf{e}_p = \mathbf{C}_p(\mathbf{x}, \mathbf{w}),\ p \in \mathcal{P}, \tag{6.14}$$

where $\mathbf{x}$ denotes the state vectors of the process, the multi-controller and the multi-estimate, and $\mathbf{w}$ is the environmental disturbance. The two basic properties for the switched system are the *matching* and *detectability* properties.

Matching Property means that the set of estimators should be designed such that each particular $\mathbf{y}_p$ provides a good approximation to the process output $\mathbf{y}$. This means that $\mathbf{e}_p$ is small whenever the actual process is inside the corresponding $\mathcal{M}_p$.

Detectability Property means that for every fixed estimator, the switched system must be detectable with respect to the estimation error $\mathbf{e}_p$ when the value of the switching is frozen at $\sigma = \chi(p) \in \mathcal{Q}$.

6.3.2 Switching Logic

The index σ of the controller in the feedback loop is determined by the switching logic which takes the estimation error vector $\mathbf{e}_p$ as an input. According to the certainty equivalence principle, when a particular estimation error e_p is the smallest element in the error vector $\mathbf{e}_p$, the index $p \in \mathcal{P}$ is the likely value of the parameter. Hence, the corresponding $p \in \mathcal{P}$ describes the ongoing process best and is mapped to the controller switching signal $\sigma = \chi(p) \in \mathcal{Q}$. To prevent chattering, a delay is introduced in the switching process. This could for instance be dwell-time switching or hysteresis switching. Since the value of p which corresponds to the smallest e_p varies, a *process switching signal* $\rho : [0, \infty) \to \mathcal{P}$ is introduced to indicate the current estimate $\rho(t) \in \mathcal{P}$ of the index p used in the feedback loop. The mapping from the process switching signal to the controller switching signal is written $\sigma = \chi(\rho)$. Note that this output for the switching logic is the one that determines which controller should be used. The *small error*

and *non-destabilization* properties need to be satisfied by the monitoring signal generator and the switching logic.

Small Error Property means that there is a bound on e_ρ in the terms of the smallest signal e_p for a process switching signal for which $\sigma = \chi(\rho)$. The norm of e_ρ should be guaranteed, by the switching logic, to be smaller than a constant times the norm of the smallest e_p.

Non-Destabilization Property The switching signal σ is said to have the non-destabilization property if it preserves the detectability in a time-varying sense, i.e. if the switched system is detectable with respect to the switched output e_ρ for ρ and $\sigma = \chi(\rho)$. This property is satisfied if:

- The switching is slow on the average by using dwell-time switching logic which strictly is used among linear models and controllers.
- The switching stops in finite time using scale-independent switching logic which can be used in switching between both linear and nonlinear models and controllers.

For the switching logic there is a conflict between the desire to switch to the smallest estimation error to satisfy the small error property, and the concern of too much switching which may violate the non-destabilization property.

6.3.3 Scale-Independent Hysteresis Switching

Since the modeling of the riser system is nonlinear, the scale-independent hysteresis switching based on Hespanha (2001) will be used. The hysteresis switching logic in general slows down the switching based on the observed growth in estimation error vector $\mathbf{e}_p$ instead of for a fixed dwell-time. The monitoring signal μ_p for each process is based on the norm of the estimation error and is defined by Hespanha (2001) as

$$\dot{\mu}_p = -\lambda\mu_p + \gamma(\|e_p\|),\ p \in \mathcal{P}, \tag{6.15}$$

where λ is a non-negative forgetting factor, $\mu(0) > 0$, γ is a class $\mathcal{K}$-function[1] and $\|\cdot\|$ is a norm. The switching procedure is illustrated in Fig. 6.3. h is a positive hysteresis constant, and $\rho = \arg\min \mu_p$ returns the index of the smallest monitoring signal μ_p. The monitoring signal for the prevailing model, μ_ρ, is compared to the other monitoring signals. When a new signal μ_p times the contribution from the hysteresis is smaller than the prevailing signal μ_ρ, the system switches. Otherwise, the actual value is held.

[1] A continuous function $\alpha : [0, a) \to [0, \infty)$ is said to belong to a class $\mathcal{K}$ if it is strictly increasing and $\alpha(0) = 0$ (Khalil, 2000).

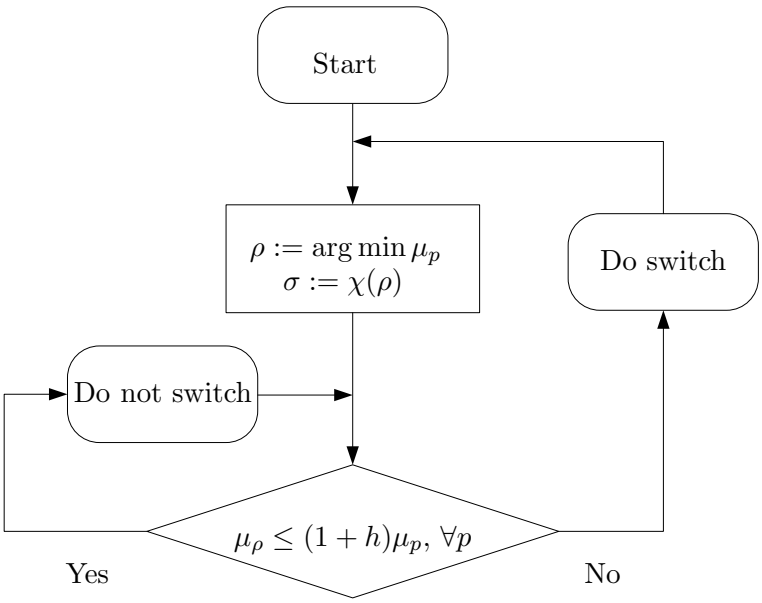

Figure 6.3: Scale-independent hysteresis switching logic (Hespanha, 2001).

To summarize, the matching and detectability properties are important for the multi-estimator and the multi-controller, respectively. The small-error property makes sure that the selected controller is the best. When the process is between two regimes, fast switching may affect the stability of the system. Non-destabilization will prevent chattering by providing switching logic such as hysteresis switching.

6.3.4 Model Concept Definitions

The supervisor described in Hespanha (2001), Hespanha and Morse (2002) and Hespanha *et al.* (2003), consists of a set of admissible models which are compared to the actual process. The model which best describes the ongoing process is used. The terms admissible process model and actual process used in their works, and also given here in Section 6.3, can not be directly transferred to the set-up and mathematical models used in this work. Furthermore, the difference between an observer and an independent model needs to be clarified.

Observers or state estimators are aiming to obtain an estimate of the current state of the dynamic system by using available measurements online (each time step). An observer often copies the dynamics of the system and add

an *injection term* constructed such that the state estimate should be a reconstruction of the unmeasured state.

Independent models are also used to estimate the states of dynamic systems. The states are estimated based on inputs and the system model. These models do not use online measurements to correct the states of the system. They are therefore dependent on accurate system models and inputs to calculate good results. Notice that also here the model will be updated based on available information and measurements. However, this is not done by an injection term.

What Hespanha (2001), Hespanha and Morse (2002), Hespanha *et al.* (2003) refer to as the actual or ongoing process, corresponds to what we denote the physical process or the process plant model (PPM). The main difference is found for the supervisor. In this work we have used only one nonlinear model type, denoted ACPM (accurate control plant model), covering all the operational regimes. This follows a similar approach as in Reite (2006).

However, the desired distance between the risers is defined according to the operational regimes. Depending on the deviation from the desired riser configuration, a model error e_p, corresponding to the estimation error, is defined and calculated for each regime $p \in \mathcal{P}$.

Hence, this independent process model (ACPM) and the resulting error models $\mathbf{e}_p$ correspond to the set of admissible process models or multi-estimators in the definitions in Section 6.3.1. The matching and detectability properties are defined for observers, and are not directly applicable for the independent model, in sense of global exponential observers. However, the matching property with respect to the accuracy of the model and the boundaries for the different regimes are meaningful. The switching logic is used, even though the observer properties are not relevant. The second part with the small error and non-destabilization properties are of importance.

6.3.5 Switched System Stability Analysis

The scale-independent hysteresis switching logic guarantees the non-destabilization and the small error properties by the following theorem:

Theorem 6.1 (Scale-Independent Hysteresis-Switching, Hespanha (2001)) *Let σ be the switching signal and $N_\sigma(\tau, t), t > \tau \geq 0$ be the number of discontinuous of σ in an open interval (t, τ). Let $\mathcal{P}$ be a finite set with m elements. For any $p \in \mathcal{P}$ we have that*

$$N_\sigma(\tau, t) \leq 1 + m + \frac{m \log(\frac{\mu_p(t)}{\epsilon + e^{-\lambda t} \epsilon_0})}{\log(1+h)} + \frac{m\lambda(t-\tau)}{\log(1+h)}, \tag{6.16}$$

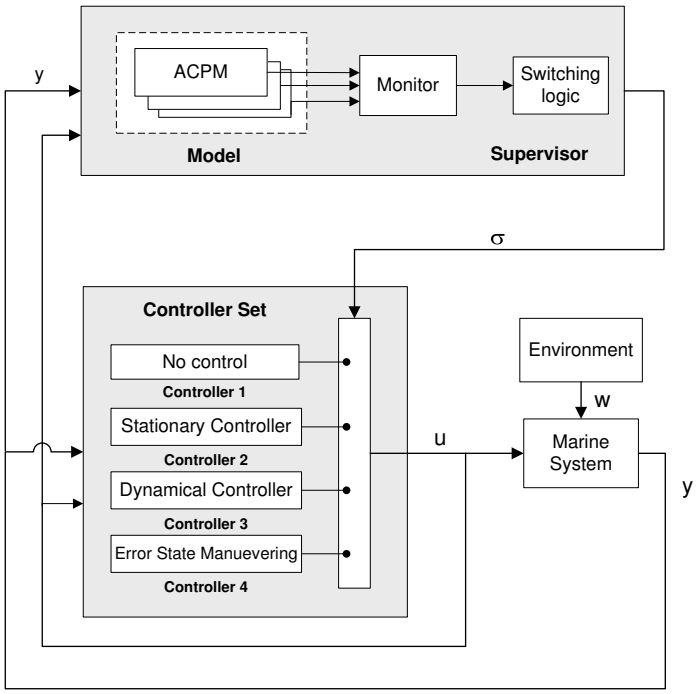

Figure 6.4: Structure of the switching control concept.

and

$$\int_0^t e^{-\lambda(t-\tau)}\gamma_p(\|e_\rho(\tau)\|)d\tau \leq (1+h)m\mu_p(t) \tag{6.17}$$

where ϵ, ϵ_0 *are nonnegative factors, with at least one of them strictly positive.*

Proof. See Hespanha *et al.* (2000). ■ (6.16) guarantees the non-destabilization of switching, while (6.17) guarantees the small error property. For details on the stability analysis, see Hespanha *et al.* (2000).

6.4 Supervisor

The supervisor's main task is monitoring of the riser array, deciding which control action to perform and trigging the correct controller. The supervisor consists of three parts; the riser model, the monitor and the switching logic, see Fig. 6.4.

The ACPM calculates the configuration of the risers and is the most accurate estimate of the riser system behavior. As inputs it takes the measured

undisturbed incoming current, the TLP motions and the top tension for each riser. One model is running for each riser.

The monitor is continuously comparing the calculated riser configuration data from the ACPM and the measured tension with a set of values describing the different regimes. Based on the regimes and the deviation from the desired riser configuration, a monitoring signal μ_p, is calculated. $p \in \mathcal{P}$ is the regime index number.

The switching decides which controller to use and which action to perform based on the inputs from the monitor.

6.4.1 Accurate Control Plant Model

The ACPM is a nonlinear, iterative FEM model of the riser system based on the PPM from Chapter 3. It is used to accurately estimate the state of the riser system and its behavior. It is characterized as an independent model, as it is not taking any measurements, in terms of an injection term, to update its estimated states.

As inputs it takes the measured undisturbed incoming current, the TLP position, velocity and acceleration, and the top tension for each riser. When we know these inputs, we can easily calculate the configuration of R1. For R2 we know its top tension, the TLP motion, the position of R1 and the undisturbed current. The current acting on R2 is a function of the incoming current on R1 and the distance between the two risers. We will therefore need iterations to find the right position of R2. For the risers further down the array, the inputs and procedures are similar.

The ACPMs are simulated with fewer elements (8-12) than the PPMs (15-20). This allows the ACPMs to run faster, but some of the accuracy is lost. However, the number of elements used for the ACPM is depending on the accuracy needed in the monitor. This is further analyzed and discussed in Chapter 7.

6.4.2 Monitor

The different regimes can be divided into five: (1-2) normal regimes where all riser nodes are close to their desired positions, or the deviations are small and the tension variations have been small for a given time period, (3) the risers have a medium deviation from the desired configuration due to slow variations from LF TLP motions and tide, (4) the risers are subject to fast and large disturbances due to TLP motions or currents, (5) the risers are in a (near) collision situation called an *error state*.

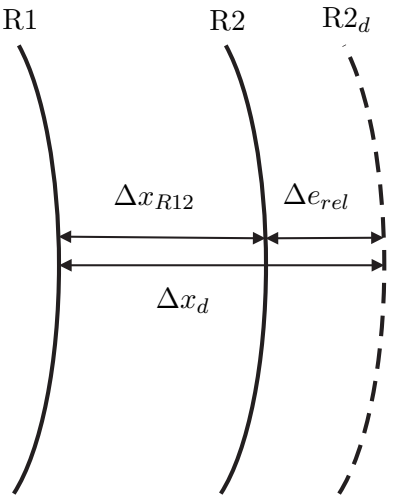

Figure 6.5: Actual and desired riser positions.

The switching conditions are mainly defined by the deviation from the desired horizontal distance between the risers

$$\Delta \mathbf{e}_{rel} = \Delta \mathbf{x}_d - \Delta \mathbf{x}_{R12}, \tag{6.18}$$

$$\Delta \mathbf{x}_{R12} = \mathbf{x}_{R2} - \mathbf{x}_{R1}, \tag{6.19}$$

where $\Delta \mathbf{x}_d$ is the vector of the desired distance between the risers in each node, $\Delta \mathbf{x}_{R12}$ is the horizontal distance between two neighboring risers, and $\mathbf{x}_{Rj}$ is the horizontal position vector of riser j. For a riser segment, the scalar values are found in Fig. 6.5. Δe_{rel} is the (scalar) deviation from the desired R2 position, R2$_d$, in the riser segment shown here. The maximum deviation along the riser is defined as $\|\Delta \mathbf{e}_{rel}\|_\infty$. The max deviation is given a value in diameters, D, depending on the regime. The monitor comparing values in Table 6.1 is based on a desired relative riser distance $\Delta x_d = 15D$, which is the distance at the top and bottom end points used in the simulations here at 1200m water depths. The model error vector $\mathbf{e}_p$ used in the calculations of the monitoring signals is mainly found from the maximum deviation from the desired riser distance. In some cases additional conditions on the horizontal R2 velocity, $\dot{\mathbf{x}}_{R2}$, or the maximum tension variations for a given period of time $|\Delta T(t, t_0)|_{\max}$ are included. The switching conditions for the error calculations are found in Table 6.1.

The relative velocity vector $\Delta \dot{\mathbf{e}}_{rel}$ tells how fast the risers are moving towards or away from each other, where how fast they are moving towards each other is of main importance. This number will be small in most cases since the risers move

Regimes	Monitor comparing values	μ_p	ρ	σ
Normal 1	$\|\Delta\mathbf{e}_{rel}\|_\infty = 0D$	μ_1	1	1
Normal 2	$\|\Delta\mathbf{e}_{rel}\|_\infty = 1.5D$ & $\|\Delta T(t,t_0)\|_{\max} \leq 20\text{kN}$	μ_2	2	1
Slowly varying	$\|\Delta\mathbf{e}_{rel}\|_\infty = 2.5D$	μ_3	3	2
Fast changing	$\|\Delta\mathbf{e}_{rel}\|_\infty = 2.5D$ & $\|\dot{\mathbf{x}}_{R2}\|_{\max} \geq 0.6\text{m/s}$	μ_4	4	3
Error state	$\|\Delta\mathbf{e}_{rel}\| \geq 13D$	μ_5	5	2

Table 6.1: The switching conditions.

slowly, such that the variance in position will be captured by considering the relative distance. Furthermore, if both risers are moving fast, for instance due to WF TLP motions, $\Delta\dot{\mathbf{e}}_{rel}$ would not necessarily capture these motions, since the relative motion might be small. On the other hand, if $\Delta\dot{\mathbf{e}}_{rel}$ is small, it may not lead to an instant collision. By considering only $\dot{\mathbf{x}}_{R2}$, the fast TLP motions are captured. If R2 is exposed to varying drag forces due hydrodynamic interaction, this could be captured both by considering $\Delta\dot{\mathbf{e}}_{rel}$ and $\dot{\mathbf{x}}_{R2}$. For activation of the dynamical controller, we will consider $\dot{\mathbf{x}}_{R2}$.

The scalar model error e_p for each regime $p \in \mathcal{P}$ is given below. The model error closest to the definition of each regime is the smallest, and its index number is used to decide the controller.

Normal 1, $p = 1$

This regime is defined as when the risers are parallel, with the desired horizontal distance between the nodes at the each water depth. Using the monitoring comparing values from Table 6.1 gives the following model error and γ-function:

$$\mathbf{e}_1 = \Delta\mathbf{e}_{rel} - 0D, \tag{6.20}$$

$$\gamma_1 = \gamma(\|\Delta\mathbf{e}_{rel}\|) = \|\Delta\mathbf{e}_{rel}\|_\infty. \tag{6.21}$$

Hence, the maximum deviation from the desired position determines the error and the monitoring signal.

Normal 2, $p = 2$

In addition to the deviation for the desired relative horizontal distance shown above, the variation in tension is also included. The function $T(t,t_0)$ is the tension for a given time window, ses Fig. 6.6. t is the current time, and t_0 is the oldest time for which information is kept, for instance $t_0 = t - 100\text{s}$. If the

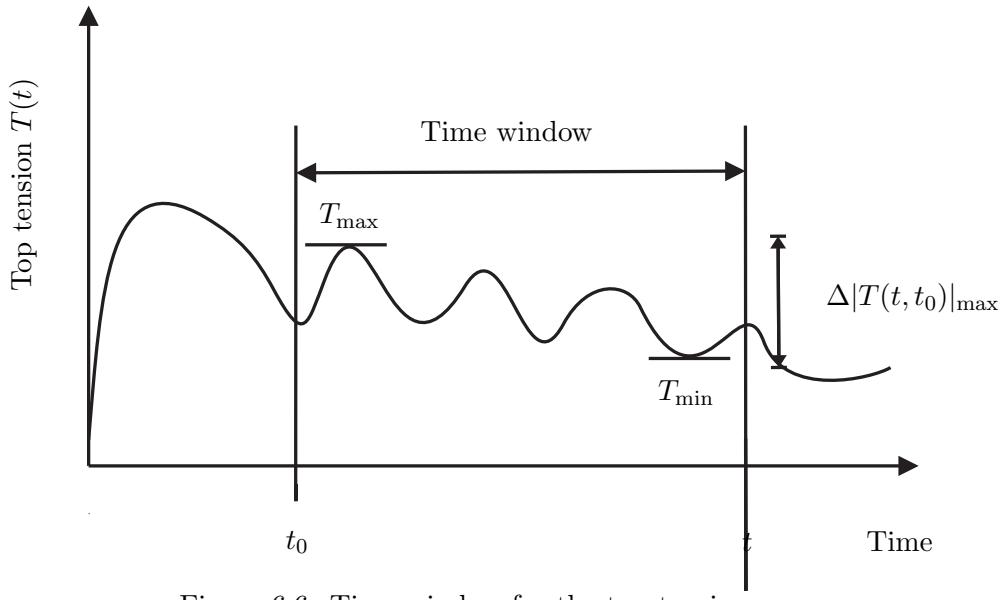

Figure 6.6: Time window for the top tension.

tension difference between maximum and minimum tension in the time window is smaller than the boundary, here 20kN, the error contribution from tension is set to zero. Otherwise, the errors are weighted and summarized.

$$|\Delta T(t,t_0)|_{\max} = |T(t,t_0)|_{\max} - |T(t,t_0)|_{\min}, \tag{6.22}$$

$$e_{2,T} = 0 \,\text{for}\, |\Delta \mathrm{T}(\mathrm{t},\mathrm{t}_0)|_{\max} \leq 20\text{kN, else} \tag{6.23}$$

$$e_{2,T} = k_T |\Delta T(t,t_0)|_{\max}, \tag{6.24}$$

$$e_{2,\Delta x} = \|\Delta \mathbf{e}_{rel} - 1.5D\|_\infty, \tag{6.25}$$

$$\mathbf{e}_2 = \begin{bmatrix} e_{2,T} & e_{2,\Delta x} \end{bmatrix}^T, \tag{6.26}$$

$$\gamma_2 = \gamma_2(\|\mathbf{e}_2\|) = \sqrt{(e_{2,T})^2 + (e_{2,\Delta x})^2}, \tag{6.27}$$

where $k_T = 1e^{-5}$, such that for $|\Delta T(t,t_0)|_{\max} > 20$kN, the error contribution for tension will be $e_{2,T} > 0.2$, whereas the contribution from the relative horizontal distance with deviation $0.5D$ gives $e_{2,\Delta x} = 0.15$. For a smaller tension deviation, the error from the relative horizontal distance is the only contribution.

Slowly varying, $p = 3$

The slowly varying regime is for LF motions and tide giving medium deviation from the desired relative distance. Like for the regime normal 1, this regime does

only consider the relative horizontal distance. Hence,

$$\mathbf{e}_3 = \Delta\mathbf{e}_{rel} - 2.5D, \tag{6.28}$$
$$\gamma_3 = \gamma_3(\|\mathbf{e}_3\|) = \|\mathbf{e}_3\|_\infty. \tag{6.29}$$

Fast changing, $p = 4$

For the fast changing regime, the risers experience faster motions due to the TLP motions or current. This can be monitored through the horizontal velocity vector of R2, $\dot{\mathbf{x}}_{R2}$, which is included in this error model in addition to the relative riser distance. Since we want to capture the fast motions, we use a high-pass filter, corresponding to the WF motions with periods $T = 5 - 20$s. We are interested in the largest velocity and how fast it changes. The largest horizontal velocity is found by

$$\dot{x}_{R2,\max} = \|\dot{\mathbf{x}}_{R2}\|_\infty. \tag{6.30}$$

If $\dot{x}_{R2,\max}$ is larger than the boundary value given in Table 6.1, we have $e_{4,\dot{x}} = 0$. Otherwise the error is given by $e_{4,\dot{x}} = 0.6\text{m/s} - \dot{\text{x}}_{\text{R2,max}}$. Since the risers are changing the direction according to the specified motion from the TLP, the resulting error will be chattering between zero and the calculated value. A low-pass filter is therefore introduced to give a mean error contribution from the velocity. The contribution from relative distance is weighted to be of less importance. Hence,

$$e_{4,\Delta x} = \frac{1}{2}\|\Delta\mathbf{e}_{rel} - 2.5D\|_\infty, \tag{6.31}$$
$$e_4 = [\ e_{4,\Delta x} \quad e_{4,\dot{x}}\ ], \tag{6.32}$$
$$\gamma_4 = \|\mathbf{e}_4\|_1 = |e_{4,\Delta x}| + |e_{4,\dot{x}}|. \tag{6.33}$$

Error State, $p = 5$

Instead of finding the max-deviation from a desired configuration, we here investigate if the closest node is in a (near) collision situation. This could be written

$$\mathbf{e}_5 = \Delta\mathbf{e}_{rel} - 13D, \tag{6.34}$$
$$\gamma_5 = \gamma_5(\mathbf{e}_5) = |\mathbf{e}_5|_{\min}. \tag{6.35}$$

This regime will also be activated if the risers are far apart, for instance if the second riser has a large deflection.

6.4.3 Switching Logic

The switching logic decides which controller to use through the controller switching signal σ, based on the value of the monitoring signal μ_p in (6.15). The

scale-independent hysteresis switching logic from Section 6.3.3 is used. The state-diagram (Fig. 6.3) shows how the process switching signal ρ is found based on the smallest monitoring signal μ_p. The mapping $\sigma = \chi(\rho)$ is found in Table 6.1.

λ_p is the forgetting factor for μ_p. A larger factor λ gives faster forgetting, while a smaller λ gives longer memory. To decrease the detection time when active control is needed, the memory is slightly decreased by choosing λ_p slightly bigger for $p \in \{3, 4, 5\}$. Rewriting (6.15) on vector form we have

$$\dot{\boldsymbol{\mu}} = -\boldsymbol{\lambda}\boldsymbol{\mu} + \boldsymbol{\gamma}(\|\mathbf{e}_p\|), \tag{6.36}$$

where $\dot{\boldsymbol{\mu}}$ is the vector of monitoring errors, $\boldsymbol{\lambda}$ is the diagonal matrix of non-negative constants (here $\boldsymbol{\lambda} = \text{diag}\begin{bmatrix} 1 & 1 & 1.5 & 2 & 1.5 \end{bmatrix}^{\mathrm{T}}$), and $\boldsymbol{\gamma}(\|\mathbf{e}_p\|)$ is the resulting vector of the class $\mathcal{K}$-functions. The initial monitoring value is set to $\boldsymbol{\mu}(0) = \begin{bmatrix} 0.9 & 1 & 1 & 1 & 1 \end{bmatrix}^T > \mathbf{0}$.

6.5 Controller Set

The controller set's main task is to prevent riser collision, and the controller best suited for the current operational conditions is determined by the switching logic. Other inputs in the controller block are the measured top tension and payout. The controller block in Fig. 6.4 consists of a set of controllers designed for each of the regimes described in Section 6.4.2 based on the ROCs from Section 6.2. The active controllers comprise of the following components:

The guidance block calculates the guidance trajectory for each riser in the array based on the control objectives.

The reference model generates the trajectory based on the guidance model. To prevent collision in an array of risers during transit to reach the desired tension, the sequence and how fast the risers are tensioned are of importance. This could be formulated as a maneuvering problem (Skjetne, 2005), and is a subject for further research.

One controller is designed specially for each operational regime. Which controller to use is decided by the supervisor which sends the controller switching signal σ to the controller block such that the most appropriate controller is used in the feedback loop. To provide a smooth transition between the controllers, a weighting function is introduced.

6.5.1 Guidance

The guidance trajectory determined by the actual control objective, described in Section 6.1. Depending on the control objective it takes relative distance, payout

and/or tension as inputs. In the guidance formulations below, we have assumed two risers, with R1 being the reference of R2. However, these principles are easily expanded to an array of risers.

Equal Payout

The equal payout guidance block needs the payout measured for the reference risers. For the payout to be equal for both risers, the guidance is written

$$\xi_{r,2}(t) = \xi_1(t), \tag{6.37}$$

where ξ_1 is the measured payout of R1 and $\xi_{r,2}$ is the guidance for R2.

Equal Effective Length

When the riser elongation due to changes in top tension is included, we need to know the prevailing top tensions, the initial top tensions and the initial riser length for both risers, in addition to the measured payout to the reference riser. Using R1 as a reference for R2 we rewrite (6.6) to

$$\xi_{r,2}(t,T) = \xi_1(t) + l_{R,1}\left(T_{0,1}\right) + \Delta l_{R,1}(T_1) - \left[l_{R,2}\left(T_{0,2}\right) + \Delta l_{R,2}(T_2)\right]. \tag{6.38}$$

If R2 is used as a reference, the indexes are switched. For an array of risers, one could be chosen as the leader, and the payout for all the other risers could be calculated relative to this one.

Relative Horizontal Distance

Here we measure the relative horizontal distance between the risers at one predefined water depth z. The desired distance is Δx_d, and the guidance is written

$$\Delta x_{R12,r}(z) = \Delta x_d. \tag{6.39}$$

The error (6.51) later, indicates that when R1 approaches R2, the relative distance is reduced. If only R2 is controlled, the top tension of R2 needs to be decreased to maintain the same relative distance.

6.5.2 Reference Model

To provide a smooth trajectory and high performance, a reference model is designed for the different guidance models. The reference is introduced to calculate

a feasible trajectory for the payout or the relative horizontal distance decided in the guidance block. The following third order filter is demonstrated appropriate

$$\ddot{\xi}_d + 2\zeta_d\omega_d\dot{\xi}_d + \omega_d^2\xi_d = \omega_d^2\xi_{ref}, \tag{6.40}$$

$$\dot{\xi}_{ref} = -\frac{1}{t_d}\xi_{ref} + \frac{1}{t_d}\xi_r, \tag{6.41}$$

where ξ_d and its derivatives are the desired payout position, velocity and acceleration trajectories. ξ_r is the new reference coordinates in the same frame, and ξ_{ref} is the low pass filtered coordinate. ζ_d is the relative damping ratio, ω_d is natural frequency, and t_d is the cut-off period period of the low pass filter in (6.41). This provides a smooth transfer between different setpoints.

For the relative horizontal distance the corresponding third order filter is written

$$\Delta\ddot{e}_{rel,d} + 2\zeta_d\omega_d\Delta\dot{e}_{rel,d} + \omega_d^2\Delta e_{rel,d} = \omega_d^2\Delta e_{rel,ref}, \tag{6.42}$$

$$\Delta\dot{e}_{rel,ref} = -\frac{1}{t_d}\Delta e_{rel,ref} + \frac{1}{t_d}\Delta e_{rel,r}, \tag{6.43}$$

where $\Delta e_{rel,d}$ and its derivatives are the desired relative horizontal distance, velocity and acceleration trajectories. $\Delta e_{rel,r}$ is the new reference coordinates in the same frame, and $\Delta e_{rel,ref}$ is the low pass filtered coordinate.

The main objective of this block is to generate a safe and legal reference trajectory for the top tension to follow. For an array of risers, changing the tension too fast for one riser and too slow for another might lead to a near collision situation between risers not originally conflicting. To avoid this problem, we have to figure out how fast each riser should follow its trajectory. This may be expressed as a maneuvering problem, with a geometric and a dynamic task. The geometric task is the path to follow, while the dynamic task is related to how fast we follow this path. This is a subject to further study. The definition of the maneuvering problem is found in Fossen (2002) and Skjetne (2005).

6.5.3 Controllers

Each riser has a pretension $T_{0,j}$. The total top tension in each riser is equal to the pretension, plus the contribution from the controller

$$T_j = T_{0,j} + \tau_{c,j}. \tag{6.44}$$

The controllers are designed for each of the regimes defined in Section 6.2.

Controller 1, σ_1 is for normal conditions and low current velocities, where the top tensions are kept constant, to reduce unnecessary wear and tear. The tensions are equal to the previous controller in time, but possibly at different values for the two risers. The initial tension is equal to the pretension.

Controller 2, σ_2 is for slow changes and stationary conditions, calculating the new top tensions based on the payout, top tension and riser length. A PI-controller could be appropriate.

Controller 3, σ_3 is for faster changing conditions, and the derivative properties should be included. Hence, a PID-controller could be used.

Controller 4, σ_4 is called *error state maneuvering* (ESM). It is used when we experience fault conditions and is structurally different from the other controllers. For two risers only, the ESM controller can be the same PI-controller as for controller 2. For an array of risers, the controller algorithm and the calculation of the reference trajectory may be more complicated to avoid collisions.

For the first control objective principle the controllers can be written

$$\begin{aligned}
\tau_{c1,j} &= const, && (6.45)\\
\tau_{c2,j} &= -K_{P2,j}e_j - K_{I,j}\int e_j dt, && (6.46)\\
\tau_{c3,j} &= -K_{P3,j}e_j - K_{I,j}\int e_j dt - K_{D3,j}\dot{e}_j, && (6.47)\\
\tau_{c4,j} &= \tau_{c2,j}, && (6.48)\\
e_j &= \xi_{d,j} - \xi_j, \quad j = 1, 2, && (6.49)
\end{aligned}$$

where e_j is the error between the desired payout $\xi_{d,j}$ and the actual payout ξ_j for riser j. $K_{I,j} = \frac{K_{P2,j}}{T_{I,j}}$ is the integrator gain, and $K_{D3,j} = K_{P3,j}T_{D3,j}$ is the derivation gain. The integrator is the same in both controllers 2 and 3, and integrator anti-windup is included to avoid saturation of the actuator.

For the second control objective principle based on the relative horizontal distance we propose a PI-controller

$$\begin{aligned}
\tau_{c2,j} &= -K_{P,j}\Delta e_{rel} - K_{I,j}\int \Delta e_{rel} dt, && (6.50)\\
\Delta e_{rel}(z) &= \Delta e_{rel,d} - \Delta x_{R12,m}(z), && (6.51)
\end{aligned}$$

where $K_{P,j}$ and $K_{I,j}$ are tuned for this control objective.

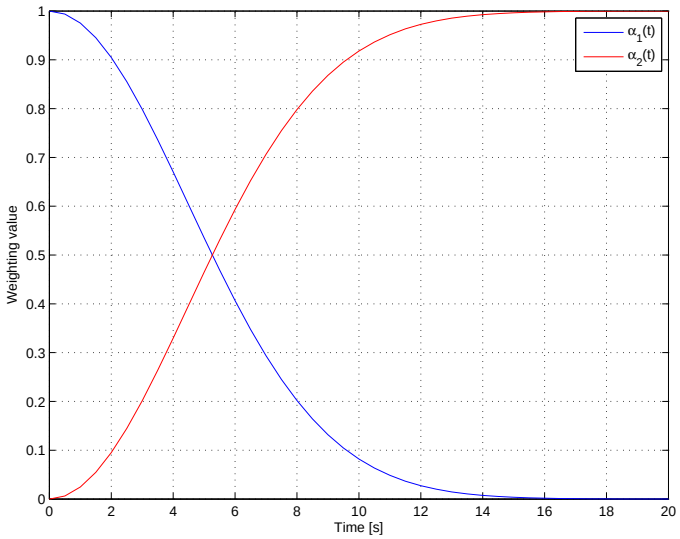

Figure 6.7: Weighting functions α_1 and α_2.

6.5.4 Transition

To ensure smooth transition when switching between the controllers, a weighting function is used such that

$$\tau_{c,j} = \alpha_1(t)\tau_{old} + \alpha_2(t)\tau_{new}, \tag{6.52}$$

$$\alpha_1 = \exp\left[-10\left((t/20)\right)^2\right], \tag{6.53}$$

$$\alpha_2 = 1 - \exp\left[-10\left((t/20)\right)^2\right], \tag{6.54}$$

where $\tau_{c,j}$ is the resulting controller, τ_{old} the previous and τ_{new} the new controller output in time, respectively. α_1 and α_2 are weighting functions dependent on the time from the switching moment. Their sum is always 1. The functions are seen in Fig. 6.7. The switching between the controllers is tuned to approximately 20s here. In real life the switching may take longer time and is dependent on how fast the environmental conditions change.

6.5.5 Integrator Anti-Windup

A controller with integral action in combination with an actuator which may become saturated might give undesirable effects. If the error is so large over a period of time that the integrator saturates the actuator, the feedback path will

be broken. The integrator may continue to integrate up to a large value. When the error finally is reduced, the integrator value may be so large that it takes time to discharge it. This effect is called *integrator windup*. To prevent it, we can stop updating the integrator when the actuator saturates, or we can discharge it. The second method is implemented here.

The error difference between the actuator output and the controller output times a gain is fed back to the system. When the actuator is in saturation, this error signal works to discharge the integrator such that the controller output is at the saturation limit. When the actuator is not in saturation, the error is zero. This could be written

$$\dot{u}_I = \frac{K_p}{T_i} e(t) - \frac{1}{T_i}[v(t) - u(t)], \tag{6.55}$$

$$v(t) = \text{sat(u(t))}, \tag{6.56}$$

where u is the controller output and v is the actuator output (Egeland, 1993, Åström and Wittenmark, 1997).

Chapter 7

Control Plant Model Analysis

In Chapter 3, a mathematical model for a riser is derived. This model was implemented in Simulink and verified by comparing it to the commercial FEM software RIFLEX (Fylling *et al.*, 2005) in Chapter 4. The model had the same physical behavior as RIFLEX in all deep water cases, and could be said to be close to the real world and a good model of the riser process. The model used in the verifications had 20 elements, and satisfied the desired level of accuracy. As defined in Chapter 3, the purpose of the PPM is to describe the actual physical process as accurately as possible. For the purpose of control applications, the CPM should be computationally fast, however, still describe the main physics. This is motivated by the realtime requirements for control systems. A low order model gives small system matrices and keeps the number of numerical operations down. A simple processor could then be able to run the model online. Small, simple computers help to keep the costs to a minimum, while large and fast computers cost more.

In this chapter we investigate how many elements are needed to keep a desired level of accuracy, both for the PPM and for the CPM. Different means to measure the performance of a model are considered. Generally, better performance is expected for more elements. How many elements are good enough? And which cases might need more elements to keep the desired level of accuracy?

7.1 Analysis Input Data and Set-Up

The riser top is assumed to be at the level of free sea surface, i.e. 1200m above the seabed. The RIFLEX model has 400 elements, each of length 3m. The number of elements for the Simulink riser models are common multiples of 400, ranging from 2 to 20, i.e. $N = \{2, 4, 5, 8, 10, 16, 20\}$. This is done to get the nodes at the same height above the seabed, and hence more easily

compare the horizontal displacements, especially of interest in the quasi-static analyses. With a water depth of 1200m, the element lengths were respectively $l_0 = \{600, 400, 240, 150, 120, 75, 60\}$m for the different models and increasing number of elements. The Simulink models are hereafter called CPMs. These 7 versions of the model are identical except for the number of elements, and are compared under the same environmental conditions. Two current profiles were run in all tests. These are:

- Uniform current with velocity 0.7m/s.
- One year return period Ormen Lange current profile, with surface velocity 1.15m/s and velocity close to the seabed 0.5m/s, illustrated in Fig. 3.2.

For some of the cases, additional profiles were run to investigate and illustrate special phenomena. The test set-up was otherwise similar to what was used in Sections 4.2-4.5. The tension and the TLP motions are specified in each section. The simulation results for the RIFLEX model are the same as in Sections 4.2-4.5 and are used in the analysis to illustrate the assumed correct solution.

7.2 Quasi-Static Analysis with Increasing TLP Position

The quasi-static CPMs were run with increasing TLP position in steps of 5m, from 0m to 70m. Three of these positions (0m, 30m and 50m) were subject for more detailed investigations. The top tension was kept constant at 1800kN. To investigate the error introduced with few elements, different measurements and methods were used. These could be summarized as:

- Deflections/Deformation shapes.
- Error norms for horizontal positions.
- Riser top angle.
- Area under the curve.
- Payout.

Most of these methods are mainly of theoretical interest. The measurement of the (absolute) horizontal positions along the riser is expensive and not accurate enough to be a part of the control loop. On the other hand, both top and bottom riser inclinations and payout are already measured today.

7.2.1 Error Norms for Horizontal Positions

The idea behind this method is to compare the horizontal displacement for nodes at the same vertical position, i.e. all nodes for each CPM is compared to the RIFLEX model. To be able to compare the models better, we apply metrical norms, see Appendix A.5. The three norms used here are:

1. l_1-norm: $\|\mathbf{x}\|_1 = (|x_1| + |x_2| + \cdots + |x_n|)$.
2. l_2-norm: $\|\mathbf{x}\|_2 = \sqrt{(x_1^2 + x_2^2 + \cdots + x_n^2)}$.
3. l_∞-norm: $\|\mathbf{x}\|_\infty = \max_j |x_j|$.

Here x is replaced by the horizontal error vector given by

$$\Delta x_{N=i}(j) = x_R(j) - x_{N=i}(j), \tag{7.1}$$

where i is the number of elements, j is the height of the actual node, x_R is the RIFLEX solution, and x_N the horizontal positions for the CPM with N elements. Two of the norms above could then be more commonly explained as:

- l_1-norm - sum of errors in all nodes.
- l_∞-norm - maximum displacement error.

Both the l_1- and l_2-norms are dependent on the number of elements and are therefore divided by the number of nodes, except for the top and bottom nodes, which are always located at the same place. Hence, the normalized l_1- and l_2-norms, accounted for the number of nodes can be written

$$l_1 : \frac{\|\mathbf{x}\|_1}{N-1}, \quad l_2 : \frac{\|\mathbf{x}\|_2}{N-1}. \tag{7.2}$$

This makes it easier to compare the various models. Fig. 7.1 shows the riser configuration without TLP offsets for all CPMs. The models with 2, 4, and 5 elements are all seen to give rather rough estimates of the riser configuration. The 10 elements model give a good impression of the riser curve. For more elements, the deviation is even smaller. The same color code as in Fig. 7.1 is used throughout this chapter, unless otherwise specified. The different error norms for this TLP position are given in Fig. 7.2. All the error norms converge to zero when N is increasing, and the norms are close to zero when $N \geq 16$. However, at $N = 10$, the error norm is increasing, which is clearest seen for the l_1- and l_∞-norms, i.e. the sum of errors and the maximum error. The maximum deflection error were found at 600m above the seabed, and is larger for $N = 10$ than for $N = 8$, which is opposite of what is expected. Zooming in on the

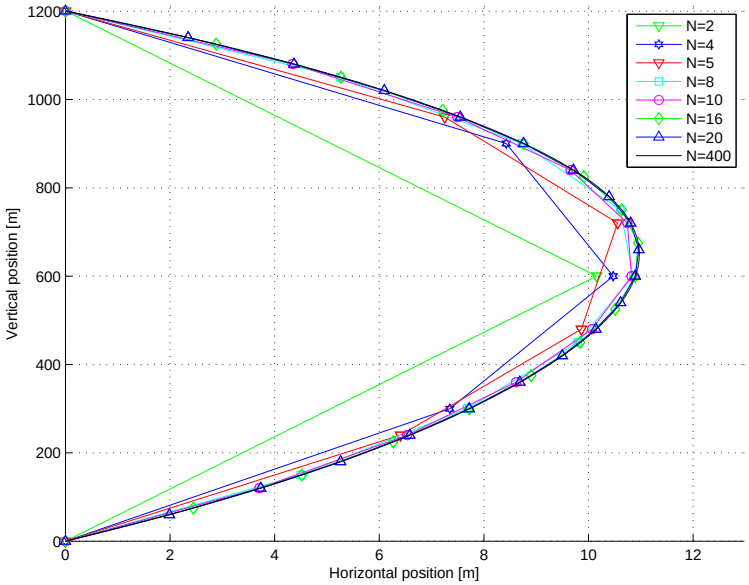

Figure 7.1: Riser configuration without TLP offset for an increasing number of elements exposed to the Ormen Lange design current.

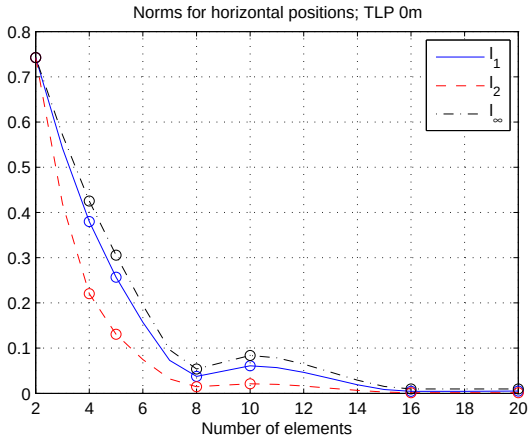

Figure 7.2: The different error norms for the horizontal nodes without TLP offset, exposed to the Ormen Lange design current.

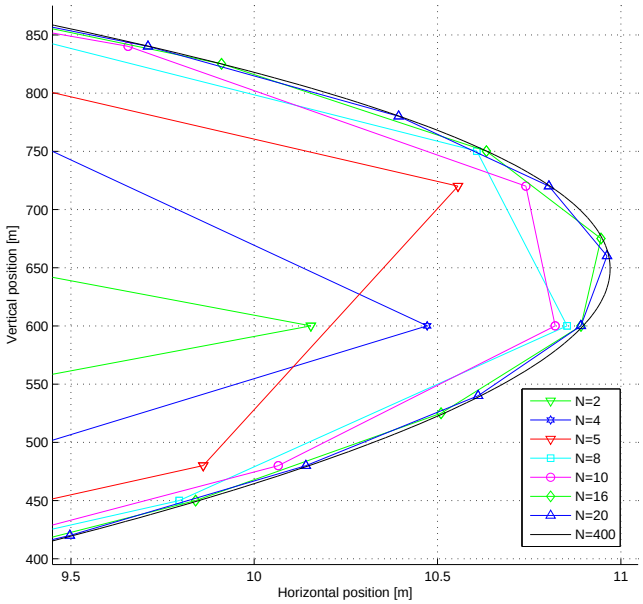

Figure 7.3: Zoomed riser configuration without TLP offset for an increasing number of elements exposed to the Ormen Lange design current.

riser configuration (Fig. 7.3) we see that the model with 8 elements match the RIFLEX solution better in the node points, while $N = 10$ follow the curve better in general. Also note that each norm method gives approximately the same norm curve independent of the TLP offset, see Fig 7.4.

To summarize, using this method with error norms on the horizontal displacement only to quantify the performance of each model is not reliable. It is dependent on how good each node matches the RIFLEX solution for a given current profile and number of elements. For other current profiles, another number of elements could indicate to be the best. The different norms show various sensitivity. The l_2-norm seems to be least sensitive to the single node error (Fig. 7.4).

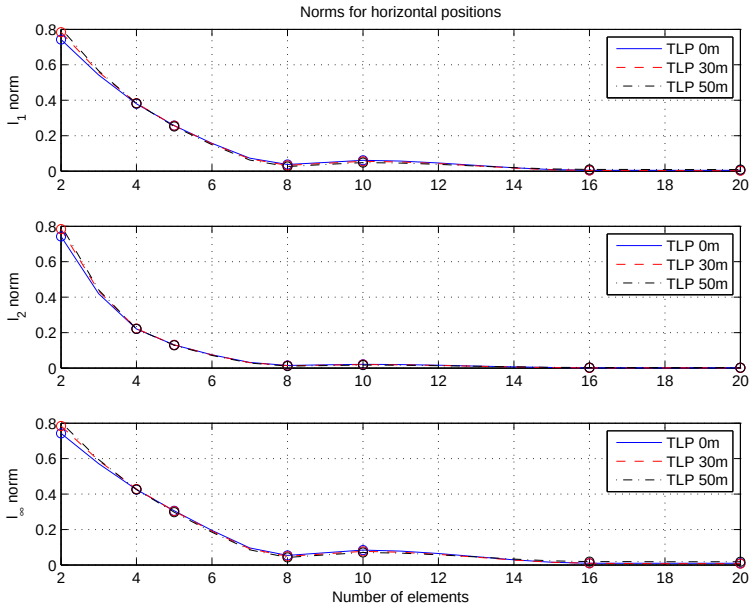

Figure 7.4: The different norms for the TLP offsets, exposed to the Ormen Lange design current.

7.2.2 Riser Top Angle

Today the top and bottom riser angles are measurements available offshore. These are used to calculate the riser configuration and may be used as inputs to the DP systems of floaters (Sørensen *et al.*, 2002, Høklie *et al.*, 2002). Production risers usually have bending stiffeners in their top and bottom end connections, while our model assumes free end rotations, which is the case for drilling risers. The riser inclination calculated here might therefore be larger than what could be measured for production risers in the industry. However, we would like to investigate the riser top angle as it tells something about the riser configuration, the deflection and the accuracy of the riser model.

In Fig. 7.5 the riser top angles are given for the three TLP offset. For a TLP without offsets, all inclinations have correct sign. For a TLP offset of 30m (see Fig. 7.6), two elements are too few to describe the riser configuration and gives a positive sign, while the inclination should have been negative. At a TLP offset of 50m (Fig. 7.7) three models $N = \{2, 4, 5\}$ are all seen to give the wrong sign, while for $N > 8$ the top angle is approaching the correct value. Here we have used the angle given by the straight line between the two upper nodes to represent the top angle. An alternative method would be to assume constant

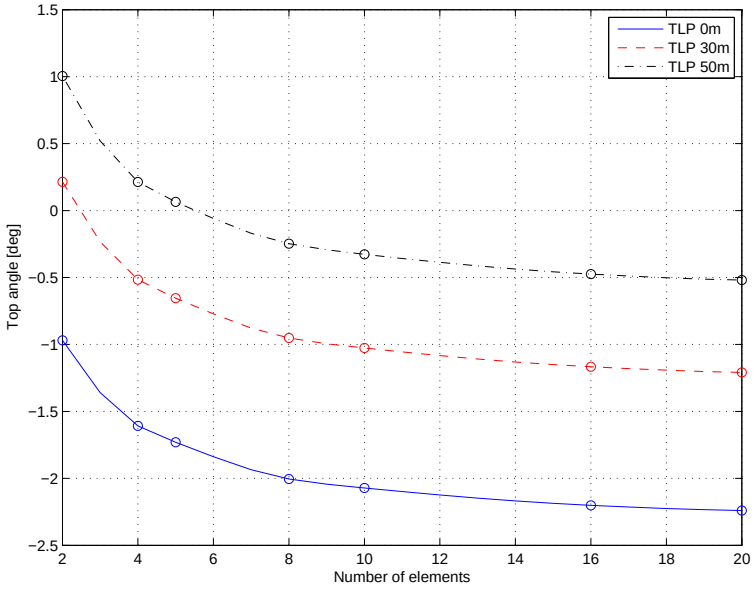

Figure 7.5: The riser top angles with different TLP offsets, exposed to the Ormen Lange design current.

curvature in the upper element and apply the tangent at the upper node as the top angle. This would give a better angle estimate for few element CPMs, but converge to the same result for more elements. Anyhow, these analyses show the importance of having enough elements in the model, especially when using inclinations in the measurements in the control feedback loop. The phenomenon described here is dependent on the TLP offset, current profile and velocity. It is more likely to be observed in a large offset and medium to large current velocity. The max deflection will then be slightly larger than the TLP offset and near the top. However, this example is from the Ormen Lange current, with an offset at 50m, which is a most realistic case.

7.2.3 Area Under Curve

A better way to compare the performance of the models is to consider the area under the riser curves, recall Fig. 7.1. The area under the riser curve, A_N, for each CPM can be found by summarizing the area of the trapezoids between $x = 0$

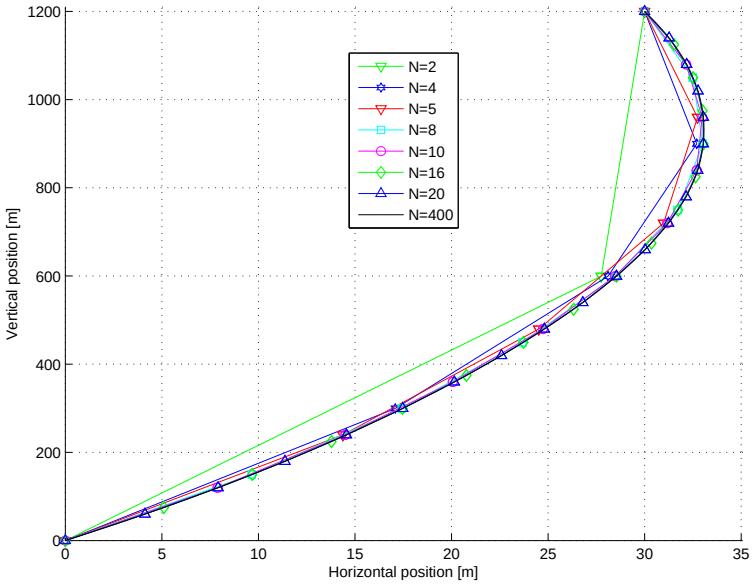

Figure 7.6: Riser configuration with TLP offset of 30m for an increasing number of elements exposed to the Ormen Lange design current.

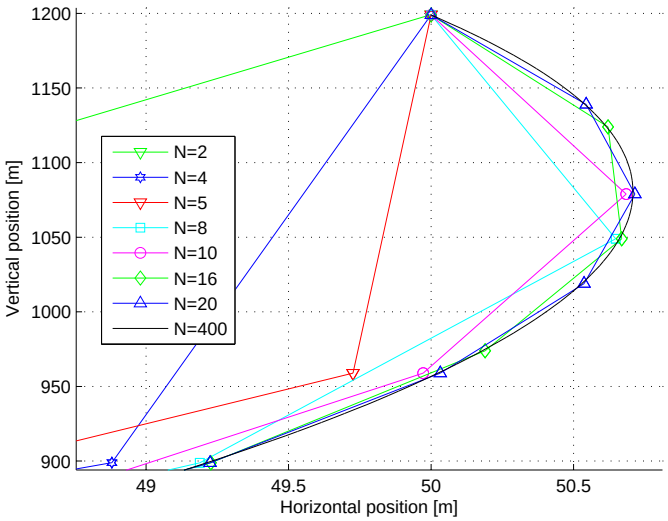

Figure 7.7: Zoomed riser configuration with 50 TLP offset for an increasing number of elements exposed to the Ormen Lange design current.

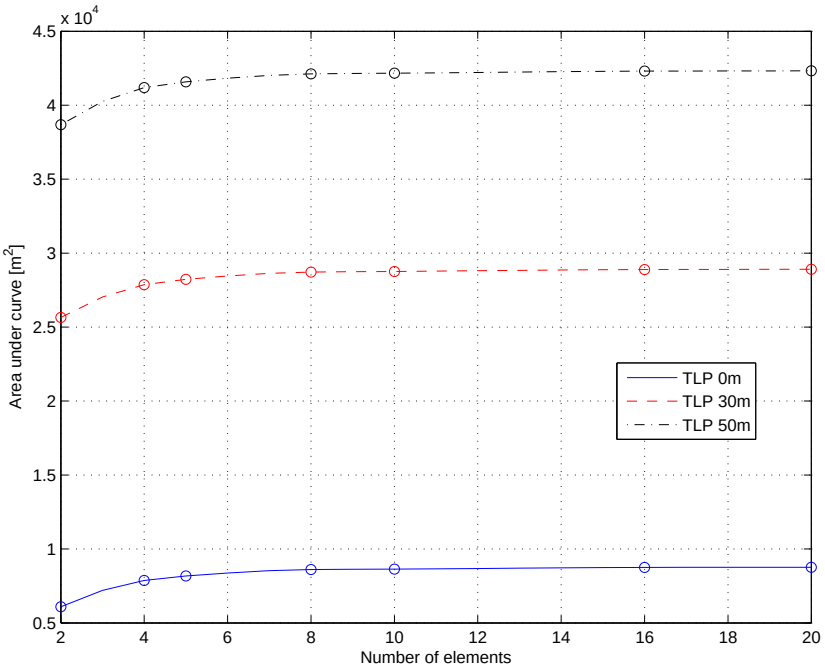

Figure 7.8: The area under the riser curves for TLP offsets.

and the riser curve for each pair of nodes

$$A_N = \sum_{i=0}^{N} \frac{x_i + x_{i+1}}{2} l_0, \tag{7.3}$$

where x_i is the horizontal position of node i, and l_0 is the element length. Shorter riser elements will capture the deflection better with more trapezoids. The riser areas are seen to converge to the desired value for $N \geq 10$ (Fig. 7.8). This method is less dependent on how the selected nodes match the correct solution, since all node values and not only the common multiplier are included in the calculations. The relative error under the curve is illustrated in Fig. 7.9 and given by

$$e_A = \frac{A_{RIFLEX} - A_{N=i}}{A_{RIFLEX}} \cdot 100\%, \tag{7.4}$$

where A_R is the RIFLEX area for 400 elements. For $N \geq 8$, the relative error is less than 3% for all TLP positions. It should be noted that $N = 10$ gives better results than $N = 8$, which is expected. Hence, this method gives overall a better evaluation of the convergence of the various riser models than the method

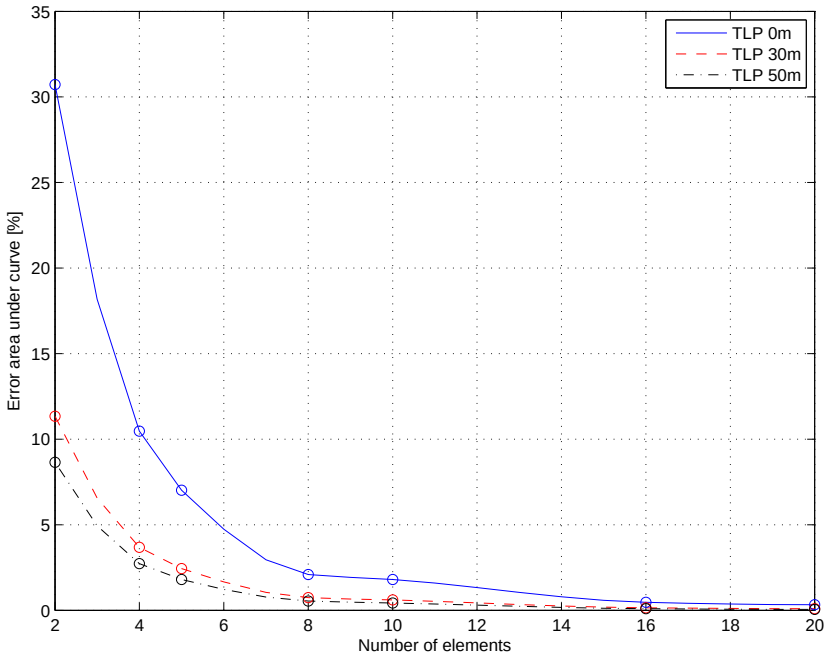

Figure 7.9: The relative error in the area under the riser curves for TLP offsets.

with horizontal error norms. For CPMs with few elements, applying Simpson's method to find the area would give better estimates. For more elements, the estimate of the area will converge to the same value for both methods.

7.2.4 Payout

The payout is a direct result of the deflection and how well the CPMs correspond to the correct curve. It is similar to the method with area under the curve presented in Section 7.2.3. However, while the area under the curve is a theoretical calculation, the payout can actually be measured and used in the feedback loop. The static payout for the different TLP offsets and various models are shown in Fig. 7.10. The payouts converge to the desired values for increasing number of elements, and at $N \geq 8$ the payout error is less than 2%, see Fig. 7.11. Hence, the payout is a good and robust method.

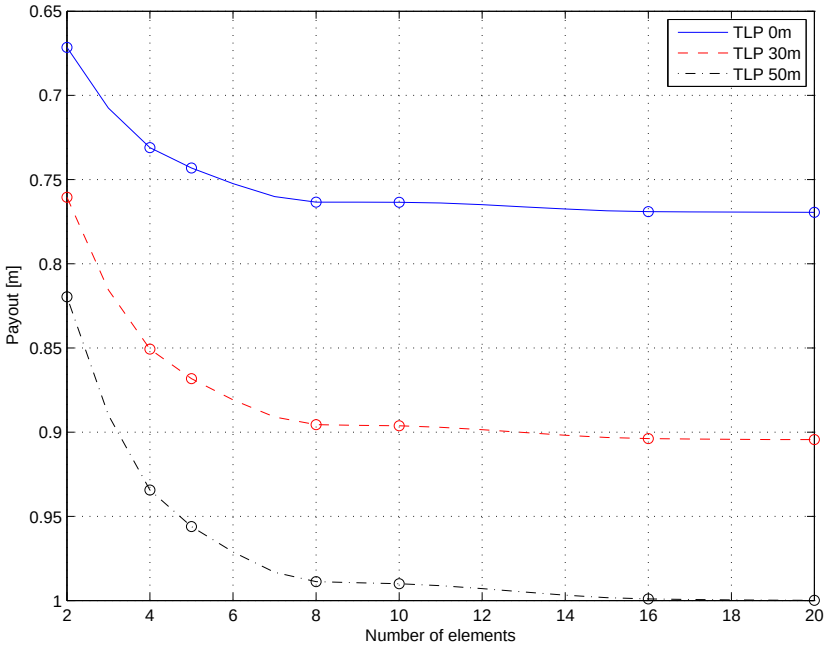

Figure 7.10: The payout error for TLP offsets.

7.2.5 Discussion

Four methods have been investigated; horizontal error norms, top angle, area and payout. All methods showed, as expected, that increasing the number of elements gave a better model closer to the correct solution. The horizontal error norms were sensitive to the prevailing current profile such that a lower number of elements appeared to have better accuracy than the true situation. This was especially seen for the l_∞-norm and the l_1-norm. The l_2-norm was the least sensitive method.

Too few elements could give the opposite sign on the riser top angle for some environmental conditions. When using inclinations in the feedback loop for riser control or DP operations, one should be careful when deciding the number of elements in the model. Calculation of the area showed good robustness. Anyhow, this method could not be used online as it requires accurate measurements of the horizontal positions. Finally, payouts proved to be a robust and accurate method, which is easily measured and can be used in feedback. For the rest of the analysis, only payout will be used. The results are summarized in Table 7.1.

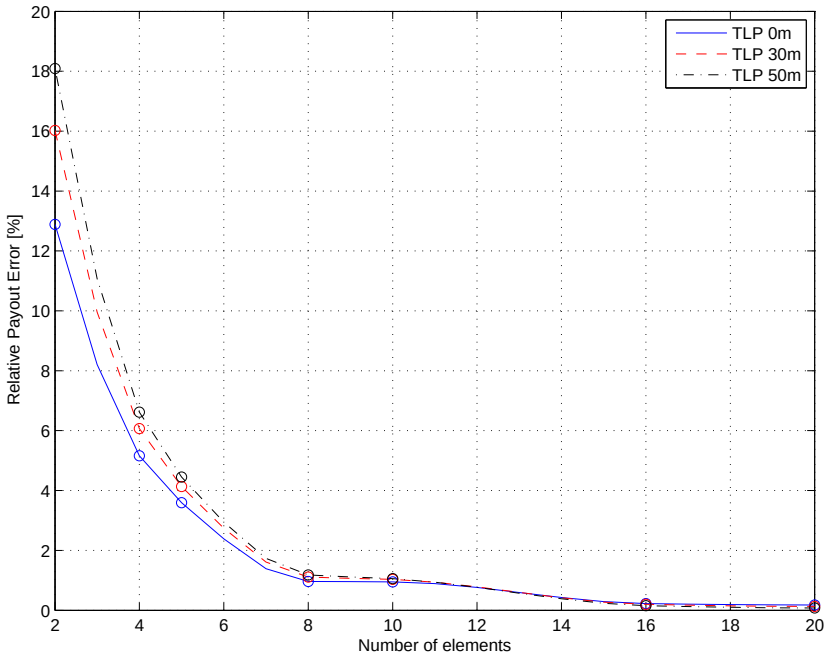

Figure 7.11: The relative error in payout for the different TLP offsets.

Method	Robustness	Possible to measure
Horizontal error norms	Sensible for single node errors and current profiles	Theoretical
Top angle	Wrong sign for low order models	Measurements
Area	Robust	Theoretical
Payout	Robust	Measurements

Table 7.1: The pros and cons for the different methods to quantify the performance of the CPMs.

7.3 Analysis of Quasi-Static Tension Variations

The quasi-static CPMs were analyzed with increasing top tension from 1200kN to 2700kN in steps of 50kN. The TLP was positioned in zero offset. The riser models were exposed to the bidirectional current, in addition to the uniform and the Ormen Lange currents. The physics of the riser behavior and the relations between the top tension, top position and the maximum deflection were explained in Sec-

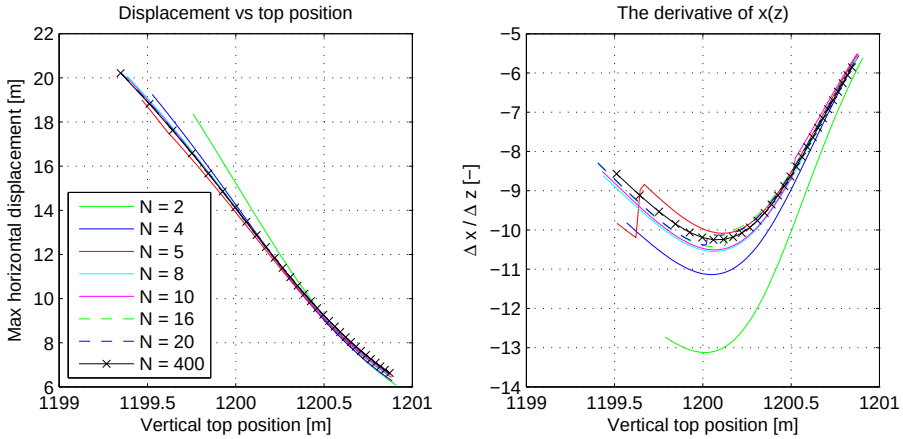

Figure 7.12: Maximum deflection as a function of top position (a), and its derivative (b) for the CPMs exposed to the Ormen Lange current.

tion 4.3. In this section we mainly focus on the error introduced by decreasing the number of elements. Fig. 7.12 shows the relation between the maximum horizontal deflection as a function of the vertical top position $x(z)$ and its derivative $\Delta x/\Delta z$. Note that the physical interpolation of $\frac{\Delta x}{\Delta z}$ is "How much will the maximum horizontal deflection change for a unit variation of vertical position of the upper riser end." For a low top position and small top tension, Fig. 7.12a) shows that 2 elements are too few, such that the maximum horizontal displacement is too small. $N = \{4, 5\}$ match better. For all these low element order CPMs, the maximum deflections at the lowest tensions are 1-2m too small such that the riser end is assumed to be 0.25-1m higher than the correct value. For eight or more elements, the $x(z)$-curves match fairly well with the RIFLEX solution. For larger tensions and higher top positions all CPMs match the solution better than for lower tensions. The same is seen for the derivatives in Fig. 7.12b). For the three lowest number of elements, the derivatives deviate noticeably from the RIFLEX solution. For all higher number of elements, the curves match the RIFLEX solution satisfactorily. The values of the derivatives for $N = \{5, 10, 16, 20\}$ have a sudden discontinuity. This can be explained by looking at the snapshots in Fig. 7.13. For each step in tension the node with max deflection is found. This node number will vary, depending on the tension. The change in vertical position Δz is dependent on the length of the element. This will give a drop in $\Delta x/\Delta z$, and is due to the numerical way of finding the derivatives. The RIFLEX model does not have any noticeable discontinuities. The element length is only 3m, such that the change Δz is much smaller. Longer discontinuities were seen for longer

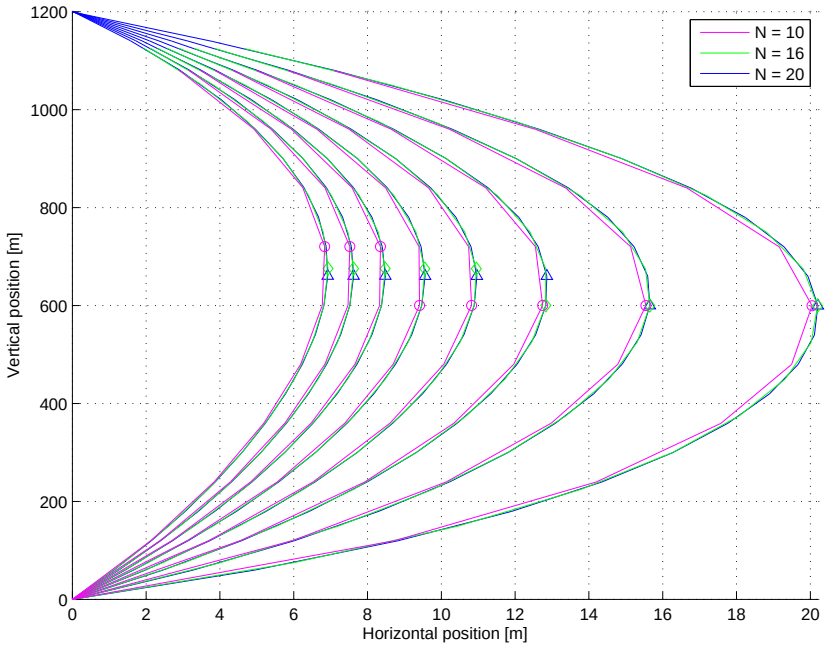

Figure 7.13: Riser configuration for 10 (o-pink), 16 (*-green) and 20 (Δ–blue) elements and their maximum deflection.

element lengths. Note that these discontinuities are due to numerical errors in calculation of the derivatives, while the simulation model experience continuous derivatives.

Maximum deflection versus top tension $x(T)$ and its derivatives are seen in Fig. 7.14. The variation in tension from one step to another is constant. When the node for which the maximum deflection is changed, Δx is slightly larger than when it is kept at the same height. Due to this, some smaller discontinuities were noticed in Fig. 7.14b). At high tensions, the derivatives converge to the same value. The $x(T)$ curves all have the same shape. The three CPMs with least elements do not have the same maximum deflection as for the higher order models. The absolute error in top position as a function of tension relative to the RIFLEX solution, is found in Fig. 7.15 and given by

$$|e_{z(T)}| = |z_R(T) - z_{N=i}(T)|, \tag{7.5}$$

where z_R is the RIFLEX top position and z_N is the top position for each CPM. Three tensions are chosen; a medium initial tension (1800kN), and the lower and upper tension limits, 1200kN and 2700kN, respectively. The error is seen to de-

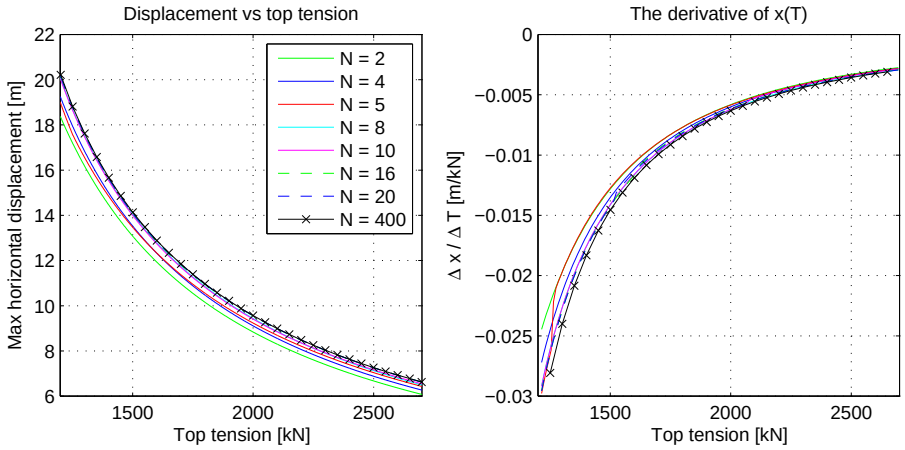

Figure 7.14: Maximum deflection as a function of top tension (a), and its derivative (b) for the CPMs exposed to the Ormen Lange current.

crease with increasing number of elements and also increasing tension. Neglected effects in the CPM seem to be more significant for low tensions. For instance bending stiffness (EI) is more important for low tensions than for higher tensions, where the geometric stiffness is dominating. For higher tensions the dominance of elastic flexibility over geometric flexibility is noticed. In Fig. 7.16a) the relationship between the vertical top position and top tension $z(T)$ is plotted. For low tensions, the graphs are spread. For high tensions, all curves approach the same asymptote. The same is seen in Fig. 7.16b). The effect on the top position by increasing the top tension is largest for low tensions. For higher tensions, the increase in the top positions is mainly due to the increase in length.

This is particularly obvious when considering the two element model with bidirectional current, see Fig. 7.17. The two element model does not capture the current forces and is vertical. The only increase in top tension is therefore due to elasticity. In Fig. 7.18, $z(T)_{N=2}$ is an asymptote which the other CPMs are approaching, when the tension increases and the contribution to z from the geometry due to deflection decreases. The derivatives are seen in Fig. 7.18b). As expected, $\Delta z/\Delta T_{N=2}$ is constant and the others are approaching this level. Approximately the same value for $\Delta z/\Delta T$ is seen for all current profiles as it is only dependent on the elasticity of the riser material. This can be derived from

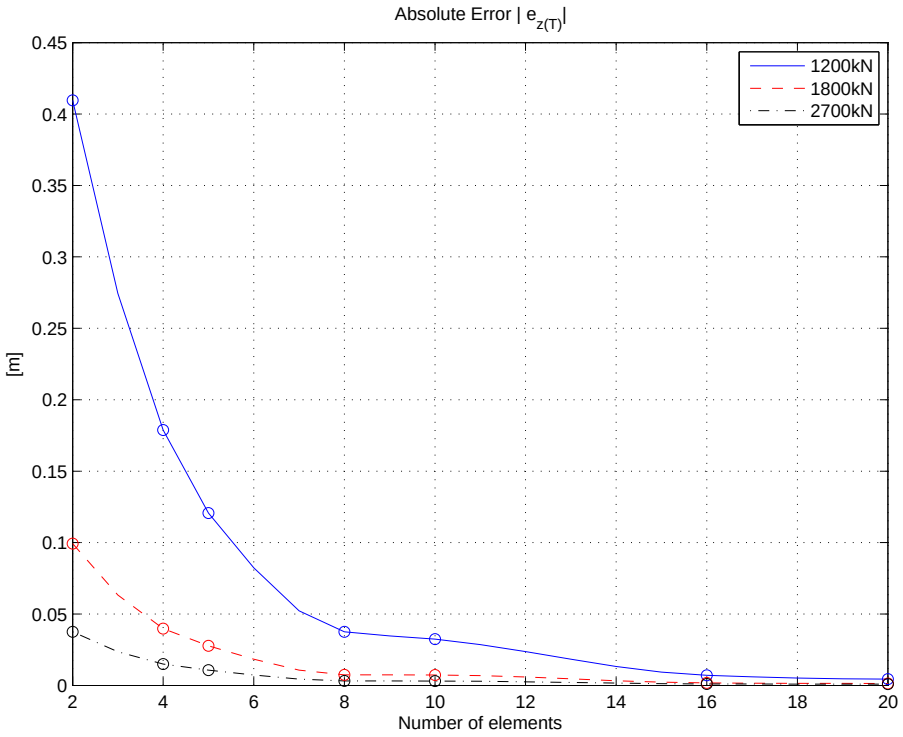

Figure 7.15: Error in top position for the various tensions.

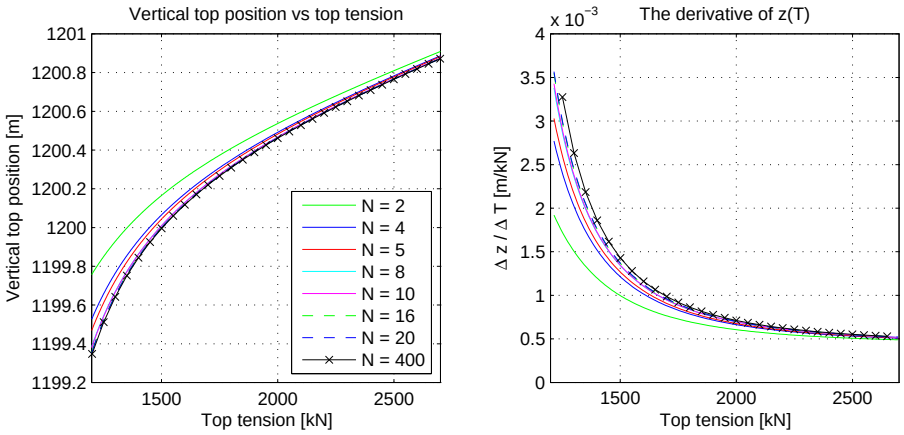

Figure 7.16: Maximum top position as a function of top tension (a), and its derivative (b) for the CPMs exposed to the Ormen Lange current.

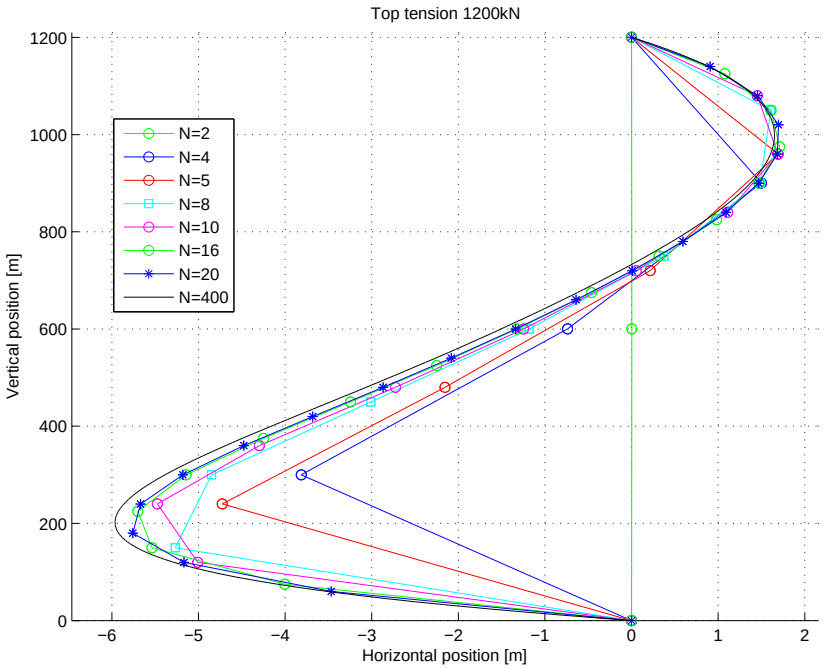

Figure 7.17: Riser configuration for the CPMs exposed to the bidirectional current velocity profile.

(3.22).

$$T_0 + \Delta T = \frac{EA}{l_0}(z_0 - l_0 + \Delta z), \tag{7.6}$$

$$\Rightarrow \Delta T = \frac{EA}{l_0}\Delta z, \tag{7.7}$$

$$\frac{\Delta z}{\Delta T} = \frac{z_0}{EA} \tag{7.8}$$

$$= \frac{1200m}{2.06e^{11}\mathrm{N/m}^2 \cdot 0.0134\mathrm{m}^2} = 4.35e^{-4}\mathrm{m/kN}. \tag{7.9}$$

This value is the same as in Fig. 7.18b).

Remark: The riser configuration as shown in Fig. 7.17 is also of interest from a mode shape point of view. The bidirectional current velocity profile excites the second mode shape. FEM can be considered as a spatial discretization of the riser configuration, similar to what can be found for time varying signals. For time varying systems, the slowest sampling frequency is decided by Shannon's sampling theorem and the Nyquist frequency: If the sampling frequency is higher

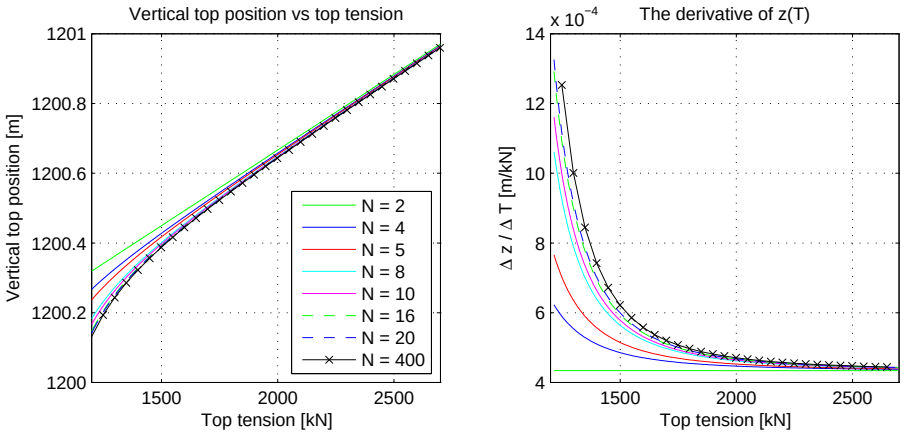

Figure 7.18: Maximum top position as a function of top tension (a), and its derivative (b) for the CPMs exposed to the bidirectional current profile.

than twice the frequency of the highest frequency component of the continuous signal, it can be reconstructed completely from the sampled signal (Ogata, 1995). This is the time reconstruction of a signal. A parallel could here be drawn to our spatial model reconstruction. How many elements are needed to represent the main riser configuration? For $N = 2$, none of the deflections are captured. For the other low order CPMs, the main configuration is seen. For the highest order CPMs, the riser is drawn with fair accuracy.

7.4 Dynamically Moving TLP

The dynamic CPMs were then exposed to harmonic TLP motions using the same setup as in Section 4.4. Figs. 7.19 a) and b) show the payout versus time and TLP position, respectively, for TLP periods 60s and the Ormen Lange current profile. All CPMs are close to the RIFLEX solution at large offsets where the risers are straight. When the TLP is moving from right to left (see Fig.4.6a)) the deflection is increasing, and also the payout. The two element model does not capture the large deflection, and their change in payout is only half as much as for the RIFLEX solution. The other few element CPMs ($N = \{4, 5\}$) capture the main deflection. The medium order CPMs ($N = \{8, 10\}$) follow the solution nicely, while the highest order CPMs ($N = \{16, 20\}$) are hardly seen as they are on the curve for the RIFLEX solution.

The payout in Fig. 7.19 a) shows that the first mode corresponding to the TLP motion is dominating. The TLP motion and setdown is seen in Fig. 7.20

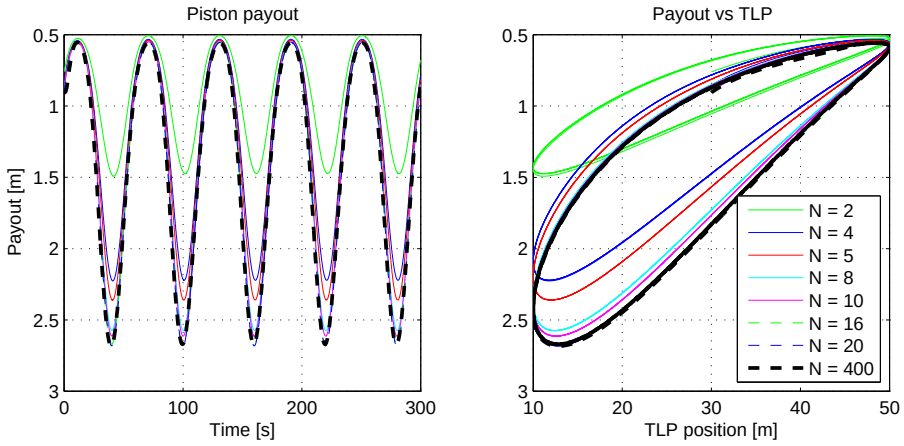

Figure 7.19: Payout as a function of time (a) and TLP offset(b) exposed to the Ormen Lange current.

as the bottom of the cylinder in the tension system (blue, thick line). The riser tops are plotted in the same graph, such that the distance between them are the payouts. The second order riser mode shape is clearly seen in the riser tops and corresponds to the second order mode shape in Fig. 4.6b) where the TLP moves from left to right. The payout error

$$|e_\xi| = |\xi_R - \xi_{N=i}|, \tag{7.10}$$

is plotted in Fig. 7.21. For the low order CPMs, the first mode dominates. The error for $N = 2$ is up to 45% for the smallest TLP offset with the largest deflection. Such a large error on the first mode shape dominates the second mode shape seen in Fig. 7.20. The error from first mode shape is also dominating for $N = \{4, 5\}$, with errors of approximately 20% and 15%, respectively. For the medium and high order CPMs, the total errors are less than 8% and 5%, respectively. The first mode shape errors are small such the second mode shape errors are observed. Note that these results presented here are those with largest relative error. At larger TLP periods, like 120s, the errors were smaller, especially for the low order models. At 300s, the risers were close to quasi-static and only the first mode shape was seen. Smaller current velocities gave also smaller errors.

7.5 Analysis of Dynamic Variation in Top Tension

Finally, the dynamical CPMs were analyzed with harmonically varying tension. The set-up was the same as in Section 4.5. The simulations shown here are

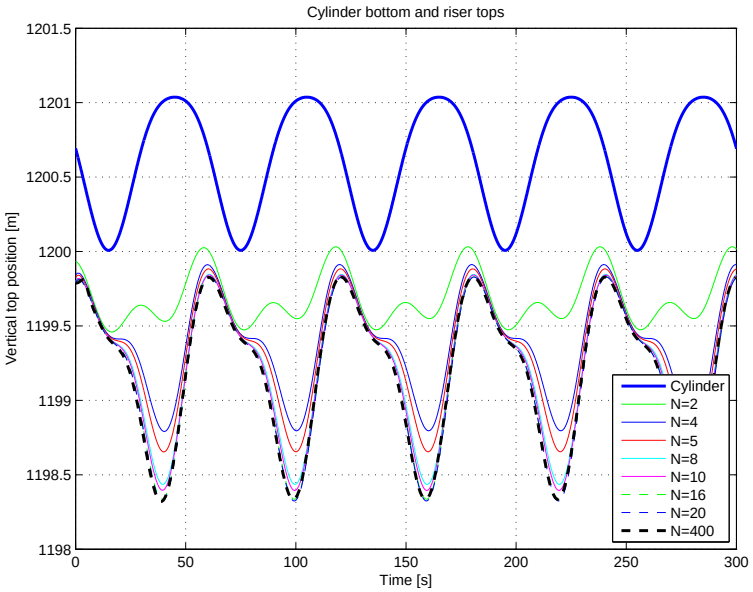

Figure 7.20: Cylinder bottom (blue line) and riser top positions for TLP motions and Ormen Lange current.

with a tension period of 120s and a riser exposed to the Ormen Lange current. Fig. 7.22 shows the top position as a function of time (a) and top tension (b). The top position versus top tension is seen to be a hysteresis function due to relative velocity and drag. Hence, a given tension does not correspond to one top position, but depends on whether the tension is increasing or decreasing as well. The deviations in top position between the models are largest for low tensions and low top positions. For higher tensions, the deviations are smaller. This is expected based on the results from Sections 7.3 and 7.4. Fig. 7.22 b) illustrates how an increasing number of elements result in a better match between the CPM model and RIFLEX. Fig. 7.23 shows the relative payout error. Maximum errors are seen for the low order CPMs, with approximately 0.22m for $N = 2$, and 0.09m for $N = 4$. For the medium and high order CPMs, the maximum error is $\pm$ 0.02m. A small second order nonlinearity and phase shifts are seen. This is due to the nonlinear viscous forces, i.e. the drag forces and difference in relative velocity when the tension is decreased and increased.

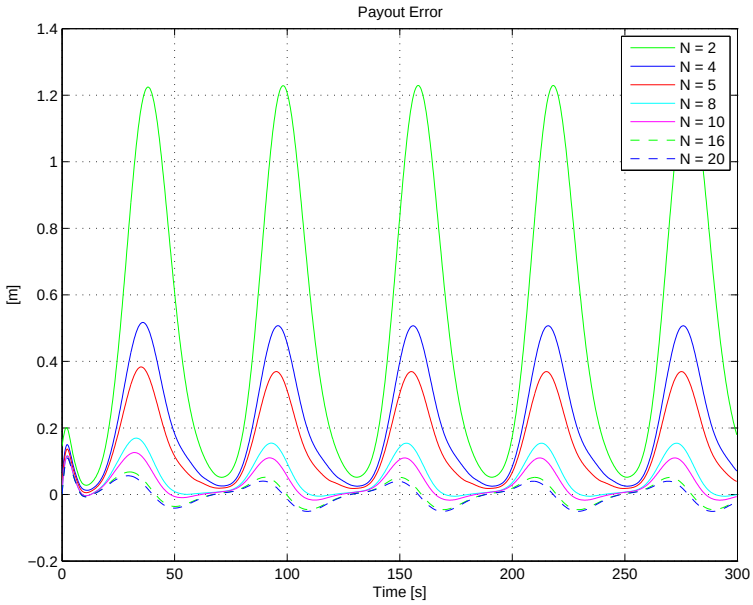

Figure 7.21: Relative payout error for harmonic TLP motions and Ormen Lange current.

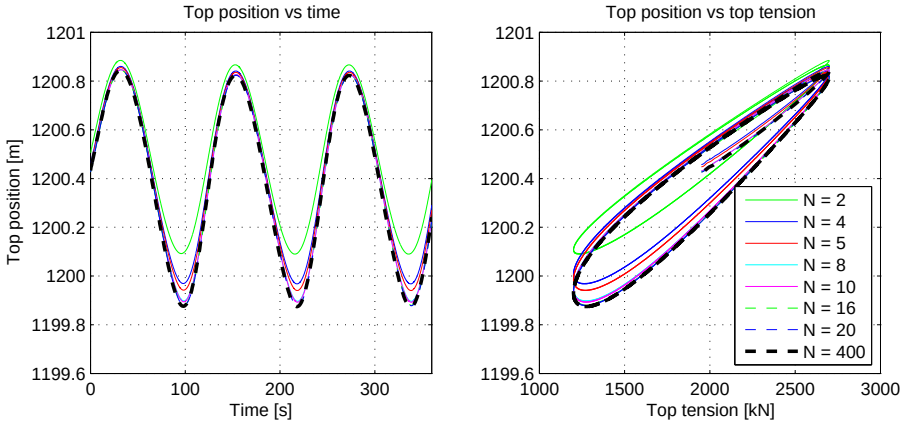

Figure 7.22: Riser tops as a function of time (a) and tension (b) exposed to the Ormen Lange current.

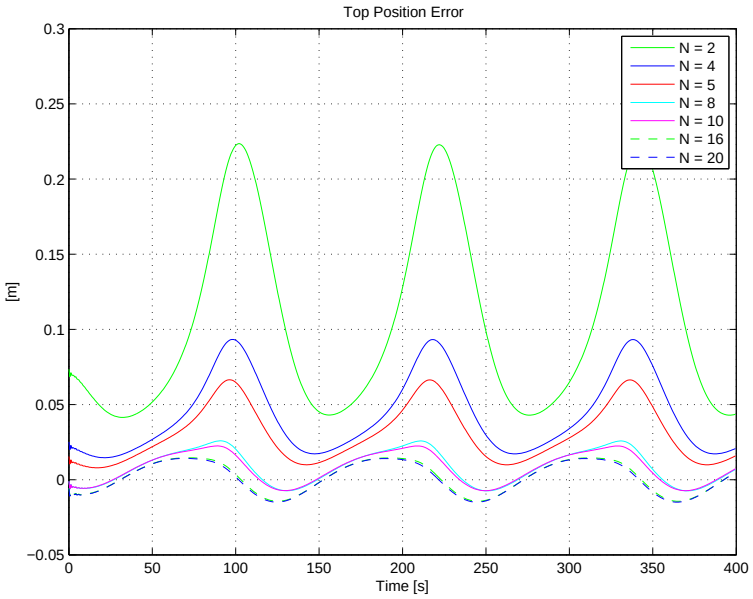

Figure 7.23: Relative payout error for a riser exposed to harmonic tension variations with periods 120s and the Ormen Lange current.

7.6 Discussion

In Chapter 4, we verified the mathematical model. In this chapter, we investigated what happens if the number of elements is decreased. From a control point of view, the possibility of realtime operations are of great importance. We therefore seek the smallest and least complex model which still afford the desired level of accuracy for the current operation. The analysis in this chapter could be divided into three levels of accuracy. These correspond to the fast control plant model (FCPM), the accurate control plant model (ACPM) and the process plant model (PPM).

Recall that the size of the system matrices are $2(n+1)\times 2(n+1)$ giving $4(n+1)^2$ matrix elements, where n is the number of riser segments. Hence, doubling the number of riser nodes increases the number of matrix elements by a multiple of four. This slows down the computation speed considerably for the time consuming matrix operations and iterations. The low order CPMs, with $N = \{4, 5\}$, follow the main configuration. A small number of elements gives small system matrices. The matrix operations are fewer, which gives shorter simulation times. The main dynamic properties are still kept in this model. The medium order CPMs, with $N = \{8, 10\}$, have small quasi-static deviations, and follow the dynamics with

Type	N	QS error	Dyn error	Description
FCPM	4-6	5-10%	15-20%	Main physics used in control analysis
ACPM	8-12	2-5%	$< 8\%$	Good model for monitoring of the risers
PPM	≥ 15	$< 1\%$	$< 5\%$	High accuracy for the riser process model

Table 7.2: The categorized results of the CPM analysis.

errors less than 8%. The high order CPMs with $N = \{16, 20\}$, have very small static deviations and follow the dynamics of the specified motion of the TLP and tension with errors less than 5%. These results are categorized in Table 7.2. The proposed limits and relative errors are based on the worst simulated case. For slower TLP dynamics and smaller current velocities, the results are better with smaller relative errors. Hence, the limit for the different model classifications could be set differently, such that the needed number of elements N are chosen to correspond to the physics of the environment.

Note that the number of elements for the FCPMs and ACPMs does not need to be a common multiple of the PPM, but can be chosen freely within the given limits. Increasing the number of elements gives a more accurate model at the expense of slower simulations due to larger system matrices.

Chapter 8

Simulation Results

The TLP/riser system was modeled in Chapter 3, and the controller system design and architecture were presented in Chapters 5 and 6, respectively. In this chapter the control objectives proposed in Section 6.1 are investigated and compared in deep waters. Two of them, the equal payout and equal effective length, are also tested in shallow waters. The best working control objective is thereafter simulated with dynamic TLP motions, and used in a case study with changing environmental conditions and supervisory switched controller.

8.1 Set Up

The riser model from Section 3.5 was verified with a large variety of current profiles in Chapter 4. However, in the simulations included in this chapter, a current profile with one year return period from the Ormen Lange field is used as a basis (Norsk Hydro, 2001). In addition a variance in the current is made by filtering white noise through a low pass filter with a period of 100s, and an amplitude within the band of 5% of the current velocity in each node. The initial center-to-center distance between the risers is 15D in 1200m waters, and each riser model consists of 10 elements, unless otherwise specified. Some limitations and assumptions are made in relation to the shielding effect and the resulting current on R2 to keep the riser and current models valid.

- The current is coming from one direction only, such that the risers are always in a tandem position, with R2 in the wake of R1.
- Small TLP velocities such that the current is larger than the riser velocities and the relative velocity always positive, keeping R2 in the wake of R1.

The latter will not be true for the last part of the case simulations with WF TLP motions. However, this part of the simulation is included to demonstrate the

effect of control. The hydrodynamic interactions for the three-dimensional case and faster relative motions should be further investigated for industrial implementations, but is outside the scope of this thesis. The riser data, current profile velocities and control gains are found in Appendix B.

8.2 Control Objectives

The four different control objectives from Section 6.1 are tested and compared. The equal tension control objective is run with two different top tension levels and 0m or 30m offset. The equal payout, equal effective length and desired horizontal distance control objectives are run with control of R2, using measurements from R1 as the reference. For the equal effective length control objective, control of R1 with the payout of R2 as a reference is also simulated.

8.2.1 Constant Equal Tension

In the first case, the top tension of the risers are constant and equal to a pretension. From (6.1) we have

$$T_1 = T_2 = T_{0,j}. \tag{8.1}$$

A medium top tension of $T_{0,j} = 1800$kN is applied, and there is no TLP offset. The incoming current profile is increased as a second order low-pass filtered step from zero to the design current profile. As the current increases, the risers are seen to slide out to the right in Fig. 8.1 (top left). The maximum horizontal deflection is seen at 600m above the seabed. Collision occurs along most of the riser (nodes 3 to 9), seen as relative horizontal distance smaller than 2D (bottom left). The payout of R1 is larger than for R2 due to the larger deflection (Fig. 8.1, bottom right).

The TLP is then put in an offset position of 30m, with increasing current, seen top left in Fig. 8.2. The TLP is not very likely to have an offset in the opposite direction of the surface current, so offsets are always simulated in the positive direction. Collision is seen to occur at the same nodes independent of the offset position. The relative horizontal distance between three selected nodes are shown in bottom left of Fig. 8.2, where it is seen that collision occurs at the first node after approximately 400s. The corresponding payout due to deflection is seen bottom right in Fig. 8.2. R1 has the largest deflection and hence setdown, which is clearly seen in the payout plot.

Increasing the top tension to the upper limit of $T_{0,j} = 2700kN$ and keeping the TLP in a no-offset position, no collision occurs at any nodes, seen in the snapshots (top left) and relative horizontal distance (bottom left) in Fig. 8.3. Keeping the tension at the upper limit, collision could be avoided for these design

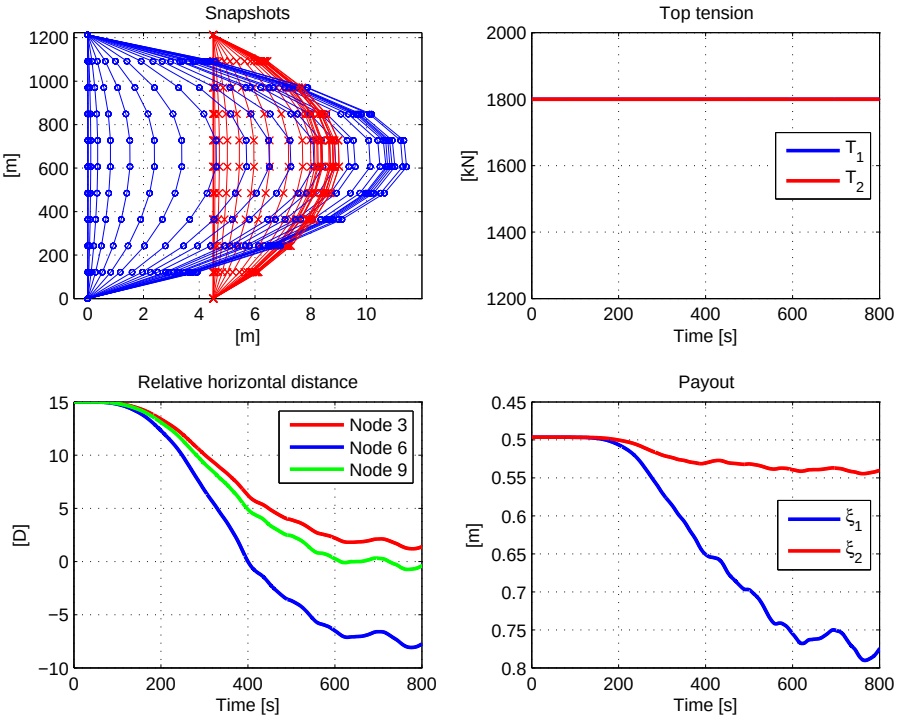

Figure 8.1: Incrementing current velocity from zero to the Ormen Lange design current. Snapshots of the riser configuration (top left), top tension (top right), relative horizontal distance (bottom left) and payout (bottom right).

currents. However, operation of the risers at this tension level is not desired due to increased stress in the riser and excessive wear of the tension system. The payouts (bottom right) are smaller than for the smaller top tensions.

For the rest of the simulations, the pretension is kept to $T_{0,j} = 1800kN$ for both risers. A fully developed current profile for the Ormen Lange field is used.

8.2.2 Equal Payout

For the equal payout controller objective, the payout of all risers should be equal, see (6.2). Using the measured payout of R1 as a reference for R2, we have from (6.37)

$$\xi_{r,2}(t) = \xi_1(t). \tag{8.2}$$

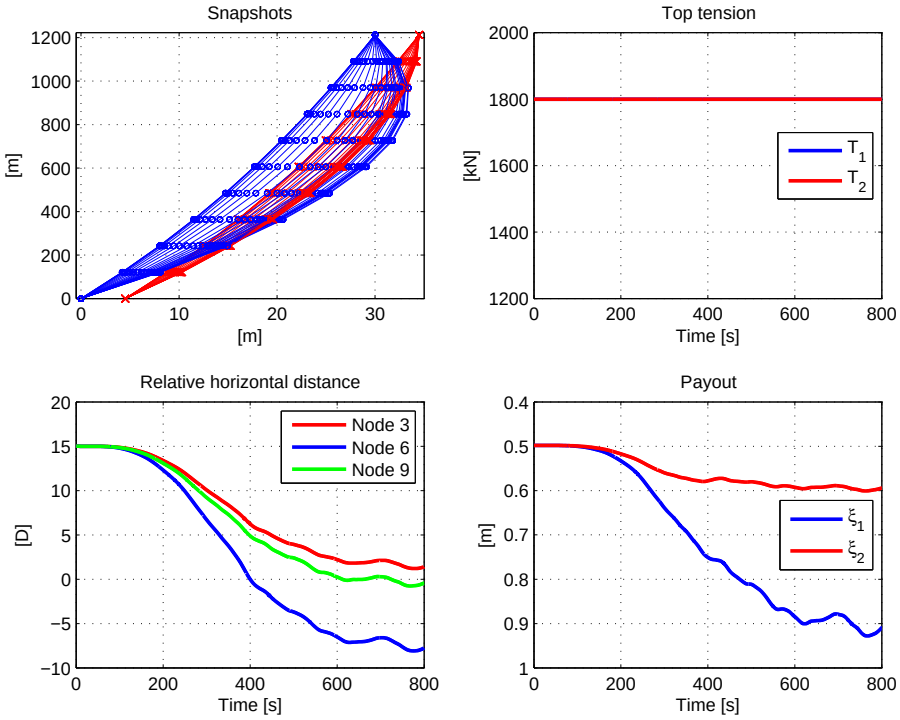

Figure 8.2: Incrementing current and 30m TLP offset. Snapshots of the riser configuration (top left), top tension (top right), relative horizontal distance (bottom left) and payout (bottom right).

Furthermore, a PI-controller for the top tension could be formulated from (6.44), (6.46) and (6.49) with parameters from Appendix B.3.

$$T_1 = T_{0,1}, \tag{8.3}$$

$$T_2 = T_{0,2} + \tau_{c,2}, \tag{8.4}$$

$$\tau_{c,2} = -K_{P,2}e_2 - K_{I,2}\int e_2 dt, \tag{8.5}$$

$$e_2 = \xi_{d,2} - \xi_2, \tag{8.6}$$

where $\xi_{d,2}$ is the guidance trajectory passed through the third order filter in (6.40)-(6.41). The results are found in Fig. 8.4, with the top tension shown in the top right figure.

This control algorithm gives equal payout for the risers, seen bottom right in Fig. 8.4. Top left shows how R2 slides out to the right due to decreased tension. However, collision still occurs, but in a smaller riser segment than with equal

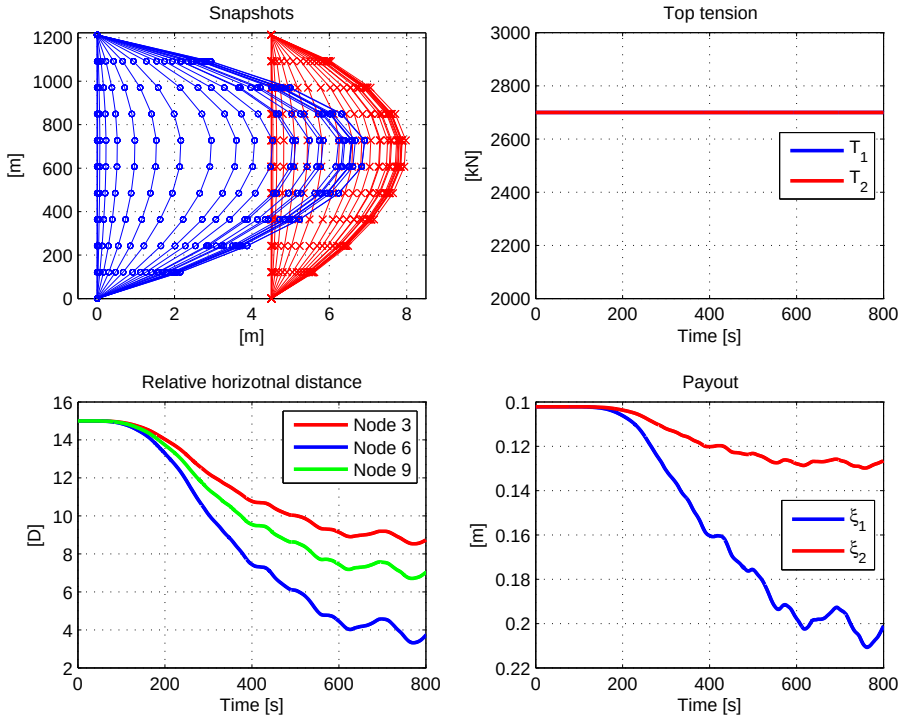

Figure 8.3: Incrementing current with top tension 2700kN. Snapshots of the riser configuration (top left), top tension (top right), relative horizontal distance (bottom left) and payout (bottom right).

tension (nodes 5 and 6), also seen for the relative distance (bottom left). The collision is caused by the lower tension in R2 compared to R1, which in turn gives less axial elongation, and a shorter length of R2 than R1. Hence, due to the elasticity of steel, collision may still occur for long risers when using the equal payout control objective.

8.2.3 Equal Effective Length

In the next control objective, the elasticity of the riser material is included. This could be done by considering the riser length plus the payout. For equal risers with the same pretension, the guidance trajectory from (6.38), using (6.3) and (6.5) is simplified to

$$\xi_{r,2} = \xi_1 + \Delta l_R. \tag{8.7}$$

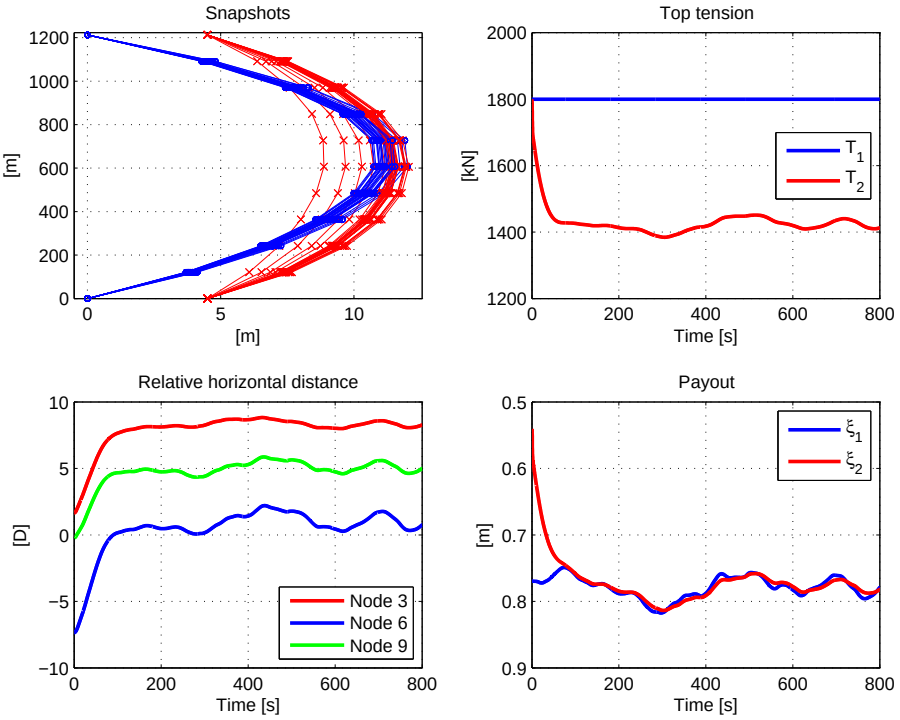

Figure 8.4: Equal payout algorithm and control of R2. Snapshots of the riser configuration (top left), top tension (top right), relative horizontal distance (bottom left) and payout (bottom right).

The controller is the same as in Section 8.2.2, (8.3) through (8.6). The results are seen in Fig. 8.5. The snapshots found top left show how the mid-position of R2 starts in front of R1 when the pretensions are equal. R2 then slides out to the right to avoid collision as the tension decreases, also seen in the relative horizontal distance to the lower left. The payout of R2 approaches the reference trajectory and both risers achieve similar deflection. The smaller variation in the horizontal position is due to variance in the current. To the bottom right in Fig. 8.5 we clearly see that R2 has a larger payout to compensate for smaller riser elongation and achieve equal effective length.

The same algorithm is applied for 30m TLP offset (Fig. 8.6). As before R2 slides out to the right with decreasing tension, increasing the horizontal distance between the risers to avoid collision, see Fig. 8.6 top left. The payouts (bottom right) are larger in the offset case than without offset due to the effects from weight and current. The top tension T_2 is seen to stabilize about 1400kN for

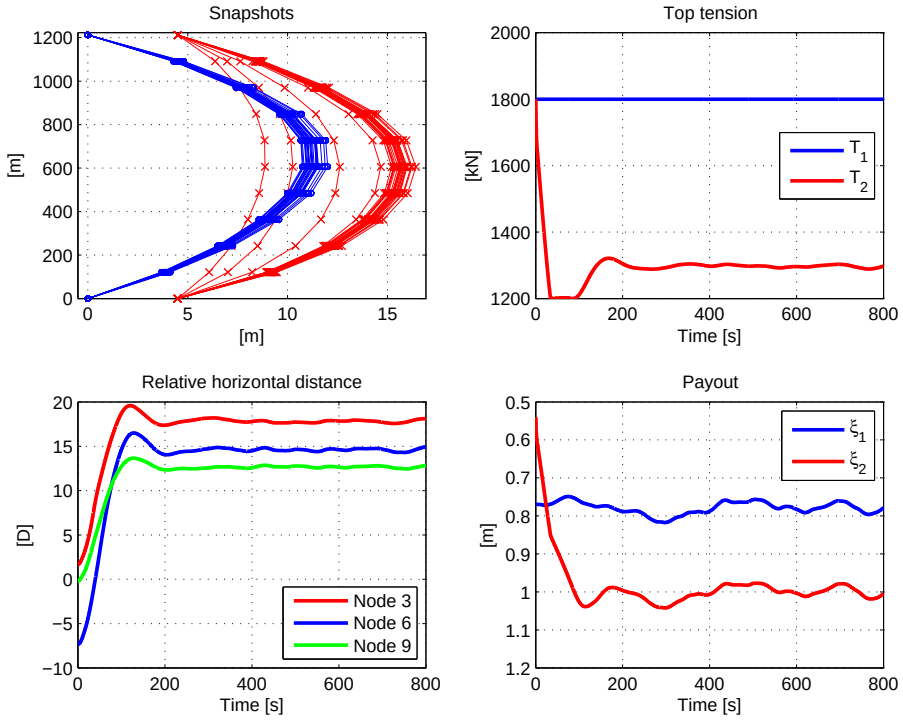

Figure 8.5: Equal effective length and control of R2. Snapshots of the riser configuration (top left), top tension (top right), relative horizontal distance (bottom left) and payout (bottom right).

the offset case and 1300kN for the no-offset case, to the upper left in Figs. 8.5 and 8.6, respectively. Hence, a smaller tension difference is needed in the offset position. This is due to a longer effective length (riser plus payout), and the relation between tension, payout and horizontal deflection. For a long riser with small tension, an increase in tension has larger effect on the lateral deflection than if the riser already has a high tension level.

Now the top tension of R1 is controlled using the payout of R2 as reference, compensated for axial elasticity. R2 is not controlled. Hence,

$$\xi_{r,1} = \xi_2 - \Delta l_R, \tag{8.8}$$
$$T_1 = T_{0,1} + \tau_{c,1}, \tag{8.9}$$
$$T_2 = T_{0,2}, \tag{8.10}$$
$$e_1 = \xi_{d,1} - \xi_1. \tag{8.11}$$

The controller is the same as for Section 8.2.2. Fig. 8.7 shows the snapshots of

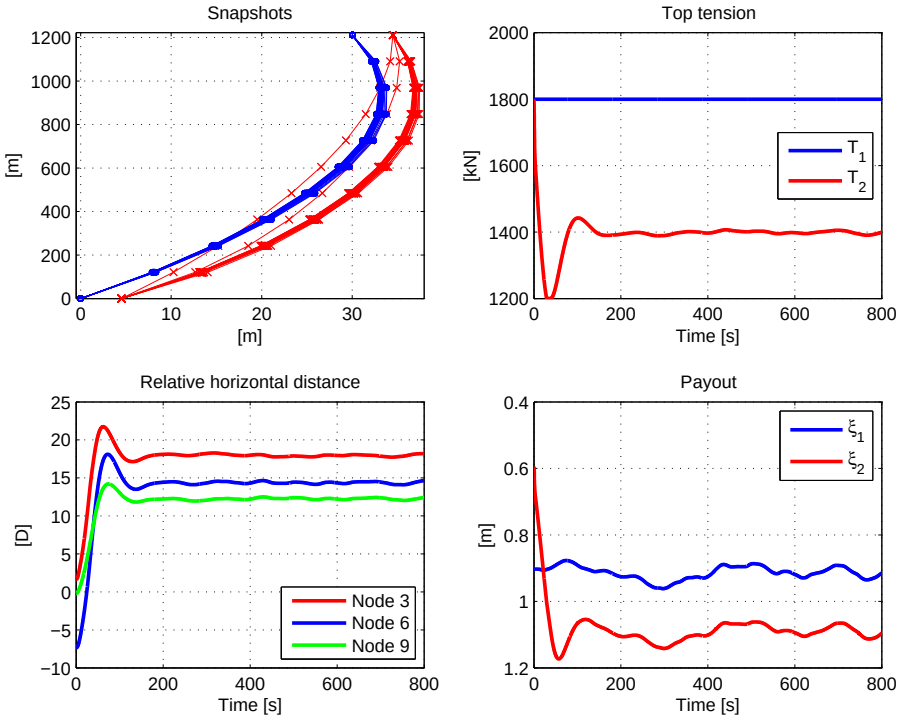

Figure 8.6: 30m TLP offset, equal effective length and control of R2. Snapshots of the riser configuration (top left), top tension (top right), relative horizontal distance (bottom left) and payout (bottom right).

the risers. As the tension in R1 increases and it is tightened up, the deflection decreases. In addition, R2 moves behind since R1 comes in front. This is due to the increased current and reduced shielding effect on R2 as the distance between the risers increases. It should be noted that the simulation is valid only when the downstream riser is more than 2D behind the upstream riser. The payouts, how the piston end of R1 is pulled in, and how the payout of R2 is slightly increased when the deflection increases, are seen (bottom right).

The TLP is placed at 30m offset. The risers behave similarly as for the case without offset, see snapshots and payouts in Fig. 8.8. Top tension was seen to decrease compared to the no-offset case and stabilize about 2650kN and 2400kN with tension differences of 850kN and 600kN, respectively shown in Figs. 8.7 and 8.8. It should also be noted that the difference and payout is larger when controlling R1 than R2. This is caused by the more straightlined configuration at higher tension levels, and a need of even more tension to straighten up to prevent

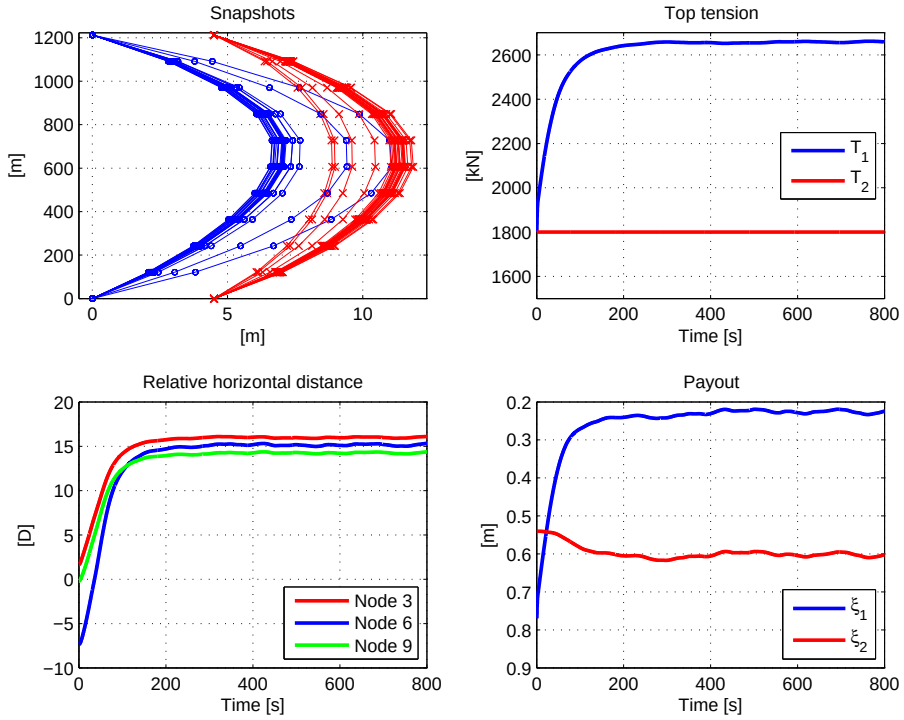

Figure 8.7: Equal effective length and control of R1. Snapshots of the riser configuration (top left), top tension (top right), relative horizontal distance (bottom left) and payout (bottom right).

collisions, due to the nonlinear relationship (cf. $\frac{\Delta x}{\Delta T}$ p. 53) between the tension and the deflection.

8.2.4 Desired Horizontal Distance

The desired horizontal distance control objective requires one or more measurements of the relative distance between the riser at predefined water depths. Keeping a desired relative distance, gives the following guidance trajectory from (6.39)

$$\Delta x_{R12,r}(z) = \Delta x_d. \tag{8.12}$$

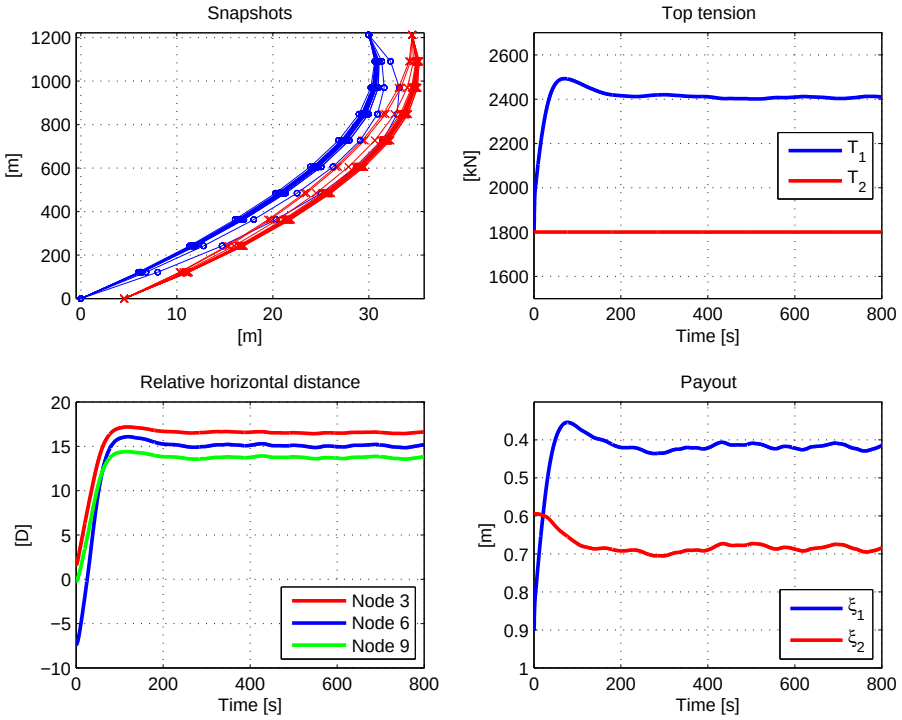

Figure 8.8: TLP offset of 30m, equal effective length and control of R1. Snapshots of the riser configuration (top left), top tension (top right), relative horizontal distance (bottom left) and payout (bottom right).

Controlling R2 with a PI-controller gives

$$T_1 = T_{0,1}, \tag{8.13}$$

$$T_2 = T_{0,2} + \tau_{c,2}, \tag{8.14}$$

$$\tau_{c,2} = -K_{P,2}\Delta e_{rel} - K_{I,2}\int \Delta e_{rel} dt, \tag{8.15}$$

$$\Delta e_{rel}(z) = \Delta e_{rel,d} - \Delta x_{R12,m}(z), \tag{8.16}$$

using (6.44), (6.50) and (6.51). The tension is found in Fig. 8.9 (top right). The snapshots (top left) show how R2 slides to the right when the tension decreases and removes the risers from the error state. The corresponding payout is seen bottom right.

This control objective is seen to effectively remove the risers from a collision situation. However, it is dependent on measurement(s) along the riser, located where the risers are most likely to collide.

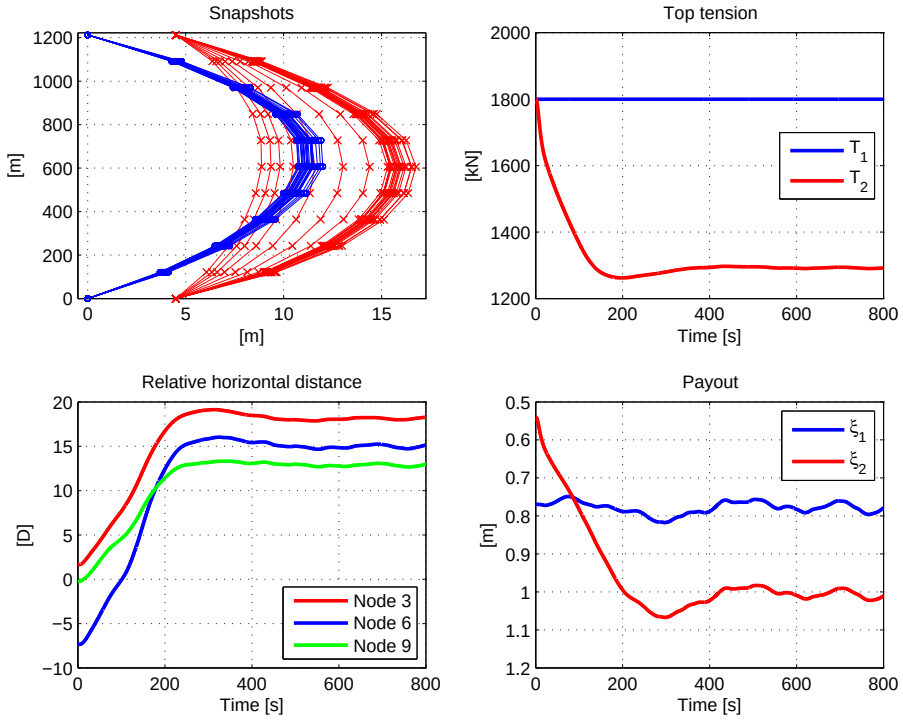

Figure 8.9: Desired relative horizontal distance and control of R1. Snapshots of the riser configuration (top left), top tension (top right), relative horizontal distance (bottom left) and payout (bottom right).

8.3 Effect of Shallow Water

The control objectives equal payout and equal effective length, are based on payout and tension measurements at the wellhead and available today, and might therefore more likely be implemented by the industry. Hence, the equal payout and equal effective length control objectives are subject for the next investigation in shallow waters.

The risers are located at 300m water depth and the current profile from the Ormen Lange field is scaled to this depth, keeping the same velocity in each node. The risers have the same physical dimensions as before except for the length. The center-to-center distance is decreased to 8D. Keeping the same riser diameter, the upper tension limit could be the same due to stress considerations, whereas the lower tension limit is due to effective weight. Here, the water depth and also the effective weight is one fourth of the previously simulated depth of 1200m. The

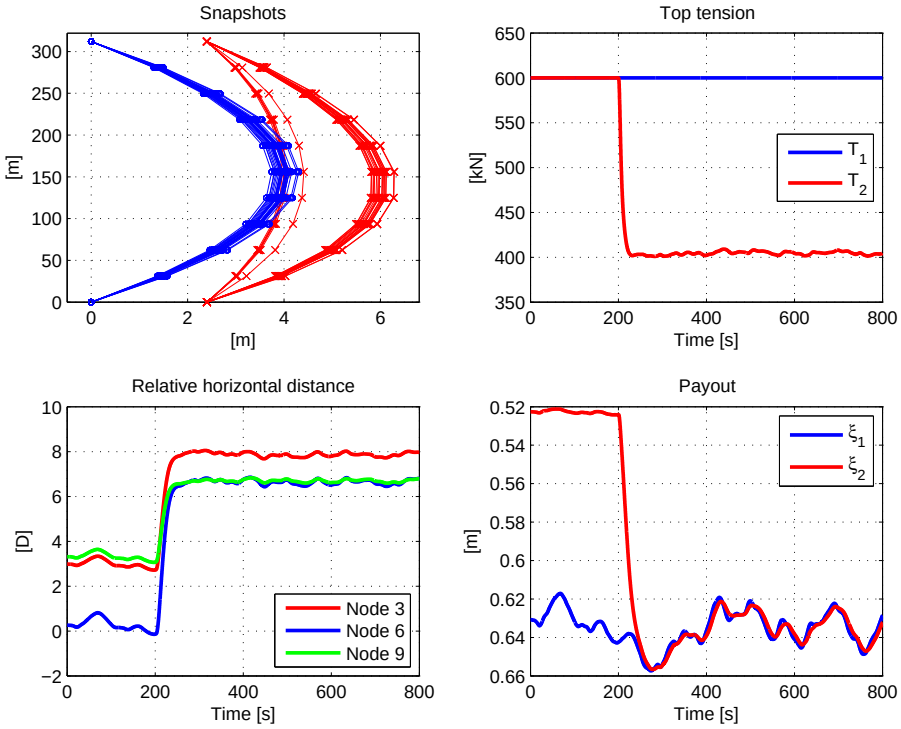

Figure 8.10: Equal payout control of R2 at 300m water depth. Snapshots of the riser configuration (top left), top tension (top right), relative horizontal distance (bottom left) and payout (bottom right).

lower tension limit could be as low as 350kN at 300m water depth. The tension level is much lower and the axial elongation therefore smaller, and hence excepted to be of less importance. The equal payout and the equal effective length control objectives are tested with an initial top tension of 600kN, zero offset and control of R2, starting after 200s. Fig. 8.10 (top left) shows how R2 slides out to the right due to the decreased tension when the control is turned on. The payout is seen to be equal for the two risers in Fig. 8.10 (bottom right). For the equal effective length control objective in Fig. 8.11, R2 slides slightly more to the right, and the payout is seen to be 2-3cm larger for R2 than for R1, due to the compensation of the elasticity. The tension of R2 is right above 400kN using equal payout and right below 400kN using the equal effective length control objective. The smallest relative horizontal distance between the risers is about 6.7D in the first case and 7.2D in the latter. Hence, a small effect of taking the elasticity into account is seen even at 300m water depth. However, it is of far less importance than in

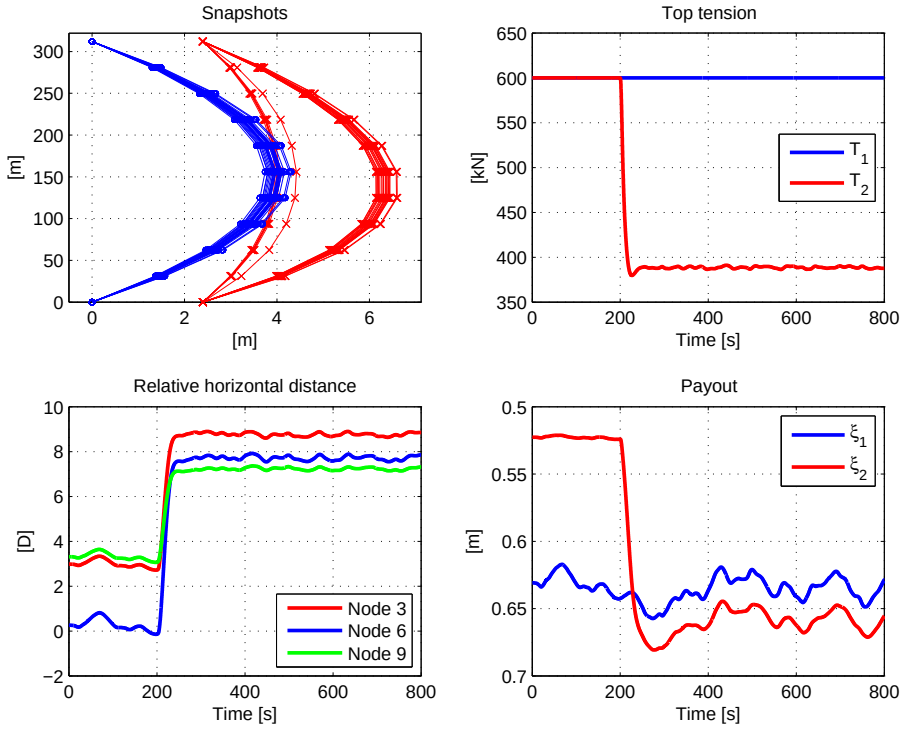

Figure 8.11: Equal effective length control of R2. Snapshots of the riser configuration (top left), top tension (top right), relative horizontal distance (bottom left) and payout (bottom right).

deeper waters.

8.4 TLP Dynamics

For the simulations with dynamic TLP motions, 1200m water depth is used. In this case, the TLP moves with harmonic motions in surge about a static offset of 30m. The period is 120s, and the peak-to-peak amplitude 40m. The controllers are enabled after 400s. Fig. 8.12 shows the horizontal positions for three selected nodes. It is seen in these plots, as expected, that the upper nodes are most influenced by the TLP motion. In this case where R2 is controlled, we see that the collision is avoided by increasing the horizontal position of R2. When R1 was controlled, the horizontal positions of R1 decreased, and the horizontal positions for R2 increased at the same time due to reduced shielding, not shown here.

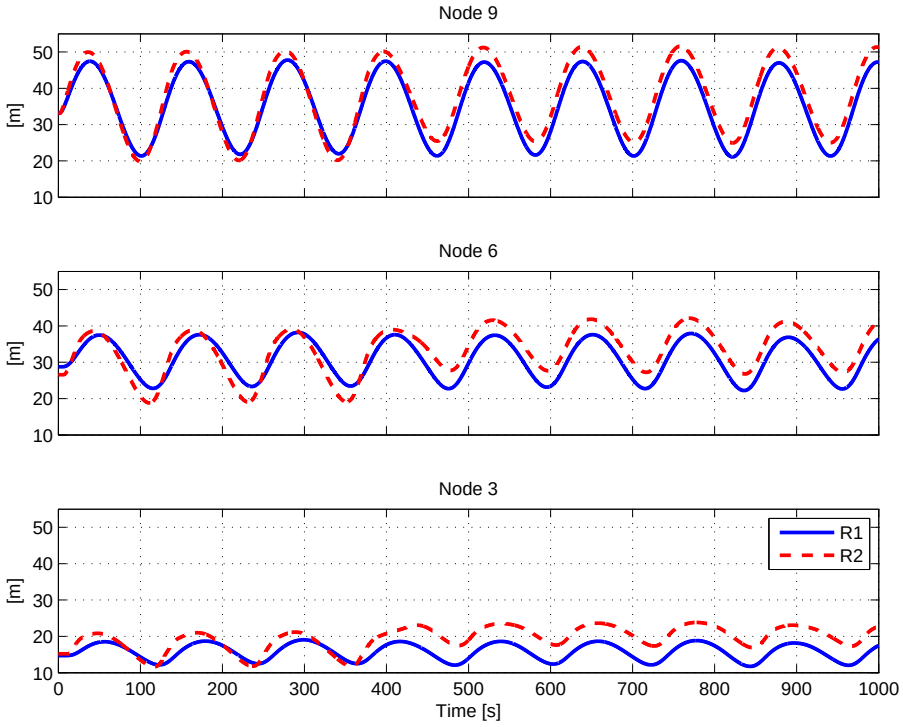

Figure 8.12: Dynamic TLP motions and control of R2 enabled after 400s. Horizontal positions for node 3, 6 and 9 for R1 and R2.

The riser slides out to the right when the payout ξ_2 increases, see Fig. 8.13. The relative horizontal position between the same three nodes is seen in Fig. 8.13 (bottom left). The effect of control is clearly seen. Before the controller is turned on, collision occurs twice for each cycle. After 400s, the controller is turned on, and the mean distance is about 15D, equal to the top and bottom distance, for all nodes, giving a similar configuration for the two risers. Also, the variation in distance between corresponding nodes decreases significantly. The payout with control of R1 and R2 are given in Figs. 8.13 and 8.14, respectively. For the uncontrolled first 400s, the dynamic stroke of R1 is 1.6m and 0.8m for R2. This difference is caused by larger drag and deflection of R1. R2 has a more straightlined configuration due to reduced drag forces. Note that when R2 comes in front, the model is not valid and R2 keeps its straight configuration.

When R1 is the reference, the stroke of R2 is increased, and the stroke of R1 is slightly decreased, giving a dynamic stroke about 1.5m for both risers. The mean tension of R2 is decreased to about 1450kN, giving a tension difference of 350kN

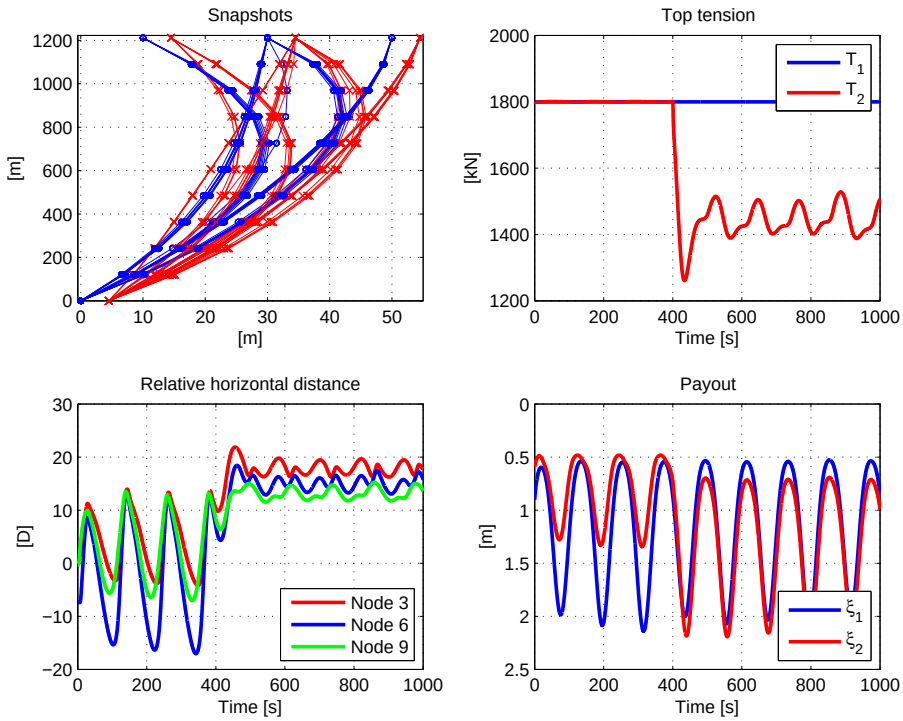

Figure 8.13: Dynamic TLP motions and control of R2 enabled after 400s. Snapshot of the riser configuration (top left), top tension (top right), relative horizontal distance (bottom left) and payout (bottom right).

between the risers, see Fig. 8.13. The smaller mean tension compared to the static case is due to longer payout and total effective length, such that a smaller tension difference is needed to avoid collision. The dynamic tension variation has a period of 120s as for the TLP motions, and a peak-to-peak amplitude about 120-140kN.

When R2 is the reference for R1, its dynamic stroke decreases, giving both R1 and R2 a dynamic stroke about 1m, see Fig. 8.14. The mean tension level is increased with 400kN for T_1, seen in Fig. 8.14. The dynamic tension variation was about 120-130kN. Increasing the TLP period to 300s, a more quasi-static riser behavior is seen with less dynamic deflection. This gives less need for stroke, a smaller payout and effective length and a larger tension difference closer to the static case.

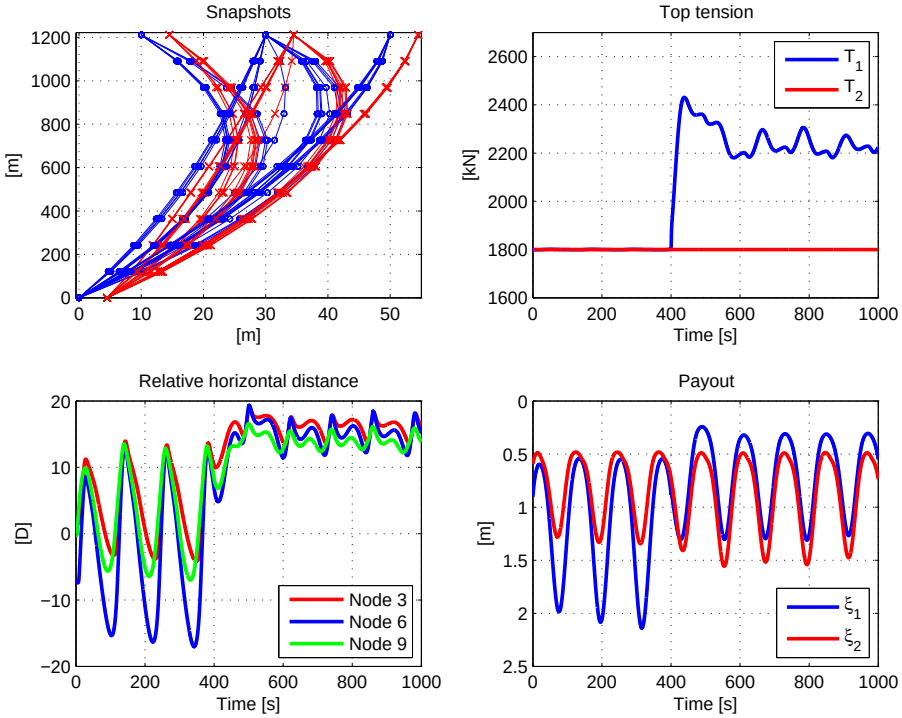

Figure 8.14: Dynamic TLP motions and control of R1 enabled after 400s. Snapshot of the riser configuration (top left), top tension (top right), relative horizontal distance (bottom left) and payout (bottom right).

8.5 Supervisory Switched Controller

For permanent installations, like the TLP, the all-year weather changes must be taken into consideration, also when designing the control system. The different ROCs should be identified and the control actions adjusted to each regime. This includes controlling the top tension of the risers depending on the prevailing situation, and also turning off the controller in calm weather to avoid unnecessary wear and tear of the cylinders. Switching between the different regimes and control actions are illustrated in this section.

8.5.1 Case Set-Up

The initial current is of factor 0.8 of the Ormen Lange design current with the same variation as used before. The TLP is in a no-offset position, and the center-to-center distance between the risers is 15D at the top and bottom end points.

At 400s, an additional, uniform tide current increases from 0m/s to 0.3m/s over 300s. This total current velocity is used for the rest of the simulations. At 500s, the TLP starts moving to an offset position of 30m, which it uses approximately 300s to reach. When the TLP has almost arrived the offset position, a LF motion in surge with a period of 120s and a peak-to-peak amplitude of 40m starts (800s). At 1200s, an additional extreme WF motion is superimposed on the LF TLP motion. This extreme wave has a 12s period and an amplitude of 20m. The linear wave-induced surge motion on the TLP can be found from the response amplitude operator (RAO) for the TLP ASM600, see Faltinsen (1990). This gives a WF TLP surge motion with the same period of 12s and a peak-to-peak amplitude of 10m. The changes in current and TLP motions are given in Table 8.1 and illustrated in Fig. 8.15. It should be noted that the changes in mean current velocity and the different environmental conditions happen faster than in real life, but the magnitudes themselves are representative.

Disturbance	Start time [s]
Tide current	400
TLP offset	500
TLP LF	800
TLP WF	1200

Table 8.1: Case simulation.

The PPMs consist of 16 elements, while the ACPMs consist of 8 elements. Only R2 is controlled, using the payout from R1, ξ_1, as a reference. Due to the deep water, the riser elongation Δl_R is included, giving the payout reference

$$\xi_{r,2} = \xi_1 + \Delta l_R, \quad \Delta l_R = \frac{\Delta T}{EA} l_0. \tag{8.17}$$

8.5.2 Simulations without Control

First the simulation case is run without control for two different pretensions, see Fig. 8.16. To the left simulations with a pretension of 1800kN for both risers are seen. The risers are close to collision from the start, but actual collision is seen for node 9 after 200s, due to the small variations in current velocity. The relative distance is smaller than 2D (bottom left). The collision is present until 400s. A new collision is seen at 450s, and is lasting for the rest of the simulation. Recall that the model is not valid for riser distances smaller than 2D, and we can only say that for smaller relative distance than this, collision is likely to occur.

With a pretension of 2700kN for both risers (Fig. 8.16, right), collision first happens after 600s, when the current velocity is increased due to tide. For LF

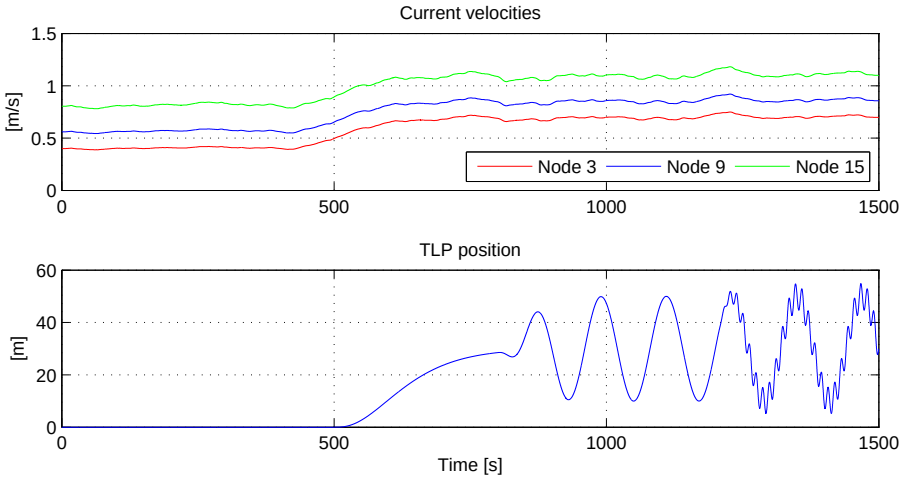

Figure 8.15: Disturbances from current (top) and TLP (bottom), acting on the risers.

TLP motions, the risers are in a no collision situation in the rightmost TLP offset, where the risers are most straightlined. When the TLP moves to the left, the risers experience larger relative velocities. R1 experiences larger drag forces than R2, and hence a larger deflection and increased risk of collision. Notice the difference in payout values in the top plots. The medium pretension of 1800kN results in a payout approximately twice as big as the payout for the pretension of 2700kN. The relative distance between the risers are similar.

8.5.3 Simulations with Control

The risers are exposed to the same environmental set-up, but now control of top tension is introduced. R2 is controlled by switching between the controllers described in (6.45) to (6.49) as described in Section 6.4.

The initial top tension is 1800kN for both risers. Due to the shielding effect which gives differences in drag forces, the risers are starting in a state close to collision, with 3D being the smallest distance between the risers (see Fig. 8.18). The monitoring signal is smallest for process μ_5, leading to the process switching signal $\rho = 5$ which maps to the controller switching signal $\sigma = 2$ and the PI-controller (see Fig. 8.17). The tension for R2, T_2, is decreasing such that the distance between the risers is increasing to a level about 15D (Fig 8.18). The payout for the two risers are also found in Fig. 8.18, showing a difference of 0.2m, corresponding to the riser elongation due to tension.

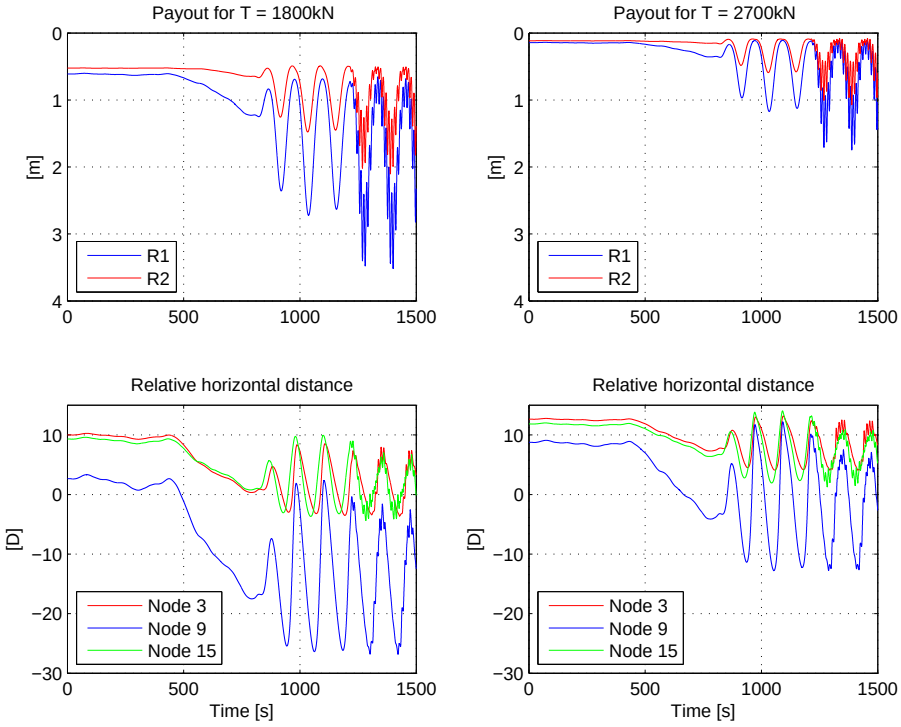

Figure 8.16: Effects of the constant top tension, 1800kN (left) and 2700kN (right), payouts (top) and relative horizontal distance between the risers (bottom).

As the riser distance increases, the monitoring signal for the slowly varying process, μ_3, is the smallest, and the process switching signal switches to $\rho = 3$. The same controller is kept, as it still maps to the same controller switching signal $\sigma = 2$. After approximately 310s, R2 has reached a stable position near the desired horizontal riser distance and a small variation in tension the last 100s. The smallest monitoring signal is found for normal state μ_2, giving $\rho = 2$ and $\sigma = 1$ (Fig. 8.17). The top tension T_2 is set constant and equal the prevailing value at the switching moment (Fig. 8.18).

From 550s, the smallest distance between the risers decreases, due to increasing current velocity from tide. The PI-controller for T_2 is turned on when μ_3 is the least monitoring signal, giving $\rho = 3$ and $\sigma = 2$ (Fig. 8.17). The same controller is kept when the TLP starts moving with LF motions. An additional WF TLP motion is superimposed, starting at 1200s, see Fig. 8.19. At 1250s, when the WF motions have achieved almost full amplitude, μ_4 is the smallest monitoring signal, giving $\rho = 4$ and $\sigma = 3$ (Fig. 8.17), and the PID-controller is

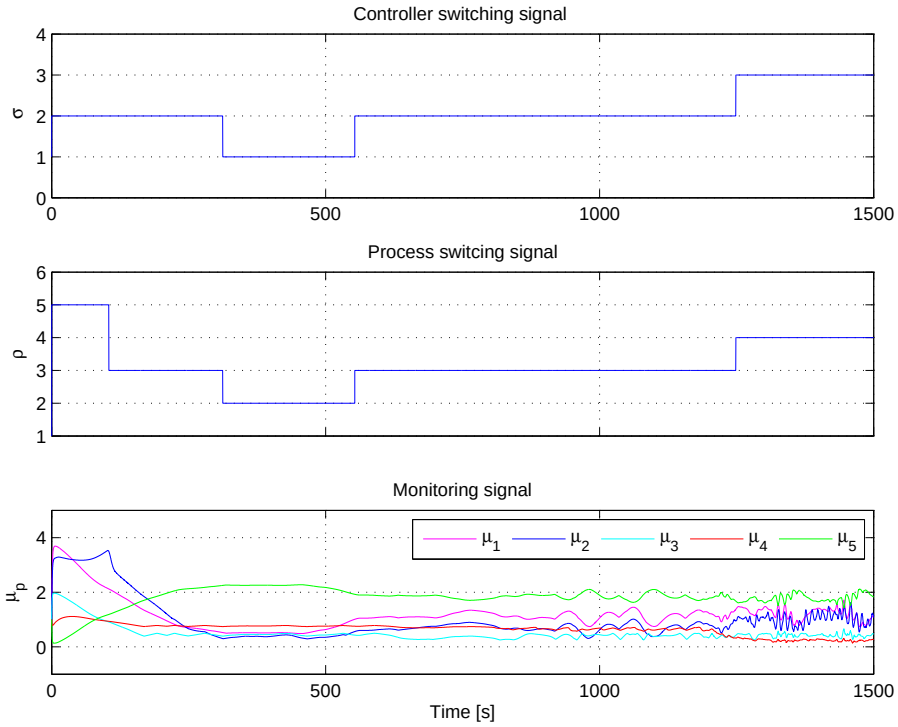

Figure 8.17: From the top: Controller switching signal σ, process switching signal ρ and switching error μ_p.

phased in. The effects of the TLP WF motions on the top tension and payout are seen in Fig. 8.19. The top tension desired by the controller (–) and the saturated tension from the actuator (- -) are seen in the middle graph. The switching from the PI- to the PID-controller happens at 1250s, with a smooth transition lasting 20s, such that at 270s the PID-controller is working alone. T_2 is in rate saturation with the PI-controller just before the PID-controller is phased in. The tension variations are larger for the PI-controller than the PID-controller due to a larger proportional gain. Anyhow, the PID-controller is also seen to be in rate saturation every 120s, corresponding to the LF TLP motions, where the TLP moves from right to left, giving the largest deflections.

When the TLP moves against the current velocity, the relative velocity increases, and hence the drag forces increase with the square of the velocity. For increasing relative velocity, the riser feels stiffer, and to straighten the riser or even maintain the same curvature, a higher tension is needed. For a pure LF motion the tension rates are not exceeded, but for an additional WF motion,

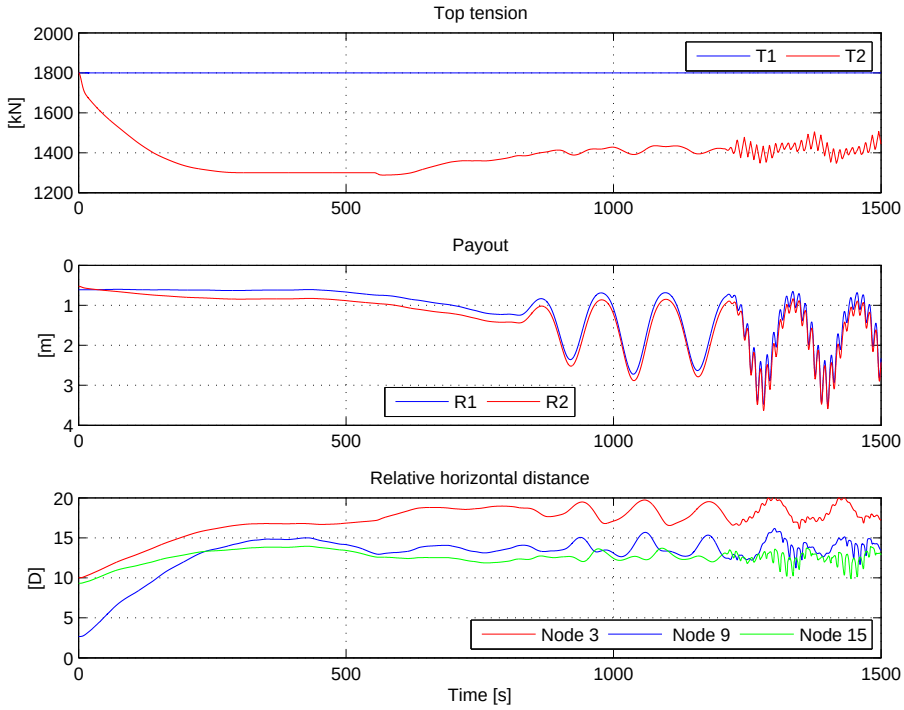

Figure 8.18: Effects of the controller. From the top: Top tension, payout and relative riser distance.

large and fast changes in tension are requested, and rate saturation occurs. This rate saturation is seen to affect the payout of R2. The difference in payouts for R1 and R2 corresponds to the riser elongation due to the tension difference in the unsaturated periods. While the tension is in rate saturation, the payout for R2 is not large enough, such that the payouts for R1 and R2 are close to equal. However, this is not a problem with respect to collision for such fast motions here. Regardless of this, we can not neglect that this could be a problem for risers with different physical properties and dynamics.

The relative distance between the upper nodes is naturally more affected by the WF motions than the nodes further down the riser (Fig. 8.18). For instance, node 15 experiences more dynamics, with larger motions over a longer period of time. It takes some time for the motions to travel down the riser. The riser top seems most sensitive to the WF motions when it is in a nearly Straightlined configuration, corresponding to a TLP movement from left to right. The least variation in relative distance is seen when the TLP moves in the opposite

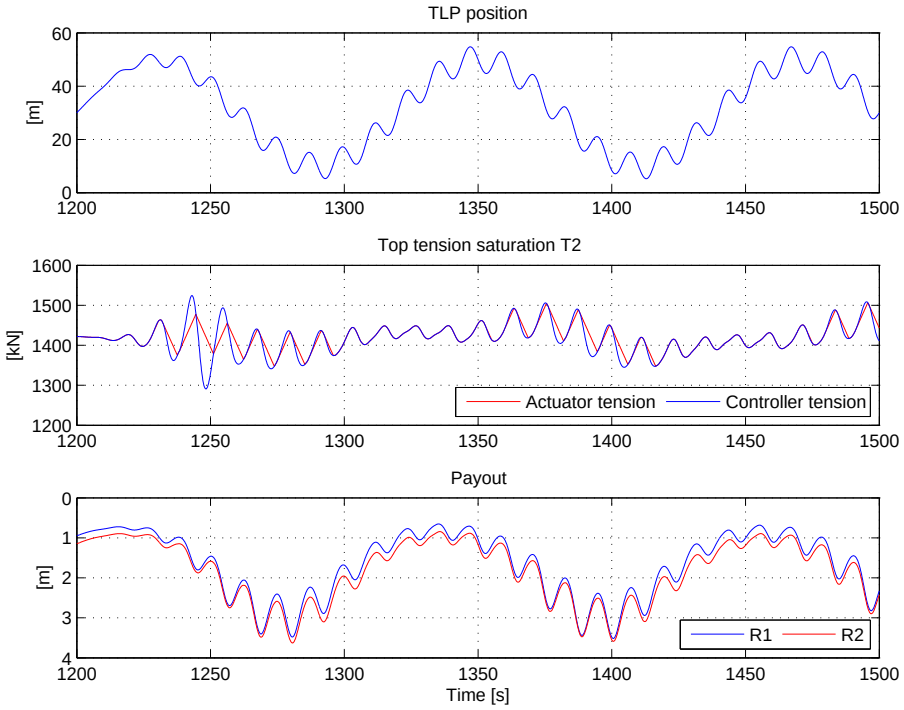

Figure 8.19: The WF motion. From the top: TLP position, top tension and saturation for T2 and payout.

direction and the deflection is largest. This means that when the first mode is the dominating mode shape, higher order mode shapes are less pronounced.

8.6 Discussion

The controller objective may change according to the ROC. For low current velocities, constant tension may be a sufficient solution. Equal payout is shown to be appropriate in shallow waters (∼300m). However, the effects of elasticity and riser elongation need to be included in the control strategy in order to prevent riser collision in deep waters when top measurements are used. The desired relative horizontal distance control objective indirectly includes the elasticity and showed promising results, but the measurements along the riser used in this algorithm are not easily available offshore. Instead, a model is used to estimate the distance between the risers, and used in the monitor to trigger switching between the different controllers. If measurements were easily available, they could be used

instead. Note that the model used here is verified for LF TLP motions. For large riser or TLP velocities, the wake model is no longer valid. However, WF TLP motions are included in the simulation study to illustrate the effect of control also in this regime.

Chapter 9

Concluding Remarks

9.1 Conclusion

This thesis has focused on modeling, simulation and control of top tensioned marine risers. More specifically, we have considered how we can prevent collision between risers in an array, exposed to platform motions, current and hydrodynamic interaction forces by controlling the top tension. The main conclusion from this study is that it may be possible to prevent riser collision by use of top tension control.

A two-dimensional mathematical model of a riser/TLP system was developed. This included the current velocity profiles, hydrodynamic interaction between risers, TLP motions, the riser model and the actuator. The hydrodynamic interaction could be described by three different components; the mean shielding effects, WIO and VIV. Here, only the first one was considered, as this was assumed to be of major importance for the risers' relative position. The risers were modeled with FEM and integrated load and equilibrium iterations. Simplifications were made by neglecting the bending stiffness and assuming free end rotations.

The riser model was verified with the commercial software RIFLEX (Fylling *et al.*, 2005). At 1200m water depth, the riser model with 20 elements was compared to a RIFLEX model with 400 elements. These verifications showed good agreement, both with respect to payout and horizontal deflections. The agreement was better for high tensions and when the curvature was small. For a larger curvature, more elements were needed to maintain the same accuracy. A quasi-static model was also verified for shallow waters, and compared to RIFLEX models with and without a stress joint at the seabed. The stress joint was seen to be of importance in shallow waters, whereas it had less impact on the global geometry in deep waters and could be considered insignificant. Hence, when simulating production risers in shallow waters, the stress joint should be included.

For a drilling riser which actually has a balljoint at the lower end, free end rotation was a more correct way of modeling.

The riser model was then run with 2 to 20 elements and compared to the RIFLEX model with 400 elements. This was motivated by the purpose of real-time control applications which require computationally fast models, while still being able to describe the main physics with desired accuracy. The performance of the quasi-static model with increasing TLP offset was investigated through error norms of the horizontal position, riser top inclination, area under the riser curve and payout. Simulations showed that payout best reflected the models' performance. This method was therefore used to compare the performance of the dynamic model with different number of elements. Based on the payout error, the various element models were classified for different applications. With more than 15 elements, we achieved high accuracy and an accurate description of the physical process (PPM). The models with 8-12 elements showed good agreement and rather accurate estimates of the process. They are appropriate for ACPM purposes, where both fast simulations and high accuracy are required. For few elements models (4-6), the errors were larger, but the main physics were still captured. This model could be used in control analysis or fast simulations (FCPM).

A control system design for control of top tensioned marine risers has been proposed and needed instrumentation has been suggested. Instrumentation includes payout and top tension at the TLP wellhead and the relative horizontal distance along the riser. The different control objectives to prevent riser collision were proposed. These included equal top tension, equal payout, equal effective length and desired horizontal distance. Equal top tension is used by the industry today, whereas equal payout was proposed by Huse and Kleiven (2000). We have in this thesis extended these results to also include equal effective length and desired horizontal distance as new control objectives.

In deep waters equal top tension resulted in collision for medium current velocities. However, for very low current velocities, equal tension can be appropriate. Equal payout gave collision in a smaller riser segment, but collision still occurred. By taking the riser elongation into account by introducing equal effective length, collision was prevented. These two latter control objectives were also simulated in shallow waters (300m). Here equal payout showed to be satisfactory, as the relative riser elongation was observed to be much smaller and hence of less importance. However, in deeper waters the effect of elasticity and riser elongation needs to be included in the control strategy in order to avoid riser collision. Desired horizontal distance included the elasticity indirectly and showed promising results. Anyhow, the measurements used in this method is not easily available offshore today.

The different regimes for riser operations were defined, and a relation between

regime and control action was proposed. A simulation study with supervisory switched control showed a case, with switching between the different controllers depending on the prevailing regime. These results may be of industrial interest, and further studies should be carried out to investigate the possibility of physical implementation offshore.

9.2 Proposals for Further Work

This work has focused on a two-dimensional model of risers in a tandem arrangement. A simple two-dimensional wake model was applied. In these analyses we have focused on two equal risers. Further analyses using the same model should include riser for different purposes (drilling, production, etc.) giving different riser characteristics (diameter, pretension, fluid density, etc.) and thereby physical behavior. As a next step, more than two risers should be included in an array or matrix. To simulate risers placed in a matrix structure a three-dimensional model is needed. The largest challenge will be to make a good three-dimensional wake model, meaning that lift forces should be included, but also other hydrodynamic interaction effects such as WIO and VIV should be considered added in the model. In addition the current can have varying direction profiles. Also direct wave loads and the first order floater motions should be investigated. These effects are not included in the implemented wake model, and some modifications might be needed to make the wake model valid in this regime. This modeling, implementation and simulation study should be performed before full scale tests can be carried out.

Within the field of control several interesting challenges are found. These could be summarized as:

- Formulating the tension reference trajectory as an optimization problem with relative horizontal distance between the risers and energy consumptions as possible parameters in an objective function.
- Synchronization of risers in an array or matrix, choosing one riser as a leader and the others as followers.
- Preventing new collisions between risers in an array or matrix during transition from an error situation to reach their desired positions and tension trajectories. The sequence of the risers and how fast each riser should reach its optimal tension trajectory is of importance. This could be formulated as a maneuvering problem and called error state maneuvering here.

The proposed tasks could be solved for the two-dimensional case first and thereafter extended to the three-dimensional case. Lastly, both model tests and full

scale experiments would be of importance for the actual implementation of top tension control of risers to prevent collision aboard installations offshore.

Bibliography

Aamo, O. M. (2002). Modeling and Control of Fluid Flows and Marine Structures. PhD thesis. Departement of Engineering Cybernetics, Norwegian University of Science and Technology (NTNU). Trondheim, Norway.

Aker Kværner (2007). Compensator and tensioners. [Online; accessed May 18]. URL http://www.akerkvaerner.com.

Aker Maritime (2002). Ormen Lange TLP with full processing facilities. Technical Report 37-00-NN-X15-00117.

Allen, D. W., D. L. Henning and L. Lee (2005). Riser interferense tests on flexible tubulars at prototype reynolds number. In: *Proc. of the 37th Annual Offshore Technology Conference*. Houston, TX. OTC17290.

American Petroleum Institute (1987). Recommended practice for planning, designing and constructing tension leg platforms. Technical Report API RP 2T. Washinton D.C., USA.

Åström, K. J. and B. Wittenmark (1997). *Computer-Controlled Systems - Theory and Design*. 3rd ed.. Prentice Hall.

Baarholm, R., T. Kristiansen, H. Lie and K. Herfjord (2005). Experimental investigation of dual riser interaction. In: *Proc. of 24th International Conference on Offshore Mechanics and Arctic Engineering*. OMAE2005-67100.

Berge, S., A. Engseth, I. Fylling, C. M. Larsen, B. J. Leira and A. Olufsen (1992). Handbook on design and operation of flexible pipes. Handbook STF70 A92006. Structural Engineering, SINTEF. Trondheim, Norway.

Blevins, R. D. (1994). *Flow Induced Vibrations*. Krieger publishing company.

Blevins, R. D. (2005). Forces on the stability of a cylinder in a wake. *Journal of Offshore Mechanics and Arctic Engineering* **127**, 39–45.

Bokaian, A. and F. Geoola (1985). Hydrodynamic forces on a pair of cylinders. In: *Proc. of the 17th Annual Offshore Technology Conference*. Vol. 3. Houston, TX. pp. 413–420. OTC5007.

Chaudhury, G. and C.-Y. Ho (2000). Coupled dynamic analysis of platforms, risers, and moorings. In: *Proc. of the 32nd Annual Offshore Technology Conference*. Houston, TX. OTC12084.

Chen, X., J. Zhang, P. Y. F. Liagre, J.M. Niedzwecki and P. Teigen (2002). Coupled dynamic analysis of a mini TLP: Comparison with measurements. In: *Proc. of the 21st International Conference on Offshore Mechanics and Arctic Engineering*. Oslo, Norway. OMAE2002-28536.

Dean, Q. W. (1980). A riser angle positioning system (raps). In: *Proc. of the 12th Annual Offshore Technology Conference*. Vol. 2. Houston, TX. pp. 169–179. OTC3755.

Demirbilek, Z. (1989*a*). Tension leg platform - an overview of the concept, analysis and design. In: *Tension Leg Platform - A state of the art review* (Z. Demirbilek, Ed.). American Society of Civil Engineers.

Demirbilek, Z., Ed. (1989*b*). *Tension Leg Platform - A state of the art review*. American Society of Civil Engineers.

DNV (2003). Global analysis procedure for riser interaction. Revision No. 3 issued to NDP Report No. 2002-1539. Det Norske Veritas.

DNV (2005). Recommended practice for riser interference. Industry version issued DNV-RP-F203. Det Norske Veritas.

Duggal, A. S. and J. M. Niedzwecki (1993). An experimental study of tendon/riser pairs in waves. In: *Proc. of the 25th Annual Offshore Technology Conference*. Houston, TX, USA. pp. 323–333. OTC7239.

Egeland, O. (1993). *Servoteknikk*. Tapir Forlag.

Ersdal, S. (2004). An Experimental Study of Hydrodynamic Forces on Cylinders and Cables in Near Axial Flow. PhD thesis. Departement of Marine Technology, Norwegian University of Science and Technology (NTNU).

European Commission (2007). GALILEO - European Satellite Navigation System. [Online; accessed February 5]. URL http://ec.europa.eu/dgs/energy_transport/galileo/index_en.htm.

Faltinsen, O. M. (1990). *Sea Loads on Ships and Offshore Structures*. Cambridge University Press. Cambridge, UK.

Fard, M. P. (2000). Modelling and Control of Mechanical Flexible Systems. PhD thesis. Departement of Engineering Cybernetics, Norwegian University of Science and Technology (NTNU). Trondheim, Norway.

Fontaine, E., J. Capul, T. Rippol and P. Lespinasse (2007). Experimental and numerical study on wake interference and clashing between steel catenary risers. In: *Proc. of the 26th Internaltional Conference on Offshore Mechanics and Arctic Engineering*. San Diego, CA. OMAE2007-29149.

Fossen, T. I. (2002). *Marine Control Systems - Guidance, Navigation and Control of Ships, Rigs and Underwater Vehicles*. Marine Cybernetics. Trondheim, Norway.

Fredheim, A. (2005). Current Forces on Net Strucutres. PhD thesis. Departement of Marine Technology, Norwegian University of Science and Technology (NTNU). Trondheim, Norway.

Fylling, I. J., C. M. Larsen, N. Sødahl, H. Omberg, A. G Engseth, E. Passano and K. Holthe (2005). Theory Manual RiflexTM-34-rev0. SINTEF Marintek. Trondheim, Norway.

Gopalkrishnan, R., A. G. C. Ekvall, R. B. McDaniel, T. B. Heckler, J. E. Smith, J. H. Haws and D. W. McMillan (1994). TLP production riser spacing: Steady drag and lift on two moderately spaced oscillating cylinders. Technical Progress Report BRC 41-94. Shell Development Company. Houston, TX.

Halse, K. H. (2000). Norwegian deepwater program: Improved predictions of vortew-induced vibrations. In: *Proc. of the 32nd Annual Offshore Technology Conference*. Houston, TX. OTC11996.

Herfjord, K., T. Holmås, B. Leira, M. Brydum and T. Hanson (2002). Computation of interaction between deepwater risers, collision statistics and stress analysis. In: *21th Int. Conf. on Offshore Mech. and Arctic Eng.*. Oslo, Norway. OMAE2002-28152.

Hespanha, J. P. (2001). Tutorial on Supervisory Control. In: *Lecture Notes for the Workshop Control Using Logic and Switching for the 40th Conference on Decision and Control*. Orlando, FL.

Hespanha, J. P. and A. S. Morse (2002). Switching between stabilizing controllers. *Automatica* **38**(11), 1905–1917.

Hespanha, J. P., D. Liberzon and A. S. Morse (2000). Bounds on the number of switching with scale-independent hystersis: Application to supervisory control. In: *Proc. of the 39th IEEE Conference on Decision and Control*. Sidney, Australia.

Hespanha, J. P., D. Liberzon and A. S. Morse (2003). Hystersis-based switching algorithms for supervisory control of uncertain systems. *Automatica* **39**(2), 263–272.

Høklie, M., N. A. Jensen and I. Ciatti (2002). Position reference based on instrumented drilling riser. In: *14th Deep Ocean Technology & Exhibition*. New Orleans, LA.

Huang, S., J. Bolstad and A. Marn (2004). Experimental study of wake shielding effect of the three cylinders in currents. In: *Proc. of the 23rd International Conference on Offshore Mechanics and Arctic Engineering*. Vancouver, British Columbia, Canada. OMAE2004-51001.

Huse, E. (1987). Drag in oscillatory flow interpreted from wake considerations. In: *Proc. of the 19th Annual Offshore Technology Conference*. Houston, TX. pp. 135–142. OTC5370.

Huse, E. (1993). Interaction in deep-sea riser arrays. In: *Proc. of the 25th Annual Offshore Technology Conference*. Houston, TX. pp. 313–322. OTC7237.

Huse, E. (1996). Experimental investigation of deep sea riser interaction. In: *Proc. of the 28th Annual Offshore Technology Conference*. Houston, TX. pp. 367–372. OTC8070.

Huse, E. and G. Kleiven (2000). Impulse and energy in deepsea riser collisions owing to wake interference. In: *Proc. of the 32nd Annual Offshore Technology Conference*. Houston, TX. OTC11993.

Imakita, A., S. Tanaka and Y. Amitani ans S. Takagawa (2000). Intelligent riser angle control DPS. In: *Proc. of ETCE/OMAE Joint Conference*. New Orleans, LA. OMAE2000/OSU OFT-3001.

Johansen, T. A., T. I. Fossen, S. I. Sagatun and F. G. Nielsen (2003). Wave synchromizimg crane control during water enrty in offshore moonpool operations - experimental results. *IEEE Journal of Oceanic Engingeering* **28**(4), 720–178.

Johansen, V., S. Ersdal, A. J. Sørensen and B. Leira (2006). Modelling of inextensible cable dynamics with experiments. *International Journal of Non-Linear Mechanics* **41**(4), 543–555.

Kaasen, K. E., H. Lie, F. Solaas and J. K. Vandiver (2000). Norwegian deepwater program: Analysis of vortex-induced vibrations of marine risers based on full-scale measurements. In: *Proc. of the 32nd Annual Offshore Technology Conference*. Houston, TX. OTC11997.

Kalleklev, A. J., K. J. Mørk, N. Sødahl, M. K. Nygård and A. M. Horn (2003). Design guidelines for riser collision. In: *Proc. of the 35th Annual Offshore Technology Conference*. Houston, TX. OTC15383.

Kavanagh, W. K., L. Imas, H. Thompson and L. Lee (2000). Genesis spar risers: Interference assessment and VIV model testing. In: *Proc. of the 32nd Annual Offshore Technology Conference*. Houston, TX. OTC11992.

Khalil, H. K. (2000). *Nonlinear Systems*. 3rd ed.. Prentice-Hall Inc.. New Jersey.

Korde, U. A. (1998). Active heave compensation on drill-ships in irregular waves. *Ocean Engineering* **25**(7), 541–561.

Kreyszig, E. (1999). *Advanced Engineernig Mathematics*. 8th ed.. John Wiley & Sons, Inc.

Langen, I. and R. Sigbjörnsson (1979). *Dynamisk analyse av konstruksjoner*. Tapir. Trondheim, Norway.

Larsen, C. M. (1993). Analysis of tensioner system stroke for marine risers. Technical Report STF70 F93011. SINTEF Structures and Concrete.

Larsen, C. M. (1995). Tension Leg Platforms, Lecture notes NA550/665. Technical report. Dept. of Naval Architecture and Marine Engineering, University of Michigan.

Leira, B. J., T. Holmås and K. Herfjord (2002). Estimation of extreme response and fatigue damage for colliding risers. In: *Proc. of the 21st International Conference Offshore Mechanichs and Arctic Engineering*. Oslo, Norway. OMAE2002-28435.

Litton, R. W. (1989). TLPs and other deepwater platforms. In: *Tension Leg Platform - A state of the art review* (Z. Demirbilek, Ed.). pp. 15–20. American Society of Civil Engineers.

Ma, W., M.-Y. Lee, J. Zou and E. W. Huang (2000). Deepwater nonlinear coupled analysis tool. In: *Proc. of the 32nd Annual Offshore Technology Conference*. Houston, TX. OTC12085.

Mekha, B. B., C. P. Johnson and J. M. Roesset (1996). Implications of tendon modeling on nonlinear response of TLP. *Journal of Structural Engineering* **122**(2), 142–149.

Ministry of Petroleum and Energy and the Norwegian Petroleum Directorate (2007). *Facts - the Norwegian petroleum sector*.

Mortazavi, M., R. B. Campbell and C. R. Brinkmann (2001). Modeling and analysis of top-tensioned risers. In: *Proc. of the 20th International Conference on Offshore Mechanichs and Arctic Engineering*. Rio de Janeiro, Brazil. OMAE2001/OFT-1168.

National Oilwell Varco (2007*a*). Homepage. [Online; accessed June 8]. URL http://www.nov.com/.

National Oilwell Varco (2007*b*). N-Line Tensioner Course. Technical report. Kristiansand, Norway.

Neto, E. T., C. Ruggieri and J. A. Ferrari (2002). Numerical representation of collision interaction mass for dual risers systems. In: *Proc. of 21st International Conference on Offshore Mechanics and Arctic Engineering*. ASME. Oslo, Norway. OMAE2002-28336.

Nguyen, T. D. (2006). Design of Hybrid Marine Control Systems for Dynamic Positioning. PhD thesis. National University of Singapore (NUS).

Nguyen, T. D., A. J. Sørensen and S. T. Quek (2007). Design of hybrid controller for dynamic positioning from calm to extreme sea conditions. *Automatica* **43**(5), 768–785.

Nielsen, F. G. (2004). Lecture Notes TMR4225 Marine Operations. Technical Report UK-2004-86. Dept. of Marine Technology, NTNU.

NOAA Coastal Services Center (2007). Loop Current. [Online; accessed April 21]. URL http://www.csc.noaa.gov/crs/definitions/loop_current.html.

Norsk Hydro (2001). Environmental Conditions. Ormen Lange Project 37-00-NH-F50-00001.

Nowlin, W. D., A. E. Jochens, S. T. DiMarco, R. O. Reid and M. K. Howard (2001). Deepwater physical oceanography reanalysis and synthesis of historical data. Synthesis Report MMS 2001-064. Dept. of Oceanography, Texas A & M Univeristy. New Orleans, USA.

Nygård, M.K., F. R. Botros and H. Hannus (2001). Evalution of effect of contact between top tensioned risers in deep and ultra deep waters. In: *Proc. of the 11th International Offshore and Polar Engineering Conference*. Vol. 2. Stavanger, Norway. pp. 222–226.

Offshore Tecnology (2007). The website for offshore oil & gas industry. [Online; accessed August 9].

Often, O. (2000). Dry tree semi - reduced costs for dry well completions in deepwater west africa by application of proven semisubmersible and riser technology. In: *Proc. of the 32nd Annual Offshore Technology Conference*. Houston, TX. OTC11876.

Ogata, K. (1995). *Discrete-Time Control Systems*. 2 ed.. Prentice Hall.

Ormberg, H. and K. Larsen (1997). Coupled analysis of floater motion and mooring dynamics for a turret moored tanker. In: *Proc. of the 8th International Confeerence on the Behaviour of Offshore Structures (BOSS)* (J. H. Vugts, Ed.). Vol. 2. The Netherlands. pp. 469–483.

Ormberg, H., I. Fylling, K. Larsen and N. Sødahl (1997). Coupled analysis of vessel motions and mooring and riser system dynamics. In: *Proc. of the 16th International Conference Offshore Mechanics and Arctic Engineering*. Vol. 1A. Yokohama, Japan. pp. 91–99.

Ormberg, H., N. Sødahl and O. Steinkjer (1998). Efficient analysis of mooring systems using de-coupled and coupled analysis. In: *Proc. of the 17th International Confonference Offshore Mechanics and Arctic Engineering*. Lisbon, Portugal. OMAE98-0351.

Paganie, D. (2006). Shell restarts Mars TLP, includes industry firsts. *Offshore Magazine* **66**(6), URL http://www.offshore–mag.com/.

Perez, T., A. J. Sørensen and M. Blanke (2006). Marine vessel models in changing operational conditions - a tutorial. In: *14th IFAC Symposium on System Identification (SYSID)*. Newcastle, Australia.

Perez, T. and P. Steinmann (2007). Modelling and performance of an active heave compensation for offshore operations. In: *Proc. of IFAC Conference on Control Applications in Marine Systems (CAMS07)*. Bol, Croatia.

Pollack, J., L. Poldervaart and M. Naciri (2000). A surface tree riser tensioning system for FPSOs. In: *Proc. of the 32nd Annual Offshore Technology Conference*. Houston, TX. OTC11902.

Price, S. J. (1975). Wake induced flutter of power transimission conductors. *Journal of Sound and Vibration* **38**(1), 125–147.

RD Instruments (2006). Marine Measurements. [Online]. URL http://www.rdinstruments.com.

Reite, K.-J. (2006). Modeling and Control of Trawl Systems. PhD thesis. Departement of Marine Technology, Norwegian University of Science and Technology (NTNU).

Rigzone (2007). Field development projects. [Online; accessed August 9]. URL http://www.rigzone.com/.

Rustad, A. M., A. J. Sørensen and C. M. Larsen (2007*a*). Supervisory switched control of marine risers. In: *Proc. of the IFAC Conference on Control Applications in Marine Systems (CAMS07)*. Bol, Croatia.

Rustad, A. M., C. M. Larsen and A. J. Sørensen (2007*b*). Deep water riser collision avoidance by top tension control. In: *Proc. of the 26th International Conference on Offshore Mechanics and Arctic Engineering*. San Diego, CA. OMAE2007-29172, ISSN 1523-651x.

Rustad, A. M., C. M. Larsen and A. J. Sørensen (2007*c*). FEM modelling and control for collision prevention of top tensioned risers. *Marine Structures*. Elsevier, ISSN 0951-8339, Available online July 5.

Rustad, A. M., C. M. Larsen, M. S. Triantafyllou, F. S. Hover, A. H. Jacobsen and A. J. Sørensen (2006). Modelling and control of colliding top tensioned risers in deep waters. In: *7th IFAC Conference on Manoeuvering and Control of Marine Crafts (MCMC06)*. Lisbon, Portugal.

Sabri, R., C. Putot, F. Biolley, C. Le Cunff, Y. Creff and J. Lévine (2006). Automatic control methods for positioning the lower end of a filiform structure, notably an oil pipe, at sea. United States Patent 7,066,686 B2.

Sabri, R., J. Lévine, F. Biolley, Y. Creff, C. Le Cunff and C. Putot (2003). Connection of the riser to the subsea wellhead using active control. In: *Proc. of the 2003 IEEE International Conference on Robotics and Automation (ICRA03)*. Taipei, Taiwan.

Sagatun, S. I. (2002). Active control of underwater installation. *IEEE Transactions on control systems technology* **10**(5), 743–748.

Sagatun, S. I., K. Herfjord and T. Holmås (2002). Dynamic simulation of marine risers moving relative to each other due to vortex and wake effects. *Journal of Fluids and Structures* **16**(3), 375–390.

Sagatun, S. I., K. Herfjord, F. G Nielsen and E. Huse (1999). Participating mass in colliding risers. *Journal of Marine Science and Technology* **4**(2), 58–67.

Sarpkaya, T. and R. L. Shoaff (1978). A discrete vortex analysis of flow about stationary and transversely oscillating circular cylinders. Technical Report NPS-069SL790011. Naval Postgraduate School.

Schlichting, H. (1968). *Boundary Layer Theory*. McGraw Hill Book Company Inc. New York.

Simpson, A. (1971). On flutter of a smooth circular cylinder in a wake. *The Aeronautical Quarterly* **22**(1), 25–41.

Skjetne, R. (2005). The Maneuvering Problem. PhD thesis. Departement of Engineering Cybernetics, Norwegian University of Science and Technology (NTNU). Trondheim, Norway.

Sørensen, A. J. (2005). Structural issues in the design and operations of marine control systems. *Annual Reviews in Control* **29**, 125–149.

Sørensen, A. J., B. J. Leira, C. M. Larsen and P. E. Høiskar (2002). Riser angle based position reference system. In: *Proc. of the 21st International Conference on Offshore Mechanics and Arctic Engineering*. Oslo, Norway. OMAE2002-28077.

Sørensen, A. J., B. Leira, J. P. Strand and C. M. Larsen (2001). Optimal setpoint chasing in dynamic positioning of deep-water drilling and intervention vessels. *Int. J. Robust Nonlinear Control* **11**, 1187–1205.

Sparks, C. P. (1984). The influence of tension, pressure and weigth on pipe and riser deformations and stresses. *Journal of Energy Resources Technology* **106**, 46–54. Transactions of ASME.

Stølen, S. F. (2007). Heave compensating systems for deep water drilling. Master's thesis. NTNU. Trondheim, Norway.

Sumer, B. M. and J. Fredsøe (1997). *Hydrodynamics Around Cylindrical Structures*. Vol. 12 of *Advanced Series on Ocean Engineering*. World Scientific.

Suzuki, H., K. Watanabe and K. Yoshida (1995). Operability improvment of deepsea riser by active control. In: *Proc. of the 14th International Confonference on Offshore Mechanics and Arctic Engineering*. Vol. I-B. Copenhagen, Denmark. pp. 289–297.

Tsahalis, D. T. (1984). Experimental study and modelling of the vortex-induced vibrations of a pair of risers/tethers of a compliant structure. Technical Progress Report WRC 57-83. Shell Development Company. Houston, TX.

Tsui, Y. T. (1977). On wake-induced flutter of a circular cylinder in the wake of another. *Journal of Applied Mechanics* **44**, 194–200.

Türkyilmaz, Y. (2004). Modelling and Control of Towed Seismic Cables. PhD thesis. Departement of Engineering Cybernetics, Norwegian University of Science and Technology (NTNU). Trondheim, Norway.

van Smirren, J. R., J. Romeo and M. Vogel (1999). Developements in acoustic doppler current profiling and its technical application in deepwater drilling. In: *Proc. of the 31st Annual Offshore Technology Conference*. Houston, TX. OTC 10752.

Vandiver, K. (1983). Drag coefficients of long-flexible cylinders. In: *Proc. of the Annual Offshore Technology Conference*. Houston, TX. pp. 405–410. OTC4490.

Wanvik, L. and J. Koos (2000). Two tier well top tensioning system. In: *Proc. of the 32nd Annual Offshore Technology Conference*. Houston, TX. OTC11904.

Wikipedia (2007*a*). Loop current - Wikipedia, the free encyclopedia. [Online; accessed April 21]. URL http://en.wikipedia.org/wiki/Loop_Current.

Wikipedia (2007*b*). Sonars - Wikipedia - the free encyclopedia. [Online; accessed July 2]. URL http://en.wikipedia.org/wiki/Sonar.

Wroldsen, A. (2007). Modeling and Control of Tensegrity Structures. PhD thesis. Departement of Marine Technology, Norwegian University of Science and Technology (NTNU). Trondheim, Norway.

Wu, W., S. Huang and N. Barltrop (1999). Lift and drag forces on a cylinder in the wake of an upstream cylinder. In: *Proc. of the 18th International Conference on Offshore Mechanics and Arctic Engineering*. St. John, Canada. OMAE99/OFT-4211.

Wu, W., S. Huang and N. Barltrop (2001*a*). Multiple stable/unstable equilibria of a cylinder in the wake of an upstream cylinder. In: *Proc. of the 20th International Conference on Offshore Mechanics and Arctic Engineering*. Rio de Janeiro, Brazil. OMAE2001/OFT-1170.

Wu, W., S. Huang and N. Barltrop (2001*b*). Stationary and hopf bifurcations of equilibrium positions of a cylinder situated in the near and far wake fields of an upstream cylinder. In: *Proc. of the 11th International Offshore and Polar Engineering Conference*. Stavanger, Norway. pp. 214–221.

Wu, W., S. Huang and N. Barltrop (2002). Wake-induced large amplitude low-frequency motions of a vertical riser in the wake of an upstream riser. In: *Proc. of the 21st International Conference on Offshore Mechanics and Arctic Engineering*. Oslo, Norway. OMAE2002-28035.

Zdravkovich, M. M. (1977). Review of flow interference between two circular cylinders in various arrangements. *Journal of Fluids Engineering* **99**(4), 618–633.

Zdravkovich, M. M. (1985). Forces on pipe clusters. In: *Proc. of the Conference Separated Flow around Marine Structures*. Norwegian Institute of Technology. Trondheim, Norway. pp. 201–226.

Zdravkovich, M. M. (2003). *Flow around circular cylinders*. Vol. 2. Oxford Science Publications. Oxford.

Appendix A

Mathematics and Algorithm for the FEM Model

This appendix includes a more detailed explanation of the wake field model applied in the system. The mass and stiffness matrices for an element are derived, and the damping model discussed. The load on the risers and the quasi-static algorithm are carefully explained.

A.1 Wake Field of a Single Cylinder

The downstream riser (R2) will experience shielding effects due to the upstream riser (R1). The prediction of the current on the downstream riser will be based on wake and momentum considerations given by Huse (1993) and references therein such as Schlichting (1968). Schlichting (1968) solved the equations of motion in a wake. By assuming two-dimensional motions, neglecting viscous stress and holding the pressure constant through the fluid, the turbulent wake field can be expressed as

$$b = 0.25\sqrt{C_{D1}D_1 x_s}, \tag{A.1}$$

$$U_0 = V_c\sqrt{\frac{C_{D1}D_1}{x_s}}, \tag{A.2}$$

$$u(y) = U_0 \exp\left(-0.693\left(\frac{y}{b}\right)^2\right), \tag{A.3}$$

where b is the half width of the wake, D_1 is the diameter of the riser generating the wake, x_s is the distance from the wake source, U_0 is the maximum velocity in the velocity profile, V_c is the undisturbed free stream velocity, u is the wake velocity profile and C_{D1} is the drag coefficient of the riser generating the wake.

Equation (A.1) is only expected to be valid some distance downstream of R1. Close to R1, this will give a wake peak which is too high and narrow, and hence lead to erroneous results when calculating the force on R2 placed in the wake. In order to correct for this, a virtual source upstream of R1 is introduced. This means that the distance x_s in the equation above is substituted by

$$x_s = x + x_v, \tag{A.4}$$

where x_v is the distance from the virtual source to the upstream riser, and x is the distance between the centers of the wake generating riser R1, and the downstream riser R2, on which the force is calculated. By requiring that

$$b = \frac{D_1}{2}, \tag{A.5}$$

at R1, where

$$x_s = x_v, \tag{A.6}$$

we can find x_v by

$$\frac{1}{4}\sqrt{C_{D1}D_1x_v} = \frac{D_1}{2}, \tag{A.7}$$

$$\frac{1}{4}C_{D1}D_1x_v = D_1^2, \tag{A.8}$$

$$x_v = \frac{4D_1}{C_{D1}}. \tag{A.9}$$

At large distances this correction does not make much contribution, whereas it makes a large difference in the wake field close to R1. The drag force on each element of R2 can now be found by Morison's equation

$$f_{drag,R2} = 0.5\rho D_2 C_{D2} \left|V_c - u_2\right| \left(V_c - u_2\right). \tag{A.10}$$

A problem is though that u_2 varies over the space occupied by the riser R2, such that this velocity is not well defined. This can be solved by using the root mean square (RMS) average over the riser diameter. The analytic RMS value is given by

$$u_{RMS}\left(x_s\right) = \sqrt{\frac{\int_{-D/2}^{D/2} u_2\left(x_s, y\right) y^2 dy}{\int_{-D/2}^{D/2} u_2\left(x_s, y\right) dy}}. \tag{A.11}$$

The discrete RMS value (in general) is given by

$$R\left(x\right) = \sqrt{\frac{\Sigma_{i=1}^{n} x_i^2}{n}}, \tag{A.12}$$

such that the numeric RMS value for the current on the riser diameter is

$$u_{nRMS}\left(x_s\right) = \sqrt{\frac{\Sigma_{i=1}^{m} u_n\left(x_s, y\right)_i^2}{m}}. \tag{A.13}$$

Since it is a symmetric Gaussian function, five half-side integrating points should be appropriate.

A.2 System Matrices

Dynamic analysis by the finite element method consists of four steps (Langen and Sigbjörnsson, 1979). The first step, discretization, is to subdivide the structure into elements. The second step, element analysis, is to establish the mass and stiffness matrices and the load vector for each element. The third step, system analysis, is to compute the mass and stiffness matrices and the load vector for the whole structure by concatenating the corresponding element matrices. The fourth and last step is the dynamic equilibrium equation. The second step for the mass and stiffness matrices are derived here. The steps three and four are given in Chapter 3. The load vector is derived in Appendix A.3.

A.2.1 Mass

The mass matrix is denoted *consistent* because the same interpolation polynomial is used for derivation of the displacement for both the mass and the stiffness matrices. From Langen and Sigbjörnsson (1979) the consistent mass matrix for each element is written

$$\mathbf{m} = \int_V \rho \mathbf{N}^T \mathbf{N} dV = \rho A \int_0^l \mathbf{N}^T \mathbf{N} dx, \tag{A.14}$$

where the interpolation polynomial for each pair of coordinates (x_1, x_2) and (z_1, z_2) is given by

$$\mathbf{N} = \left[\begin{array}{cc} 1 - \frac{x}{l}, & \frac{x}{l} \end{array} \right]. \tag{A.15}$$

l is the element length, such that

$$\begin{aligned} \mathbf{m}_{2\times 2} &= \int_V \rho \mathbf{N}^T \mathbf{N} dV = \rho A \int_0^l \mathbf{N}^T \mathbf{N} dx & \text{(A.16)} \\ &= \rho A \int_0^l \left[\begin{array}{cc} \left(1 - \frac{1}{l}x\right)^2 & \frac{1}{l}x\left(1 - \frac{1}{l}x\right) \\ \frac{1}{l}x\left(1 - \frac{1}{l}x\right) & \frac{1}{l^2}x^2 \end{array} \right] dx & \text{(A.17)} \\ &= \frac{\rho A l}{6} \left[\begin{array}{cc} 2 & 1 \\ 1 & 2 \end{array} \right]. & \text{(A.18)} \end{aligned}$$

The total structural mass matrix for one element is then

$$\mathbf{m}_{si} = \frac{\rho_s A l}{6} \begin{bmatrix} 2 & 0 & 1 & 0 \\ 0 & 2 & 0 & 1 \\ 1 & 0 & 2 & 0 \\ 0 & 1 & 0 & 2 \end{bmatrix}, \tag{A.19}$$

where A is the cross sectional area of the riser and ρ_s is the density of the riser material steel. The shape of the mass for the internal fluid is similar

$$\mathbf{m}_{fi} = \frac{\rho_f A_i l}{6} \begin{bmatrix} 2 & 0 & 1 & 0 \\ 0 & 2 & 0 & 1 \\ 1 & 0 & 2 & 0 \\ 0 & 1 & 0 & 2 \end{bmatrix}, \tag{A.20}$$

where A_i is the internal area of the riser and ρ_f is the density of the internal fluid. The added mass does only have components in the x-direction. The matrix for the added mass is given below as

$$\mathbf{m}_{ai} = \frac{\rho_w A_e l}{6} \begin{bmatrix} 2 & 0 & 1 & 0 \\ 0 & 0 & 0 & 0 \\ 1 & 0 & 2 & 0 \\ 0 & 0 & 0 & 0 \end{bmatrix}, \tag{A.21}$$

where A_e is the external area and ρ_w the density of water.

A.2.2 Stiffness

The stiffness matrix for one element is given in Langen and Sigbjörnsson (1979) as

$$\mathbf{k} = \int_0^l EA\mathbf{B}^T\mathbf{B}dx, \tag{A.22}$$

where E is Young's modulus of elasticity and the interpolation polynomial is given by

$$\mathbf{B} = \frac{d}{dx}\mathbf{N} = \begin{bmatrix} \frac{1}{l}, & \frac{1}{l} \end{bmatrix}, \tag{A.23}$$

such that

$$\mathbf{k}_{2\times 2} = \int_0^l EA\mathbf{B}^T\mathbf{B}dx \tag{A.24}$$

$$= \frac{EA}{l} \begin{bmatrix} 1 & -1 \\ -1 & 1 \end{bmatrix}. \tag{A.25}$$

The elastic stiffness is acting in the axial direction, and gives the local elastic stiffness matrix for each element i

$$\mathbf{k}_{EA_i} = \frac{EA}{l}\begin{bmatrix} 0 & 0 & 0 & 0 \\ 0 & 1 & 0 & -1 \\ 0 & 0 & 0 & 0 \\ 0 & -1 & 0 & 1 \end{bmatrix}. \tag{A.26}$$

The geometric stiffness acts in the lateral direction, and the geometric stiffness matrix for one element is given by

$$\mathbf{k}_{G_i} = \frac{P_i}{l_i}\begin{bmatrix} 1 & 0 & -1 & 0 \\ 0 & 0 & 0 & 0 \\ -1 & 0 & 1 & 0 \\ 0 & 0 & 0 & 0 \end{bmatrix}. \tag{A.27}$$

A.2.3 Damping

The damping matrix describes the structure's ability to dissipate energy. When damping is present in a system, the kinetic energy in this system will decrease. If it does not, an external energy supply is added. To model the damping correctly is difficult, but simplified models do usually give representative solutions; in this case, a linear viscous (velocity proportional) damping in the structure itself is used.

When a structure oscillates in a fluid, a part of the dynamic fluid pressure on the structure will be in phase with its velocity. This pressure is referred to as the hydrodynamic damping. This hydrodynamic damping usually consists of two terms. The first term is proportional to velocity and referred to as potential damping caused by wave generation. The second term is the drag force due to formation of vortices and is described by Morison's equation, see (3.25). When the cross section of the structure is small compared to the wavelength, i.e. a slender structure, the nonlinear drag term will dominate and the linear term be negligible. As a rule of thumb, the structure is slender if

$$\frac{\lambda_w}{D} > 5, \tag{A.28}$$

where λ_w is the wave length, and D is the diameter of the slender structure. Drag damping is taken into account by direct use of Morison's equation.

Structural damping should also be accounted for. A simple way of modeling this effect is to apply the Rayleigh damping given by

$$\boldsymbol{C} = \alpha_1 \boldsymbol{M} + \alpha_2 \mathbf{K}. \tag{A.29}$$

The inertia proportional term will damp out the low frequencies, while the stiffness proportional term has the opposite effect and will tend to damp out the higher frequencies. Using orthogonality properties from Langen and Sigbjörnsson (1979), we see that $\mathbf{C}$ will have the same properties as $\mathbf{M}$ and $\mathbf{K}$

$$\phi_i^T \mathbf{C} \phi_j = \alpha_1 \phi_i^T \mathbf{M} \phi_j + \alpha_2 \phi_i^T \mathbf{K} \phi_j = 0 \quad \text{for} \quad \text{i} \neq \text{j}. \tag{A.30}$$

The modal damping coefficients are given by

$$c_i = \phi_i^T \mathbf{C} \phi_i = \alpha_1 m_i + \alpha_2 k_i, \tag{A.31}$$

where ϕ_i is the mode shapes and λ_i the damping relation given by

$$\lambda_i = \frac{c_i}{2 m_i \omega_i} = \frac{1}{2} \left(\frac{\alpha_1}{\omega_i} + \alpha_2 \omega_i \right). \tag{A.32}$$

Hence, for $\alpha_1 = 0$, λ_i is proportional to ω_i and for $\alpha_2 = 0$, λ_i is inverted proportional to ω_i. If we know the overall damping level for two frequencies we can determine α_1 and α_2 by

$$\alpha_1 = \frac{2\omega_1\omega_2}{\omega_2^2 - \omega_1^2} \left(\lambda_1 \omega_2 - \lambda_2 \omega_1 \right), \tag{A.33a}$$

$$\alpha_2 = \frac{2 \left(\lambda_2 \omega_2 - \lambda_1 \omega_1 \right)}{\omega_2^2 - \omega_1^2}. \tag{A.33b}$$

The inertia term leads to damping from rigid body motions in the same way as these motions give inertia forces. This damping contribution is not wanted since structure damping is mainly caused by strains in the material of the structure. Hence, the inertia term in Rayleigh damping should not be included. The stiffness term $\alpha_2 \mathbf{K}$ is directly related to strains in the structure and can model interior structural damping adequately. The damping ratio will, however, increase with increasing frequency. The damping level, λ_i, must therefore be correct at the actual response frequency. The influence from damping at higher frequencies is without significance for the solution, and may in fact contribute to a more smooth time history since false oscillations caused by the numerical method might be suppressed.

A.3 Load on the Risers

The risers will experience load in the global horizontal direction due to currents. The current loads will induce forces on the riser, which we will find by using Morison's equation. The algorithm for loads, forces and displacements for the static initialization procedure could be summarized as follows:

1. Decompose the current from the global frame to the local frame.
2. Calculate the load at each node for each element locally.
3. Calculate the forces at each node for each element locally.
4. Transform the forces back to the global system.
5. Add the forces for each node to find the total force in the global frame.
6. Introduce load terms from for the specified motions from the TLP.
7. Find the displacement vector by $\mathbf{r} = \mathbf{K}^{-1}\mathbf{R}$.

Below each point is explained in detail.

Decompose the current from the global frame to the local frame. First the current, given in the global frame, has to be decomposed into the local frame of the node at which the current attacks. It is assumed that the global current velocity vector in each node i, $\mathbf{v}^f_{cur,i}$, only has a horizontal component, such that the v^f_z-component is zero. The flow is linear, i.e. there are no vortices in the flow. The decomposed current in i-frame is then

$$\mathbf{v}^f_{cur,i} = \begin{bmatrix} v^f_x \\ v^f_z \end{bmatrix}_i = \begin{bmatrix} v^f_x \\ 0 \end{bmatrix}_i, \tag{A.34}$$

$$\mathbf{v}^i_{cur,i} = \mathbf{T}^i_{0,f}\mathbf{v}^f_{cur,i}, \tag{A.35}$$

$$\begin{bmatrix} v^i_x \\ v^i_z \end{bmatrix}_i = \begin{bmatrix} \cos\theta_i & -\sin\theta_i \\ \sin\theta_i & \cos\theta_i \end{bmatrix} \begin{bmatrix} v^f_x \\ 0 \end{bmatrix}_i \tag{A.36}$$

$$= \begin{bmatrix} v^f_x \cos\theta_i \\ v^f_x \sin\theta_i \end{bmatrix}_i = \begin{bmatrix} v^f_{x,i} \cos\theta_i \\ v^f_{x,i} \sin\theta_i \end{bmatrix}. \tag{A.37}$$

Calculate the load at each node for each element locally. The loads in each element's two nodes are found by Morison's equation for the axial and transverse direction

$$f^i_{ext,x} = \frac{1}{2}\rho_w D_i C_{Dn} l_i v^i_x \left|v^i_x\right|, \tag{A.38}$$

$$f^i_{ext,z} = \frac{1}{2}\rho_w D_i C_{Dt} l_i v^i_z \left|v^i_z\right|, \tag{A.39}$$

where $f^i_{ext,x}$ is the external force in x_i-direction for element i. When a force, stiffness matrix etc. is described in the i-frame, it is implicitly for element i only.

ρ_w is the density of the displaced fluid, D_i the diameter of element i, and C_{Dn} and C_{Dt} the drag force coefficients in normal and tangential direction. v_x^i and v_z^i are the current velocities in the local i-frame. The load in each direction is given by

$$q_{x,1}^i = \frac{1}{2}\rho_w C_{dn} D_i v_{x,1}^i \left|v_{x,1}^i\right|, \tag{A.40}$$

$$q_{z,1}^i = \frac{1}{2}\rho_w C_{dt} D_i v_{z,1}^i \left|v_{z,1}^i\right|. \tag{A.41}$$

This gives the load in each of the two nodes of an element to be

$$q_{xi,1} = \frac{1}{2}\rho_w C_{dn} D_i v_{x,i}^f \cos\theta_i \left|v_{x,i}^f \cos\theta_i\right|, \tag{A.42}$$

$$q_{zi,1} = \frac{1}{2}\rho_w C_{dt} D_i v_{x,i}^f \sin\theta_i \left|v_{x,i}^f \sin\theta_i\right|, \tag{A.43}$$

$$q_{xi,2} = \frac{1}{2}\rho_w C_{dt} D_i v_{x,i+1}^f \cos\theta_i \left|v_{x,i+1}^f \cos\theta_i\right|, \tag{A.44}$$

$$q_{zi,2} = \frac{1}{2}\rho_w C_{dn} D_i v_{x,i+1}^f \sin\theta_i \left|v_{x,i+1}^f \sin\theta_i\right|. \tag{A.45}$$

Calculate the forces at each node for each element locally. Assuming linearly varying transverse and axial load, the load on a bar is found in Fylling *et al.* (2005) and is given as

$$\mathbf{f}_n^i = \frac{l}{6}\begin{bmatrix} 2q_{x1} + q_{x2} \\ 0 \\ q_{x1} + 2q_{x2} \\ 0 \end{bmatrix}, \tag{A.46}$$

$$\mathbf{f}_t^i = \frac{l}{6}\begin{bmatrix} 0 \\ 2q_{z1} + q_{z2} \\ 0 \\ q_{z1} + 2q_{z2} \end{bmatrix}, \tag{A.47}$$

where $\mathbf{f}_n^i$ is the normal and $\mathbf{f}_t^i$ the tangential forces. The sum of forces acting on each local element in its frame is then given by

$$\mathbf{f}^i = \mathbf{f}_t^i + \mathbf{f}_n^i. \tag{A.48}$$

This could be simplified to include forces in the x_i-direction only since these are far larger than the forces in the z_i-direction. The forces in z_i-directions will not have major impact on the dynamics, hence they could be neglected. The resulting

external force in each element is then given in the same direction as the load as

$$\mathbf{f}^i = \frac{l}{6}\begin{bmatrix} 2q_{x1} + q_{x2} \\ 0 \\ q_{x1} + 2q_{x2} \\ 0 \end{bmatrix}. \tag{A.49}$$

Transform the forces back to the global system. Before adding the forces acting at each node, they have to be represented in the same frame. The forces are transformed from its local frame to the global frame the same way as the displacements

$$\mathbf{f}_i^f = \mathbf{T}_i^f \mathbf{f}^i, \tag{A.50}$$

where $\mathbf{f}_i^f$ is the external force in the two nodes in element i given in the global f-frame.

Add the forces for each node to find the total force in the global frame. After the forces at all nodes are transformed back to the global coordinate system, the forces and moments are summarized in each node

$$f_{x,i}^f = f_{x_1,i}^f + f_{x_2,i-1}^f, \tag{A.51}$$

$$f_{z,i}^f = f_{z1,i}^f + f_{z2,i-1}^f. \tag{A.52}$$

After summarizing the forces at each node, the total force vector in f-frame due to the current forces is called $\mathbf{f}_{drag}$.

Introduce load terms for the specified motions from the TLP. The specified motions for the quasi-static case are accounted for by correction terms in the load vector. These are found from

$$\mathbf{f}_{corr} = \mathbf{f}_{drag} - \mathbf{k}_{spe} x_{TLP}, \tag{A.53}$$

where $\mathbf{f}_{corr}$ is the corrected force vector, $\mathbf{k}_{spe}$ is the specified stiffness vector and x_{TLP} is the scalar TLP motion in surge. $\mathbf{f}_{corr}$ is a vector due to the two-dimensional model, and $\mathbf{k}_{spe}$ is a vector due to the specified motion at the top node in surge only. All vectors are described in the global f-frame.

Find the displacement vector by $\mathbf{r} = \mathbf{K}^{-1}\mathbf{R}$. The displacements of the riser for the quasi-static case is then found to be

$$\mathbf{r} = \mathbf{K}^{-1}\mathbf{R}, \tag{A.54}$$

where $\mathbf{R}$ is the force vector. Upper case is used here since this is most common within the field of structural mechanics for load and force vectors. See the following iteration algorithm for equilibrium between internal and external forces.

A.4 Quasi-Static Algorithm

This algorithm seeks to find the equilibrium between the internal and external forces at each node. This includes corrected element lengths due to the elongation and top tension, and the setdown correction at each node due to current loads and deflections. The internal forces are the axial forces and are found from the position of each node, the Pythagorean theorem, Δl_i and elastic stiffness $\frac{EA}{l}$. The external forces are given by the top tension in the upper node, weight and current loads.

Step 1, Initialization

1. l_0 is the length of each element i for a stressfree configuration.

2. The initial top tension P_{top} of the vertical, tensioned riser is applied.

3. Find the axial effective tension in the middle of each element given as the tension in the element above, minus half the weight of the above and the current element. The effective tension in each element is found by

$$P_n = P_{top} - \frac{1}{2} w_{eff,n}, \tag{A.55}$$

$$P_i = P_{i+1} - \frac{1}{2}\left(w_{eff,i} + w_{eff,i+1}\right), \quad i = \{1, \ldots, n-1\}, \tag{A.56}$$

$$w_{eff,i} = \left(w_t - \rho_w \cdot g \cdot A_e + \rho_i \cdot g \cdot A_i\right)_i l_{0,i}, \tag{A.57}$$

   where P_i is the effective tension in element i positive vertical upwards, and $w_{eff,i}$ is the effective weight of element i. w_t is the true weight in air and n is the number of elements.

4. Find the new length of each element given by

$$l_i = l_0 + \frac{P_i}{EA} l_0 + \text{pressure terms}. \tag{A.58}$$

   The pressure terms take care of the contribution from external and internal pressure in the riser, but are constant in time as long as the pressure components are constant. It is hence not necessary to include these terms in the present analysis, see Sparks (1984) and Larsen (1993).

   The element lengths will not be equally long and an updated stiffness matrix for the new element lengths is needed.

5. Correct for the new element lengths and finding the new vertical positions of the nodes. Starting from the bottom and building the vector upwards, we have

$$z_1 = 0, \tag{A.59}$$
$$z_i = z_{i-1} + l_i, \tag{A.60}$$
$$z_{n+1} = z_n + l_n = z_{top}. \tag{A.61}$$

The x_i-positions are all zero, due to the vertical riser. The updated vertical z_i-positions are together with the x_i-positions stored in the vertical displacement vector $\mathbf{r}_0$.

6. Find the local stiffness matrices for each element. This gives

$$\mathbf{k}_i = \mathbf{k}_{EA_i}(l_i, P_i) + \mathbf{k}_{G_i}(l_i, P_i). \tag{A.62}$$

In this first iteration with the vertical riser, all the inclinations θ_i will be zero, such that the global and local frames are parallel. Hence,

$$\boldsymbol{\theta}_i = 0, \tag{A.63}$$
$$\mathbf{T}_i^f = \begin{bmatrix} 1 & 0 \\ 0 & 1 \end{bmatrix}. \tag{A.64}$$

7. Concatenate the local stiffness matrices to make the global stiffness matrix. This gives

$$\mathbf{K} = \begin{bmatrix} \bar{\mathbf{k}}_{11}^1 & \bar{\mathbf{k}}_{12}^1 & & & & \\ \bar{\mathbf{k}}_{21}^1 & \bar{\mathbf{k}}_{22}^1 + \bar{\mathbf{k}}_{11}^2 & \bar{\mathbf{k}}_{12}^2 & & & \\ & \bar{\mathbf{k}}_{21}^2 & \bar{\mathbf{k}}_{22}^2 + \bar{\mathbf{k}}_{11}^3 & & & \\ & & & \ddots & & \\ & & & & \bar{\mathbf{k}}_{22}^{n-1} + \bar{\mathbf{k}}_{11}^n & \bar{\mathbf{k}}_{12}^n \\ & & & & \bar{\mathbf{k}}_{21}^n & \bar{\mathbf{k}}_{22}^n \end{bmatrix}. \tag{A.65}$$

This matrix $\mathbf{K}$ is the incremental stiffness matrix for the vertical riser. Incremental means stiffness against further displacements from the deformed state. The matrix with rows and columns corresponding to the non-prescribed degrees of freedom is named $\mathbf{K}_{incr}$, whereas prescribed motions are stored in a matrix $\mathbf{K}_{pre}$.

Step 2, Move the TLP to an offset position and add current forces to the system. The top tension and effective weight are now included in $\mathbf{K}_{incr,k}$.

k is the number of iterations within the time step, $\Delta\mathbf{r}_k$ is the displacement correction term and $\Delta\mathbf{R}_k$ is the forces from current loads and TLP displacement. The forces from top tension and effective weight are already included in the stiffness matrix.

1. Solve the first iteration

$$\mathbf{K}_{incr,1}\Delta\mathbf{r}_1 = \Delta\mathbf{R}_1, \tag{A.66}$$

by following the list below.

a) Find the external load. In this first iteration, the inclination is zero, such that the global and local frames are parallel. $\mathbf{f}_{drag}$ is found from the current load and Morison's equation. Calculate the external load q in each element i, and the corresponding forces. Add the forces to find the global vector. This is described in detail in Appendix A.3.

b) The force correction due to the boundary conditions in TLP is found from

$$\Delta\mathbf{R}_{corr,1} = \mathbf{f}_{drag} - \mathbf{k}_{spe} \cdot \mathbf{r}_{TLP,1}. \tag{A.67}$$

The initial value of the current velocity on the downstream riser is assumed to be equal to the undisturbed free stream velocity in this initialization, such that the risers are standing in parallel.

c) Here the new positions for the riser elements are found after the TLP-position is included

$$\Delta\mathbf{r}_1 = \mathbf{K}^{-1}_{incr,1}\Delta\mathbf{R}_{corr,1}, \tag{A.68}$$

$$\mathbf{r}_{update} = \mathbf{r}_0 + \Delta\mathbf{r}_1, \tag{A.69}$$

where $\mathbf{r}_{update}$ is the updated riser position vector and $\Delta\mathbf{r}_1$ is the contribution from the iteration. In the vector $\mathbf{r}_0$, $x_i = 0$ and the z_i-positions are given from the updated length elements.

2. Geometric correction of the vertical position due to deflection. The element lengths l_i found in Step 1.4 are assumed correct, and the horizontal displacements are accepted. This is used to correct the displacements in the vertical direction and identify the vertical position. This will give the setdown of the top node of the riser. The new, corrected vertical position for node i is found by the Pythagorean theorem

$$z_{i,pyth} = \sqrt{l_i^2 - \Delta x_i^2}, \tag{A.70}$$

$$\Delta x_i = x_{i+1} - x_i, \tag{A.71}$$

which means that Δx_i is positive if the upper node is to the right of the node below. Starting from the bottom node, the vertical positions are given by

$$z_{1,corr} = 0, \tag{A.72}$$

$$z_{i,corr} = z_{i-1,cor} + z_{i-1,pyth}, \quad i = \{2, \ldots, n+1\}, \tag{A.73}$$

with origin of the global coordinate system in the bottom node, and z_i positive upwards. The vertical position of the next node is found by taking the previous node as the starting point for the next one. The corrected vertical position is the sum of the starting point and the distance found by (A.70). The corrected displacement vector $\mathbf{r}_{corr,1}$ is now found as the sum of the corrected vertical positions, whereas the previous values from the $\mathbf{r}_{update}$-vector are kept for the x_i-positions

$$\mathbf{r}_{corr,1} = \mathbf{r}_{update,x} + \mathbf{r}_{corr,z}. \tag{A.74}$$

The $\sin\theta_i$ and $\cos\theta_i$ values to be used in transformations between local and global coordinate systems are found from

$$\cos\theta_i = \frac{z_{i,pyth}}{l_i}, \tag{A.75}$$

$$\sin\theta_i = \frac{\Delta x_i}{l_i}. \tag{A.76}$$

Step 3, Equilibrium iterations. In this position, we start the equilibrium iterations in each node. In the initialization procedure only the static situation is considered, whereas in the time simulation, the solution is for the dynamic system.

The resulting internal force vector $\mathbf{f}^f_{int,i}$ at each node should be balanced with the external load $\mathbf{f}^f_{ext,i}$ at each node, see Fig. 3.9. The effective weight should be included in the external force when finding the equilibrium balance with the internal forces. The nodes and freedoms considered are the same as found in the stiffness matrix for the non-prescribed degrees of freedom. Hence, the two degrees of freedom in the bottom node and the horizontal degree of freedom in the top node, will not be considered in the equilibrium iterations.

1. To find the internal forces in the global frame in this equilibrium iteration, we use the inclination values found in Step 2.2, and the axial tension from Step 1.3, assuming that the internal axial force is the same along each element.

Decomposing the forces to find $\mathbf{f}_{int,i}$ at each node, we use the inclination of this element, and transform the two axial tensions to this frame. $\mathbf{P}_i^i$ is the local internal axial force vector of element i in frame i. In the first iteration, it is the effective tension found in previous steps, since this is the one we believe most in at this point of the algorithm. P_{i-1} is downwards, whereas P_i is upwards, seen from node i

$$\mathbf{P}_i^i = \begin{bmatrix} 0 \\ P_i \end{bmatrix}, \tag{A.77}$$

$$\mathbf{P}_i^f = \mathbf{T}_i^f \mathbf{P}_i^i, \tag{A.78}$$

$$\mathbf{P}_{i-1}^f = \mathbf{T}_{i-1}^f \mathbf{P}_{i-1}^{i-1}, \tag{A.79}$$

$$\mathbf{f}_{int,i}^f = \mathbf{P}_i^f - \mathbf{P}_{i-1}^f. \tag{A.80}$$

The resulting force from the axial forces at the nodes are calculated from secants for each element.

2. The secant angle over two elements between nodes $i-1$ and $i+1$ is used as an approximation for the tangent at node i

$$\sin\sigma_i = \frac{\Delta x_i}{\sqrt{\Delta x_i + \Delta z_i}}, \tag{A.81}$$

$$\cos\sigma_i = \frac{\Delta z_i}{\sqrt{\Delta x_i + \Delta z_i}}, \tag{A.82}$$

$$\Delta x_i = x_{i+1} - x_{i-1}, \tag{A.83}$$

$$\Delta z_i = z_{i+1} - z_{i-1}. \tag{A.84}$$

This inclination is found in the global system, and is used to calculate external force due to the current, $\mathbf{f}_{drag,k}$ normal to the element at each node. For the upper element we have

$$\sigma_n = \theta_n. \tag{A.85}$$

The drag forces are found using Morison's equation locally at each node. The force is thereafter transformed back to the global system. For the downstream risers, the current is a function of the distance from the upstream risers. At the upper node, we find the reaction force which gives equilibrium in the horizontal direction. The unbalanced force in the vertical direction is included in the equilibrium iterations.

3. To find the total external forces $\mathbf{f}_{ext}$, we subtract the effective weight, $\mathbf{w}_{eff}^f$, at each node (i.e. half element over and under, assumed constant) from the drag forces. The effective weight is positive downwards in the global system.

$$\mathbf{f}_{ext,k}^f = \mathbf{f}_{drag,k}^f - \mathbf{w}_{eff}^f. \tag{A.86}$$

4. The unbalanced force vector $\Delta\mathbf{R}^f_{unb,k}$ is the sum of internal and external forces as these are pointing in opposite directions

$$\mathbf{f}^f_{ext,k} - \mathbf{f}^f_{int,k} = \Delta\mathbf{R}^f_{unb,k}. \tag{A.87}$$

The resultants should be equal, but in opposite directions.

5. The criteria for ending the iteration is given by the p-norm of the unbalanced force for each degree of freedom at each node. Here we have used the l_2-norm.

$$|\mathbf{x}|_p = \left(\sum_i |x_i|^p\right)^{1/p}, \tag{A.88}$$

$$\left|\Delta\mathbf{R}^f_{unb,k}\right|_p = \left(\sum_i \left|\Delta\mathbf{R}^f_{unb,k,i}\right|^p\right)^{1/p}, \tag{A.89}$$

$$\sqrt{\sum_{i=1}^{n+1}\left[(f_{ext,x,i} - f_{int,x,i})^2 + (f_{ext,z,i} - f_{int,z,i})^2\right]} < 0.1\%P_{top}. \tag{A.90}$$

If this difference is larger than the given acceptance level, for instance 0.1% of the applied top tension, we have to start an iteration process to find the equilibrium.

6. The iteration procedure: The element lengths are still assumed to be correct. The stiffness matrix $\mathbf{K}_k$ is updated with the new positions, $\mathbf{r}_{corr,1}$ and the local matrices are the same as in Step 1.6. The transformation matrix $\mathbf{T}^f_i$ is used to transform the local matrices to the global frame calculations

$$\mathbf{k}_{ik} = \mathbf{T}^f_i \left(\mathbf{k}_{EA_i}\left(l_i, P_i\right) + \mathbf{k}_{G_i}\left(l_i, P_i\right)\right)\mathbf{T}^i_f, \tag{A.91}$$

$$\mathbf{K}_k = \begin{bmatrix} \bar{\mathbf{k}}^1_{11} & \bar{\mathbf{k}}^1_{12} & & & & \\ \bar{\mathbf{k}}^1_{21} & \bar{\mathbf{k}}^1_{22} + \bar{\mathbf{k}}^2_{11} & \bar{\mathbf{k}}^2_{12} & & & \\ & \bar{\mathbf{k}}^2_{21} & \bar{\mathbf{k}}^2_{22} + \bar{\mathbf{k}}^3_{11} & & & \\ & & & \ddots & & \\ & & & & \bar{\mathbf{k}}^{n-1}_{22} + \bar{\mathbf{k}}^n_{11} & \bar{\mathbf{k}}^n_{12} \\ & & & & \bar{\mathbf{k}}^n_{21} & \bar{\mathbf{k}}^n_{22} \end{bmatrix}. \tag{A.92}$$

The full stiffness matrix is found, but only the nonprescribed degrees of freedom are included in the matrix used in the equilibrium equations.

7. The incremental riser displacement is found from

$$\mathbf{K}_{incr,k}\Delta\mathbf{r}_k = \Delta\mathbf{R}_{unb,k}, \tag{A.93}$$

where $\mathbf{K}_{incr,k}$ is the updated stiffness matrix, $\Delta\mathbf{r}_k$ is the incremental riser displacement vector and $\Delta\mathbf{R}_{unb,k}$ is the unbalanced force for iteration k.

8. The incremental riser vector is added to the previous corrected riser vector $\mathbf{r}_{corr,k}$

$$\mathbf{r}_{corr,k+1} = \mathbf{r}_{corr,k} + \Delta\mathbf{r}_{k+1}. \tag{A.94}$$

9. New axial force in each element in the new, corrected position is calculated locally by the Pythagorean theorem. The new positions are calculated locally by

$$\begin{aligned} l_{new,i} &= \sqrt{\Delta x_i^2 + \Delta z_i^2}, && \text{(A.95)} \\ \Delta x_i &= x_{i+1} - x_i, && \text{(A.96)} \\ \Delta z_i &= z_{i+1} - z_i, && \text{(A.97)} \\ \Delta l_i &= l_{new,i} - l_0, && \text{(A.98)} \\ P_i &= \frac{EA}{l}\Delta l_i. && \text{(A.99)} \end{aligned}$$

   The new inclinations θ_i and σ_i are found in the same step as before.

10. We can then find the internal and external forces and hence the unbalanced force. For the downstream riser, the current is updated for the new position and hence the new relative distance.

A.5 Metrical Norms

The vector norms are defined in Kreyszig (1999). The norm $\|\mathbf{x}\|$ of a vector $\mathbf{x}$ is a real-valued function with the properties:

- $\|\mathbf{x}\|$ is a nonnegative real number.
- $\|\mathbf{x}\| = 0$ if and only if $\mathbf{x} = 0$.
- $\|k\mathbf{x}\| = k\|\mathbf{x}\|$ for all k.
- $\|\mathbf{x} + \mathbf{y}\| \leq \|\mathbf{x}\| + \|\mathbf{y}\|$.

The norms are labeled with subscripts. The most important is the p-norm, defined by

$$\|\mathbf{x}\|_p = (|x_1|^p + |x_2|^p + \cdots + |x_n|^p)^{1/p}, \tag{A.100}$$

where p is a fixed number. In practice, the norms most used are is $p = \{1,\, 2\,\infty\}$, that is

1. l_1-norm: $\|\mathbf{x}\|_1 = (|x_1| + |x_2| + \cdots + |x_n|)$.
2. l_2-norm: $\|\mathbf{x}\|_2 = \sqrt{(x_1^2 + x_2^2 + \cdots + x_n^2)}$.
3. l_∞-norm: $\|\mathbf{x}\|_\infty = \max_j |x_j|$.

Appendix B

Simulation Data

The data used in the verifications in Chapter 4 and the simulations in Chapters 7 and 8 are given here. This includes the environmental data, the riser characteristics and controller gains.

B.1 Environmental Data

The environmental data presented here include the current velocity profiles introduced in Section 3.1. Furthermore, data for tide and TLP offset and dynamics are included for fulfillment and validation of the values used in the simulations in this thesis. These data are from the Ormen Lange Field in the North Sea and data are found in Norsk Hydro (2001) and Aker Maritime (2002).

B.1.1 Current

The data for the current velocity profiles presented in Section 3.1 and illustrated in Fig. 3.2 are given here. The theoretical profiles, i.e. uniform, linearly sheared and bidirectional profiles are given in Table B.1. All current velocities are given in m/s. The geographically based profiles from GoM are found in Table B.2. They are based on Nowlin *et al.* (2001) and scaled to 1200m water depth and surface velocity of 1m/s. Recall that GoM1 is a wind driven profile and GoM2 has a loop eddy in the top layer. "-" means that the current velocity is linear between the values at two given water depths. The profile OL1 from the Ormen Lange field is based on Herfjord *et al.* (2002) and scaled to 1200m waters. It is also found in Table B.2. The Ormen Lange design current profile, OL2, which is used in most simulations and figures in this thesis is found in Norsk Hydro (2001) and Aker Maritime (2002), and reproduced here in Table B.3 for 1, 10 and 100 years return periods.

Depth [m]	Velocity[m/s]		
	Uniform	Linearly Sheared	Bidirectional
0	1.0	1.0	1.0
1200	1.0	0	-1.0

Table B.1: The theoretical current profiles.

Depth [m]	Velocity[m/s]		
	GoM1	GoM2	OL1
0	1.0	1.0	1.0
120	0.8	0.4	-
240	0.5	0.18	-
360	0.5	0.15	-
480	0.25	0.3	0.65
600	0.2	0.4	-
720	-	0.45	-
840	-	0.55	0.65
960	-	0.65	-
1200	0.2	0.65	0

Table B.2: The geographically based design current profiles.

B.1.2 Tide

The tidal range with 100 year return period is according to Norsk Hydro (2001) equal to 2.2m gives a tidal amplitude of 1.1m. The tide will have a period around 6 hours.

B.1.3 TLP Offset and Dynamics

The extreme case vessel offset is based on the 100 year wave, 100 year wind plus 10 year current. This gives a mean offset of 50m and a dynamic offset of

Depth below sea level [m]	Velocity[m/s]		
	1 year	10 year	100 year
0 (surface)	1.15	1.30	1.40
20	1.15	1.30	1.40
50	1.15	1.30	1.40
100	1.10	1.25	1.35
200	1.05	1.20	1.25
300	1.00	1.05	1.10
400	0.95	1.05	1.10
600	0.75	0.80	0.95
750	0.55	0.60	0.70
850	0.55	0.60	0.70

Table B.3: Ormen Lange design current velocity profile for various return periods.

17m. The maximum offset is then said to be 67m (Aker Maritime, 2002). We mainly used 30m static offset, 20m dynamic LF offset and 12m WF offset in the simulations.

B.2 Riser Data

The riser data decide the static and dynamic riser characteristics. The riser data for 1200m and 300m water depth are found in Tables B.4 and B.5, respectively.

B.3 Controller Gains

The controller gains used in the simulations in Chapter 8 are given in this section. Table B.6 gives the controller gains for both risers used in the investigation of the first control objective principle. Table B.7 gives the controller gains for the second control objective principle. In Table B.8 the controller gains used in shallow water simulations are found, and Table B.9 gives the control parameters for the supervisory switched control in Section 8.5.3.

Parameter	Description	Value	Dimension
α_2	Damping coefficient	0.0477	[-]
D_e	Diameter	0.3	[m]
d	Water depth	1200	[m]
t_h	Wall thickness	0.015	[m]
C_D	Drag coefficient	1.0	-
C_M	Mass coefficient	2.0	-
E	Modulus of elasticity	206	[GPa]
f_u	Yield stress steel	500	[MPa]
l_r	Riser length	1212	[m]
l_t	Tendon length	1166	[m]
$T_{\max}$	Upper tension limit	2700	[kN]
$T_{\min}$	Lower tension limit	1200	[kN]
ξ_0	Initial payout	0.5	[m]
ρ_s	Specific weight for steel	7850	[kg/m^3]
ρ_f	Specific weight for filling	800	[kg/m^3]
ρ_w	Specific weight for sea water	1026	[kg/m^3]
Δx_d	Initial riser distance	15	[D]

Table B.4: Riser data for 1200m water depth.

Parameter	Description	Value	Dimension
α_2	Damping coefficient	0.0477	[-]
D_e	Diameter	0.3	[m]
d	Water depth	300	[m]
t_h	Wall thickness	0.015	[m]
C_D	Drag coefficient	1.0	-
C_M	Mass coefficient	2.0	-
E	Modulus of elasticity	206	[GPa]
f_u	Yield stress steel	500	[MPa]
l_r	Riser length	312	[m]
l_t	Tendon length	266	[m]
$T_{\max}$	Upper tension limit	2700	[kN]
$T_{\min}$	Lower tension limit	350	[kN]
ξ_0	Initial payout	0.5	[m]
ρ_s	Specific weight for steel	7850	[kg/m^3]
ρ_f	Specific weight for filling	800	[kg/m^3]
ρ_w	Specific weight for sea water	1026	[kg/m^3]
Δx_d	Initial riser distance	8	[D]

Table B.5: Riser data for 300m water depth.

Parameter	Description	Value	Dimension
K_P	Proportional gain	607500	-
T_I	Integration time	8	[s]

Table B.6: Controller gains used for both risers in Sections 8.2.2, 8.2.3 and 8.4.

Parameter	Description	Value	Dimension
K_P	Proportional gain	20250	-
T_I	Integration time	30	[s]

Table B.7: Controller gains for the second control objective principle in Section 8.2.4.

Parameter	Description	Value	Dimension
K_P	Proportional gain	1000000	-
T_I	Integration time	8.5	[s]

Table B.8: Controller gains for shallow water in Section 8.3.

Parameter	Description	Value	Dimension
K_{P2}	Proportional gain 2	81000	-
K_{P3}	Proportional gain 3	27000	-
T_{D3}	Derivation time	0.2	[s]
T_I	Integration time	20	[s]
h	Switching hysteresis	0.3	-
$\Delta\mathbf{x}_d$	Desired distance	15	[D]

Table B.9: Controller gains for supervisory switched control in Section 8.5.3.

R A P P 0 R T E R
UTGITT VED
INSTITUTT FOR MARIN TEKNIKK
(tidligere: FAKULTET FOR MARIN TEKNIKK)
NORGES TEKNISK-NATURVITENSKAPELIGE UNIVERSITET

UR-79-01 Brigt Hatlestad, MK:	The finite element method used in a fatigue evaluation of fixed offshore platforms. (Dr.Ing.Thesis)
UR-79-02 Erik Pettersen, MK:	Analysis and design of celluar structures. (Dr.Ing.Thesis)
UR-79-03 Sverre Valsgård, MK:	Finite difference and finite element methods applied to nonlinear analysis of plated structures. (Dr.Ing.Thesis)
UR-79-04 Nils T. Nordsve, MK:	Finite element collapse analysis of structural members considering imperfections and stresses due to fabrication. (Dr.Ing.Thesis)
UR-79-05 Ivar J.Fylling, MK:	Analysis of towline forces in ocean towing systems. (Dr.Ing.Thesis)
UR-80-06 Nils Sandsmark, MM:	Analysis of Stationary and Transient Heat Conduction by the Use of the Finite Element Method. (Dr.Ing.Thesis)
UR-80-09 Sverre Haver, MK:	Analysis of uncertainties related to the stochastic modeling of Three-Dimensional Flow Past Lifting Surfaces and Blunt Bodies. (Dr.Ing.Thesis)
UR-85-46 Alf G. Engseth, MK:	Finite element collapse analysis of turbular steel offshore structures. (Dr.Ing.Thesis)
UR-86-47 Dengody Sheshappa, MP:	A Computer Design Model for Optimizing Fishing Vessel Designs Based on Techno-Economic Analysis. (Dr.Ing.Thesis)
UR-86-48 Vidar Aanesland, MH:	A Theoretical and Numerical Study of Ship Wave Resistance. (Dr.Ing.Thesis)
UR-86-49 Heinz-Joachim Wessel, MK:	Fracture Mechanics Analysis of Crack Growth in Plate Girders. (Dr.Ing.Thesis)
UR-86-50 Jon Taby, MK:	Ultimate and Post-ultimate Strength of Dented Tubular Members. (Dr.Ing.Thesis)

UR-86-51 Walter Lian, MH:	A Numerical Study of Two-Dimensional Separated Flow Past Bluff Bodies at Moderate KC-Numbers. (Dr.Ing.Thesis)
UR-86-52 Bjørn Sortland, MH:	Force Measurements in Oscillating Flow on Ship Sections and Circular Cylinders in a U-Tube Water Tank. (Dr.Ing.Thesis)
UR-86-53 Kurt Strand, MM:	A System Dynamic Approach to One-dimensional Fluid Flow. (Dr.Ing.Thesis)
UR-86-54 Arne Edvin Løken, MH:	Three Dimensional Second Order Hydrodynamic Effects on Ocean Structures in Waves. (Dr.Ing.Thesis)
UR-86-55 Sigurd Falch, MH:	A Numerical Study of Slamming of Two-Dimensional Bodies. (Dr.Ing.Thesis)
UR-87-56 Arne Braathen, MH:	Application of a Vortex Tracking Method to the Prediction of Roll Damping of a Two-Dimension Floating Body. (Dr.Ing.Thesis)
UR-87-57 Bernt Leira, MR:	Caussian Vector Processes for Reliability Analysis involving Wave-Induced Load Effects. (Dr.Ing.Thesis)
UR-87-58 Magnus Småvik, MM:	Thermal Load and Process Characteristics in a Two-Stroke Diesel Engine with Thermal Barriers (in Norwegian) (Dr.Ing.Thesis)
MTA-88-59 Bernt Arild Bremdal, MP:	An Investigation of Marine Installation Processes - A Knowledge- Based Planning Approach. (Dr.Ing.Thesis)
MTA-88-60 Xu Jun, MK:	Non-linear Dynamic Analysis of Space-framed Offshore Structures. (Dr.Ing.Thesis)
MTA-89-61 Gang Miao, MH:	Hydrodynamic Forces and Dynamic Responses of Circular Cylinders in Wave Zones. (Dr.Ing.Thesis)
MTA-89-62 Martin Greenhow, MH:	Linear and Non-Linear Studies of Waves and Floating Bodies. Part I and Part 11. (Dr.Techn.Thesis)
MTA-89-63 Chang Li, MH:	Force Coefficients of Spheres and Cubes in Oscillatory Flow with and without Current.(Dr.Ing.Thesis)
MTA-89-64 Hu Ying, MP:	A Study of Marketing and Design in Development of Marine Transport Systems. (Dr.Ing.Thesis)

MTA-89-65	Arild Jæger, MH:	Seakeeping, Dynamic Stability and Performance of a Wedge Shaped Planing Hull. (Dr.Ing.Thesis)
MTA-89-66	Chan Siu Hung, MM:	The dynamic characteristics of tilting-pad bearings.
MTA-89-67	Kim Wikstrøm, MP:	Analysis av projekteringen for ett offshore projekt. (Licenciat-avhandl.)
MTA-89-68	Jiao Guoyang, MR:	Reliability Analysis of Crack Growth under Random Loading, considering Model Updating. (Dr.Ing.Thesis)
MTA-89-69	Arnt Olufsen, MK:	Uncertainty and Reliability Analysis of Fixed Offshore Structures. (Dr.Ing.Thesis)
MTA-89-70	Wu Yu-Lin, MR:	System Reliability Analyses of Offshore Structures using improved Truss and Beam Models. (Dr.Ing.Thesis)
MTA-90-71	Jan Roger Hoff, MH:	Three-dimensional Green function of a vessel with forward speed in waves. (Dr.Ing.Thesis)
MTA-90-72	Rong Zhao, MH:	Slow-Drift Motions of a Moored Two-Dimensional Body in Irregular Waves. (Dr.Ing.Thesis)
MTA-90-73	Atle Minsaas, MP:	Economical Risk Analysis. (Dr.Ing.Thesis)
MTA-90-74	Knut-Aril Farnes, MK:	Long-term Statistics of Response in Non-linear Marine Structures. (Dr.Ing.Thesis)
MTA-90-75	Torbjørn Sotberg, MK:	Application of Reliability Methods for Safety Assessment of Submarine Pipelines. (Dr.Ing.Thesis)
MTA-90-76	Zeuthen, Steffen, MP:	SEAMAID. A computional model of the design process in a constraint-based logic programming environment. An example from the offshore domain. (Dr.Ing.Thesis)
MTA-91-77	Haagensen, Sven, MM:	Fuel Dependant Cyclic Variability in a Spark Ignition Engine - An Optical Approach. (Dr.Ing.Thesis)
MTA-91-78	Løland, Geir, MH:	Current forces on and flow through fish farms. (Dr.Ing.Thesis)
MTA-91-79	Hoen, Christopher, MK:	System Identification of Structures Excited by Stochastic Load Processes. (Dr.Ing.Thesis)

MTA-91-80	Haugen, Stein, MK:	Probabilistic Evaluation of Frequency of Collision between Ships and Offshore Platforms. (Dr.Ing.Thesis)
MTA-91-81	Sødahl, Nils, MK:	Methods for Design and Analysis of Flexible Risers. (Dr.Ing.Thesis)
MTA-91-82	Ormberg, Harald, MK:	Non-linear Response Analysis of Floating Fish Farm Systems. (Dr.Ing.Thesis)
MTA-91-83	Marley, Mark J., MK:	Time Variant Reliability Under Fatigue
MTA-91-79	Hoen, Christopher, MK:	System Identification of Structures Excited by Stochastic Load Processes. (Dr.Ing.Thesis)
MTA-91-80	Haugen, Stein, MR:	Probabilistic Evaluation of Frequency of Collision between Ships and Offshore Platforms. (Dr.Ing.Thesis)
MTA-91-81	Sødahl, Nils, MK:	Methods for Design and Analysis of Flexible Risers. (Dr.Ing.Thesis)
MTA-91-82	Ormberg, Harald, MK:	Non-linear Response Analysis of Floating Fish Farm Systems. (Dr.Ing.Thesis)
MTA-91-83	Marley, Mark J., MK:	Time Variant Reliability Under Fatigue Degradation. (Dr.Ing.Thesis)
MTA-91-84	Krokstad, Jørgen R., MH:	Second-order Loads in Multidirectional Seas. (Dr.Ing.Thesis)
MTA-91-85	Molteberg, Gunnar A., MM:	The application of system identification techniques to Performance Monitoring of four stroke turbocharged Diesel Engines. (Dr.Ing.Thesis)
MTA-92-86	Mørch, Hans Jørgen Bjelke, MH:	Aspects of Hydrofoil Design; with Emphasis on Hydrofoil Interaction in Calm Water. (Dr.Ing.Thesis)
MTA-92-87	Chan Siu Hung, MM:	Nonlinear Analysis of Rotordynamic Instabilities in High-speed Turbomachinery. (Dr.Ing.Thesis)
MTA-92-88	Bessason, Bjarni, MK:	Assessment of Earthquake Loading and Response of Seismically Isolated Bridges. (Dr.Ing.Thesis)
MTA-92-89	Langli, Geir, MP:	Improving Operational Safety through exploitation of Design Knowledge - an investigation of offshore platform safety. (Dr.Ing.Thesis)

MTA-92-90	Sævik, Svein, MK:	On Stresses and Fatigue in Flexible Pipes. (Dr.Ing.Thesis)
MTA-92-91	Ask, Tor Ø., MM:	Ignition and Flame Growth in Lean Gas-Air Mixtures. An Experimental Study with a Schlieren System. (Dr.Ing.Thesis)
MTA-86-92	Hessen, Gunnar, MK:	Fracture Mechanics Analysis of Stiffened Tubular Members. (Dr.Ing.Thesis)
MTA-93-93	Steinebach, Christian, MM:	Knowledge Based Systems for Diagnosis of Rotating Machinery. (Dr.Ing.Thesis)
MTA-93-94	Dalane, Jan Inge, MK:	System Reliability in Design and Maintenance of Fixed Offshore Structures. (Dr.Ing.Thesis)
MTA-93-95	Steen, Sverre, MH:	Cobblestone Effect on SES. (Dr.Ing.Thesis)
MTA-93-96	Karunakaran, Daniel, MK:	Nonlinear Dynamic Response and Reliability Analysis of Drag-dominated Offshore Platforms. (Dr.Ing.Thesis)
MTA-93-97	Hagen, Arnulf, MP:	The Framework of a Design Process Language. (Dr.Ing.Thesis)
MTA-93-98	Nordrik, Rune, MM:	Investigation of Spark Ignition and Autoignition in Methane and Air Using Computational Fluid Dynamics and Chemical Reaction Kinetics. A Numerical Study of Ignition Processes in Internal Combustion Engines. (Dr.Ing.Thesis)
MTA-94-99	Passano, Elizabeth, MK:	Efficient Analysis of Nonlinear Slender Marine Structures. (Dr.Ing.Thesis)
MTA-94-100	Kvålsvold, Jan, MH:	Hydroelastic Modelling of Wetdeck Slamming on Multihull Vessels. (Dr.Ing.Thesis)
MTA-94-101		(Dr.Ing.Thesis) *Ikke godkjent.*
MTA-94-102	Bech, Sidsel M., MK:	Experimental and Numerical Determination of Stiffness and Strength of GRP/PVC Sandwich Structures. (Dr.Ing.Thesis)
MTA-95-103	Paulsen, Hallvard, MM:	A Study of Transient Jet and Spray using a Schlieren Method and Digital Image Processing. (Dr.Ing.Thesis)
MTA-95-104	Hovde, Geir Olav, MK:	Fatigue and Overload Reliability of Offshore Structural Systems, Considering the Effect of Inspection and Repair. (Dr.Ing.Thesis)

MTA-95-105 Wang, Xiaozhi, MK:	Reliability Analysis of Production Ships with Emphasis on Load Combination and Ultimate Strength. (Dr.Ing.Thesis)
MTA-95-106 Ulstein, Tore, MH:	Nonlinear Effects of a Flexible Stern Seal Bag on Cobblestone Oscillations of an SES. (Dr.Ing.Thesis)
MTA-95-107 Solaas, Frøydis, MH:	Analytical and Numerical Studies of Sloshing in Tanks. (Dr.Ing.Thesis)
MTA-95-108 Hellan, øyvind, MK:	Nonlinear Pushover and Cyclic Analyses in Ultimate Limit State Design and Reassessment of Tubular Steel Offshore Structures. (Dr.Ing.Thesis)
MTA-95-109 Hermundstad, Ole A., MK:	Theoretical and Experimental Hydroelastic Analysis of High Speed Vessels. (Dr.Ing.Thesis)
MTA-96-110 Bratland, Anne K., MH:	Wave-Current Interaction Effects on Large-Volume Bodies in Water of Finite Depth. (Dr.Ing.Thesis)
MTA-96-111 Herfjord, Kjell, MH:	A Study of Two-dimensional Separated Flow by a Combination of the Finite Element Method and Navier-Stokes Equations. (Dr.Ing.Thesis)
MTA-96-112 Æsøy, Vilmar, MM:	Hot Surface Assisted Compression Ignition in a Direct Injection Natural Gas Engine. (Dr.Ing.Thesis)
MTA-96-113 Eknes, Monika L., MK:	Escalation Scenarios Initiated by Gas Explosions on Offshore Installations. (Dr.Ing.Thesis)
MTA-96-114 Erikstad, Stein O.,MP:	A Decision Support Model for Preliminary Ship Design. (Dr.Ing.Thesis)
MTA-96-115 Pedersen, Egil, MH:	A Nautical Study of Towed Marine Seismic Streamer Cable Configurations. (Dr.Ing.Thesis)
MTA-97-116 Moksnes, Paul O., MM:	Modeling Two-Phase Thermo-Fluid Systems Using Bond Graphs. (Dr.Ing.Thesis)
MTA-97-117 Halse, Karl H., MK:	On Vortex Shedding and Prediction of Vortex-Induced Vibrations of Circular Cylinders. (Dr.Ing.Thesis)
MTA-97-118 Igland, Ragnar T., MK:	A Thesis Submitted in Partial Fulfilment of the Requirements for the Degree of "Doktor Ingeniør". (Dr.Ing.Thesis)

MTA-97-119 Pedersen, Hans-P., MP:	Levendefiskteknologi for fiskefartøy. (Dr.Ing.Thesis)
MTA-98-120 Vikestad, Kyrre, MK:	Multi-Frequency Response of a Cylinder Subjected to Vortex Shedding and Support Motions. (Dr.Ing.Thesis)
MTA-98-121 Azadi, Mohammad R.E., MK:	Analysis of Static and Dynamic Pile-Soil-Jacket Behaviour. (Dr.Ing.Thesis)
MTA-98-122 Ulltang, Terje, MP:	A Communication Model for Product Information. (Dr.Ing.Thesis)
MTA-98-123 Torbergsen, Erik, MM:	Impeller/Diffuser Interaction Forces in Centrifugal Pumps. (Dr.Ing.Thesis)
MTA-98-124 Hansen, Edmond, MH:	A Descrete Element Model to Study Marginal Ice Zone Dynamics and the Behaviour of Vessels Moored in Broken Ice. (Dr.Ing.Thesis)
MTA-98-125 Videiro, Paulo M., MK:	Reliability Based Design of Marine Structures. (Dr.Ing.Thesis)
MTA-99-126 Mainçon, Philippe, MK:	Fatigue Reliability of Long Welds Application to Titanium Risers. (Dr.Ing.Thesis)
MTA-99-127 Haugen, Elin M., MH:	Hydroelastic Analysis of Slamming on Stiffened Plates with Application to Catamaran Wetdecks. (Dr.Ing.Thesis)
MTA-99-128 Langhelle, Nina K., MK:	Experimental Validation and Calibration of Nonlinear Finite Element Models for Use in Design of Aluminium Structures Exposed to Fire. (Dr.Ing.Thesis)
MTA-99-129 Berstad, Are J., MK:	Calculation of Fatigue Damage in Ship Structures. (Dr.Ing.Thesis)
MTA-99-130 Andersen, Trond M., MM:	Short Term Maintenance Planning. (Dr.Ing.Thesis)
MTA-99-131 Tveiten, Bård Wathne, MK:	Fatigue Assessment of Welded Aluminum Ship Details. (Dr.Ing.Thesis)
MTA-99-132 Søreide, Fredrik, MP:	Applications of underwater technology in deep water archaeology. Principles and practice. (Dr.Ing.Thesis)
MTA-99-133 Tønnessen, Rune, MH:	A Finite Element Method Applied to Unsteady Viscous Flow Around 2D Blunt Bodies With Sharp Corners. (Dr.Ing.Thesis)

MTA-99-134 Elvekrok, Dag R., MP:	Engineering Integration in Field Development Projects in the Norwegian Oil and Gas Industry. The Supplier Management of Norne. (Dr.Ing.Thesis)
MTA-99-135 Fagerholt, Kjetil, MP:	Optimeringsbaserte Metoder for Ruteplanlegging innen skipsfart. (Dr.Ing.Thesis)
MTA-99-136 Bysveen, Marie, MM:	Visualization in Two Directions on a Dynamic Combustion Rig for Studies of Fuel Quality. (Dr.Ing.Thesis)
MTA-2000-137 Storteig, Eskild, MM:	Dynamic characteristics and leakage performance of liquid annular seals in centrifugal pumps. (Dr.Ing.Thesis)
MTA-2000-138 Sagli, Gro, MK:	Model uncertainty and simplified estimates of long term extremes of hull girder loads in ships. (Dr.Ing.Thesis)
MTA-2000-139 Tronstad, Harald, MK:	Nonlinear analysis and design of cable net structures like fishing gear based on the finite element method. (Dr.Ing.Thesis)
MTA-2000-140 Kroneberg, André, MP:	Innovation in shipping by using scenarios. (Dr.Ing.Thesis)
MTA-2000-141 Haslum, Herbjørn Alf, MH:	Simplified methods applied to nonlinear motion of spar platforms. (Dr.Ing.Thesis)
MTA-2001-142 Samdal, Ole Johan, MM:	Modelling of Degradation Mechanisms and Stressor Interaction on Static Mechanical Equipment Residual Lifetime. (Dr.Ing.Thesis)
MTA-2001-143 Baarholm, Rolf Jarle, MH:	Theoretical and experimental studies of wave impact underneath decks of offshore platforms. (Dr.Ing.Thesis)
MTA-2001-144 Wang, Lihua, MK:	Probabilistic Analysis of Nonlinear Wave-induced Loads on Ships. (Dr.Ing.Thesis)
MTA-2001-145 Kristensen, Odd H. Holt, MK:	Ultimate Capacity of Aluminium Plates under Multiple Loads, Considering HAZ Properties. (Dr.Ing.Thesis)
MTA-2001-146 Greco, Marilena, MH:	A Two-Dimensional Study of Green-Water Loading. (Dr.Ing.Thesis)
MTA-2001-147 Heggelund, Svein E., MK:	Calculation of Global Design Loads and Load Effects in Large High Speed Catamarans.

	(Dr.Ing.Thesis)
MTA-2001-148 Babalola, Olusegun T., MK:	Fatigue Strength of Titanium Risers - Defect Sensitivity. (Dr.Ing.Thesis).
MTA-2001-149 Mohammed, Abuu K., MK:	Nonlinear Shell Finite Elements for Ultimate Strength and Collapse Analysis of Ship Structures. (Dr.Ing.Thesis)
MTA-2002-150 Holmedal, Lars E., MH:	Wave-current interactions in the vicinity of the sea bed. (Dr.Ing.Thesis)
MTA-2002-151 Rognebakke, Olav F., MH:	Sloshing in rectangular tanks and interaction with ship motions (Dr.Ing.Thesis)
MTA-2002-152 Lader, Pål Furset, MH:	Geometry and Kinematics of Breaking Waves. (Dr.Ing.Thesis)
MTA-2002-153 Yang, Qinzheng, MH:	Wash and wave resistance of ships in finite water depth. (Dr.Ing.Thesis)
MTA-2002-154 Melhus, Øyvin, MM:	Utilization of VOC in Diesel Engines. Ignition and combustion of VOC released by crude oil tankers. (Dr.Ing.Thesis)
MTA-2002-155 Ronæss, Marit, MH:	Wave Induced Motions of Two Ships Advancing on Parallel Course. (Dr.Ing.Thesis)
MTA-2002-156 Økland, Ole D., MK:	Numerical and experimental investigation of whipping in twin hull vessels exposed to severe wet deck slamming. (Dr.Ing.Thesis)
MTA-2002-157 Ge, Chunhua, MK:	Global Hydroelastic Response of Catamarans due to Wet Deck Slamming. (Dr.Ing.Thesis)
MTA-2002-158 Byklum, Eirik, MK:	Nonlinear Shell Finite Elements for Ultimate Strength and Collapse Analysis of Ship Structures. (Dr.Ing.Thesis)
IMT-2003-1 Chen, Haibo, MK:	Probabilistic Evaluation of FPSO-Tanker Collision in Tandem Offloading Operation. (Dr.Ing.Thesis)
IMT-2003-2 Skaugset, Kjetil Bjørn, MK	On the Suppression of Vortex Induced Vibrations of Circular Cylinders by Radial Water Jets. (Dr.Ing.Thesis)
IMT-2003-3 Chezhian, Muthu	Three-Dimensional Analysis of Slamming (Dr.Ing.Thesis)

IMT-2003-4 Buhaug, Øyvind	Deposit Formation on cylinder Liner Surfaces in Medium Speed Engines (Dr.Ing.Thesis)
IMT-2003-5 Tregde, Vidar	Aspects of Ship Design; Optimization of Aft Hull with Inverse Geometry Design (Dr.Ing.Thesis)
IMT-2003-6 Wist, Hanne Therese	Statistical Properties of Successive Ocean Wave Parameters (Dr.Ing.Thesis)
IMT-2004-7, Ransau, Samuel	Numerical Methods for Flows with Evolving Interfaces (Dr.Ing.Thesis)
IMT-2004-8, Soma, Torkel	Blue-Chip or Sub-Standard. A data interrogation approach of identity safety characteristics of shipping organization (Dr.Ing.Thesis)
IMT-2004-9 Ersdal, Svein	An experimental study of hydrodynamic forces on cylinders and cables in near axial flow (Dr.Ing.Thesis)
IMT-2005-10 Brodtkorb, Per Andreas	The Probability of Occurrence of Dangerous Wave Situations at Sea (Dr.Ing.Thesis)
IMT-2005-11 Yttervik, Rune	Ocean current variability in relation to offshore engineering (Dr.Ing.Thesis)
IMT-2005-12 Fredheim, Arne	Current Forces on Net-Structures (Dr.Ing.Thesis)
IMT-2005-13 Heggernes, Kjetil	Flow around marine structures (Dr.Ing.Thesis)
IMT-2005-14 Fouques, Sebastien	Lagrangian Modelling of Ocean Surface Waves and Synthetic Aperture Radar Wave Measurements (Dr.Ing.Thesis)
IMT-2006-15 Holm, Håvard	Numerical calculation of viscous free surface flow around Marine structures (Dr.Ing.Thesis)
IMT-2006-16 Bjørheim, Lars G.	Failure Assessment of Long Through Thickness Fatigue Cracks in Ship Hulls (Dr.Ing.Thesis)
IMT-2006-17 Hansson, Lisbeth	Safety Management for Prevention of Occupational Accidents (Dr.Ing.Thesis)
IMT-2006-18 Zhu, Xinying	Application of the CIP Method to Strongly Nonlinear Wave-Body Interaction Problems (Dr.Ing.Thesis)
IMT-2006-19 Reite, Karl Johan	Modeling and Control of Trawl Systems (Dr.Ing.Thesis)

IMT-2006	Smogeli, Øyvind Notland	Control of Marine Propellers. From Normal to Extreme Conditions (PhD Thesis)
IMT-2007-20	Storhaug, Gaute	Experimental Investigation of Wave Induced Vibrations and Their Effect on the Fatigue Loading of Ships. (Dr.Ing.Thesis).
IMT-2007-21	Sun, Hui	A Boundary Element Method Applied to Strongly Nonlinear Wave-Body Interaction Problems. (PhD Thesis) (CeSOS).
IMT-2007-22	Rustad, Anne Marthine	Modeling and Control of Top Tensioned Risers (PhD Thesis) (CeSOS)